Universidade de Aveiro
Departamento de Eletrónica, Telecomunicações e Informática,
2018

Gil Gonçalo Martins Fernandes

Optical and Digital Signal Processing in Space-Division Multiplexing Transmission Systems

Processamento Ótico e Digital de Sinal em Sistemas de Transmissão com Multiplexagem por Divisão Espacial

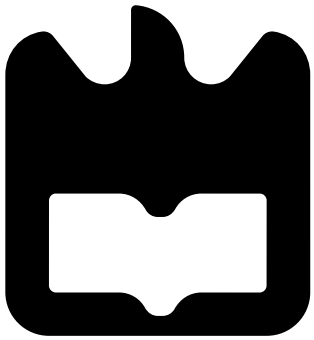

Universidade de Aveiro Departamento de Eletrónica, Telecomunicações e Informática,
2018

Gil Gonçalo Martins Fernandes

Optical and Digital Signal Processing in Space-Division Multiplexing Transmission Systems

Processamento Ótico e Digital de Sinal em Sistemas de Transmissão com Multiplexagem por Divisão Espacial

Tese apresentada à Universidade de Aveiro para cumprimento dos requisitos necessários à obtenção do grau de Doutor em Engenharia Eletrotécnica, realizada sob a orientação científica do Doutor Armando Humberto Moreira Nolasco Pinto, Professor Associado do Departamento de Eletrónica, Telecomunicações e Informática da Universidade de Aveiro, e coorientação do Doutor Nelson de Jesus Cordeiro Muga, Investigador no Instituto de Telecomunicações.

Apoio financeiro da Fundação para a Ciência e a Tecnologia através da bolsa de doutoramento FRH/BD/102631/2014 e dos projectos
CONLUZ - PTDC/FIS/112624/2009,
DiNEq - PTDC/EEI-TEL/3283/2012,
DSPMetroNet-POCI-01-0145-FEDER-029405,
MCTechs-POCI-01-0145-FEDER-029282 and UID/EEA/50008/2013
(actions SoftTransceiver and OPTICAL-5G).

o júri / the jury

presidente / president

Doutor Vitor Miguel Carneiro de Sousa Ferreira
Professor Catedrático da Universidade de Aveiro

vogais / examiners committee

Doutor Henrique José Almeida da Silva
Professor Professor Associado da Universidade de Coimbra

Doutor Adolfo da Visitação Tregeira Cartaxo
Professor Catedrático do Instituto Universitario de Lisboa

Doutor Henrique Manuel de Castro Faria Salgado
Professor Associado da Universidade do Porto

Doutor Paulo Miguel Nepomuceno Pereira Monteiro
Professor Auxiliar da Universidade de Aveiro

Doutor Armando Humberto Moreira Nolasco Pinto
Professor Auxiliar da Universidade de Aveiro (orientador)

Agradecimentos / Acknowledgements

O culminar desta etapa só foi possível com o apoio e a inestimável ajuda de várias pessoas, a todos os meus sinceros agradecimentos.

As minhas primeiras palavras vão para o meu orientador, o Professor Doutor Armando Nolasco Pinto, e ao meu coorientador, o Doutor Nelson Jesus Muga. Ao Professor Doutor Armando Nolasco Pinto, agradeço ter aceite orientar-me neste Doutoramento, assim como toda a atenção dispensada, motivação e o acompanhamento constante, sem esquecer as enriquecedoras discussões. Ao Doutor Nelson Jesus Muga, agradeço a imensa disponibilidade que sempre demonstrou, bem como a motivação proporcionada e os seus comentários inspiradores.

Aos meus colegas do Instituto de Telecomunicações, Nuno Silva, Ana Rocha, Ali Shahpari, Somayeh Ziaie e Carlos Marques, com quem partilhei estes anos de trabalho, um bem haja, por todas as discussões e sugestões. Nestes, gostaria de salientar o Álvaro Almeida e o Fernando Guiomar que com a sua boa disposição me ajudaram a ultrapassar os dias mais difíceis. Um obrigado, ao Professor Doutor Manfred Niehus e à Professora Doutora Margarida Facão pela partilha de saber e pelo estímulo por ir mais além! Deixo ainda uma palavra especial a todos os meus colegas e amigos do grupo de comunicações óticas do Instituto de Telecomunicações, pelo companheirismo e amizade que tornaram esta caminho mais fácil de percorrer. Agradeço também à Universidade de Aveiro e ao Instituto de Telecomunicações, este último na qualidade de entidade de acolhimento, por colocarem ao meu dispor todas as condições necessárias para a realização deste trabalho.

Aos meus pais, a quem devo a minha educação mas sobretudo todo o amor que depositaram em mim e que me permitiu chegar até aqui.

Finalmente, a ti, Joaquina, pela força, o alento e o carinho que me impeliram ao longo destes anos.

Palavras Chave

Sistemas de comunicação ótica, sistemas de transmissão com multiplexagem por diversidade espacial, processamento ótico de sinal, comutação entre modos/núcleos, efeito acusto-óptico, mistura de quatro ondas multimodal, processamento digital de sinal, desmultiplexagem espacial, compensação das perdas dependentes do modo, esferas de Poincaré de ordem superior.

Resumo

A presente tese tem por objectivo o desenvolvimento de técnicas de processamento ótico e digital de sinal para sistemas coerentes de transmissão ótica com multiplexagem por diversidade espacial. De acordo com a magnitude de diafonia espacial, estes sistemas podem ser agrupados em sistemas com e sem seletividade espacial, alterando drasticamente o seu princípio de funcionamento. Em sistemas com seletividade espacial, o acoplamento modal é negligenciável e, portanto, um canal espacial arbitrário pode ser encaminhado de forma independente através da rede ótica e pós-processado no recetor ótico coerente. Em sistemas sem seletividade espacial, o acoplamento modal tem um papel fulcral pelo que os canais espaciais são transmitidos e pós-processados conjuntamente. Perante este cenário, foram desenvolvidas técnicas de comutação entre canais espaciais para sistemas com seletividade espacial, ao passo que para sistemas sem seletividade espacial, foram desenvolvidas técnicas digitais de desmultiplexagem espacial.

O efeito acústico-ótico foi analisado em fibras com alguns modos (FMF) e em fibras com múltiplos núcleos (MCF) com o intuito de desenvolver técnicas de comutação de sinal no domínio ótico. Em FMF, demonstrou-se numérica e experimentalmente a comutação do sinal entre dois modos de propagação arbitrários através de ondas acústicas transversais ou longitudinais, enquanto, em MCF, a comutação entre dois núcleos arbitrários é mediada por um processo de acoplamento duplamente ressonante induzido por ondas acústicas transversais. Ainda neste contexto, analisou-se a propagação do sinal no regime multimodal não linear. Foi deduzida a equação não linear de Schrödinger na presença de acoplamento modal, posteriormente usada na análise do processo multimodal de mistura de quatro ondas. Nas condições adequadas, é demonstrado que este processo permite a comutação ótica de sinal entre dois modos de propagação distintos.

A representação de sinal em esferas de Poincaré de ordem superior é introduzida e analisada com o objetivo de desenvolver técnicas de processamento digital de sinal. Nesta representação, um par arbitrário de sinais tributários é representado numa esfera de Poincaré onde as amostras surgem simetricamente distribuídas em torno de um plano de simetria. Com base nesta propriedade, foram desenvolvidas técnicas de desmultiplexagem espacial e de compensação das perdas dependentes do modo de propagação, as quais são independentes do formato de modulação, não necessitam de sequências de treino e tendem a ser robustas aos desvios de frequência e às flutuações de fase. As técnicas referidas foram validadas numericamente, e o seu desempenho é avaliado mediante a penalidade remanescente na relação sinal-ruído do sinal pós-processado. Por fim, a complexidade destas é analiticamente descrita em termos de multiplicações reais por amostra.

keywords

Space-division multiplexing, optical signal processing, mode/core-switching, acousto-optic effect, multimodal four wave mixing, digital signal processing, space-demultiplexing, mode-dependent losses compensation, higher-order Poincaré spheres.

Abstract

The present thesis focuses on the development of optical and digital signal processing techniques for coherent optical transmission systems with space-division multiplexing (SDM). According to the levels of spatial crosstalk, these systems can be grouped in the ones with and the ones without spatial selectivity; drastically changing its operation principle. In systems with spatial selectivity, the mode coupling is negligible and therefore, an arbitrary spacial channel can be independently routed through the optical network and post-processed at the optical coherent receiver. In systems without spatial selectivity, mode coupling plays a key role in a way that spatial channels are jointly transmitted and post-processed at the optical coherent receiver. With this in mind, optical switching techniques for SDM transmission systems with spatial selectivity are developed, whereas digital techniques for space-demultiplexing are developed for SDM systems without spatial selectivity.

With the purpose of developing switching techniques, the acoustic-optic effect is analyzed in few-mode fibers (FMF)s and in multicore fibers (MCF)s. In FMF, the signal switching between two arbitrary modes using flexural or longitudinal acoustic waves is numerically and experimentally demonstrated. While, in MCF, it is shown that a double resonant coupling, induced by flexural acoustic waves, allows for the signal switching between two arbitrary cores. Still in the context of signal switching, the signal propagation in the multimodal nonlinear regime is analyzed. The nonlinear Schrödinger equation is deduced in the presence of mode coupling, allowing the meticulous analysis of the multimodal process of four-wave mixing. Under the right conditions, it is shown that such process allows for the signal switching between distinguishable optical modes.

The signal representation in higher-order Poincaré spheres is introduced and analyzed in order to develop digital signal processing techniques. In this representation, an arbitrary pair of tributary signals is represented in a Poincaré sphere, where the samples appear symmetrically distributed around a symmetry plane. Based on this property, spatial-demultiplexing and mode dependent loss compensation techniques are developed, which are independent of the modulation format, are free of training sequences and tend to be robust to frequency offsets and phase fluctuations. The aforementioned techniques are numerically validated, and its performance is assessed through the calculation of the remaining penalty in the signal-to-noise ratio of the post-processed signal. Finally, the complexity of such techniques is analytically described in terms of real multiplications per sample.

"*I invented nothing new. I simply assembled the discoveries of other men behind whom were centuries of work ... progress happens when all the factors that make for it are ready and then it is inevitable.*"

Henry Ford

À minha mãe.

À Joaquina.

À Maria e à Sara.

Contents

List of Figures

List of Tables

List of Acronyms

ADC	analog-to-digital converter
A-O	acoust-optic
AWG	arrayed waveguide grating
BER	bit-error rate
CC	coupled-core
CCG	coupled-core group
CMA	constant modulus algorithm
DA	data-aided
DC	dispersion-compensated
DD	direct-detection
DMGD	differential mode group delay
DSP	digital signal processing
DRA	distributed Raman amplification
EDF	Erbium-doped fiber
EDFA	Erbium-doped fiber amplifier
EVM	error vector magnitude
FDE	frequency domain equalization
FIR	finite impulse response
FMF	few-mode fibers
FPGA	field programmable gate array
FWHM	full width at half maximum
FWM	four-wave mixing
GSS	generalized Stokes space

HeMCF heterogeneous MCF

HoMCF homogeneous MCF

HoPs higher-order Poincaré sphere

LO local oscillator

LP linearly polarized

LPG long period fiber grating

MCF multicore fibers

MCT mode coupling theory

MD modal dispersion

MDG mode differential gain

MDM mode-division multiplexing

MDL mode dependent losses

MIMO multiple-input multiple-output

MMF multimode fiber

NLSE nonlinear Schrödinger equation

NLMS normalised least mean squares

OAM orbital angular momentum

OFDM orthogonal frequency division multiplexing

OSNR optical signal-to-noise ratio

PCF photonic crystal fiber

PDI propagation direction interleaving

PDM polarization-division multiplexing

PDL polarization-dependent loss

PM polarization-multiplexed

PMD polarization-mode dispersion

PolDemux polarization de-multiplexing

PRBS pseudorandom binary sequence

PZT piezoelectric transducer

QAM quadrature amplitude modulation

QPSK quaternary phase-shift keying

RF radio frequency

ROADM reconfigurable optical add-drop multiplexer

SSMF standard single-mode fiber

SMF single-mode fiber

SLM spatial light modulator

SDM space-division multiplexing

SE spectral efficiency

SpDemux space-demultiplexing

SPM self-phase modulation

SNR signal-to-noise ratio

SRS stimulated Raman scattering

SWSS space-wavelength-selective switch

S-Mux spatial-multiplexer

S-DeMux spatial-demultiplexer

TDE time domain equalization

WDM wavelength-division multiplexing

WSS wavelength-selective switch

XPM cross-phase modulation

List of Symbols

Symbol	Designation
$\mathcal{A}$	electric complex amplitudes
$\mathcal{B}$	magnetic complex amplitudes
c	speed of light in vacuum
c^{+}	complex amplitude to the forward wave
c_p^{-}	complex amplitude to the backward wave
c_d	bulk dilatational wave velocity
c_t	transverse wave velocity
D	central point of the constellation
d	central point of the constellation along the axis Ψ_1
d_t	summation of D parameter for all HoPs
$\mathbf{F}$	transverse distributions of the electric field[1]
$\boldsymbol{F}$, $\boldsymbol{U}_2$, $\boldsymbol{U}_3$	rotation matrix
f_{R}	fractional contribution of the Raman response
$\mathbf{G}$	transverse distributions of the magnetic field
G_{CR}	complexity reduction gain
$h(\tau)$	delayed Raman response
J_m	Bessel function of the first kind
k	propagation constant of the acoustic wave
$\boldsymbol{M}_{\mathrm{tot}}$	propagation operator
$\boldsymbol{M}_{\mathrm{MD}}$	mode-dependent effects operator
N_p	normalization coefficient
$N_{\mathrm{HoPs,\ ref}}$	number of HoPs required by the static algorithm
N_{HoPs}	number of HoPs required by a SpDemux filter
N_{m}	number of real multiplications

[1] Throughout this thesis the vectors are denoted by bold, while matrices are in italic and bold.

N_{s}	number of real additions
n	refractive index
n_2	nonlinear refractive index
$\mathbf{n}_p$	normal to the planne
$\bar{n}_{\mathrm{eff}}$	effective refractive index
δn_{eff}	amplitude of the index perturbation
$\mathbf{P}_{\mathrm{NL}}$	nonlinear induced electric polarization
$R(t)$	normalized nonlinear response function
$\mathbf{r}$	spatial coordinate
r	radial coordinate
r_c	microwire radius
$\bar{r}$	average microwire radius
δr	variation of the microwire radius
S_{zz}	strain distribution along the fiber
$\boldsymbol{T}^{(f,g)}$	translation matrices
t	temporal coordinate
$\boldsymbol{U},\ \boldsymbol{V}$	random unitary matrices
U	axial variation of the radial displacement component
u_r	radial displacement component
u_ϕ	azimuthal displacement component
u_z	longitudinal displacement component
V	axial variation of the azimuthal displacement component
W	axial variation of the longitudinal displacement component
$\mathbf{x}$	spatial coordinates in the transverse plane
z	longitudinal coordinate
α	optical losses
β	propagation constant
β^0	propagation constant for the fundamental mode
β_j^p	jth order dispersion coefficient for the p mode
$\bar{\beta}_2$	mode-averaged chromatic dispersion per unit length
$\boldsymbol{\Gamma}$	mode dependent losses vector
Γ_{lm}	mode coupling coefficient normalized to the index perturbation
γ	nonlinear coeficient
Δ	SNR penalty

$\Delta\beta$	phase-matching condition
δ_{pm}	Kronecker delta
ζ	summation of the absolute value of the residuals
κ	normalization parameter
λ_M, μ_M	Lame's constants
$\boldsymbol{\Lambda}$	generalized Pauli matrices
$\boldsymbol{\Lambda}^{(f,g)}$	Pauli spin vector in a HoPs
λ	wavelength
μ_0	vacuum permeability
μ	step size for the NLMS algorithm
ω	angular frequency
ϕ	azimuthal coordinate
ε	electric permittivity
ε_0	vacuum permittivity
ε_r	relative permittivity
ϑ	coupling coefficient
Ω	angular frequency of the acoustic wave
Ω_{Ad}	adiabatic angle
$\boldsymbol{\Phi}$	circumferential displacement distribution
Φ_r	radial component of the circumferential displacement distribution
Φ_ϕ	azimuthal component of the circumferential displacement distribution
Φ_z	longitudinal component of the circumferential displacement distribution
ρ_M	material density
χ	elasto-optic coefficient
τ_{plmn}	shock time constant
$\chi^{(3)}$	3rd order susceptibility
∇	gradient operator
∇_T	gradient operator operator over the transverse coordinates
$\|\psi\rangle$	multimodal signal
υ	tributary signal
$\boldsymbol{\Psi}$	generalized Stokes vector
$\boldsymbol{\Psi}^{(g,f)}$	Stokes vector in a HoPs
ε_{R}	relative variation of the absolute value of the residuals
$\varepsilon_{\mathrm{ST}}$	maximum relative variation of the he absolute value of the residuals

ρ	square root of the gain/loss for a tributary signal

Chapter 1

Introduction

In the past three decades, the aggregated bit-rate of commercial fiber-optic transmission systems has increased by a factor of four orders of magnitude by means of multiplexing techniques that use time, and wavelength and polarization of light to encode information [1–3]. Nevertheless, the optical losses of silica-based SSMF along with the gain window of the Erbium-doped fiber amplifier (EDFA), both main cornerstones of commercial fiber-optic transmission systems, limit its bandwidth; where the last one is generally considered as the key factor [4]. The aggregated bit-rate of such transmission systems was further increased by means of optical coherent detection, which provides access to an additional degree of freedom to encode and transmit information: the phase [3]. With the possibility to retrieve phase and amplitude information of the optical carrier, a cascade of powerful digital signal processing (DSP) subsystems was developed to successfully compensate for the linear [5, 6] and even for the deterministic nonlinear transmission impairments [7, 8]. However, and despite the huge efforts to develop alternative reduced-complexity algorithms [8], nonlinear equalization is still presenting a high computational complexity, making its hardware implementation challenging from a technical and economic point of view. As a result of such remarkable achievements, the aggregated bit-rate transmitted through a SSMF has reached more than 100 Tbits s^{-1} [9, 10]; approaching to the expected maximum value of the aggregated bit-rate for a SSMF-based transmission systems taking into account the currently available technology, i.e., laser sources and EDFA [4, 11, 12], see Fig. 1.1.

Due to the growing popularity of "Big Data", cloud computing, social networking, real-time gaming, high definition video streaming and many others bandwidth-hungry applications [13, 14], the demand for higher aggregated bit-rates will certainly continue. Moreover, the next-generation mobile broadband (5G) along with the Internet of Things will need be supported by fiber-optic transmission systems, leading to an expected Internet traffic grow rate around 23% per year [15]. Considering such forecasted Internet traffic growth and considering also the actual network capacity, it is expected that the network capacity will be exhausted in a few years [15]. To tackle this huge challenge, industry and academia have carried out a tremendous research effort to increase the aggregated bit-rate transmitted through a SSMF; however, by each research effort to increase the aggregated bit-rate has resulted in marginal returns. This scenario, commonly named of "capacity crunch" of optical transmission systems, has driven the scientific community and the commercial partners to look for alternatives to overcome this major obstacle. In that way, a new paradigm in fiber-optic transmission systems must be laid out using novel ways to increase the number of parallel channels transmitted

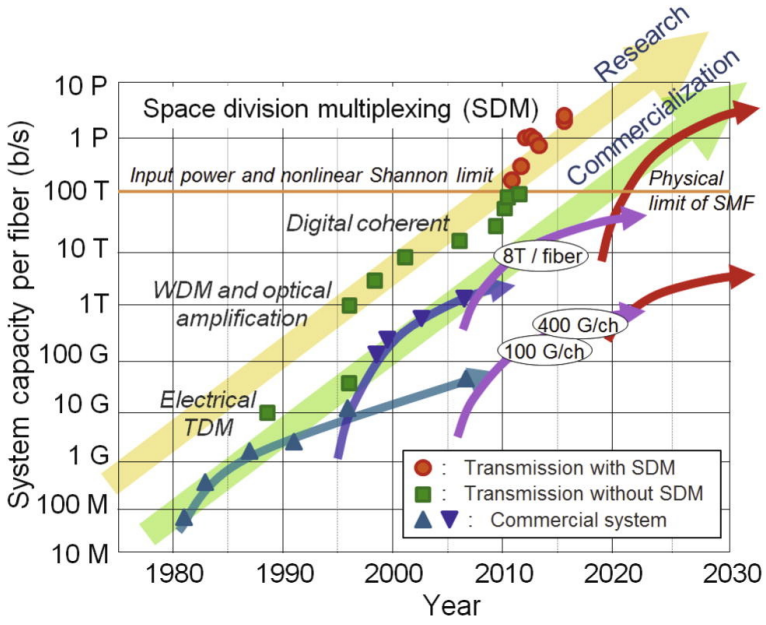

Figure 1.1: Evolution of the aggregated bit-rate per fiber in fiber-optic transmission systems. The key technological breakthroughs include the development of WDM, high-spectral efficiency coding via DSP-enabled coherent transmission and more recently SDM. SDM appears technically capable of providing the next step change in terms of aggregated bit-rate; from [11].

through a single fiber or, in other words, by exploring an additional orthogonal multiplexing dimension. Against this backdrop, space emerges as the unique untapped dimension provided by the optical fiber that enables to address this challenge.

Spatial-multiplexing comprises different multiplexing techniques that establish multiple distinguishable spatial data pathways through multiple fibers or through a single fiber [16]. In the first approach, an aggregate of several independent SSMFs (or thin single-mode fiber (SMF)s) are packed together to create a ribbon cable (or a multi-element fiber), without any increment in the aggregated bit-rate per fiber link [2]. In the second approach special fibers are employed with several distinguishable data pathways. In principle, the aggregated bit-rate of the fiber link can be increased by a factor proportional to the number of distinguishable data pathways [17]. But also, and perhaps more importantly, the overall energy efficiency of the transmission system can be enhanced, leading to an additional decrease in terms of the cost-per-bit [16, 18, 19]. Hereafter, the term space-division multiplexing (SDM) is only employed to refer spatial multiplexing techniques through a single fiber.

When several spatial channels are transmitted through the same fiber, mode/core coupling tends to unavoidably mix all the spatial channels. The optical power transferred between the spatial channels, or the spatial crosstalk[1], depends mainly on the physical properties of the optical fiber and on the link length. In the absence of crosstalk, the transmission system with SDM remains quite similar to their counterparts based in SSMF; the signals are independently routed through the network being detected and post-processed by a standard optical coherent receiver. In contrast, in the presence of crosstalk, the routing strategies and the post-processing techniques at the coherent receiver must be properly adapted, changing

[1]Henceforward, the term "crosstalk" is employed to designate the "spatial crosstalk".

the operation principle of the transmission system. In that way, SDM transmission systems can be grouped into two main sets: the ones with and the ones without spatial selectivity. Usually, transmission systems with spatial selectivity have been concretized by using long lengths of multicore fibers (MCF)s, where the data streams are transmitted through distinguishable silica cores, or short lengths of few-mode fibers (FMF)s, in which the orthogonal modes of a FMFs are employed to guide the optical signals [17, 20]. On the other hand, in transmission systems without spatial selectivity a plurality of coupled modes are employed to transmit several independent data streams through a FMF/multimode fiber (MMF) or a coupled-core (CC)-MCF [16, 20]; being the tributaries jointly routed and post-processed at the optical coherent receiver.

With an aggregated bit-rate higher than 1 Pbit s^{-1} per fiber [21], SDM appears as an unavoidable step in the development of next-generation fiber-optic transmission systems. Such capacity, integration and energy efficiency gains, must be extended to next-generation networks in different application areas, from data-center interconnections up to long-haul transmission systems [22–24]. Nowadays, the feasibility of SDM has been widely demonstrated using both MCF and FMF approaches [16, 18, 25], although further developments in the design and fabrication of this kind of fibers are expected. In parallel, spatial-multiplexing interfaces have also been investigated and experimentally demonstrated for both aforementioned approaches. Notice that spatial-multiplexer (S-Mux)s and spatial-demultiplexer (S-DeMux)s are fundamental building blocks for the sustainable development of SDM-based transmission systems. However, some challenges in terms of rooting (or switching), all-optical amplification and DSP still persisting, hindering the commercial development of transmissions systems with SDM.

1.1 Motivation and objectives

SDM represents the last frontier of multiplexing, enormously increasing the number of tributaries transmitted through an optical fiber. The combination of space- and wavelength-division multiplexing results into an unprecedented value of overall aggregated bit-rate. Although all the SDM approaches share the same cornerstone (i.e., increasing the number of spatial channels per fiber), the crosstalk levels may fundamentally changes the operation principle of the SDM network and its main subsystems. Such key changes are particularly evident in reconfigurable optical add-drop multiplexer (ROADM)s, responsible for the routing at the nodes of the optical network, and the DSP subsystems at the optical coherent receiver, in which the signal impairments must be compensated an/or equalized. In transmission systems with spatial selectivity, the spatial and wavelength channels can be independently routed, or switched, making possible a more efficient exploitation of the potentialities of this kind of optical channels and networks. In contrast, in transmission systems without spatial selectivity, the set of tributaries space-multiplexed must be jointly switched in order to be post-processed by multiple-input multiple-output (MIMO) algorithms at the digital subsystems of the optical coherent receiver; hence enabling the digital space-demultiplexing (SpDemux) of the received signal. It should be emphasized that the increased number of tributaries imposes new challenges in the development of MIMO algorithms that must be able to support the next-generation flexible optical networks based on SDM.

In this thesis, we aim to investigate optical and digital techniques for signal processing for future SDM transmission systems. Therefore, the work of this thesis has been planned to

accomplish the following three main objectives:

i) modeling of optical signal propagation in SDM links taking into account the linear and nonlinear fiber-optic propagation effects;

ii) development of switching techniques and devices with spatial and wavelength selectivity for SDM transmission systems;

iii) development of DSP techniques for future flexible optical transmission systems based on SDM.

1.2 Thesis outline

The following Chapters present theoretical, numerical and experimental investigations on signal propagation in MCF and FMF, as well as novel optical and digital techniques for signal processing in fiber-optic transmission systems based on SDM. This thesis is comprised of six Chapters, organized as follows:

- Chapter 2 presents a brief state-of-the-art of SDM transmission systems and main building blocks, including a review of novel fibers for SDM, spatial (de-)multiplexers, MCF- and FMF-based in-line amplifiers, switching devices and DSP subsystems. In addition, the progress of the aggregated bit-rate and reach mark records achieved in the past years are also revisited.

- Chapter 3 deals with the subject of signal switching in SDM transmission systems with spatial selectivity. Anchored in the mode coupling theory (MCT), we investigate the resonant coupling induced by the acoust-optic (A-O) effect in FMFs and MCFs. Firstly, the mode switching in FMFs induced by the A-O effect was investigated. By properly choosing the kind (longitudinal and flexural) and the frequency of the acoustic wave, we show that an efficient mode conversion between two arbitrary modes can be achieved. Secondly, we address the core switching in MCF, investigating how the spatial orientation of flexural waves determines the efficiency of the energy transfer between cores in homogeneous and heterogeneous MCF.

- Chapter 4 deals with the subject of optical signal processing in SDM transmission systems. We extended the multimodal generalised nonlinear Schrödinger equation (NLSE) to take into account the mode coupling. Based on such propagation equation, we investigate the nonlinear process of multimodal four-wave mixing (FWM). The intermodal and intramodal phase-matching condition are investigated in optical microwires, which is a multimodal and highly nonlinear waveguide. Lastly, we analyse the energy transfer induced by the multimodal FWM in optical microwires.

- Chapter 5 focuses on the issue of DSP in SDM-based transmission systems without spatial selectivity; more precisely in the subject of digital space-demultiplexing. We start by introducing the signal representation in higher-order Poincaré sphere (HoPs)s and its intrinsic connection with the generalized Stokes space (GSS). We show that an arbitrary space-multiplexed signal can be fully represented in several HoPs. A given pair of tributaries can be represented in a HoPs, in which the crosstalk between both tributaries change the spatial orientation of the best fit plane. Thus, the crosstalk can

be compensated by realigning this plane. However, the successful space-demultiplexing relies on a suitable sequence of all considered HoPss. Such sequence can be found by properly analyzing the symmetry of the samples around the best fit plane in all the HoPss.

- Chapter 6 deals with the subject of monitoring and compensation of mode dependent losses (MDL). We show that MDL can be monitored and compensated in the digital domain by analyzing the received samples in HoPss. When an arbitrary pair of tributaries is represented in the respective HoPs, the MDL induces a shift of the constellation. The entire MDL vector can be accurately estimated by computing this shift in all HoPss. Hence, the signal distortions arising from MDL can be successfully compensated by moving the constellation to the original position in the respective HoPs.

- Finally, the main conclusions and suggestions for future research topics are summarized in Chapter 7.

This thesis also includes a list of acronyms, figures, tables and symbols.

1.3 Main contribution

In this thesis, there are developed models that are able to address the signal propagation in the multimodal regime, along with novel optical and digital techniques for signal processing in SDM transmission systems. In the author opinion, the most important results reported in this thesis are the following:

i) development, numerical assessment and experimental validation of switching techniques for SDM transmission systems based on the A-O effect [26–29];

ii) analytical formulation of the multimodal generalized NLSE and numerical analysis of the multimodal process of FWM in optical microwires [30, 31];

iii) investigation of the signal representation in HoPss and discussion of its intrinsic connection with the GSS [32, 33];

iv) development and numerical assessment of novel DSP techniques based on the signal representation in HoPss [32–35].

1.4 List of publications

The major achievements obtained from the work of this thesis were submitted for peer-review by the international scientific community through the following list of publications.

Papers in international journals

12. **Gil M. Fernandes**, Nelson J. Muga and Armando N. Pinto, “Digital monitoring and compensation of mode-dependent losses based on higher-order Poincaré spheres”, to be submitted to IEEE Photonics Journal.

11. **Gil M. Fernandes**, Nelson J. Muga and Armando N. Pinto, " Reduced-complexity algorithm for space-demultiplexing based on higher-order Poincaré spheres", OSA Optics Express, Vol. 26, pp. 13506–13506, 2018.

10. **Gil M. Fernandes**, Nelson J. Muga and Armando N. Pinto, "Space-demultiplexing based on higher-order Poincaré spheres", OSA Optics Express, Vol. 25, pp. 3899–3899, 2017.

9. Somayeh Ziaie, Nelson J. Muga, Fernando P. Guiomar, **Gil M. Fernandes**, Ricardo M. Ferreira, Ali Shahpari, António L. Teixeira and Armando N. Pinto, "Experimental assessment of the adaptive Stokes space-based polarization demultiplexing for optical metro and access networks", IEEE/OSA Lightwave Technology, Journal of, Vol. 33, No. 23, pp. 4968–4974, 2015.

8. **Gil M. Fernandes**, Nelson J. Muga, Ana M. Rocha and Armando N. Pinto, "Switching in multi-core fibers using flexural acoustic waves", OSA Optics Express, Vol. 23, pp. 26313–26325, 2015.

7. **Gil M. Fernandes**, Nelson J. Muga and Armando N. Pinto, "Four-wave mixing in microwires to all-optical signal processing in mode-division multiplexing systems ", Fiber and Integrated Optics, Vol. 34, No. 1–2, pp. 38–52, 2015.

6. Andis Supe, **Gil M. Fernandes**, Nelson J. Muga, Armando N. Pinto and Mário Ferreira, "Polarization effects on the nonlinearity of a highly nonlinear fiber", Fiber and Integrated Optics, Vol. 34, No. 1–2, pp. 3–13, 2015.

5. Bruno Tiburcio, **Gil M. Fernandes**, Jorge Monteiro, Silvia Rodrigues, Mario Ferreira, Margarida Facão, Maria I. Carvalho and Armando N. Pinto, "EIT in hollow-core fibers for optical communications devices", Microwave and Optical Technology Letters, Vol. 57, No. 2, pp. 348–352, 2015.

4. **Gil M. Fernandes**, Nelson J. Muga and Armando N. Pinto, "Tunable mode conversion using acoustic waves in optical microwires", IEEE/OSA Lightwave Technology, Journal of, Vol. 32, No. 19, pp. 3257–3265, 2014.

3. Margarida Facão, Maria I. Carvalho, **Gil M. Fernandes**, Ana M. Rocha and Armando N. Pinto, "Continuous wave supercontinuum generation pumped in the normal group velocity dispersion regime on a highly nonlinear fiber", Journal of Optical Society of America B, Vol. 30, No. 4, pp. 959–966, 2013.

2. **Gil M. Fernandes**, Álvaro J. Almeida, Manfred Niehus and Armando N. Pinto, "Theoretical analysis of multimodal four-wave mixing in optical microwires", IEEE/OSA Lightwave Technology, Journal of, Vol. 31, No. 2, pp. 195–202, 2013.

1. Ana M. Rocha, **Gil M. Fernandes**, Fátima Domingues, Manfred Niehus, Armando N. Pinto, Margarida Facão and Paulo S. André, "Halting the fuse effect propagation using tapered optical fibers", OSA Optics Express, Vol. 20, pp. 21083–21088 (2012).

Papers in conference proceedings

13. Nelson J. Muga, **Gil M. Fernandes**, Mário J. N. Lima, Armando N. Pinto, Paulo S. André, Margarida Facão, Ana M. Rocha, "Optical and digital key enabling techniques for SDM-based optical networks", In proceedings of *International Conference on Transparent Optical Networks* ICTON, Bucareste, Romania, paper We.D1.2, July, 2018.

12. Nelson J. Muga, **Gil M. Fernandes**, Somayeh Ziaie, Ricardo M. F. Ferreira, Ali Shahpari, Antonio Teixeira, Armando N. Pinto, "Advanced digital signal processing techniques based on Stokes space analysis for high-capacity coherent optical systems", In proceedings of *International Conference on Transparent Optical Networks* ICTON, Girona, Spain, paper We.C1.1, July, 2017.

11. **Gil M. Fernandes**, Nelson J. Muga, Armando N. Pinto "MIMO processing based on higher-order Poincaré spheres". In proceedings of *III International Conference on Applications in Optics and Photonics* AOP, Faro, Portugal, paper AO100-177 , May, 2017.

10. Bruno Tiburcio, **Gil M. Fernandes**, Jorge M. Monteiro, Sílvia Rodrigues, M. Inês Carvalho, Margarida Facão, Mário Ferreira, Armando N. Pinto "Experimental setup for electromagnetically induced transparency observation in hollow-core fibers". In proceedings of *Second International Conference on Applications of Optics and Photonics* AOP, Aveiro, Portugal, Vol. 9286, pp. 92860H-1–992860H-6, August, 2014.

9. **Gil M. Fernandes**, Nelson J. Muga, Armando N. Pinto "Mode conversion based on the acousto-optic effect for mode division multiplexed transmission". In proceedings of *Second International Conference on Applications of Optics and Photonics* AOP, Aveiro, Portugal, Vol. 9286, pp. 92863J-1–92863J-8, August, 2014.

8. Andis Supe, **Gil M. Fernandes**, Nelson J. Muga, Armando N. Pinto, Mário Ferreira, "Effective nonlinear parameter measurement using FWM in a highly nonlinear fiber". In Workshop on *Specialty Optical Fibers and their Applications* (WSOF), paper W3.27, Sigtuna, Sweden, August, 2013.

7. **Gil M. Fernandes**, Bruno Tiburcio, Nelson J. Muga, Armando N. Pinto "Wavelength-shift-free Mamyshev regenerator". In proceedings of *8th Iberoamerican Optics Meeting and 11th Latin American Meeting on Optics, Lasers, and Applications* RIAO/OPTILAS, Porto, Portugal, Vol. 8785, pp. 8785F3-1–8785F3-6, July, 2013.

6. Andis Supe, **Gil M. Fernandes**, Nelson J. Muga, Armando N. Pinto, Mário Ferreira, "Pump and filtering optimization in Mamyshev regenerator". In proceedings of *8th Iberoamerican Optics Meeting and 11th Latin American Meeting on Optics, Lasers, and Applications* RIAO/OPTILAS, Porto, Portugal, Vol. 8785, pp. 8785CI-1–8785CI-5, July, 2013.

5. Bruno Tiburcio, **Gil M. Fernandes**, Armando N. Pinto, "Extremely small-core photonic crystal fiber fusion splicing with a single-mode fiber". In proceedings of *8th Iberoamerican Optics Meeting and 11th Latin American Meeting on Optics, Lasers, and Applications* RIAO/OPTILAS, Porto, Portugal, Vol. 8785, pp. 8785FF-1–8785FF-5, July, 2013.

4. Andis Supe, **Gil M. Fernandes**, Nelson J. Muga, Armando N. Pinto, Mário Ferreira, "Experimental characterization of a highly nonlinear fiber". In proceedings of *8th Iberoamerican Optics Meeting and 11th Latin American Meeting on Optics, Lasers, and Applications* RIAO/OPTILAS, Porto, Portugal, Vol. 8785, pp. 87854D-1–87854D-6, July, 2013.

3. Nelson J. Muga, **Gil M. Fernandes**, Armando N. Pinto, "Nonlinear polarizers in low-birefringence optical fibers". In proceedings of *8th Iberoamerican Optics Meeting and 11th Latin American Meeting on Optics, Lasers, and Applications* RIAO/OPTILAS, Porto, Portugal, Vol. 8785, pp. 8785F4-1–8785F4-5, July, 2013.

2. **Gil M. Fernandes**, Margarida Facão, M. Inês Carvalho, Sílvia Rodrigues, J. Heidarialamdarloo, Armando N. Pinto, Mário Ferreira, "Continuous wave supercontinuum generation aided by a weaker pulse laser". In proceedings of *SPIE Photonic*, Bruxelles, Belgium, Vol. 8434, pp. 843413-1–843413-8, April, 2012.

1. **Gil M. Fernandes**, Manfred Niehus, Carlos A. F. Marques, Rogerio Nogueira, Armando N. Pinto, "Acousto-Optic tunable mode coupler". In proceedings of the *Optical Fiber Conference* OFC, Los Angeles, USA, paper JTh2A, March, 2012.

Book chapters

1. **Gil M. Fernandes**, Nelson J. Muga and Armando N. Pinto, "Space-Division Multiplexing in Fiber-Optic Transmission Systems", Chapter in, Optical Fibers: Technology, Communications and Recent Advances, Mário F. S. Ferreira, Nova Publisher, New York, 2017.

Bibliography

[1] G. P. Agrawal, *Lightwave Technology Telecommunication Systems.* University of Rochester, New York: John Wiley & Sons, 2005.

[2] J. Hecht, *City of Light: The Story of Fiber Optics.* Oxford University Press, 1999.

[3] R.-J. Essiambre, P. J. Winzer, X. Q. Wang, W. Lee, C. A. White, and E. C. Burrows., "Electronic predistortion and fiber nonlinearity," *IEEE Photonics Technology Letters*, vol. 18, no. 17, pp. 1804–1806, Sept 2006.

[4] D. J. Richardson, "New optical fibres for high-capacity optical communications," *Philosophical Transactions of the Royal Society A*, vol. 374, no. 2062, p. 20140441, 2016.

[5] S. Savory, "Digital filters for coherent optical receivers," *Optics Express*, vol. 16, no. 2, pp. 804–817, Jan 2008.

[6] S. Savory, "Digital coherent optical receivers: algorithms and subsystems," *IEEE Journal of Selected Topics in Quantum Electronics*, vol. 16, no. 5, pp. 1164–1179, 2010.

[7] E. M. Ip and J. M. Kahn, "Fiber impairment compensation using coherent detection and digital signal processing," *IEEE/OSA Journal of Lightwave Technology*, vol. 28, no. 4, pp. 502–519, Feb 2010.

[8] F. P. Guiomar and A. N. Pinto, "Simplified Volterra series nonlinear equalizer for polarization-multiplexed coherent optical systems," *IEEE/OSA Journal of Lightwave Technology*, vol. 31, no. 23, pp. 3879–3891, Dec 2013.

[9] A. Sano, T. Kobayashi, S. Yamanaka, A. Matsuura, H. Kawakami, Y. Miyamoto, K. Ishihara, and H. Masuda, "102.3-Tb/s (224 x 548-Gb/s) C- and extended L-band all-Raman transmission over 240 km using PDM-64QAM single carrier FDM with digital pilot tone," in *Optical Fiber Conference (OFC)*. Optical Society of America, 2012, p. PDP5C.3.

[10] D. Qian, E. Ip, M.-F. Huang, M. Li, A. Dogariu, S. Zhang, Y. Shao, Y.-K. Huang, Y. Zhang, X. Cheng, Y. Tian, P. Ji, A. Collier, Y. Geng, J. Linares, C. Montero, V. Moreno, X. Prieto, and T. Wang, "1.05Pb/s transmission with 109b/s/Hz spectral efficiency using hybrid single- and few-mode cores," in *Frontiers in Optics 2012/Laser Science XXVIII*. Optical Society of America, 2012, p. FW6C.3.

[11] T. Mizuno and Y. Miyamoto, "High-capacity dense space division multiplexing transmission," *Optical Fiber Technology*, vol. 35, no. Supplement C, pp. 108 – 117, 2017.

[12] R. Essiambre, G. Kramer, P. J. Winzer, G. J. Foschini, and B. Goebel, "Capacity limits of optical fiber networks," *IEEE/OSA Journal of Lightwave Technology*, vol. 28, no. 4, pp. 662–701, Feb 2010.

[13] T. Mizuno, H. Takara, A. Sano, and Y. Miyamoto, "Dense space division multiplexed transmission over multi-core and multi-mode fiber," in *Optical Fiber Communications (OFC)*, March 2015, p. Th1D.2.

[14] W. Klaus, B. J. Puttnam, R. S. Luis, J. Sakaguchi, J. M. D. Mendinueta, Y. Awaji, and N. Wada, "Advanced space division multiplexing technologies for optical networks [invited]," *IEEE/OSA Journal of Optical Communications and Networking*, vol. 9, no. 4, pp. C1–C11, April 2017.

[15] P. J. Winzer and D. T. Neilson, "From scaling disparities to integrated parallelism: A decathlon for a decade," *IEEE/OSA Journal of Lightwave Technology*, vol. 35, no. 5, pp. 1099–1115, March 2017.

[16] D. J. Richardson, J. M. Fini, and L. E. Nelson, "Space-division multiplexing in optical fibres," *Nature Photonics*, vol. 7, pp. 354–362, May 2013.

[17] P. Sillard, "Next-generation fibers for space-division-multiplexed transmissions," *IEEE/OSA Journal of Lightwave Technology*, vol. 33, no. 5, pp. 1092–1099, March 2015.

[18] G. Li, N. Bai, N. Zhao, and C. Xia, "Space-division multiplexing: the next frontier in optical communication," *Advances in Optics and Photonics*, vol. 6, no. 4, pp. 413–487, Dec 2014.

[19] J. M. Kahn and D. A. Miller, "Communications expands its space," *Nature photonics*, vol. 11, no. 1, p. 5, 2017.

[20] T. Morioka, Y. Awaji, R. Ryf, P. Winzer, D. Richardson, and F. Poletti, "Enhancing optical communications with brand new fibers," *IEEE Communications Magazine*, vol. 50, no. 2, pp. s31–s42, February 2012.

[21] B. J. Puttnam, R. S. Luis, W. Klaus, J. Sakaguchi, J. M. D. Mendinueta, Y. Awaji, N. Wada, Y. Tamura, T. Hayashi, M. Hirano, and J. Marciante, "2.15 Pb/s transmission using a 22 core homogeneous single-mode multi-core fiber and wideband optical comb," in *European Conference on Optical Communication (ECOC)*, Sept 2015, pp. 1–3.

[22] D. L. Butler, M. J. Li, S. Li, Y. Geng, R. R. Khrapko, R. A. Modavis, V. N. Nazarov, and A. V. Koklyushkin, "Space division multiplexing in short reach optical interconnects," *IEEE/OSA Journal of Lightwave Technology*, vol. 35, no. 4, pp. 677–682, Feb 2017.

[23] C. Xia, N. Chand, A. Velázquez-Benítez, Z. Yang, X. Liu, J. Antonio-Lopez, H. Wen, B. Zhu, N. Zhao, F. Effenberger, R. Amezcua-Correa, and G. Li, "Time-division-multiplexed few-mode passive optical network," *Optics Express*, vol. 23, no. 2, pp. 1151–1158, Jan 2015.

[24] C. Simonneau, A. D'amato, P. Jian, G. Labroille, J.-F. Morizur, and G. Charlet, "4×50Gb/s transmission over 4.4 km of multimode OM2 fiber with direct detection using mode group multiplexing," in *Optical Fiber Conference (OFC)*. Optical Society of America, 2016, p. Tu2J.3.

[25] R. Ryf, N. Fontaine, M. Montoliu, S. Randel, S. Chang, H. Chen, S. Chandrasekhar, A. Gnauck, R.-J. Essiambre, P. J. Winzer, T. Taru, T. Hayashi, and T. Sasaki, "Space-division multiplexed transmission over 3×3 coupled-core multicore fiber," in *Optical Fiber Conference (OFC)*. Optical Society of America, 2014, p. Tu2J.4.

[26] G. M. Fernandes, M. Niehus, C. A. F. Marques, R. Nogueira, and A. N. Pinto, "Acousto-optic tunable mode coupler," in *Optical Fiber Conference (OFC)*. Optical Society of America, 2012, p. JTh2A.2.

[27] G. M. Fernandes, N. J. Muga, and A. N. Pinto, "Tunable mode conversion using acoustic waves in optical microwires," *IEEE/OSA Journal of Lightwave Technology*, vol. 32, no. 19, pp. 3257–3265, Oct 2014.

[28] G. M. Fernandes, N. J. Muga, and A. N. Pinto, "Mode conversion based on the acousto-optic effect for mode division multiplexed transmission," in *Second International Conference on Applications of Optics and Photonics (AOP)*, vol. 9286, 2014, pp. 9286–1–9286–8.

[29] G. Fernandes, N. Muga, A. Rocha, and A. Pinto, "Switching in multicore fibers using flexural acoustic waves," *Optics Express*, vol. 23, no. 20, pp. 26 313–26 325, Oct 2015.

[30] G. M. Fernandes, A. J. Almeida, M. Niehus, and A. N. Pinto, "Theoretical analysis of multimodal four-wave mixing in optical microwires," *IEEE/OSA Journal of Lightwave Technology*, vol. 31, no. 2, pp. 195–202, Jan 2013.

[31] G. M. Fernandes, N. J. Muga, and A. N. Pinto, "Four-wave mixing in microwires to all-optical signal processing in mode-division multiplexing systems," *Fiber and Integrated Optics*, vol. 34, no. 1-2, pp. 38–52, 2015.

[32] G. M. Fernandes, N. J. Muga, and A. N. Pinto, "Space-demultiplexing based on higher-order Poincaré spheres," *Optics Express*, vol. 25, no. 4, pp. 3899–3915, Feb 2017.

[33] G. M. Fernandes, N. J. Muga, and A. N. Pinto, "Digital monitoring and compensation of mode-dependent losses based on higher-order Poincaré spheres," *to be submitted to IEEE Photonics Journal*.

[34] G. M. Fernandes, N. J. Muga, and A. N. Pinto, "MIMO processing based on higher-order Poincaré spheres," in *III International Conference on Applications in Optics and Photonics (AOP)*, vol. 10453, 2017, pp. 1–6.

[35] G. M. Fernandes, N. J. Muga, and A. N. Pinto, "Reduced-complexity algorithm for space-demultiplexing based on higher-order Poincaré spheres," *Optics Express*, vol. 26, no. 10, pp. 13 506–13 506, May 2018.

Chapter 2

SDM transmission systems

In this Chapter, a brief state-of-the-art of optical transmission systems based on SDM, as well as of their fundamental building blocks is presented. Furthermore, it is also introduced the main physical phenomena behind the signal distortion on SDM transmission systems such as crosstalk, MDL, and modal dispersion (MD). The effect of each aforementioned phenomenon on the signal quality are discussed along with the main strategies that can be adopted for their mitigation.

In section 2.1, we start by introducing the concept of SDM link and their associated subsystems. In section 2.2, the developments in the design and fabrication of SDM fibers are reviewed. Section 2.3 and 2.4 are devoted to describe space-(de)multiplexing interfaces and space-selective-switches devices, respectively. In-line amplification for SDM systems is reviewed in section 2.5. In section 2.6, we describe the coherent receiver with spatial-diversity and its main DSP subsystem, emphasizing the MIMO post-processing. In section 2.7 are pointed out the main achievements, in terms of transmission capacity and reach, currently reported for SDM systems. Finally, the main conclusions are presented in section 2.8.

2.1 Transmission link

Over the past decade, it has become clear that SDM appears as a promising cost-efficient solution able to address the forthcoming capacity crunch. With unparallel aggregate bit-rates per fiber, SDM arises as a foreseeable step in the development of next-generation fiber-optic transmission systems in different application areas, from data-center interconnections up to long-haul transmission systems. Initially, SDM was proposed for long-haul transmission systems [1]. With typically length scales of a few thousand kilometers, in this transmission systems, the fiber deployment costs dominate over the capital costs of the network. Therefore, it is highly desired to deploy multiplexing techniques that enable to increase the available transmission capacity per fiber link. As a result of the overall increased demand for capacity, it is also envisioned that SDM technology will be extended for access and data-center networks. For short reach transmission systems, SDM can take advantage of their high degree of integration, saving space and avoiding the construction of new infrastructures. Recently, it was also demonstrated that SDM can boost the aggregated bit-rate per fiber link and improve the power budget in a cost-efficient way, potentially increasing the number of users per optical line terminal [2].

A transmission system with SDM needs the same building blocks of their counterparts

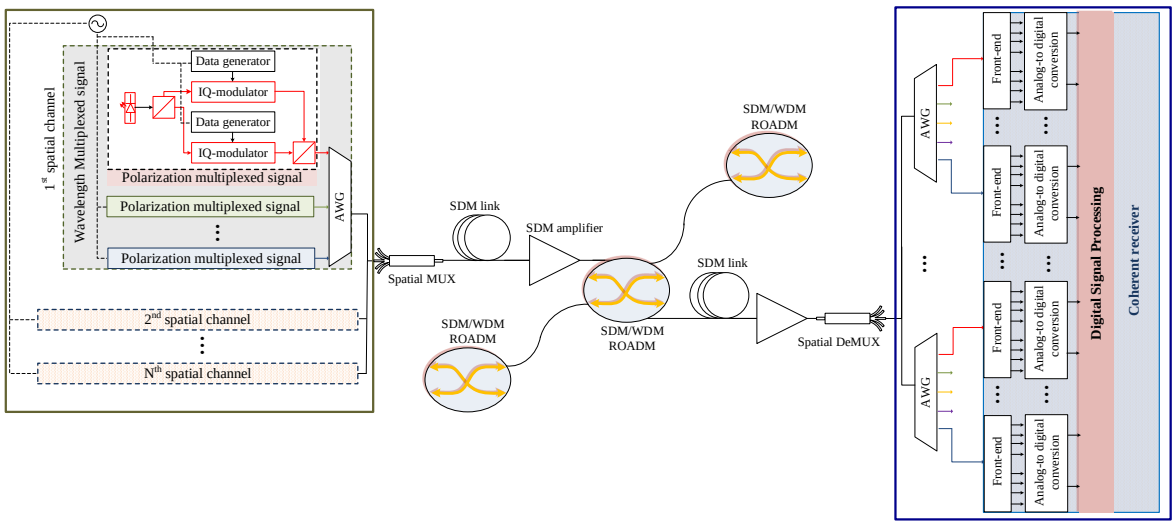

Figure 2.1: Schematic diagram of an optical link based on SDM without spatial selectivity.

based on SMF, in that way they are quite similar. To illustrate such similarities, but also to emphasize the novel subsystems required by this technology, an arbitrary SDM transmission system without spatial selectivity, the more general case, is schematically represented in Fig. 2.1. As it happens in SMF based transmission systems, two optical carriers with the same wavelength are modulated by two independent optical modulators and multiplexed by means of a polarization-multiplexer or polarization beam combiner. Then, all the carriers with distinct wavelengths are combined using an arrayed waveguide grating (AWG). By employing a space-multiplexer, the N sets of wavelength-multiplexed signals are launched in n distinguishable data pathways or spatial channels. During the fiber propagation, the optical signals are attenuated and may require in-line signal amplification. In principle, a single in-line amplifier can compensate the optical losses of all the available spatial channels with similar gains and noise figures. According to the crosstalk levels, the signals are jointly or independently routed at the ROADM. At the end of the fiber link, the received signal passes through a space-demultiplexer, a wavelength-demultiplexer, a polarization-demultiplexer and it is finally detected at the receiver. For SDM transmission systems with spatial selectivity, the crosstalk between distinct spatial signals can be neglected, the transmitted signal can be independently detected and therefore direct detection or coherent detection can be employed at the receiver. However, for transmission systems with non-negligible crosstalk, coherent detection is highly desirable in order to enable the use of MIMO post-processing at the optical coherent receiver [3]. The optical coherent receivers comprise an optical front-end part, where the optical signal is passed to the electric domain, a data conversion part, where high-speed analog-to-digital converter (ADC)s transform the analog signal into the digital domain, followed by an array of DSP subsystems responsible for the mitigation of channel impairments and symbol decoding [4].

In terms of hardware components, the SDM transmission system above described is quite similar to a standard SMF based transmission link. Although, for the same aggregated bit-rate, it is highly desirable that the components required by the SDM transmission system have a lower cost than the equivalent amount of their counterparts for SMF based transmission systems. In that way, the integration of several components to support the cost reduction will

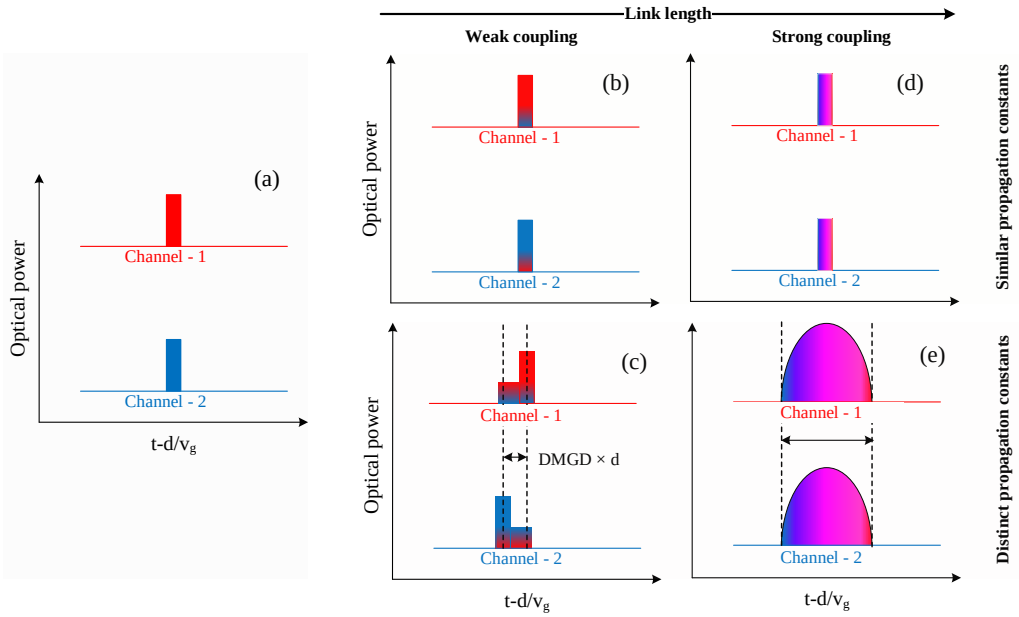

Figure 2.2: Schematic diagram of the impulse response channel at the end of a SDM transmission system with distinct and similar propagation constants in the presence of moderately coupled and strongly coupled channels. (a) Input signals. (b) and (c) Signals in the presence of moderate coupling assuming similar and distinct propagation constants, respectively. (d) and (e) Signals in the presence of strong coupling assuming similar and distinct propagation constants, respectively. The parameter v_g and d denote the group velocity and the link length, respectively.

play a crucial role. Such savings are particularly relevant at the space-wavelength-selective switch (SWSS) placed at the ROADM and in the in-line amplifiers; as clearly explained in the following sections 2.4 and 2.5, respectively. Furthermore, the optical transmitter and the optical coherent receiver can also share some fundamental components and subsystems, e.g., laser sources and some DSP subsystems, decreasing the overall cost and energy consumption of the transmission system. In addition and crucially, SDM technology must also contribute to decrease the overall power consumption and hence the cost-per-bit, the other fundamental parameter in the network design.

2.1.1 Operation regime

In general, SDM transmission systems can operate on four distinct operation regimes. Each one of these regimes is characterized by a particular kind of impulse response channel; schematically represented in Fig. 2.2. For shorter transmission distances, or smaller interaction lengths, and non overlapping transverse electrical fields, the crosstalk can be virtually neglected. Therefore, all the transmitted signals are “uncoupled” and they can be independently received and post-processed, which is the case of moderate or long lengths of MCF or weakly-coupled MCF [5], see Fig. 2.2(b). Besides MCFs, weakly-coupled FMFs with negligible crosstalk are also part of this group. If the interaction length is quite short, crosstalk can be neglected (the power coupled is still very low) and the tributaries can be independently post-processed. In the multimodal case, the tributaries travel at distinct group velocities, v_g, through the fiber link arriving at the receiver in different time periods or time slots. In

Fig. 2.2(c), the two tributaries are separated by the MD, which depends on the differential mode group delay (DMGD) of the FMF and in the length of the fiber link, d. Such regime can be observed in moderated lengths of FMFs and in short lengths of MMFs. It should be noted that increasing the interaction length a weak crosstalk starts to appear producing an almost uniform crosstalk plateau around the peaks. Such plateau is produced by the coupling between spatial channels that have distinct propagation constants. This coupling phenomena tends to start between the neighbor cores of a MCF or between spatial modes of the same linearly polarized (LP) mode-group in FMFs and MMFs. Further increasing the link length, the level of crosstalk increases, whose tends to dominate the channel impulse response. Then, the received signal presents a Bell shaped curve, or Gaussian curve, with a full width at half maximum (FWHM) determined by the dispersive effects [3], namely modal dispersion, see Fig. 2.2(e). Hence, the tributaries can no longer be independently detected. For spatial channels with similar propagation constants, the crosstalk mixes the spatial channels resulting, however, in a smaller (or even negligible) MD at the end of the fiber link, see Fig. 2.2(d). In that way, the resulting impulse response channel determines the architecture of the overall transmission systems with particular impact in the design of the coherent receiver and their associated DSP subsystems.

Crosstalk does not fundamentally limit the transmission capacity, it only mixes the tributaries. If none of the spatial channels is substantially attenuated in respect to the others (i.e., low values of MDL), it is possible undo any level of crosstalk using MIMO post-processing in combination with coherent detection. The computational effort required by the MIMO post-processing is mainly determined by the accumulated MD. When the spatial channels have similar propagation constants, the computational effort is therefore minimized. In this case, the MIMO post-processing only requires a single tap (or a few taps) to successfully compensate the crosstalk and MD. As the gap between propagation constants increases, the crosstalk levels tend to decrease but the DMGD and hence the number of taps required for MIMO post-processing tends to increase.

2.2 Optical fibers for space-multiplexing

In order to support SDM, it has been proposed several kinds of MCFs and FMFs with distinct physical proprieties, see for instance Fig. 2.3. Like transmission systems, the optical fibers can be roughly categorized into:

i) spatial selectivity fibers;

ii) scrambling fibers.

If the transverse optical fields guided by the fiber do not overlap, or such value of overlap can be neglected, the distinguishable spatial channels tend to not couple and the SDM link is free of crosstalk; hence MIMO post-processing can be avoided. As a matter of fact, in SDM through a single fiber the overlap via evanescent field is always present. In that way, residual crosstalk along with large interaction lengths may induce inter/intra-symbolic distortions in the received signal. As the interaction length increases, the tributaries of neighbor cores or degenerated modes start to be coupled. Further increasing the interaction length, the coupling is extended to all the tributaries guided by the SDM fiber. It should be noted that the interaction length depends on the link length and on the group velocity of both tributaries. For tributaries with similar propagation constants, the walk-off tends to occur

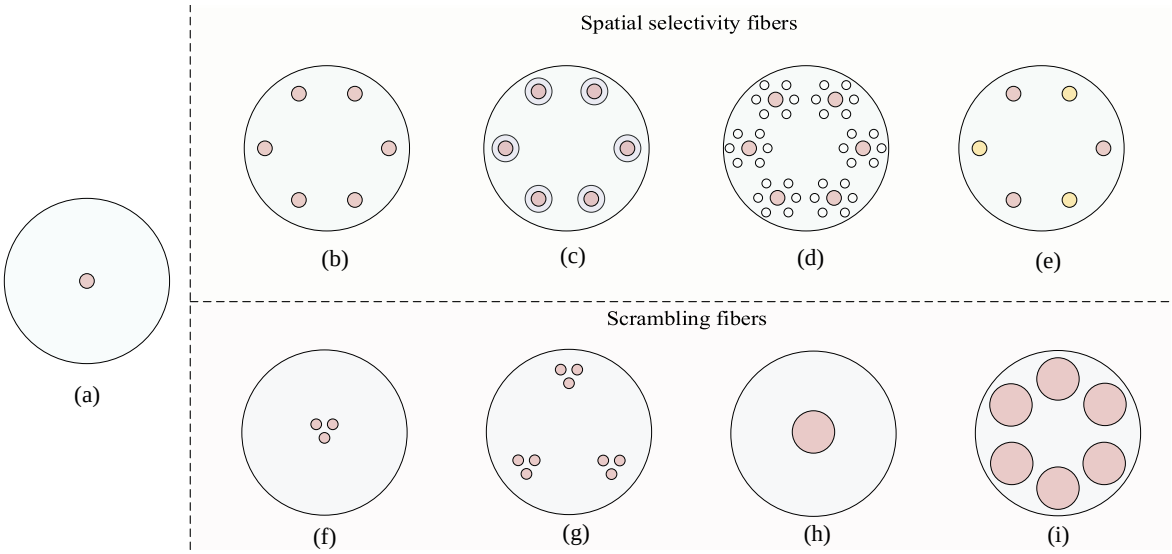

Figure 2.3: Schematic diagram of: (a) standard SMF, (b) 6-cores MCF, (c) trenched assisted 6-cores MCF (d) hollow assisted 6-cores MCF, (e) heterogeneous 6-cores MCF, (f) CC-MCF (g) CCG-MCF (h) FMF and (i) few-mode-MCF.

over long distances resulting in long interaction lengths. In contrast, signals with different propagation constants tends to quickly break the walk-off producing short interaction length. In this sense, fibers with non-negligible crosstalk can be categorized in two main classes:

i) with similar propagation constants or low DMGD;

ii) with distinct propagation constants or higher DMGD.

In the first category, the tributaries arise at the receiver strongly coupled and nearly at the same time. Such fibers are characterized by lower DMGD and therefore short impulse response channel in the time domain. In the second category, the levels of the crosstalk tend to be lower because the phase matching between the distinguishable spatial channels is in principle avoided. For short lengths of fiber, the system can be considered free of crosstalk and the MIMO post-processing can be avoided. For long or moderated interaction lengths, the residual crosstalk may result in a large impulse response channel in the time domain due to the large value of DMGD. Therefore, such systems tend to require heavy MIMO post-processing. In Fig. 2.4, it is shown the fundamental kinds of novel fibers proposed to implement SDM, grouped on the aforementioned fiber classification.

2.2.1 Multicore fibers

In contrast to standard SMF, in MCF the same common cladding contains multiple cores. This concept was experimentally demonstrated in 1979 by manufacturing a 7-cores MCF in a hexagonal geometry [6]. This first generation of MCF suffered from crosstalk between neighboring cores induce by small variations in the core geometry or in the index profile. In addition, there was the difficulty in connecting and splicing MCF. The development of this kind of fibers was not pursued at that time due to the growth transmission capacity

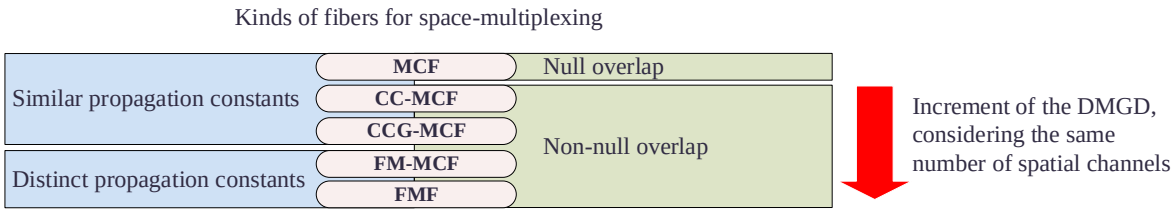

Figure 2.4: Fibers for SDM categorized by their physical properties: transverse optical field overlapping and propagation constant.

of optical transmission systems based on SMFs. However, the current bandwidth scarcity provided by SMF and the increasing demand for capacity has led to a renaissance of research in MCFs [7]. Nowadays, it is possible to manufacture MCFs with negligible variations in the core geometry and/or in the index profile due to the tremendous progress made on optical fiber fabrication over the past two decades. Despite such progress, the long interaction lengths (and the residual evanescent field at the neighboring cores) can still induce residual crosstalk between cores.

Weakly-coupled multicore fibers

In weakly-coupled MCFs, also simply referred as MCFs, each core is used as an individual waveguide and, in principle, any kind of interaction with the remaining cores supported by the optical fiber can be neglected. Despite the low value of coupling between cores, the crosstalk can achieve non-negligible values for ultra long transmission links. However, the transmission system can be properly designed to maintain the crosstalk levels below an operation threshold. As MIMO post-processing can be avoided, this approach has received most attention among all the proposed SDM solutions. In MCFs, the simplest way to limit the crosstalk is to ensure that the fiber cores are well separated in order to avoid the overlap between transverse optical fields guided in the same fiber. On the other hand, the aggregated bit-rate of MCF-based transmission systems depends on the number of available cores. It should be also emphasized that silica-based optical fibers with cladding diameters greater than ~ 200 μm may have mechanical problems because they are susceptible to fracture [8]. This physical limitation imposes a fairly rigid limit on the number of cores that can be incorporated in MCFs with negligible crosstalk [8]. To address this issue, several core configurations have been proposed in order to increment the number of cores maintaining the crosstalk at tolerable levels[1], including the hexagonal packed structure with one-ring, dual-ring structure, and two-pitch structures[2] [8].

In order to decrease the crosstalk between neighboring cores, MCFs with refractive index profiles incorporating a trench around the cores have been produced, see Fig. 2.3(c). The trench enables to reduce the evanescent field in the neighboring cores; decreasing the crosstalk levels [9]. At the cost of harder fabrication requirements, the index trench can be replaced by a hollow structure around the cores further decreasing the crosstalk levels, see Fig. 2.3(d). On the other hand, the mode coupling can be also substantially mitigated by reducing the interaction length. For the same fiber length, the interaction length can be substantially

[1]Note that the maximum value of crosstalk must be properly chosen according to the modulation format considered.

[2]Pitch denotes the core-to-core spacing in optical fibers with more than a single core.

reduced by avoiding the phase-matching between neighboring cores. Thus, the propagation constant for each core must be slightly changed by handling the diameter or the index profile of each individual core. Usually, this kind of MCF is referred as heterogeneous MCFs, see Fig. 2.3(e). Heterogeneous MCF based on different core doping profile allows to decrease the crosstalk and additionally increasing the core density. The heterogeneous approach was also merged with the trench-assisted technique in order to produce trench-assisted heterogeneous MCF. Heterogeneous trench-assisted MCF supporting up to 30 cores was experimentally demonstrated in [10].

Coupled-core multicore fibers

In CC-MCF, the pitch or the spacing between the cores is smaller than in weakly-coupled MCF, which results in a higher spatial density of cores but also on crosstalk, see Fig. 2.3(f). In fact, in this kind of fibers, the optical carriers are not guided into the fiber cores but in several degenerated super-modes guided by the core arrangement inside the fiber. The value of the DMGD can be adjusted by handling the core arrangement, the pitch, and the core index profile [8]. In contrast to weakly-coupled MCF, in CC-MCF-based transmission systems the received signal suffer from crosstalk requiring MIMO post-processing at the optical coherent receiver. However, the carriers travel nearly at the same group velocity resulting in lower values of DMGD. Hence, such kind of transmission systems tends to need lighter MIMO post-processing than their counterparts based on FMFs. As the carriers are simultaneously guided by the core arrangement inside the fiber cladding, and not inside of a single core, CC-MCF tends to have a larger effective area than weakly-coupled MCF reducing the nonlinear distortions. In addition, the strong crosstalk also averaged to zero the MDL [11]. The signal transmission over several thousands of kilometers of CC-MCF was successfully demonstrated employing 3-cores, 4-cores and 6-cores CC-MCF [12].

A distinct approach based on independent groups of coupled cores coexisting in a single fiber was also proposed, see Fig. 2.3(g). In coupled-core group (CCG)-MCF, the tributaries of the same group are coupled with each other giving rise to a supermode. However, the cores of different groups remain isolated [11]. When compared with CC-MCF, CCG-MCF allow to substantially increase the spatial diversity with the added benefit of enabling adjust the complexity of the MIMO post-processing by properly choosing the number of cores in each group. Furthermore, CCG-MCF have the same advantages of CC-MCF in terms of MDL and nonlinearities. Despite such advantages, to the best of our knowledge, only a single CCG-MCF with 3-cores × 3-groups was fabricated [13].

2.2.2 Few-mode fibers

In the first generation of fiber-optic transmission systems, MMFs were used due to their advantage of easy splicing and facility of coupling the light to the core. With large cores and high numerical apertures, this kind of fibers can support a large number of modes with distinct propagation constants. However, due to small variations in the core geometry or refractive index perturbations along the MMF, the mode coupling may lead to the spreading of a particular tributary, transmitted in a given mode, by the remaining modes of the MMF [3]. Since each mode has a characteristic group velocity, it can also lead to a spreading of such signal in the time domain; resulting in inter/intra-symbol distortions. Due to the large number of modes supported by MMFs, the impulse response channel is characterized by high values of

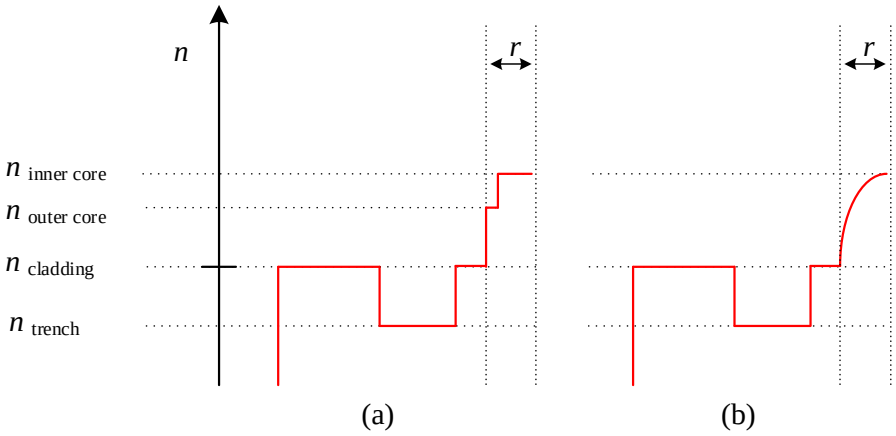

Figure 2.5: Schematic diagram of the refractive index profiles: (a) step index FMF and (b) graded-index FMF. The parameter n and r denote the refractive index and the core radius, respectively [14].

MD. In contrast, FMFs support a limited number of orthogonal modes allowing the parallel transmission of several carriers through distinct spatial channels with moderate values of MD, see the schematic representation in Fig. 2.3(h) [1].

SDM transmission systems based on FMF require novel fibers with low MDL, to enable the DSP at the coherent receiver, and low MD to make feasible the DSP with current technology. Moreover, FMFs must be able to support a considerable number of LP modes, typically ranging from 2 to 20 modes, to produce a capacity gain of one order of magnitude [8, 11]. In order to meet these requirements, the scientific community has been working mainly in the design of index profile and manufacturing process of two types of FMFs: multistep index [15], see Fig. 2.5(a), and graded-index profile [16], see Fig. 2.5(b). In multistep index profile, the radius and the index difference between the two core layers are adjusted to control the number of modes supported by the FMF and the magnitude and sign of their DMGD. Usually, FMF with multistep index profile have large gaps between the propagation constants of the guided modes; hence this kind of profile is preferable to develop weakly coupling FMFs. In graded-index fibers, the shape of the index profile is used to define the number of modes supported by the fiber and to fine tuning the DMGD. Graded-index FMFs tend to have lower DMGD than step-index FMFs and therefore they tend to have higher levels of crosstalk [14]. It is worth noting that both index profiles can additionally have an inner cladding trench to improve the light confinement, reducing the losses and enabling the fine tuning of the DMGD.

Weakly-coupled few-mode fibers

Weakly-coupled FMFs aim to reduce the crosstalk of the fiber link, and therefore ideally avoid the MIMO post-processing. The fiber is engineered to maximize the difference between the propagation constants of the fiber modes. However, residual crosstalk results in a large time response channel making unfeasible the practical implementation of such kind of fibers for long-haul transmission systems. On the other hand, weakly-coupled FMFs have been successfully employed for short reach transmission systems with few kilometers [17]. Furthermore, this kind of FMFs can also be employed in dispersion compensated links in which several fiber spans with opposite DMGD are concatenated, i.e., FMFs with positive and negative DMGD are concatenated to ideally vanish the DMGD of the fiber link. If the fiber spans

are free of crosstalk, the dispersion compensated link tends to achieve lower values of DMGD. In that sense, weakly-coupled FMFs are desirable to develop dispersion compensated links.

Strongly coupled few-mode fibers

Strongly coupled FMFs tends to have smaller impulse response channel than weakly-coupled FMFs. The fiber modes have nearest propagation constants increasing the crosstalk levels. Hence, the several carriers appear fully mixed at the coherent receiver, making unavoidable the use of MIMO post-processing. The strong crosstalk also reduces the DMGD and the MDL. Notice that the crosstalk can be also introduced in the transmission system by means of discrete devices distributed along the fiber link, such as long period fiber grating (LPG) [18].

2.2.3 Few-mode multicore fibers

To further increase the capacity of the SDM systems, it is possible to combine the multicore and the mode-multiplexing approaches. In this regard, it was manufactured an array of spatially isolated few-mode cores enabling mode-division multiplexing (MDM) to be overlaid directly onto the multicore approach, see Fig. 2.3(i) [8, 11]. Such technique allows to substantially increase the number of spatial channels per fiber with the additional benefit of reducing the nonlinear distortions induced during the fiber propagation. Moreover, few-mode MCF needs lighter MIMO post-processing than FMF with similar number of spatial channels [19].

2.3 Spatial-multiplexers

In general, a S-Mux convert a set of n spatially separated signals guided on independent SMFs into a set of n spatial channels guided in a single fiber. In other words, a S-Mux (S-DeMux) enables to launch (collect) the optical signal in (from) a given spatial channel, analogously to an AWG enables to launch/collect carriers with distinct wavelengths in transmission systems with wavelength-division multiplexing (WDM). Like fibers and the transmission systems itself, S-Mux can be grouped in [3]:

i) spatial-selective multiplexers;

ii) scrambling multiplexers.

Spatial-selective multiplexers present harder fabrication requirements and tends to have considerable insertion loss and MDL. In contrast, mode-group selective or fully scrambling spatial-multiplexers tend to have lower MDL and are much easier to fabricate [3]. Furthermore, in some cases, such spatial-selective transmission is not necessary because the fibers themselves do not preserve the spatial selectivity [5]. If the SDM transmission system is based on scrambling fibers (i.e., fibers with non-negligible crosstalk), the MIMO post-processing allows to compensate for the crosstalk induced by the fibers and the S-Mux and S-DeMux interfaces.

For SDM based transmission systems with spatial selectivity, the spatial light transformation can be carried out by means of indirect or direct coupling schemes. Indirect coupling consists in a free-space optics scheme that relies on lens and/or mirrors systems to collect (launch) light from (for) each spatial channel. On the other hand, in direct coupling schemes, a waveguide directly connects the special fiber for SDM to a set of SSMFs [20].

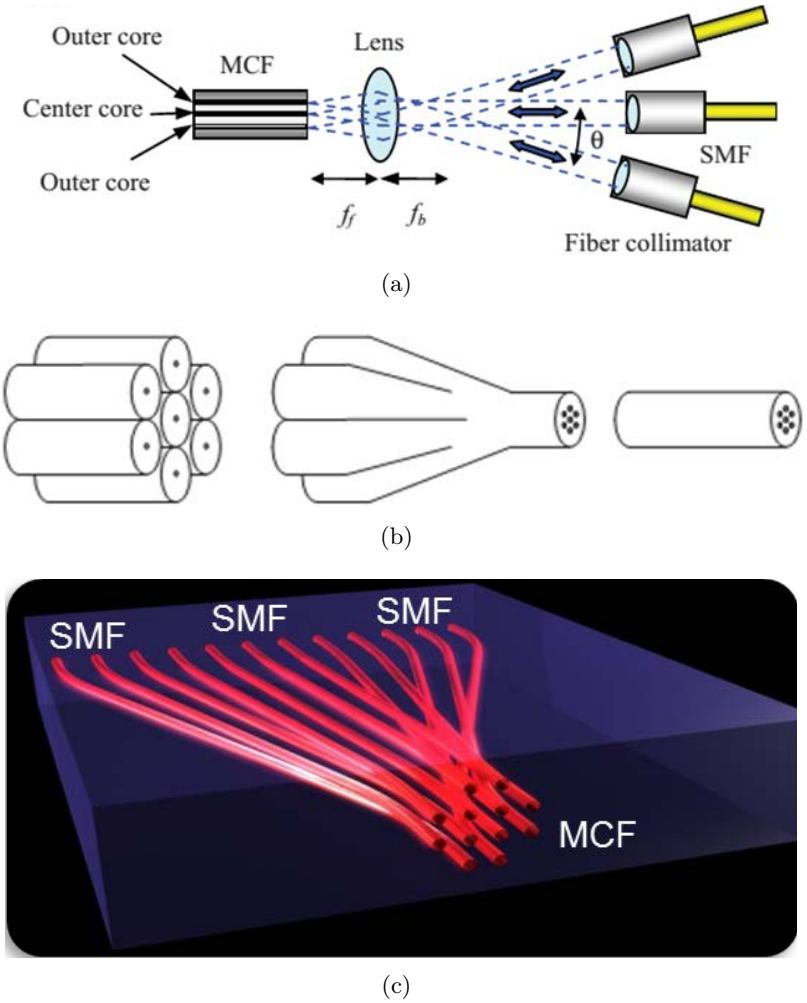

Figure 2.6: Schematic representation of space multiplexers for MCFs: (a) free-space based core multiplexer. (b) photonic lantern or fiber bundle fan-in/fan-out (c) waveguide coupling based core multiplexer (figure from [20]).

2.3.1 Spatial-multiplexers for transmission systems based on MCFs

In weakly-coupled MCFs, the connectivity to individual cores may result difficult due to the high core density. Nevertheless, several devices based on direct and indirect coupling schemes were demonstrated to selectively launch/collect the optical beams from the MCF facet. In S-Mux for MCF based on indirect coupling schemes the optical signal from the MCF facet is converted by a lens (or a set of lens) in collimated beams, each propagating at a slightly different angle, see Fig. 2.6(a). After, the beams are focused on the fiber collimators and launched in different SMFs. Such king of S-Mux was successfully demonstrated for a 19-cores MCF with insertion losses of ~ 0.65 dB [21]. In spite of the aforementioned scheme can be scalable for a high number of cores with negligible crosstalk, it is usually bulky and requires extremely precise optomechanics systems.

In-line S-Mux were initially manufactured by tapering a capillary tube filled by SMFs, the so-called photonic lanterns or fiber bundle fan-in/fan-out. The core spacing and the mode

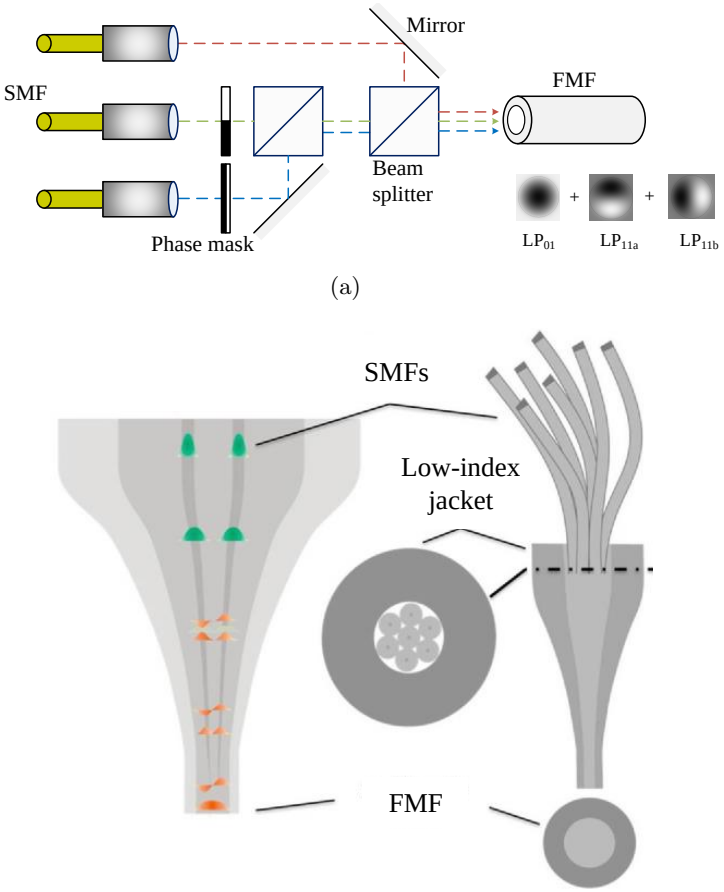

Figure 2.7: Schematic representation of mode multiplexing schemes. (a) Phase plate based mode multiplexer for a 3-mode FMF. (b) Fiber photonic lantern based mode multiplexer (figure from [24]).

field properties of the S-Mux can be handled by properly choosing the tapering angle and the final taper diameter. In order to avoid insertion losses and crosstalk, the core spacing and the mode field properties of each core at the end of the S-Mux must match with the ones of the MCF at the splicing point, see Fig. 2.6(b). S-Mux based on photonic lanterns has been manufactured with insertion loss as low as 0.45 dB [22]. Waveguide coupling is another kind of in-line S-Mux that enables to connect several SMFs to a single MCF by means of an array of several spatially isolated waveguides inscribed in a 3-D block. Each waveguide connects a single core of the MCF to a particular SMF, see Fig. 2.6(c). This kind of S-Mux was manufactured with insertion losses as lower as 0.92 dB [23].

2.3.2 Spatial-multiplexers for transmission systems based on FMFs

In FMF-based transmission systems, a S-Mux must induce a more complex spatial transformation of the launched/collected beams[3], which may result in more complex experimental arrangements. However, the growing interest given to MDM has boosted the development

[3]Notice that the spatial distribution at the end of the S-Mux and the fiber mode selected must match perfectly in order to avoid insertion losses and crosstalk.

of mode-selective multiplexers [25, 26]. In indirect coupling schemes, the mode conversion is usually followed by passive combiners (splitters) which enable to launch (collect) the multi-modal signal in (from) the fiber, see Fig. 2.7(a). The mode conversion can be induced by a phase mask printed in silica plates. Such mode conversion occurs because the phase structure of the phase mask matches the spatial phase distribution of the desired mode profile [25, 27]. This kind of S-Mux/S-DeMux have considerable insertion losses (for a 3-mode S-Mux the minimum insertion loss is 5.5 dB [25], with optimized parameters), which tends to increase with the number of multiplexed modes. However, the losses due to the beam splitter can be virtually avoided using free-space interferometers. In [28], the mode conversion with almost negligible optical losses was achieved by sending the unused optical signal from the beam splitters into the respective SDM channels [28]. Moreover, the phase-mask can be replaced by a reconfigurable spatial light modulator (SLM) that uses diffractive holograms to induce the mode conversion [5]. This scheme is very practical for optical characterization of SDM devices due to their high flexibility in terms of mode selectivity [3]. Thanks to their high degree of miniaturization and integration with current technology, silicon photonic integrated circuits were also proposed for S-Mux in MDM transmission systems. Notice that, the mode conversion in photonic integrated circuits is achieved by means of interference patterns [29].

In-line mode converters based on photonic lanterns has been attracting the attention of the scientific community due to their scalability, lower insertion losses, and low MDL. It should be noted that photonic lanterns can be produced with and without spatial selectively. If the photonic lantern has spatial selectively, it allows excite a particular mode in one end by properly choosing a fiber of an array of several SMFs in the opposite end. Such kind of mode converters can be manufactured by tapering a capillary tube filled with SMF with distinct fiber diameters or cores with distinct refractive indexes. The tapered region between both ends allows the signal conversion between the waveguides with low insertion losses [30], see Fig. 2.7(b). In contrast, if the capillary tube is filled with similar SMF, the resultant photonic lantern works as a mode scrambler with lower insertion losses and MDL. Furthermore, mode-group selective S-Mux was also fabricated by considering sets of similar fibers in the fabrication of the photonic lantern. Each set of fibers have distinct physical properties; therefore the mode conversion happens between the fundamental mode supported by the set of SMFs and a given mode-group supported by the FMF. The number of degenerated modes of a given group determines the number of fibers with the same physical properties considered in the fabrication of the photonic lantern. At the splicing point, the mode-groups exited at the end of the photonic lantern must match with the ones supported by the FMF. When compared with mode-selectivity photonic lanterns, such scheme allow to relax the fabrication requirements and reduce the losses and MDL. In addition, photonic lanterns based on waveguide inscribed in a 3-D block was also demonstrated with promising results [3].

Aside from photonic lanterns, other in-line S-Mux with mode selectivity was also reported, including nondiabetic tapered photonic crystal fiber (PCF) [31, 32] (enabling the mode conversion between the LP_{01} and the LP_{11}, and between the LP_{01} and the LP_{02} [32]) and twisted fused couplers made from FMFs [31]. Furthermore, the mode conversion between the LP_{01} and the LP_{11} was also demonstrated by means of resonant coupling induced by periodic structures such as LPG mechanically inscribed [33].

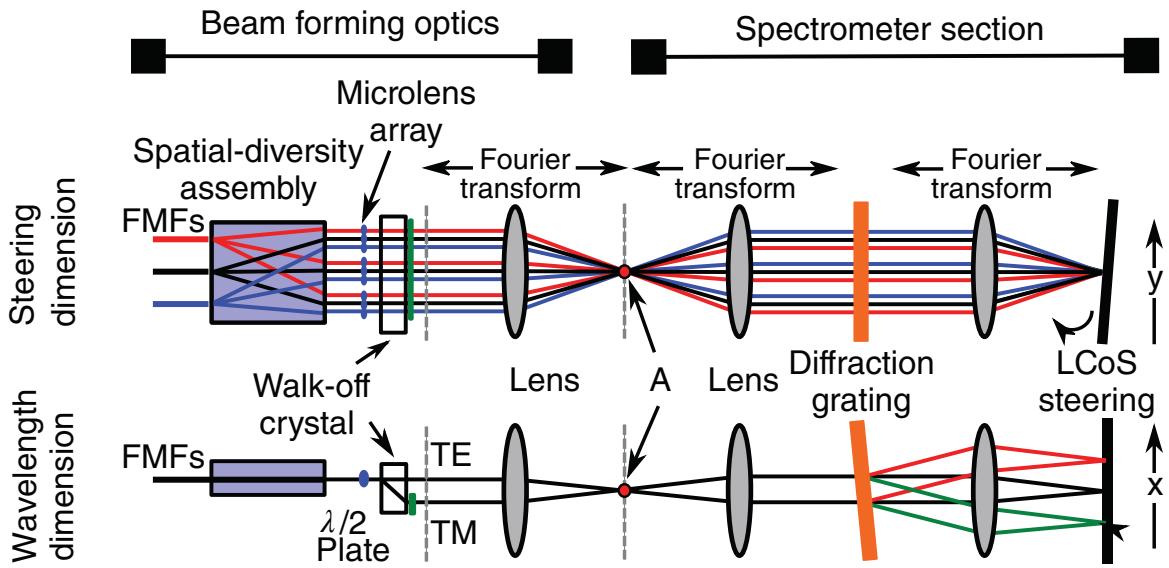

Figure 2.8: Schematic of a space-wavelength selective switching spanning two dimensions. Spatial channels are remapped to rows of the array, and switching is performed in the vertical direction (figure from [3]).

2.4 Space selective switches

Being a fundamental building block of current communications systems, a wavelength-selective switch (WSS) enables the reconfigurable wavelength routing at the nodes of an optical network. In such device, a given wavelength channel is routed from a given port to another port, or to many other ports. Analogously to their counterparts in the single-mode case, a SWSS must be able to route a given tributary signal, from an arbitrary spatial and wavelength channel to another (spatial and wavelength) channel, or to many other channels. Thus, SWSS need handle an extra dimension without many additional components providing a similar performance, when compared with current WSS, at lower cost.

The simplest implementation of a SWSS can be accomplished by using a set of standard WSS placed between a S-DeMux and a S-Mux. At the input of such device all the spatial channels are separated by a S-DeMux, the wavelength channels are subsequently switched by a set of standard WSS, then the SDM channels are launched again in the SDM link by means of a S-Mux. However, this kind of SWSS does not allow the switching between distinct spatial channels. Moreover, such approach is similar to the case of n parallel transmission systems based on SSMF and, therefore, no substantial gains are obtained in terms of energy efficiency and hardware complexity. A SWSS must be more economical than the same number of conventional WSS required to achieve a similar capacity increment by using additional SSMF-based transmission systems in parallel.

In general, a SWSS employs the perpendicular plane to the signal propagation to uncouple the spatial and the wavelength dimensions. In Fig. 2.8, it is shown a schematic of a typical SWSS based on a beam-forming stage followed by a spectroscopy stage. The spatial channels are arranged vertically in the steering dimension (y), and the wavelengths are dispersed in the wavelength dimension (x). The beam-forming stage enables the space-demultiplexing,

and the reshaping of the beam sizes before launching the light into the spectroscopy stage. The spectroscopy stage is usually comprised of a diffraction grating and a steering element. The tilt angles applied at the steering element shifts the beams vertically at the grating allowing direct the signal to the desired output spatial channels. Although several ways have been proposed to build SWSS, all tend to contain equivalent beam-forming and spectroscopy stages.

In SDM transmission systems, the crosstalk can mix the space-multiplexed tributaries, in contrast to standard WDM systems, and therefore it must be considered in the design of the SWSS. According to the crosstalk levels presented in the transmission system, it was proposed three switching architectures [34]:

i) full spatial and wavelength granularity;

ii) fractional space and full wavelength granularity;

iii) wavelength granularity.

In the first case, it is assumed that spatial and wavelength channels are fully uncoupled and therefore they can be independently routed, which may occur in MCF and in weakly-coupled FMF. The space-wavelength granularity enables the switching of a single spatial and wavelength channel fully exploiting the switching capabilities of SDM transmission systems. Despite the greatest flexibility of this architecture, their implementations are the most cumbersome. In the second case, a fractional space and full wavelength switching, it is assumed that crosstalk only mix tributaries from the same mode-group and, therefore such mode-group must be jointly switched, i.e., each mode-group can be independently switched on a wavelength basis. This may occur in FMFs, MMFs and CCG-MCFs. In the last case, the wavelength granularity switching architecture, only the wavelength dimension is considered for routing, i.e., all spatial channels are jointly switched on a wavelength basis.

In SDM transmission systems without spatial selectivity, the tributaries are received fully mixed requiring MIMO post-processing to undo the crosstalk. Therefore, such signals must be jointly processed and hence they must be kept as a group and cannot be independently switched to a distinct network destination. The implementation of SWSS only with wavelength granularity tends to simplify the switching hardware because it is inspired on modified approaches of their counterparts proposed for the single-mode case [34]. Note that, if the SWSS has full spatial and wavelength granularity, any one of the other two aforementioned scenarios can be easily addressed. With this in mind, in the two following subsections, some SWSS with spatial and wavelength granularity demonstrated for the case of MCFs and FMFs are briefly described.

2.4.1 Space-wavelength selective switches for MCF transmission systems

In MCF, the crosstalk tends to be negligible and therefore the development of switching devices with space and wavelength granularity is highly desirable. In [35], it was demonstrated a switching device with space and wavelength granularity based on SLM. The S-DeMux is performed by means of a waveguide coupling S-DeMux and the wavelength-(de)multiplexing is accomplished by a diffraction grating placed between the S-DeMux and the SLM. After crossing the grating, the beams are then launched in the SLM, which routes the wavelength channel from a given input core to the desired output core or cores. In [36], it was demonstrated a wavelength joint-switching for a 7-core MCF. The SDM signals are demultiplexed

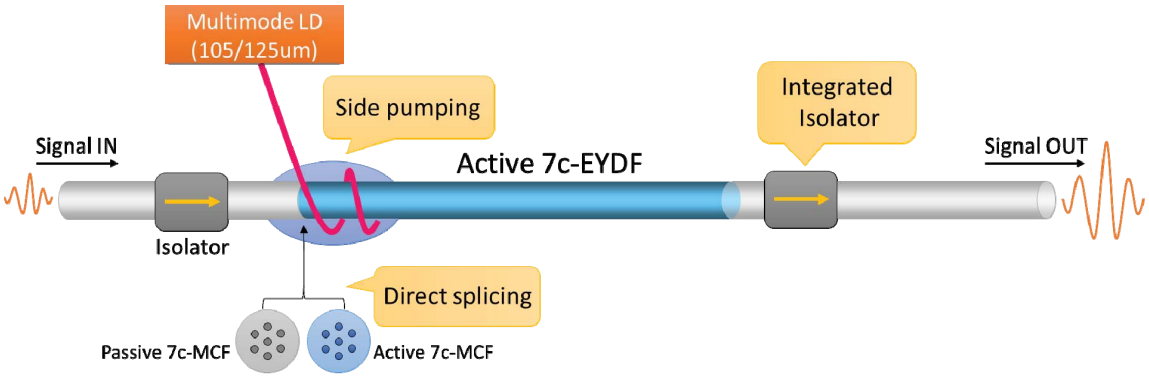

Figure 2.9: Schematic of an optical amplifier based on EDF in a cladding-pumping schemes. Note that, the operation principle for MCF and FMF based EDFA is quite similar (figure from [40]).

and attached to the dispersive element, which in turn are attached to two MCF outputs. After spatial and wavelength-demultiplexing, the signal is routed for one, or for the two, output MCF by a steering mirror.

2.4.2 Space-wavelength selective switches for FMF transmission systems

Using a similar setup to the previously reported in [35], a space and wavelength switching for MDM transmission systems was demonstrated by replacing the waveguide coupling device by several photonic lanterns [37]. In [38], the S-DeMux interfaces based on a waveguide coupling device was integrated within the WSS module in which the spatial switching is also performed by a SLM.

Last but certainly not least, a SWSS with wavelength granularity supporting three different kinds of SDM fibers (i.e., six SMFs, 6-mode FMF, and 6-core MCF) was demonstrated in [39]. In the reconfigurable optical add-drop multiplexer, the spatial channels were separated and jointly switched by a SWSS based on a waveguide coupling device and a SLM.

2.5 Optical amplification

As in current fiber-optic networks, all-optical amplification is also a key task in future SDM networks. The simplest approach for all-optical amplification in SDM transmission systems is based on n parallel single-mode EDFAs placed between a S-Mux and a S-DeMux [41]. However, due to its low energy efficiency and high number of hardware components, this scheme is unattractive from a technical and economic point of view. As in WDM systems, in SDM systems, the pump power and the hardware components must be shared among all the wavelength and spatial channels to reduce the hardware cost and the energy consumption. In this regard, all-optical amplification employing novel MCFs and FMFs has been demonstrated based on stimulated emission in Erbium-doped fiber (EDF)s and on stimulated Raman scattering (SRS) [20, 40].

Regarding the EDFAs with spatial diversity, two pump configurations were proposed: core- and cladding-pumping schemes [20]. In the first configuration, the pump signal is directly launched in the core (or cores) of the EDF in the fundamental mode for single-mode cores or in a modal mixture for few-mode cores. In contrast, in cladding-pumped amplifiers,

the pump signal is launched in the fiber cladding, which is shared by all the cores and/or modes of the SDM fiber, see Fig. 2.9. Usually, in cladding pumped amplifiers, the EDF is surrounded by a low-index polymer coating to make the cladding a multimodal waveguide. Then, the pump signal excites hundreds to thousands of cladding modes, which uniformly illuminate the entire cladding of the EDF. Since the pump signal can be directly coupled into the cladding, the use of wavelength combiners can be avoided and the pump sources can be replaced by multimode pump diodes, which tends to be cheaper and uncooled [40]. However, cladding-pumped amplifiers also present some drawback mainly because such scheme makes more difficult to achieve a full inversion in the population of the Erbium ions. For example, in a cladding pump amplifier, the cladding area is about 100 times larger than the area of a single core EDF, which implies that the pump power should be also at least 100 times larger to obtain a similar performance. Hence, longer EDFs are needed to obtain an optical gain similar to standard EDFA, pushing the gain toward the L-band. However, this challenge can be addressed by decreasing the cladding area (to increase the pump intensity) and increasing the size of the cores (to reduce the signal intensity). In addition, the cores can also be co-doped with Ytterbium to enhance the pump absorption [40].

2.5.1 Optical amplification in MCFs

In multicore EDFs, the Erbium-doped cores are embedded in a common cladding of silica. In core-pumped schemes, an independent pump fuels an individual core and, therefore the gain for each core can be adjusted by tuning their associated pump. This approach achieves an excellent performance with gains and noise figures comparable to those of conventional EDFA based on SMF [40]. However, core-pumped EDFA require S-Mux/S-DeMux interfaces, along with n pumps and n wavelength combiners making their implementation unattractive from a technical and economic point of view [42]. In cladding-pumped amplifiers, a single pump can be launched in the cladding modes to fuel all the cores. However, the reduced level of inversion achieved in this scheme results in an additional penalty of ~1 dB in the noise figure. Furthermore, such kind of EDFAs does not allow independent gain control per-core [40]. In [43], the pump signal is coupled into the cladding modes via evanescent field through the side of the fiber; spreading subsequently by all the cores. Recently, a cladding pumped amplifier based on 32-core EDF was developed and used in a long haul transmission experiment over more than 1000 km [44]. The aforementioned amplifier was employed to regenerate 15 WDM channels generated in a 50 GHz grid ranging from 1555 nm to 1561 nm with a noise figure of 2 dB.

In distributed Raman amplification (DRA), the signal regeneration takes place in the transmission fiber without needed additional spans of special fibers. Based on a 7-core MCF, it was developed a DRA with a gain of 12 dB and low noise figure [45]. Furthermore, an integrated pump source for DRA, in which the cores share the same pump diode, was also demonstrated with gains of 5.7 dB over the entire C-band [46].

2.5.2 Optical amplification in FMFs

In few-mode EDFs, a single Erbium-doped core is embedded in a silica cladding. The index profile of the core has a key role to play in the reduction of the differential gain, which is the main challenge to be met in the development of optical amplification solutions for MDM transmission systems. The early few-mode-EDFA demonstrated had high (or moder-

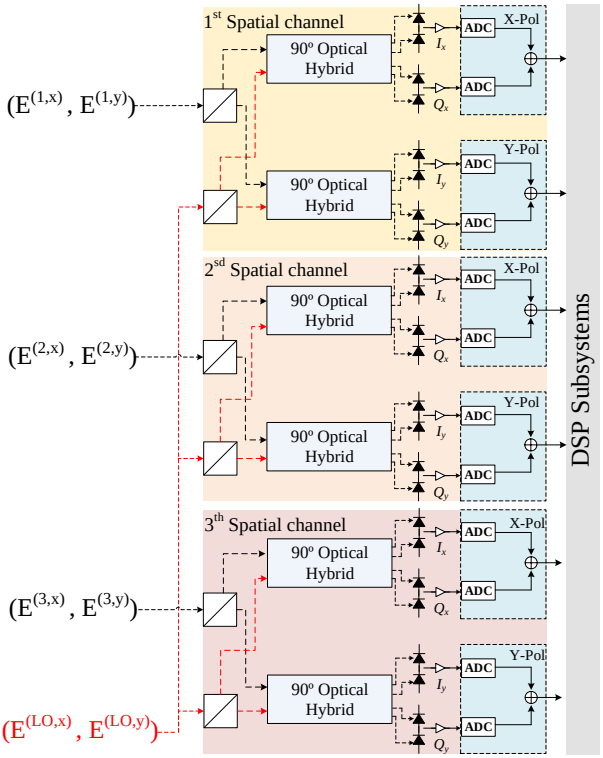

Figure 2.10: Schematic structure of a space and polarization-diversity optical coherent receiver. The optical and electrical signals are represented by dash and solid lines, respectively.

ate) values of mode differential gain (MDG), which has been minimized by optimizing the few-mode-EDF profile and the pump power distribution across the fiber modes. The first approach proposed to decrease the MDG consists in pumping into the LP_{21} mode in a backward configuration enabling a MDG lower than 1 dB in a 2-modes-EDF [47]. It should be noted that in this experiment the EDF supports only two modes at the signal wavelength (~1550 nm; i.e., LP_{01} and LP_{11}), but four modes at the pump wavelength (~ 980 nm; i.e., LP_{01}, LP_{11}, LP_{02} and LP_{21}). However, in the entire C-band the MDG can reach values as higher as 5 dB. Afterward, an almost flat gain spectrum of 15 dB in the entire C-band was reported with a MDG as lower as 0.6 dB in [48]. In this experiment, it is used an EDF with a ring-shaped Erbium doping profile and pumping into the LP_{21} mode in a backward configuration. Using the aforementioned optimization methodologies, it was demonstrated few-mode-EDFA supporting six [49] and, more recently as many as ten modes [50] with MDG in the entire C-band lower than 2 and 3.5 dB, respectively. As in multicore-EDFAs, the adoption of cladding pumping schemes in few-mode-EDFAs allows to remove the S-Mux/S-DeMux interfaces and the wavelength combiners. Such kind of few-mode-EDFAs was proposed in [49] and more recently demonstrated in [51].

Few-mode DRA tends to have lower MDG than few-mode EDFAs because the crosstalk induced along the fiber propagation spreads the pump power among all guided modes. Besides that, the MDG can be also fine tuned by adjusting the pump power distribution launched in the fiber modes. In [52], it is pointed out that a residual MDG of 0.13 dB per 10 dB of gain can be achieved with optimization of the pump power distribution over a 2-modes FMF.

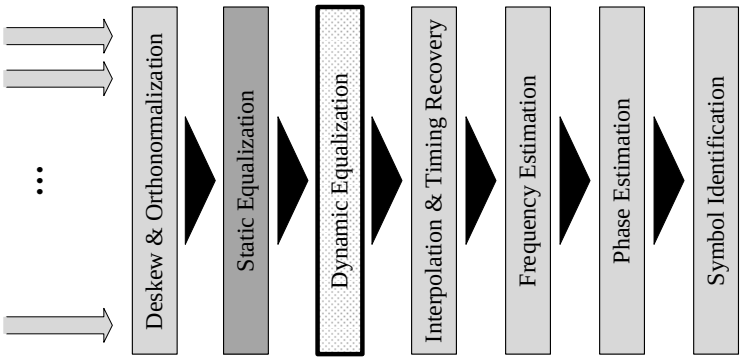

Figure 2.11: DSP subsystems of a SDM coherent optical receiver.

Experimental results show a MDG around 0.5 dB for a maximum gain of 8 dB with the pump launched into the LP_{11} mode in a backward configuration [53].

2.6 Optical coherent detection

In transmission systems with coherent detection, the information is encoded in the amplitude and phase of the optical carrier and therefore decoding entails direct measurement of the complex electrical field. In order to access such information, the optical carrier is made to interfere with a reference signal, the so-called local oscillator (LO), in an optical 90° hybrid as schematically shown in Fig. 2.10 [4]. Firstly, the LO is split in n copies by a beam-splitter and, each copy is sent to a single coherent receiver. In each coherent receiver, a polarization beam splitter is used to decompose the received signal and the LO into their orthogonal polarization components. If polarization demultiplexing is performed in the digital domain, both polarization beam splitters can be replaced by power splitters to equally split the optical power into the two optical hybrids [54]. Then, a pair of 90° optical hybrids is used to mix the received signal with the LO, each hybrid producing four optical signals outputs shifted by 90° from each other [55]. This set of signals comprise the direct detection terms, $|E^{(j,x/y)}|^2$ and $|E^{(LO,x/y)}|^2$, and the coherent detection terms, $\mathrm{Re}\{E^{(j,x/y)}\mathrm{E}^{(LO,x/y)}\}$ and $\mathrm{Im}\{E^{(j,x/y)}E^{(LO,x/y)}\}$, with j denoting the spatial channel. In the coherent detection terms, $\mathrm{Re}\{E^{(j,x/y)}\mathrm{E}^{(LO,x/y)}\}$ and $\mathrm{Im}\{E^{(j,x/y)}E^{(LO,x/y)}\}$, are contained the in-phase (I) and quadrature (Q) information, respectively. If the outputs of the 90° optical hybrid are grouped into 180° shifted optical fields, the optical-to-electrical conversion yields the in-phase, $I_{x/y}$, and quadrature, $Q_{x/y}$, electrical currents. Note that the optical-to-electrical conversion is performed by two pairs of photodiodes operating in a balanced configuration. The electrical outputs of the balanced photodiodes are then fed to linear amplifiers in order to adjust the signal excursion entering in the ADCs. Finally, the electrical I and Q components are sampled and quantized by independent ADCs and sent to the DSP subsystem for post-processing.

2.6.1 DSP Subsystems

Although the digital equalization can be performed in a single DSP block, it is more beneficial split the DSP block into several subsystems [56]. The two main blocks consider the static equalization, in which linear deterministic effects can be compensated, and dynamic

equalization, in which the randomly evolving phenomena can be tracked and equalized. The structure of DSP at the coherent receiver with spatial diversity is schematically shown in Fig. 2.11. The description of each subsystem is follows:

1. The deskew and orthonormalization subsystem compensates the imperfections in the optical front end. The deskew synchronizes the digital signals with respect to one another. The orthonormalization process compensates imbalances in amplitude, which is mainly caused by imperfections in the 90° hybrid and responsivity mismatch between the photodiodes [4].

2. Deterministic effects, such as chromatic dispersion and possibly nonlinear effects, can be compensated within a static equalization (with weak adaptation or even absent).

3. The dynamic equalization based on MIMO post-processing allows to compensate the randomly evolving phenomena, including crosstalk, MD and MDL. In addition, this subsystem can be also used to compensate residual amounts of deterministic effects, which may have been undercompensated or overcompensated by the static equalization stage.

4. The difference between the symbol clock and the ADC sampling rate can lead to some deviation from the ideal sampling instant (which can even vary in time). This non-ideal sampling behavior can be mitigated by digital interpolation and timing recovery.

5. Carrier recovery comprises frequency and phase estimation. The frequency estimation block aims to determine and remove the frequency deviation between the received signal and the LO. The frequency estimation allows to perform the most part of carrier recovery with a simplified algorithm, reducing the amount of phase that needs be tracked by the phase estimation block.

6. Finally, the digital samples are launched to the symbol identification subsystem to retrieve the transmitted symbols. Further binary processing often includes forward error correction, which is able to reduce the probability of error at the cost of some bit overhead, allowing to substantially reduce the bit-error rate (BER).

2.6.2 Multiple-input multiple-output post-processing

A MIMO equalizer is comprised of an array of $2N \times 2N$ finite impulse response (FIR) filters that enable to compensate the signal distortions arising from crosstalk, MD and MDL. For instance, in an arbitrary SDM-based transmission system with a spatial diversity of $N = 2$, the MIMO equalizer has $4 \times 4 = 16$ FIR filters, as schematically shown in Fig. 2.12(a). A single FIR filter, w^{ij}, with i and j ranging from 1 to $2N$, can be written as

$$w^{(i,j)}(t) = \sum_{l=1}^{m} \zeta_l^{(i,j)} \left[t - \tau_l^{(i,j)} \right], \tag{2.1}$$

where $\zeta_l^{(i,j)}$ and $\tau_l^{(i,j)}$ represent the inverse value of the strength and the time delay, respectively, associated with the lth discrete coupling event[4]. In Fig. 2.12(b), it is shown a schematic

[4]In uncoupled MCF, the fiber cores are ideally isolated requiring only the typical DSP employed at standard transmission systems based on SMF. In such transmission systems, the MIMO post-processing accounts only for polarization-demultiplexing. However, weakly-coupled MCF may also have nonnegligible crosstalk levels requiring in that way MIMO post-processing which takes into account all the space-multiplexed signal.

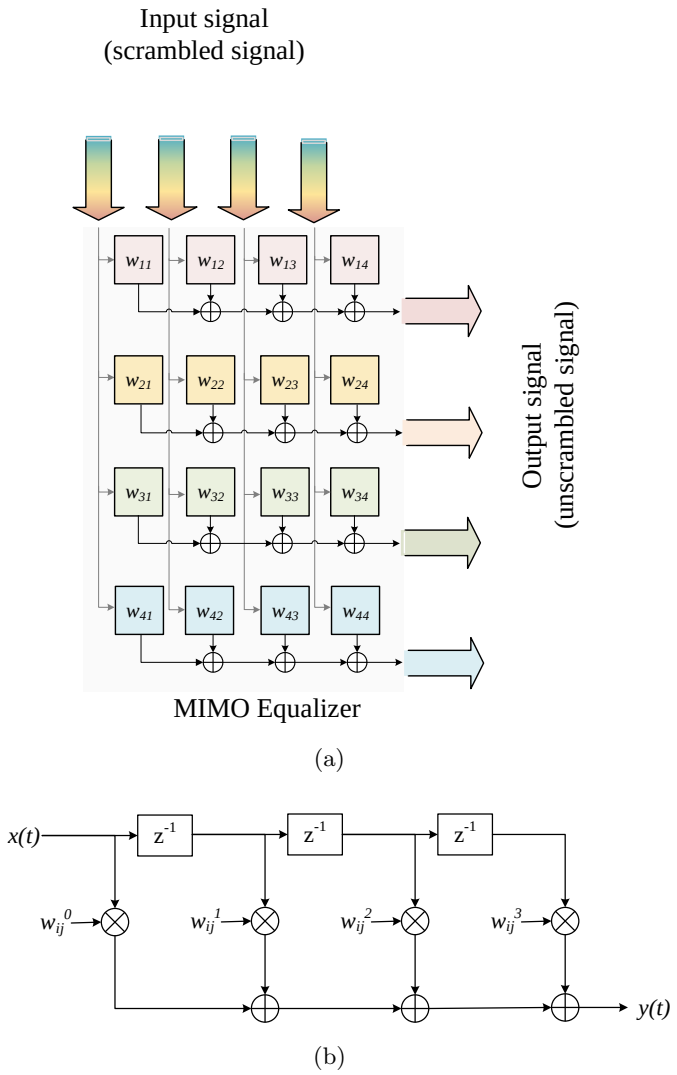

Figure 2.12: (a) Schematic overview for a MIMO equalizer. (b) Schematic of a FIR filter.

of a FIR filter with four taps, i.e., the calculations of the inverse channel matrix must comprise four consecutive samples to fully compensate the intra/inter-symbolic distortions. The maximum value of $\tau_l^{(i,j)}$ or, in other words, the required number of taps of a given FIR filter can be roughly estimated as [5],

$$N_{Tap} = BR_s\tau_{MD}\,, \tag{2.2}$$

where B and R_s denote the symbol rate (or baud-rate) and the sampling rate (samples/symbol) of the transmission system, respectively. The parameter τ_{MD} denotes the total MD spreading for the entire link.

In general, the MIMO equalizer is estimated by reversing the impulse response channel of the fiber link using blind or data-aided (DA) algorithms. In blind algorithms, the filter coefficients can be estimated using information of the received signal itself. These algorithms are usually based on gradient descent methods, in which the cost-function is defined by a mathematical property of the modulated signal. However, such equalization tends to have a

slower rate of convergence, worse performance for low optical signal-to-noise ratio (OSNR) and also tends to be more unstable when compared to DA equalization [57]. In DA-MIMO algorithms, a known training sequence is inserted in the preamble of each data frame enabling the calculation of each coefficient of the $4N^2$ FIR filters. The inverse channel matrix is calculated by means of gradient descent methods that compare the training samples with the received samples. Afterward, when the channel matrix is successfully inverted, the algorithm is switched from the DA estimation to direct-detection (DD) mode. In the DD mode, the received samples themselves are used to slowly tracking the variations of the channel matrix. In order to guide the gradient descendent method in their search for the inverse channel matrix, several cost functions have been analyzed including least-mean-square, normalized least-mean-square, and recursive least squares [5, 25, 58]. To date, the wide amount of SDM transmission experiments were carried out employing DA-MIMO post-processing because of their robustness and fast convergence. It should be also emphasized that MIMO algorithms can be implemented in the time [59] or in the frequency [60] domain. For the same value of BER, the MIMO-frequency domain equalization (FDE) can reduce the computational complexity of the MIMO-time domain equalization (TDE) post-processing by a factor of 8.5 in the case of MDM transmission systems [5, 61]. Such saves in the computational complexity come from the large time delays that must be accommodated by the FIR filters in the time domain, which can be substantially reduced in the frequency domain.

2.7 System demonstrations

With a reduced number of distinguishable spatial channels per fiber, the first SDM transmission experiments started around 2011. Since then, the spatial diversity of special fibers for SDM transmission has been increased several folds; see for instance Fig. 2.13(a)-2.13(d) that shows the evolution of the spatial diversity for MCF, and CC-MCF, and FMF, and few-mode-MCF, respectively. From Fig. 2.13, it is clear that FM-MCF achieve by far the largest value of spatial diversity. As the aggregated bit-rate scales with the available number of spatial channels, it is expected that FM-MCF also present the largest values of aggregated bit-rate, see Fig. 2.13(a)-2.13(d). However, this kind of fibers have considerable values of MD, which constrain the aggregated bit-rate distance product. FMF and FM-MCF are therefore more suitable for short reach transmission systems; whereas, MCF and CC-MCF can be used in short or long-haul transmission systems. MCF works ideally as a set of independent standard SMF placed in a common cladding. In this way, no substantial improvements in the aggregated spectral efficiency per core are expected. With this in mind, we introduce another parameter, the spectral efficiency (SE) per unity of cladding area, which allows to quantify the spatial and spectral efficiency of the transmission systems[5]. This parameter is shown in Fig. 2.13(i)-2.13(l) as a function of the transmission distance. Notice that the characteristic values achieved by a SMF-based transmission system is also pointed out in Fig. 2.13(i)-2.13(l). MCF-based transmission systems show improvements in terms of SE per cladding area and transmission distance. Despite the few experimental demonstration of transmission systems based on CC-MCF, they are the most promising kind of SDM fiber for long-haul transmission

[5]Due to reliability problems in silica fiber fabrication, the diameter of the fiber are typically limited to ~ 200 μm. Therefore, the usual aggregated SE must be replaced by the SE per area to take into account the physical limitations of silica fibers but also, and perhaps more important, the spatial efficiency of the SDM technology.

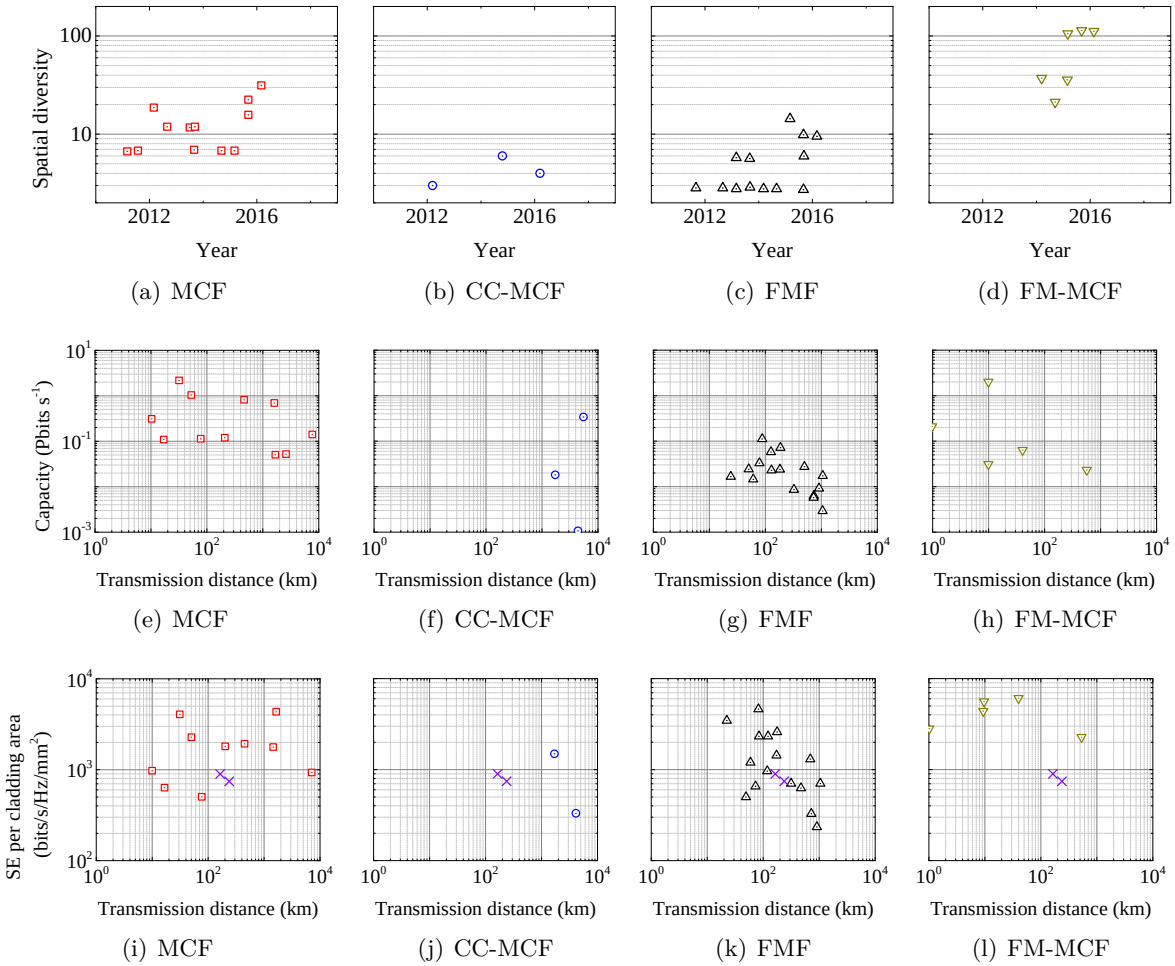

Figure 2.13: (a)-(d) Number of aggregated spatial channels for single fiber. (e)-(h) Aggregated bit-rate transmitted through a single fiber. (i)-(l) Spectral efficiency per cladding area experimentally reported. The points signaled by crosses are the achieved spectral efficiency per cladding area for SSMF. Notice that the kind of the fiber employed in the experiments are pointed out in the subcaption of each figure.

due to their low MD and MDL, but specially due to the reduced nonlinear distortions [62]. While FMF and FM-MCF enable tremendously increase the aggregated bit-rate for short reach transmission systems, they are very limited in terms of transmission distance.

In the author's opinion, the most relevant SDM based transmission experiments carried out in the last years are shown in Fig. 2.13. These experiments are also summarized in Table 2.1, in which the aggregated bit-rate[6], aggregated bite-rate distance product, SE per channel and other additional information are included. The experiments are grouped into four sets, highlighted by different colors. Each set is related with a kind of SDM fiber, which includes MCF, CC-MCF, FMF, and FM-MCF.

Table 2.1: SDM systems demonstrations. Notice that the experiments are grouped in four set which are highlighted by a distinct color. Each set corresponds to a kind of SDM fiber, i.e., MCFs, CC-MCF, FMF and FM-MCF. The N_{Cores} and M_{Modes} is the number of cores and modes, respectively. Spac. Div. denotes the spatial diversity of the SDM transmission system. Note that, a 2-mode FMF guided three distinguishable LP modes. The column called of Mod. Form. contains the modulation format employed in the transmission experiment. In the column S-Mux the spatial interfaces are abbreviated using F.S.:free-space, B.F.: tapered bundle, P.L.: photonic lantern, and PLC: photonics light circuits. N_{Spans} and L. are the number of spans and the length of the span. The remaining parameters, Cap., SE/Channel and Cap.×Dist. are the aggregated bit-rate, the SE per channel and the capacity distance product, respectively.

SDM Fiber		Spac.	Mod.	MIMO	S-MUX	Amp.	Dist.		Cap.	SE/Channel	Cap.× Dist.	Ref.
N_{Cores}	M_{Modes}	Div.	Form.				N_{Spans}	L. (km)	(Tb/s)	(b/Hz/s)	(Pb km/s)	
2	1	3	QPSK	✓	F.S.	FM-EDFA	1	50	26.4	2.09	1.3	[63]
2	1	3	32QAM	✓	F.S	FM-EDFA	1	119	57.6	4	6.8	[64]
2	1	3	QPSK	✓	F.S.	FM-EDFA	20	50	3.04	5.5	3	[48]
4	1	6	16QAM	✓	P.L.	1c-EDFA	3	59	24.6	32	4.3	[65]
4	1	6	QPSK	✓	P.L.	1c-EDFA	12	59	6.1	15.25	4.3	[66]
4	1	6	QPSK	✓	P.L.	-	1	74.17	34.68	1.3	2.5	[67]
6	1	10	QPSK	✓	P.L.	-	1	125	23.2	2.9	2.9	[68]
9	1	15	QPSK	✓	B.F.+P.L	-	1	22.8	17.28	2.9	0.4	[69]
1	3	3	QPSK	✓	F.S	1c-EDFA	70	60	1.2	4.03	5.04	[70]
1	6	6	QPSK	✓	P.L.+ B.F.	1c-EDFA	55	31	18	18	30.6	[71]
1	4	4	16QAM	✓	B.F.	1c-EDFA	50	110	34	11	190	[62]
1	7	7	QPSK	-	F.S.	-	1	16.8	109	1.6	1.7	[72]
1	7	7	QPSK	-	B.F.	-	1	76.8	112	2.0	8.8	[22]
1	7	7	QPSK	-	B.F.	7c-EDFA	161	45.5	140.7	4.0	1030	[73]
1	7	7	32QAM	-	B.F.	DRA+7c-EDFA	1	204	120.7	7.6	24.6	[74]
1	7	7	QPSK	-	B.F.	7c-EDFA	63	40	51.1	1.5	128.7	[75]
1	12	12	32QAM	-	B.F.	-	1	52	1014	91.5	52.7	[76]
1	12	12	16QAM	-	B.F.	DRA+12c-EDFA	30	50	2×344	6.1	516	[77]
1	16	16	16QAM	-	B.F.	-	1	55	2×16.3	21.2	14.3	[78]
1	19	19	QPSK	-	F.S.	-	1	10.1	305	1.6	14.3	[21]
1	22	22	64QAM	-	P.L.	-	1	31	2150	9.8	66.6	[79]
1	32	32	16QAM	-	P.L.	7c-EDFA	32	51.4	50	6	82.2	[9]
2	12	36	32QAM	✓	PLC	-	1	40.8	61.78	6.88	2.5	[80]
2	7	21	32QAM	✓	P.L.	-	1	1	200	3.8	0.2	[81]
2	12	36	QPSK	✓	PLC	FM-EDFA	10	52.7	23.58	2.62	12.4	[82]
2	19	57	QPSK	✓	F.S.	-	1	9.8	2050	2.62	20.1	[83]

2.7.1 Systems based on MCFs

In 2011, for the first time, two distinct research teams accomplished simultaneously the transmission over tens of kilometers in MCFs with negligible crosstalk and at ~100 Gbit/s [22, 72]. In one of these experiments, an aggregated bit-rate of 112 Tbit/s was transmitted over 76.8 km of a 7-core MCF using dense WDM and polarization-division multiplexing (PDM)-quaternary phase-shift keying (QPSK) signal at 107 Gbit/s [72]. On the other experiment, it was transmitted 109 Tbit/s over 16.8 km of a 7-core MCF also using dense WDM and PDM-QPSK signals at 86 Gbit/s [22]. Both aforementioned experiments pave the way for current SDM transmission systems based on MCF. Thenceforth, the aggregated bit-rate transmitted over a single MCF has been enhanced by increasing the number of cores per MCFs and/or the aggregated bit-rate per single core, which can be achieved by increasing the number of WDM channels or the order of the quadrature amplitude modulation (QAM). On the other hand, crosstalk limits the density of the modulation format transmitted and therefore it is mandatory to find novel strategies to its mitigation. In 2012, an aggregated bit-rate of 305 Tbit/s was transmitted over 10.1 km of a 19-cores trench-assisted MCF using a

[6]For convenience of writing, the aggregated bit-rate transmitted is called “cap”. in table 2.1.

free-space S-Mux/S-DeMux with negligible crosstalk [21]. In this case, the aggregated bit-rate was mainly boosted by the increased number of cores supported by the MCF. In [76], the throughput was further increased by using more dense modulation formats, overcoming the barrier of 1 Pbit/s and achieving a spectral efficiency of 91.5 bit/s/Hz. In such experiment, it was employed 52 km of a 12-core trench-assisted MCF, and dense WDM with polarization-multiplexed (PM)-32QAM signals. In 2015, the available transmission capacity was doubled (2.15 Pbit/s over 31 km) by using a 22-core MCF supporting each core 399 WDM channels carrying PM-64QAM signals.

The product between the aggregated bit-rate and the link length is perhaps the fundamental parameter in the design of long-haul transmission systems; however, it has achieved less impressive improvements than the aforementioned enhancements on the SE and in the aggregated bit-rate. Such product is mainly limited by the inter/intra-symbolic distortions induced by the crosstalk, which scales with the length of the fiber link. The crosstalk can be substantially reduced by using adjacent channels for signal transmission in opposite directions; the so-called propagation direction interleaving (PDI). PDI has a similar effect to dissimilar cores in heterogeneous MCF (HeMCF); up stream and down stream cores works as two distinct types of cores. Using PDI in a 12-core MCF, an aggregated bit-rate distance product of ~ 0.5 Ebit km/s was demonstrated. In such experiment, an additional digital back propagation subsystem which accounts for the equalization of the nonlinear distortions was considered at the coherent receiver [77]. After, this product was increased for ~ 1 Ebit/s km using super Nyquist WDM and in-line multicore-EDFA [84]. More recently, it was achieved 1.5 Ebit/s km using a 32-core HeMCF [9].

2.7.2 Systems based on CC-MCFs

In 2009, for the first time, CC-MCF was conceptually proposed for MDM [85]. The proof of concept was only carried out in 2011 [86], using a 3-core CC-MCF. In [70], the long haul transmission over 4200 km of a 3-core CC-MCF was successfully demonstrated achieving a SE of 4.8 bit/s/Hz. Obviously, the following steps includes the development of CC-MCF with higher spatial diversity. In that way, a 4-core CC-MCF with optimized DMGD was employed for signal transmission over 2000 (or 5500) km achieving a SE of 43.56 (or 11.52) bit/s/Hz [62]. In this experiment, the CC-MCF and a standard SMF are also compared in terms nonlinear signal distortions induced by signal propagation. From this comparison results that CC-MCF induce lower nonlinear distortions in the transmitted signal than SSMF. To further increase the spatial diversity, a 6-core CC-MCF was also manufacture and employed for signal transmission over 1700 km [71].

To date, however, the spatial diversity delivered by CC-MCF based transmission systems are still smaller than the remaining SDM solutions currently in development. As in MCF or FM-MCF, the diversity can be increased by adding several groups of CC to the same common cladding without changing the MD of the degenerated modes supported by each group of CC. In this sense, a CCG-MCF with three groups of 3-core CC was successfully fabricated and employed for signal transmission over 715 km [13].

2.7.3 Systems based on FMFs

In 2011, the first demonstration of MDM over modern FMFs was carried out by two distinct research teams [87, 88]. In [87], two PM-orthogonal frequency division multiplex-

ing (OFDM) signals at 107 Gbit/s were space-multiplexed into two LP modes of a 2-mode FMF (i.e., LP_{01} and the LP_{11a} or LP_{01} and the LP_{11b}) and transmitted over 4.5 km. In [88], it was transmitted a 100 Gbit/s PM-QPSK signals also space-multiplexed into two LP modes (LP_{01} and LP_{11a} or LP_{01} and LP_{11b}) over 40 km of a 2-mode FMF. Even for the short lengths of FMF employed in both aforementioned experiments, the crosstalk between LP_{11a} and LP_{11b} induces inter/intra-symbolic distortions requiring the use of a 4×4 MIMO post-processing for successfully recover the transmitted signal. In [89], for the first time, the spatial diversity of a 2-mode FMF was fully exploited using a 6×6 MIMO post-processing at the optical coherent receiver. In such experiment, it was transmitted a 28 Gbit/s PM-QPSK over 10 km of fiber employing the three available modes at 1550 nm, i.e., LP_{01}, LP_{11a} and LP_{11b}. It should be noted that the computational complexity of the 6×6 MIMO post-processing is substantially higher than the 4×4 MIMO due to the increased MIMO dimensionality but mainly to the higher value of MD that needed to be equalized. Thereafter, several MDM transmission experiments have been performed with the purpose of, firstly, increase the transmission distance and, secondly, enhance the aggregated bit-rate per fiber link. In that way, the scientific community has been focused in the design and fabrication of FMFs with low DMGD and a higher number of guided modes. Thanks to such efforts, several transmission experiments over moderated transmission distances are carried out. In [63], an aggregated bit-rate of ~ 30 Tbit/s was transmitted over 50 km of a 2-mode FMF. Afterward, in-line amplification was introduced to further increase the reach of MDM transmission systems. In [48], the link length was increased for 500 (or 1000) km transmitting 33 (or 3.6) Tbit/s employing PM-16QAM (or PM-QPSK) signals. The next stage in the development of MDM systems comprise the increment of the spatial diversity. In this sense, FMF supporting a large number of modes and maintaining the MD at low or moderate levels are fabricated. In [65], a 4-mode FMF and supporting 6 distinguishable spatial channels was employed to transmit an aggregated bit-rate of 24.6 Tbit/s over 177 km. Then, a 6-mode FMF supporting 10 distinguishable spatial channels was designed and employed for transmission over 4.45 km [90], and more recently a 9-mode FMF supporting 15 distinguishable spatial channels was employed to transmitted over 22.8 km [69]. In terms of SE, the values achieved by MDM systems are less impressive than their counterparts based on MCF. For a 2-mode FMF, it was reported a spectral efficiency of 32 bit/s/Hz [65]; whereas, for 10-mode FMF was achieved a SE of 58 bit/s/Hz [91].

The high values of DMGD still persist as the main challenge in MDM systems for long-haul transmission, despite the tremendous progress made on fiber design and fabrication [14]. In that sense, dispersion-compensated (DC) links was proposed to manage the overall MD of the link. This kind of links are comprised of several spans of fiber concatenated with opposite values of DMGD, i.e., concatenated FMFs with positive and negative DMGD. If crosstalk can be neglected, the channel impulse response spread of the compensated link can be in principle fully compensated. In that sense, weakly-coupled FMFs are usually preferred to produce DC links. However, refractive index inhomogeneities and core geometry variations are always present in real fibers and, therefore, crosstalk tends unavoidably to happen affecting the performance of the DC link. On the other hand, the impulse response spread can be also significantly reduced by decreasing the size of the DMGD compensation step or the length of each span [92]. In [93], the DC link was already demonstrated with a DMGD as low as 0.5 ps/km in the entire C-band.

For short reach transmission, it is preferable avoiding the MIMO post-processing at the receiver side. Therefore, the crosstalk must be substantially reduced. As in MCFs, the PDI can be also employed in MDM systems to reduce crosstalk between neighbouring modes. In

addition, MDM based on orbital angular momentum (OAM), which are another kind of optical modes, was also proposed to further decrease the crosstalk between distinct mode-groups [94].

2.7.4 Systems based on FM-MCFs

Currently, the largest degree of spatial diversity was achieved by merging the FMF and the MCF approaches in the form of FM-MCF. The first demonstration of FM-MCF based transmission experiment goes back to 2012. In such experiment, it was transmitted an aggregated bit-rate of 1.05 Pbit/s over 3 km of a hybrid fiber with 12 single-mode cores and two 2-mode cores [19]. After, a 2-modes×12-cores FM-MCF was used to transmit 174 Tbit/s over 40 km of fiber achieving a SE of 247.9 bit/s/Hz [80]. In [95], a hole-assisted 2-modes×7-cores FM-MCF was employed to transmit an aggregated bit-rate of 5.1 Tbit/s per wavelength channel, or 255 Tbit/s using WDM, over 1 km of fiber. Further increasing the spatial diversity, a 6-mode×19-core few-mode-MCF was employed to transmit an aggregated bit-rate of 1.15 Pbit/s [96]. More recently, an aggregated bit-rate of 10.16 Pbit/s was transmitted over 11.3 km of a 6-mode×19-cores FM-MCF employing the C+L band and 16QAM and 64QAM [97].

2.8 Summary

Recent developments in fiber fabrication, S-Mux/S-DeMux interfaces and in-line amplification has enabled the remarkable progress, in terms of capacity and reach, of SDM based transmission experiments. Preliminary demonstrations of SDM links with aggregated bit-rates around Pbit/s assisted by spatial and wavelength selective switching and in-line amplification have been performed. Such achievements revealed a tremendous effort of the scientific community to experimentally demonstrate the feasibility of transmission systems based on SDM. Despite these considerable advances, it is worth mentioning that such systems are yet in a very early stage of development. Only with the maturation of all the key parts of the SDM systems will be possible achieve the desirable gains in terms of aggregated bit-rate and energy efficiency.

Future challenges for SDM solutions will certainly include crosstalk and MD management and mitigation. Mitigation of crosstalk can be addressed by improving and developing a new kind of optical fibers or by developing a more efficient MIMO post-processing techniques. In fact, any commercial solution for long haul transmission systems must involve both approaches, in which SDM-based transmission systems without spatial selectivity using superchannels and assisted by advanced DSP subsystems will be a key driver to develop high-capacity and low-cost-per-bit links. MIMO free transmission systems, i.e., transmission systems with spatial selectivity, are very interesting solutions to increase the aggregate bit-rate in short reach transmission systems. However, this kind of transmission systems require enhanced switching capabilities of the SDM-based network to independently route each individual spatial channel through the optical network. In that way, SWSS are of paramount importance in the future implementation of short reach SDM networks. Last but not least, all-optical amplification solutions for SDM will certainly entail the development of more efficient FMF/MCF-based EDFA. It is clear that their common use in fiber optic transmission systems is crucial and, therefore, more efficient solutions need to be produced.

Bibliography

[1] D. J. Richardson, J. M. Fini, and L. E. Nelson, "Space-division multiplexing in optical fibres," *Nature Photonics*, vol. 7, pp. 354–362, May 2013.

[2] C. Xia, N. Chand, A. Velázquez-Benítez, Z. Yang, X. Liu, J. Antonio-Lopez, H. Wen, B. Zhu, N. Zhao, F. Effenberger, R. Amezcua-Correa, and G. Li, "Time-division-multiplexed few-mode passive optical network," *Optics Express*, vol. 23, no. 2, pp. 1151–1158, Jan 2015.

[3] R. Ryf and N. Fontaine, *Space-Division Multiplexing and MIMO Processing.* John Wiley and Sons, Inc, 2016, pp. 547–608.

[4] S. Savory, "Digital filters for coherent optical receivers," *Optics Express*, vol. 16, no. 2, pp. 804–817, Jan 2008.

[5] G. Li, N. Bai, N. Zhao, and C. Xia, "Space-division multiplexing: the next frontier in optical communication," *Advances in Optics and Photonics*, vol. 6, no. 4, pp. 413–487, Dec 2014.

[6] S. Inao, T. Sato, S. Sentsui, T. Kuroha, and Y. Nishimura, "Multicore optical fiber," in *Optics Fiber Conference (OFC)*, 1979, p. WB1.

[7] G. Li and X. Liu, "Focus issue: space multiplexed optical transmission," *Optics Express*, vol. 19, no. 17, pp. 16 574–16 575, 2011.

[8] K. Nakajima, P. Sillard, D. Richardson, M.-J. Li, R. Essiambre, and S. Matsuo, "Transmission media for an SDM-based optical communication system," *IEEE Communications Magazine*, vol. 53, no. 2, pp. 44–51, 2015.

[9] T. Mizuno, K. Shibahara, H. Ono, Y. Abe, Y. Miyamoto, F. Ye, T. Morioka, Y. Sasaki, Y. Amma, K. Takenaga, S. Matsuo, K. Aikawa, K. Saitoh, Y. Jung, D. J. Richardson, K. Pulverer, M. Bohn, and M. Yamada, "32-core dense SDM unidirectional transmission of PDM-16QAM signals over 1600 km using crosstalk-managed single-mode heterogeneous multicore transmission line," in *Optical Fiber Conference (OFC).* Optical Society of America, 2016, p. Th5C.3.

[10] Y. Amma, Y. Sasaki, K. Takenaga, S. Matsuo, J. Tu, K. Saitoh, M. Koshiba, T. Morioka, and Y. Miyamoto, "High-density multicore fiber with heterogeneous core arrangement," in *Optical Fiber Conference (OFC).* Optical Society of America, 2015, p. Th4C.4.

[11] P. Sillard, "Next-generation fibers for space-division-multiplexed transmissions," *IEEE/OSA Journal of Lightwave Technology*, vol. 33, no. 5, pp. 1092–1099, March 2015.

[12] T. Hayashi, R. Ryf, N. Fontaine, C. Xia, S. Randel, R.-J. Essiambre, P. Winzer, and T. Sasaki, "Coupled-core multi-core fibers: High-spatial-density optical transmission fibers with low differential modal properties," in *European Conference on Optical Communication (ECOC)*, 2015, pp. 1–3.

[13] R. Ryf, N. Fontaine, M. Montoliu, S. Randel, S. Chang, H. Chen, S. Chandrasekhar, A. Gnauck, R.-J. Essiambre, P. J. Winzer, T. Taru, T. Hayashi, and T. Sasaki, "Space-division multiplexed transmission over 3×3 coupled-core multicore fiber," in *Optical Fiber Conference (OFC)*. Optical Society of America, 2014, p. Tu2J.4.

[14] F. Ferreira, D. Fonseca, and H. da Silva, "Design of few-mode fibers with M-modes and low differential mode delay," *IEEE/OSA Journal of Lightwave Technology*, vol. 32, no. 3, pp. 353–360, Feb 2014.

[15] T. Sakamoto, T. Mori, T. Yamamoto, and S. Tomita, "Differential mode delay managed transmission line for WDM-MIMO system using multi-step index fiber," *IEEE/OSA Journal of Lightwave Technology*, vol. 30, no. 17, pp. 2783–2787, Sept 2012.

[16] L. Gruner-Nielsen, Y. Sun, J. Nicholson, D. Jakobsen, K. Jespersen, R. Lingle, and B. Palsdottir, "Few mode transmission fiber with low DGD, low mode coupling, and low loss," *IEEE/OSA Journal of Lightwave Technology*, vol. 30, no. 23, pp. 3693–3698, Dec 2012.

[17] W. He, H. Yu, P. Sillard, R. A. Correa, and G. Li, "Weakly-coupled few-mode fibers and their applications," in *European Conference and Exposition on Optical Communications*, 2017, pp. 1–2.

[18] F. Ferreira, D. Fonseca, A. Lobato, B. Inan, and H. Silva, "Reach improvement of mode division multiplexed systems using fiber splices," *IEEE Photonics Technology Letters*, vol. 25, no. 12, pp. 1091–1094, June 2013.

[19] D. Qian, E. Ip, M.-F. Huang, M. Li, A. Dogariu, S. Zhang, Y. Shao, Y.-K. Huang, Y. Zhang, X. Cheng, Y. Tian, P. Ji, A. Collier, Y. Geng, J. Linares, C. Montero, V. Moreno, X. Prieto, and T. Wang, "1.05Pb/s transmission with 109b/s/Hz spectral efficiency using hybrid single- and few-mode cores," in *Frontiers in Optics 2012/Laser Science XXVIII*. Optical Society of America, 2012, p. FW6C.3.

[20] G. M. Saridis, D. Alexandropoulos, G. Zervas, and D. Simeonidou, "Survey and evaluation of space division multiplexing: From technologies to optical networks," *IEEE Communications Surveys Tutorials*, vol. 17, no. 4, pp. 2136–2156, 2015.

[21] J. Sakaguchi, B. Puttnam, W. Klaus, Y. Awaji, N. Wada, A. Kanno, T. Kawanishi, K. Imamura, H. Inaba, K. Mukasa, R. Sugizaki, T. Kobayashi, and M. Watanabe, "19-core fiber transmission of 19×100×172-Gb/s SDM-WDM-PDM-QPSK signals at 305 Tb/s," in *Optical Fiber Conference (OFC)*. Optical Society of America, 2012, p. PDP5C.1.

[22] B. Zhu, T. Taunay, M. Fishteyn, X. Liu, S. Chandrasekhar, M. F. Yan, J. M. Fini, E. M. Monberg, and F. V. Dimarcello, "112-Tb/s space-division multiplexed DWDM transmission with 14-b/s/Hz aggregate spectral efficiency over a 76.8-km seven-core fiber," *Optics Express*, vol. 19, no. 17, pp. 16 665–16 671, Aug 2011.

[23] P. Mitchell, G. Brown, R. Thomson, N. Psaila, and A. Kar, "57 channel (19×3) spatial multiplexer fabricated using direct laser inscription," in *Optical Fiber Conference (OFC)*. Optical Society of America, 2014, pp. M3K–5.

[24] S. C. Ellis and J. Bland-Hawthorn, "Speciality optical fibres for astronomy," in *Micro-structured and Specialty Optical Fibres IV*, vol. 9507, 2015, pp. 9507–1–9507–15.

[25] R. Ryf, S. Randel, A. Gnauck, C. Bolle, A. Sierra, S. Mumtaz, M. Esmaeelpour, E. Burrows, R. Essiambre, P. Winzer, D. Peckham, A. McCurdy, and R. Lingle, "Mode-division multiplexing over 96 km of few-mode fiber using coherent 6×6 MIMO processing," *IEEE/OSA Journal of Lightwave Technology*, vol. 30, no. 4, pp. 521–531, Feb 2012.

[26] B. B. Oner, M. Turduev, I. H. Giden, and H. Kurt, "Efficient mode converter design using asymmetric graded index photonic structures," *Optics Letters*, vol. 38, no. 2, pp. 220–222, Jan 2013.

[27] R. Ryf, C. Bolle, and J. von Hoyningen-Huene, "Optical coupling components for spatial multiplexing in multi-mode," in *European Conference on Optical Communications (ECOC)*. Optical Society of America, 2011, p. Th.12.B.1.

[28] K. Igarashi, D. Souma, K. Takeshima, and T. Tsuritani, "Selective mode multiplexer based on phase plates and Mach-Zehnder interferometer with image inversion function," *Optics Express*, vol. 23, no. 1, pp. 183–194, Jan 2015.

[29] C. Doerr, N. Fontaine, M. Hirano, T. Sasaki, L. Buhl, and P. Winzer, "Silicon photonic integrated circuit for coupling to a ring-core multimode fiber for space-division multiplexing," in *European Conference on Optical Communication (ECOC)*. Optical Society of America, 2011, p. Th.13.A.3.

[30] T. A. Birks, I. Gris-Sánchez, S. Yerolatsitis, S. G. Leon-Saval, and R. R. Thomson, "The photonic lantern," *Advances in Optics and Photonics*, vol. 7, no. 2, pp. 107–167, Jun 2015.

[31] A. Witkowska, S. G. Leon-Saval, A. Pham, and T. A. Birks, "All-fiber LP_{11} mode convertors," *Optics Letters*, vol. 33, no. 4, pp. 306–308, Feb 2008.

[32] K. Lai, S. G. Leon-Saval, A. Witkowska, W. J. Wadsworth, and T. A. Birks, "Wavelength-independent all-fiber mode converters," *Optics Letters*, vol. 32, no. 4, pp. 328–330, Feb 2007.

[33] I. Giles, A. Obeysekara, R. Chen, D. Giles, F. Poletti, and D. Richardson, "Fiber LPG mode converters and mode selection technique for multimode SDM," *IEEE Photonics Technology Letters*, vol. 24, no. 21, pp. 1922–1925, Nov 2012.

[34] D. M. Marom, P. D. Colbourne, A. D'errico, N. K. Fontaine, Y. Ikuma, R. Proietti, L. Zong, J. M. Rivas-Moscoso, and I. Tomkos, "Survey of photonic switching architectures and technologies in support of spatially and spectrally flexible optical networking [invited]," *IEEE/OSA Journal of Optical Communications and Networking*, vol. 9, no. 1, pp. 1–26, Jan 2017.

[35] Y. Ikuma, K. Suzuki, N. Nemoto, E. Hashimoto, O. Moriwaki, and T. Takahashi, "Low-loss transponder aggregator using spatial and planar optical circuit," *IEEE/OSA Journal of Lightwave Technology*, vol. 34, no. 1, pp. 67–72, Jan 2016.

[36] L. Nelson, M. Feuer, K. Abedin, X. Zhou, T. Taunay, J. Fini, B. Zhu, R. Isaac, R. Harel, G. Cohen, and D. Marom, "Spatial superchannel routing in a two-span ROADM system for space division multiplexing," *IEEE/OSA Journal of Lightwave Technology*, vol. 32, no. 4, pp. 783–789, Feb 2014.

[37] J. Carpenter, S. Leon-Saval, J. Salazar-Gil, J. Bland-Hawthorn, G. Baxter, L. Stewart, S. Frisken, M. Roelens, B. Eggleton, and J. Schröder, "1x11 few-mode fiber wavelength selective switch using photonic lanterns," *Optics Express*, vol. 22, no. 3, pp. 2216–2221, Feb 2014.

[38] N. K. Fontaine, R. Ryf, C. Liu, B. Ercan, J. R. S. Gil, S. G. Leon-Saval, J. Bland-Hawthorn, and D. T. Neilson, "Few-mode fiber wavelength selective switch with spatial-diversity and reduced-steering angle," in *Optical Fiber Conference (OFC)*, March 2014, p. Th4A.7.

[39] N. K. Fontaine, T. Haramaty, R. Ryf, H. Chen, L. Miron, L. Pascar, M. Blau, B. Frenkel, L. Wang, Y. Messaddeq, S. LaRochelle, R. J. Essiambre, Y. Jung, Q. Kang, J. K. Sahu, S. U. Alam, D. J. Richardson, and D. M. Marom, "Heterogeneous space-division multiplexing and joint wavelength switching demonstration," in *Optical Fiber Conference (OFC)*, March 2015, p. Th5C.5.

[40] D. Richardson, S. Jain, Y. Jung, and S. Alam, "Optical amplifiers for SDM communication systems," in *European Conference on Optical Communication (ECOC)*, 2017, pp. 1–3.

[41] S. Randel, R. Ryf, A. Gnauck, M. Mestre, C. Schmidt, R. Essiambre, P. Winzer, R. Delbue, P. Pupalaikis, A. Sureka *et al.*, "Mode-multiplexed 6× 20-GBd QPSK transmission over 1200-km DGD-compensated few-mode fiber," in *Optical Fiber Conference (OFC)*. Optical Society of America, 2012, pp. PDP5C–5.

[42] K. S. Abedin, T. F. Taunay, M. Fishteyn, M. F. Yan, B. Zhu, J. M. Fini, E. M. Monberg, F. Dimarcello, and P. Wisk, "Amplification and noise properties of an Erbium-doped multicore fiber amplifier," *Optics Express*, vol. 19, no. 17, pp. 16 715–16 721, Aug 2011.

[43] T. Theeg, H. Sayinc, J. Neumann, L. Overmeyer, and D. Kracht, "Pump and signal combiner for bi-directional pumping of all-fiber lasers and amplifiers," *Optics Express*, vol. 20, no. 27, pp. 28 125–28 141, Dec 2012.

[44] C. Castro, S. Jain, Y. Jung, and et al., "Crosstalk analysis of 32-core dense space division multiplexed system for higher order modulation formats using an integrated cladding-pumped amplifier," in *European Conference on Optical Communications (ECOC)*, 2017.

[45] H. Takara, H. Ono, Y. Abe, H. Masuda, K. Takenaga, S. Matsuo, H. Kubota, K. Shibahara, T. Kobayashi, and Y. Miaymoto, "1000-km 7-core fiber transmission of 10×96-Gb/s PDM-16QAM using Raman amplification with 6.5 W per fiber," *Optics Express*, vol. 20, no. 9, pp. 10 100–10 105, Apr 2012.

[46] K. Suzuki, H. Ono, T. Mizuno, Y. Hashizume, Y. Abe, T. Takahashi, K. Takenaga, S. Matsuo, and H. Takara, "Pump light source for distributed Raman amplification in MCFs with LD sharing circuit," *IEEE Photonics Technology Letters*, vol. 24, no. 21, pp. 1937–1940, Nov 2012.

[47] N. Bai, E. Ip, Y.-K. Huang, E. Mateo, F. Yaman, M.-J. Li, S. Bickham, S. Ten, J. L. nares, C. Montero, V. Moreno, X. Prieto, V. Tse, K. M. Chung, A. Lau, H.-Y. Tam, C. Lu, Y. Luo, G.-D. Peng, G. Li, and T. Wang, "Mode-division multiplexed transmission with inline few-mode fiber amplifier," *Optics Express*, vol. 20, no. 3, pp. 2668–2680, Jan 2012.

[48] E. Ip, M.-J. Li, K. Bennett, Y.-K. Huang, A. Tanaka, A. Korolev, K. Koreshkov, W. Wood, E. Mateo, J. Hu *et al.*, "146$\lambda\times$ 6$\times$ 19-Gbaud wavelength-and mode-division multiplexed transmission over 10×50-km spans of few-mode fiber with a gain-equalized few-mode EDFA," *IEEE/OSA Journal of Lightwave Technology*, vol. 32, no. 4, pp. 790–797, 2014.

[49] Y. Jung, E. L. Lim, Q. Kang, T. C. May-Smith, N. H. L. Wong, R. Standish, F. Poletti, J. K. Sahu, S. U. Alam, and D. J. Richardson, "Cladding pumped few-mode EDFA for mode division multiplexed transmission," *Optics Express*, vol. 22, no. 23, pp. 29 008–29 013, Nov 2014.

[50] M. Wada, T. Sakamoto, S. Aozasa, T. Mori, T. Yamamoto, and K. Nakajima, "Core-pumped 10-mode EDFA with cascaded EDF configuration," in *European Conference on Optical Communication (ECOC)*, 2016, pp. 1–3.

[51] R. Ryf, N. K. Fontaine, H. Chen, A. H. Gnauck, Y. Jung, Q. Kang, J. K. Sahu, S. U. Alam, D. J. Richardson, Y. Sun, X. Jiang, L. GrÃijner-Nielsen, R. V. Jensen, and R. Lingle, "72-tb/s transmission over 179-km all-fiber 6-mode span with two cladding pumped in-line amplifiers," in *European Conference on Optical Communication (ECOC)*, Sept 2015, pp. 1–3.

[52] R. Ryf, R. Essiambre, J. von Hoyningen-Huene, and P. Winzer, "Analysis of mode-dependent gain in Raman amplified few-mode fiber," in *Optical Fiber Conference (OFC)*. Optical Society of America, 2012, pp. OW1D–2.

[53] R. Ryf, A. Sierra, R.-J. Essiambre, S. Randel, A. Gnauck, C. A. Bolle, M. Esmaeelpour, P. J. Winzer, R. Delbue, P. Pupalaikis *et al.*, "Mode-equalized distributed Raman amplification in 137-km few-mode fiber," in *European Conference on Optical Communications (ECOC)*. Optical Society of America, 2011, pp. Th–13.

[54] T. J. Schmidt, D. R. Stauffer, and K. Gass, "Implementation agreement for intradyne coherent receivers," *Optical Internetworking Forum, Tech. Rep.*, 2010.

[55] M. Seimetz and C. M. Weinert, "Options, feasibility, and availability of 2×4 90° hybrids for coherent optical systems," *IEEE/OSA Journal of Lightwave Technology*, vol. 24, no. 3, pp. 1317–1322, March 2006.

[56] S. Arik, J. Kahn, and K.-P. Ho, "MIMO signal processing for mode-division multiplexing: An overview of channel models and signal processing architectures," *IEEE Signal Processing Magazine*, vol. 31, no. 2, pp. 25–34, 2014.

[57] M. Kuschnerov, M. Chouayakh, K. Piyawanno, B. Spinnler, E. de Man, P. Kainzmaier, M. Alfiad, A. Napoli, and B. Lankl, "Data-aided versus blind single-carrier coherent receivers," *IEEE Photonics Journal*, vol. 2, no. 3, pp. 387–403, June 2010.

[58] S. Arik, D. Askarov, and J. Kahn, "Adaptive frequency-domain equalization in mode-division multiplexing systems," *IEEE/OSA Journal of Lightwave Technology*, vol. 32, no. 10, pp. 1841–1852, May 2014.

[59] S. Randel, R. Ryf, A. Sierra, P. Winzer, A. Gnauck, C. Bolle, R. Essiambre, D. Peckham, A. McCurdy, and R. Lingle, "6×56-Gb/s mode-division multiplexed transmission over 33-km few-mode fiber enabled by 6×6 MIMO equalization," *Optics Express*, vol. 19, no. 17, pp. 16 697–16 707, Aug 2011.

[60] N. Bai and G. Li, "Adaptive frequency-domain equalization for mode-division multiplexed transmission," *IEEE Photonics Technology Letters*, vol. 24, no. 21, pp. 1918–1921, Nov 2012.

[61] N. Bai, E. Ip, M.-J. Li, T. Wang, and G. Li, "Long-distance mode-division multiplexed transmission using normalized adaptive frequency-domain equalization," in *Photonics Society Summer Topical Meeting Series, 2013 IEEE*, July 2013, pp. 135–136.

[62] R. Ryf, J. Alvarado, B. Huang, J. Antonio-Lopez, S. Chang, N. Fontaine, H. Chen, R.-J. Essiambre, E. Burrows, R. Amezcua-Correa *et al.*, "Long-distance transmission over coupled-core multicore fiber," in *European Conference on Optical Communication (ECOC)*, 2016, pp. 1–3.

[63] E. Ip, N. Bai, Y.-K. Huang, E. Mateo, F. Yaman, S. Bickham, H.-Y. Tam, C. Lu, M.-J. Li, S. Ten, A. Lau, V. Tse, G.-D. Peng, C. Montero, X. Prieto, and G. Li, "88×3×112-Gb/s WDM transmission over 50-km of three-mode fiber with inline multimode fiber amplifier," in *European Conference on Optical Communications (ECOC)*. Optical Society of America, 2011, p. Th.13.C.2.

[64] V. Sleiffer, P. Leoni, Y. Jung, J. Surof, M. Kuschnerov, V. Veljanovski, D. Richardson, S. Alam, L. Grüner-Nielsen, Y. Sun *et al.*, "20× 960-Gb/s MDM-DP-32QAM transmission over 60 km FMF with inline MM-EDFA," in *European Conference on Optical Communication (ECOC)*, 2013, pp. 1–3.

[65] R. Ryf, S. Randel, N. K. Fontaine, M. Montoliu, E. Burrows, S. Chandrasekhar, A. H. Gnauck, C. Xie, R.-J. Essiambre, P. Winzer *et al.*, "32-bit/s/Hz spectral efficiency WDM transmission over 177-km few-mode fiber," in *Optical Fiber Conference (OFC)*. Optical Society of America, 2013, pp. PDP5A–1.

[66] R. Ryf, S. Randel, N. K. Fontaine, X. Palou, E. Burrows, S. Corteselli, S. Chandrasekhar, A. H. Gnauck, C. Xie, R. J. Essiambre, P. J. Winzer, R. Delbue, P. Pupalaikis, A. Sureka, Y. Sun, L. Grüner-Nielsen, R. V. Jensen, and R. Lingle, "708-km combined WDM/SDM transmission over few-mode fiber supporting 12 spatial and polarization modes," in *European Conference on Optical Communication (ECOC)*, 2013, pp. 1–3.

[67] Y. Chen, A. Lobato, Y. Jung, H. Chen, R. Jensen, Y. Sun, L. Gruner-Nielsen, D. Richardson, V. Sleiffer, M. Kuschnerov, N. Fontaine, R. Ryf, I. Giles, R. Chen, V. Carcia-Munoz, A. Koonen, B. Lankl, and N. Hanik, "41.6 Tb/s C-band SDM OFDM transmission through 12 spatial and polarization modes over 74.17 km few mode fiber," in *European Conference on Optical Communication (ECOC)*, Sept 2014, pp. 1–3.

[68] R. Ryf, H. Chen, N. Fontaine, A. Velazquez-Benitez, J. Antonio-Lopez, C. Jin, B. Huang, M. Bigot-Astruc, D. Molin, F. Achten *et al.*, "10-mode mode-multiplexed transmission over 125-km single-span multimode fiber," in *European Conference on Optical Communication (ECOC)*, 2015, pp. 1–3.

[69] N. Fontaine, R. Ryf, H. Chen, A. Benitez, B. Guan, R. Scott, B. Ercan, S. Yoo, L. Grüner-Nielsen, Y. Sun *et al.*, "30×30 MIMO transmission over 15 spatial modes," in *Optical Fiber Conference (OFC)*. Optical Society of America, 2015, p. Th5C.

[70] R. Ryf, R. Essiambre, A. Gnauck, S. Randel, M. Mestre, C. Schmidt, P. Winzer, R. Delbue, P. Pupalaikis, A. Sureka, T. Hayashi, T. Taru, and T. Sasaki, "Space-division multiplexed transmission over 4200-km 3-core microstructured fiber," in *Optical Fiber Conference (OFC)*, 2012, p. PDP5C.2.

[71] R. Ryf, N. K. Fontaine, B. Guan, R. J. Essiambre, S. Randel, A. H. Gnauck, S. Chandrasekhar, A. Adamiecki, G. Raybon, B. Ercan, R. P. Scott, S. J. B. Yoo, T. Hayashi, T. Nagashima, and T. Sasaki, "1705-km transmission over coupled-core fibre supporting 6 spatial modes," in *European Conference on Optical Communication (ECOC)*, 2014, pp. 1–3.

[72] J. Sakaguchi, Y. Awaji, N. Wada, A. Kanno, T. Kawanishi, T. Hayashi, T. Taru, T. Kobayashi, and M. Watanabe, "109-Tb/s (7×97×172-Gb/s SDM/WDM/PDM) QPSK transmission through 16.8-km homogeneous multi-core fiber," in *Optical Fiber Conference (OFC)*. Optical Society of America, 2011, p. PDPB6.

[73] K. Igarashi, T. Tsuritani, I. Morita, Y. Tsuchida, K. Maeda, M. Tadakuma, T. Saito, K. Watanabe, K. Imamura, R. Sugizaki *et al.*, "1.03-Exabit/skm Super-Nyquist-WDM transmission over 7,326-km seven-core fiber," in *European Conference on Optical Communication (ECOC)*, 2013, pp. 1–3.

[74] H. Takara, T. Mizuno, H. Kawakami, Y. Miyamoto, H. Masuda, K. Kitamura, H. Ono, S. Asakawa, Y. Amma, K. Hirakawa *et al.*, "120.7-Tb/s (7 SDM/180 WDM/95.8 Gb/s) MCF-ROPA un epeatered transmission of PDM-32QAM channels over 204 km," in *European Conference on Optical Communication (ECOC)*, 2014, pp. 1–3.

[75] K. Takeshima, T. Tsuritani, Y. Tsuchida, K. Maeda, T. Saito, K. Watanabe, T. Sasa, K. Imamura, R. Sugizaki, K. Igarashi *et al.*, "51.1-Tbit/s MCF transmission over 2520 km using cladding-pumped seven-core EDFAs," *IEEE/OSA Journal of Lightwave Technology*, vol. 34, no. 2, pp. 761–767, 2016.

[76] H. Takara, A. Sano, T. Kobayashi, H. Kubota, H. Kawakami, A. Matsuura, Y. Miyamoto, Y. Abe, H. Ono, K. Shikama, Y. Goto, K. Tsujikawa, Y. Sasaki, I. Ishida, K. Takenaga, S. Matsuo, K. Saitoh, M. Koshiba, and T. Morioka, "1.01-Pb/s (12 SDM/222 WDM/456 Gb/s) crosstalk-managed transmission with 91.4-b/s/Hz aggregate spectral efficiency," in *European Conference on Optical Communication*. Optical Society of America, 2012, p. Th.3.C.1.

[77] T. Kobayashi, H. Takara, A. Sano, T. Mizuno, H. Kawakami, Y. Miyamoto, K. Hiraga, Y. Abe, H. Ono, M. Wada, Y. Sasaki, I. Ishida, K. Takenaga, S. Matsuo, K. Saitoh, M. Yamada, H. Masuda, and T. Morioka, "2×344 Tb/s propagation-direction interleaved

transmission over 1500-km MCF enhanced by multicarrier full electric-field digital back-propagation," in *European Conference on Optical Communication (ECOC)*, Sept 2013, pp. 1–3.

[78] M. Arikawa, T. Ito, E. L. T. de Gabory, and K. Fukuchi, "Crosstalk reduction using bidirectional signal assignment over square lattice structure 16-core fiber for gradual upgrade of SSMF-based lines," in *European Conference on Optical Communication (ECOC)*, Sept 2015, pp. 1–3.

[79] B. J. Puttnam, R. S. Luis, W. Klaus, J. Sakaguchi, J. M. D. Mendinueta, Y. Awaji, N. Wada, Y. Tamura, T. Hayashi, M. Hirano, and J. Marciante, "2.15 Pb/s transmission using a 22 core homogeneous single-mode multi-core fiber and wideband optical comb," in *European Conference on Optical Communication (ECOC)*, Sept 2015, pp. 1–3.

[80] T. Mizuno, T. Kobayashi, H. Takara, A. Sano, H. Kawakami, T. Nakagawa, Y. Miyamoto, Y. Abe, T. Goh, M. Oguma, T. Sakamoto, Y. Sasaki, I. Ishida, K. Takenaga, S. Matsuo, K. Saitoh, and T. Morioka, "12-core × 3-mode dense space division multiplexed transmission over 40 km employing multi-carrier signals with parallel MIMO equalization," in *Optical Fiber Conference (OFC)*. Optical Society of America, 2014, p. Th5B.2.

[81] R. van Uden, R. Correa, E. Antonio-Lopez, F. Huijskens, G. Li, A. Schulzgen, H. de Waardt, A. Koonen, and C. Okonkwo, "1 km hole-assisted few-mode multi-core fiber 32QAM WDM transmission," in *European Conference on Optical Communication (ECOC)*, 2014, pp. 1–3.

[82] K. Shibahara, D. Lee, T. Kobayashi, T. Mizuno, H. Takara, A. Sano, H. Kawakami, Y. Miyamoto, H. Ono, M. Oguma, Y. Abe, T. Matsui, R. Fukumoto, Y. Amma, T. Hosokawa, S. Matsuo, K. Saitoh, M. Yamada, and T. Morioka, "Dense SDM 12-core × 3-mode transmission over 527 km with 33.2-ns mode-dispersion employing low-complexity parallel MIMO frequency-domain equalization," *IEEE/OSA Journal of Lightwave Technology*, vol. 34, no. 1, pp. 196–204, Jan 2016.

[83] D. Soma, K. Igarashi, Y. Wakayama, K. Takeshima, Y. Kawaguchi, N. Yoshikane, T. Tsuritani, I. Morita, and M. Suzuki, "2.05 Peta-bit/s super-nyquist-WDM SDM transmission using 9.8-km 6-mode 19-core fiber in full C band," in *European Conference on Optical Communication (ECOC)*, Sept 2015, pp. 1–3.

[84] K. Igarashi, T. Tsuritani, I. Morita, and M. Suzuki, "Ultra-long-haul high-capacity super-Nyquist-WDM transmission experiment using multi-core fibers," *IEEE/OSA Journal of Lightwave Technology*, vol. 33, no. 5, pp. 1027–1036, March 2015.

[85] Y. Kokubun and M. Koshiba, "Novel multi-core fibers for mode division multiplexing: proposal and design principle," *IEICE Electronics Express*, vol. 6, no. 8, pp. 522–528, 2009.

[86] R. Ryf, R. Essiambre, S. Randel, A. Gnauck, P. Winzer, T. Hayashi, T. Taru, and T. Sasaki, "MIMO-based crosstalk suppression in spatially multiplexed 3×56-Gb/s PDM-QPSK signals for strongly coupled three-core fiber," *IEEE Photonics Technology Letters*, vol. 23, no. 20, pp. 1469–1471, 2011.

[87] A. Li, A. Al Amin, X. Chen, and W. Shieh, "Reception of mode and polarization multiplexed 107-Gb/s CO-OFDM signal over a two-mode fiber," in *Optical Fiber Conference (OFC)*. Optical Society of America, 2011, p. PDPB8.

[88] M. Salsi, C. Koebele, D. Sperti, P. Tran, P. Brindel, H. Mardoyan, S. Bigo, A. Boutin, F. Verluise, P. Sillard, M. Bigot-Astruc, L. Provost, F. Cerou, and G. Charlet, "Transmission at 2×100Gb/s, over two modes of 40km-long prototype few-mode fiber, using LCOS based mode multiplexer and demultiplexer," in *Optical Fiber Conference (OFC)*. Optical Society of America, 2011, p. PDPB9.

[89] R. Ryf, S. Randel, A. Gnauck, C. Bolle, R. Essiambre, P. Winzer, D. Peckham, A. McCurdy, and R. Lingle, "Space-division multiplexing over 10 km of three-mode fiber using coherent 6×6 MIMO processing," in *Optical Fiber Conference (OFC)*, March 2011, p. PDPB10.

[90] J. van Weerdenburg, A. Velàzquez-Benitez, R. van Uden, P. Sillard, D. Molin, A. Amezcua-Correa, E. Antonio-Lopez, M. Kuschnerov, F. Huijskens, H. de Waardt *et al.*, "10 spatial mode transmission using low differential mode delay 6-LP fiber using all-fiber photonic lanterns," *Optics Express*, vol. 23, no. 19, pp. 24 759–24 769, 2015.

[91] H. Chen, R. Ryf, N. Fontaine, A. Velázquez-Benítez, J. Antonio-López, C. Jin, B. Huang, M. Bigot, D. Molin, F. Achten, P. Sillard, and R. Correa, "High spectral efficiency mode-multiplexed transmission over 87-km 10-mode fiber," in *Optical Fiber Conference (OFC)*. Optical Society of America, 2016, p. Th4C.2.

[92] S. Arık, K.-P. Ho, and J. Kahn, "Delay spread reduction in mode-division multiplexing: Mode coupling versus delay compensation," *IEEE/OSA Journal of Lightwave Technology*, vol. 33, no. 21, pp. 4504–4512, 2015.

[93] R. Maruyama, N. Kuwaki, S. Matsuo, and M. Ohashi, "Two mode optical fibers with low and flattened differential modal delay suitable for WDM-MIMO combined system," *Optics Express*, vol. 22, no. 12, pp. 14 311–14 321, Jun 2014.

[94] N. Bozinovic, Y. Yue, Y. Ren, M. Tur, P. Kristensen, H. Huang, A. E. Willner, and S. Ramachandran, "Terabit-scale orbital angular momentum mode division multiplexing in fibers," *Science*, vol. 340, no. 6140, pp. 1545–1548, 2013.

[95] R. G. H. van Uden, R. A. Correa, E. A. Lopez, F. M. Huijskens, C. Xia, G. Li, A. Schülzgen, H. de Waardt, A. M. J. Koonen, and C. M. Okonkwo, "Ultra-high-density spatial division multiplexing with a few-mode multicore fibre," *Nature Photonics*, vol. 8, pp. 865–870, Nov. 2014.

[96] K. Igarashi, D. Souma, Y. Wakayama, K. Takeshima, Y. Kawaguchi, T. Tsuritani, I. Morita, and M. Suzuki, "114 space-division-multiplexed transmission over 9.8-km weakly-coupled-6-mode uncoupled-19-core fibers," in *Optical Fiber Conference (OFC)*. Optical Society of America, 2015, pp. Th5C–4.

[97] D. Soma, Y. Wakayama, S. Beppu, S. Sumita, T. Tsuritani, T. Hayashi, T. Nagashima, M. Suzuki, H. Takahashi, K. Igarashi, I. Morita, and M. Suzuki, "10.16 Peta-bit/s dense SDM/WDM transmission over low-DMD 6-mode 19-core fibre across C+L band," in *European Conference on Optical Communication (ECOC)*, 2017, pp. 1–3.

Chapter 3

Acousto-optic switching for SDM

Reconfigurable optical devices that can provide the switching capability with full spatial and wavelength granularity are of paramount importance to enable the development and commercialization of SDM transmission systems with spatial selectivity. Notice that these devices are the fundamental building block of future ROADMs. In the single-mode case, several reconfigurable devices based on the A-O effect has been demonstrated, see for instance [1–4]. In FMFs and MCFs, the A-O effect can be employed to develop switching devices with spatial and wavelength selectivity. By exciting a suitable acoustic wave in the optical fiber, the energy transfer between two arbitrary modes can be induced in a controllable way. Nevertheless, understanding the mode coupling process under different kinds of acoustic waves in FMFs and MCFs will play a key role in the development of such kind of devices.

In this chapter, we start by introducing the MCT as a fundamental tool to investigate the energy transfer in FMFs and MCFs. Afterward, we analyse the A-O effect in optical fibers and the refractive index perturbation induced by longitudinal and flexural acoustic waves. The energy transfer between modes in a few-mode microwire, a kind of FMF, is investigated. At last, an experimental validation of the proposed A-O mode switching device is carried out. In MCFs, we analyse the energy transfer between distinguishable cores of a MCF induced by a flexural wave. Supported on such analysis, we propose an A-O core switching device based on HeMCFs.

3.1 Mode coupling theory

The MCT has been playing the main role in the analyses of signal propagation in fiber-optic transmission systems based on SDM. Using the geometrical parameters and the refractive index profile of the optical fiber, such theory enables to describe the energy transfer along the fiber link. In the MCT, the energy transfer is described by a set of coupled equations, in which the coupling between two arbitrary modes is determined by an overlap integral. However, the systems of coupled equations and the mode-coupling coefficients can be written in different ways. Usually, two distinct formalisms can be employed to describe the linear propagation in optical fibers, which are based on the ideal mode and the normal mode expansion. In the ideal mode expansion, it is assumed that the electromagnetic field guided in an imperfect optical fiber with random variations of the refractive index or/and the core diameter can be expanded in terms of modes of an ideal optical fiber with uniform diameter and constant radius. The ideal mode expansion is particularly suited for optical fibers

with perfect geometry but with refractive index inhomogeneities. On the other hand, in the normal mode expansion, the electromagnetic field is expressed as a sum of several normal modes of a hypothetical waveguide, which locally match with the actual waveguide. Notice that the normal modes expansion is preferable to describe the tapered regions because in this expansion the coupling coefficients are vanishing everywhere except in those regions where the actual fiber and the ideal fiber match [5].

In this subsection, we use the local normal modes expansion to describe the energy transfer in the multimodal regime. We assume that the electromagnetic field can be described by [6]

$$\mathbf{E}(\mathbf{r},t,\omega) = \sum_p \frac{\mathbf{F}_p(\mathbf{r},\omega)}{N_p(z,\omega)} \mathcal{A}_p(z,\omega) e^{-i[\beta_p(\omega)z-\omega t]}\,, \tag{3.1a}$$

$$\mathbf{H}(\mathbf{r},t,\omega) = \sum_p \frac{\mathbf{G}_p(\mathbf{r},\omega)}{N_p(z,\omega)} \mathcal{B}_p(z,\omega) e^{-i[\beta_p(\omega)z-\omega t]}\,, \tag{3.1b}$$

where $\mathbf{E}$ and $\mathbf{H}$ denote the electric and magnetic fields, respectively. The parameter $\mathcal{A}_p(z,\omega)$ and $\mathcal{B}_p(z,\omega)$ are the electric and magnetic complex amplitudes, and $\mathbf{F}_p(\mathbf{r},\omega)$ and $\mathbf{G}_p(\mathbf{r},\omega)$ are the transverse distributions of the electric and magnetic field for the p mode at ω frequency. The $\mathbf{r} = (r,\phi,z)$ are the spatial coordinates, t denotes the temporal coordinate and β_p represents the propagation constant. The $N_p(z,\omega)$ is a normalization coefficient defined in order to make $\mathcal{A}_p(z,\omega)\mathcal{A}_p^*(z,\omega)$ equal to the optical power in the p mode,

$$\int [\mathbf{F}_p^*(\mathbf{r},\omega) \times \mathbf{G}_m(\mathbf{r},\omega) + \mathbf{F}_p(\mathbf{r},\omega) \times \mathbf{G}_m^*(\mathbf{r},\omega)] \cdot \hat{z}\, d\mathbf{x} = 4\delta_{pm} N_p^2(z,\omega)\,, \tag{3.2}$$

where $\mathbf{x} = (r,\phi)$ are the spatial coordinates in the transverse plane, and δ_{pm} represents the Kronecker delta. Then, the optical field, (3.1), is replaced into the Maxwell equations (3.3),

$$\frac{\partial}{\partial t}\varepsilon \mathbf{E}(\mathbf{r},t) = \nabla \times \mathbf{H}(\mathbf{r},t)\,, \tag{3.3a}$$

$$-\mu_0 \frac{\partial}{\partial t}\mathbf{H}(\mathbf{r},t) = \nabla \times \mathbf{E}(\mathbf{r},t)\,, \tag{3.3b}$$

where ε and μ_0 are the electric permittivity and the vacuum permeability, respectively. After some algebraic manipulations, the propagation equation can be written as,

$$\sum_p \left(i\beta_p \mathcal{A}_p(z,\omega) + \frac{\partial}{\partial z}\mathcal{B}_p(z,\omega) \right) (\hat{z} \times \mathbf{G}_p(\mathbf{r},\omega) e^{-i\beta_p(\omega)z}) + \mathcal{B}_p(z,\omega) \left(\hat{z} \times \frac{\partial}{\partial z} \mathbf{G}_p(\mathbf{r},\omega) e^{-i\beta_p(\omega)z} \right) = 0\,, \tag{3.4a}$$

$$\sum_p \left(i\beta_p \mathcal{B}_p(z,\omega) + \frac{\partial}{\partial z}\mathcal{A}_p(z,\omega) \right) (\hat{z} \times \mathbf{F}_p(\mathbf{r},\omega) e^{-i\beta_p(\omega)z}) + \mathcal{A}_p(z,\omega) \left(\hat{z} \times \frac{\partial}{\partial z} \mathbf{F}_p(\mathbf{r},\omega) e^{-i\beta_p(\omega)z} \right) = 0\,, \tag{3.4b}$$

where the refractive index perturbation is considered in the fields $\mathbf{F}_p(\mathbf{r},\omega)$ and $\mathbf{G}_p(\mathbf{r},\omega)$. Thus, the fields $\mathcal{A}_p(z,\omega)$ and $\mathcal{B}_p(z,\omega)$ are rewritten as,

$$\mathcal{A}_p(z,\omega) = c_p^+ e^{-i\beta_p^+(\omega)z} + c_p^- e^{-i\beta_p^-(\omega)z}\,, \tag{3.5a}$$

and

$$\mathcal{B}_p(z,\omega) = c_p^+ e^{-i\beta_p^+(\omega)z} - c_p^- e^{-i\beta_p^-(\omega)z}\,, \tag{3.5b}$$

where the c_p^+ and c_p^- represent the complex amplitude of the forward and the backward wave in the p mode, respectively. Notice that the propagation constants and the transverse mode distributions must satisfy the following conditions,

$$\beta_p = \beta_p^+ = -\beta_p^-\,, \tag{3.6a}$$

$$\mathbf{F}_p = \mathbf{F}_p^+ = \mathbf{F}_p^-\,, \tag{3.6b}$$

and

$$\mathbf{G}_p = \mathbf{G}_p^+ = \mathbf{G}_p^-\,. \tag{3.6c}$$

In the following calculations, we also assume a small perturbation in the refractive index, which makes possible to neglect the longitudinal variation of N_p, $\mathbf{F}_p$ and $\mathbf{G}_p$. By replacing (3.5) in (3.4) and considering (3.6), the following set of coupled equations can be obtained [6]

$$\frac{dc_p^+(z)}{dz} = \sum_{l=0}^{n} c_l^+(z)\vartheta_{pl}^{++} e^{i[\beta_p(\omega)-\beta_l(\omega)]z} + c_l^-(z)\vartheta_{pl}^{+-} e^{i[\beta_p(\omega)+\beta_l(\omega)]z}\,, \tag{3.7a}$$

$$\frac{dc_p^-(z)}{dz} = \sum_{l=0}^{n} c_l^-(z)\vartheta_{pl}^{--} e^{i[\beta_p(\omega)-\beta_l(\omega)]z} + c_l^+(z)\vartheta_{pl}^{-+} e^{i[\beta_p(z)+\beta_l(z)]z}\,, \tag{3.7b}$$

where ϑ_{pl}^{ij} represents the coupling coefficient for the p and l modes,

$$\vartheta_{pl}^{ij} = \frac{\omega}{2\left[\beta_l^i(\omega) - \beta_p^j(\omega)\right]} \int \frac{\mathbf{F}_p^j(\mathbf{x},\omega)\cdot\mathbf{F}_l^{i^*}(\mathbf{x},\omega)}{N_p(\omega)N_l(\omega)} \frac{\partial\varepsilon}{\partial z} d\mathbf{x}\,. \tag{3.8}$$

Notice that the $c_p^+(z)$ and $c_p^-(z)$ are constant in the absence of coupling. However, when the modal coupling is considered, the $c_p^+(z)$ and $c_p^-(z)$ reflect the energy transference between modes. The ϑ_{pl}^{++} and ϑ_{pl}^{--} parameters represent the coupling coefficient between the l and p mode propagating in the same way (forward and backward directions, respectively). The ϑ_{pl}^{+-} and ϑ_{pl}^{-+} parameters represent the coupling coefficient between the backward l mode and the forward p mode and the forward l mode and the backward p mode, respectively.

3.2 Acousto-optic effect in optical fibers

The A-O effect, also known as A-O Bragg diffraction, results from the interaction between the optical signal and the acoustic wave by means of a refractive index perturbation inscribed in the optical fiber by the acoustic wave [4]. If the Bragg condition between two arbitrary modes is satisfied, the resonant coupling takes place [2]. It should be emphasized that in such process the momentum and energy conservation is required [4],

$$\beta_l(\omega_l) - \beta_p(\omega_p) \;=\; k\,, \tag{3.9a}$$

and

$$\omega_l - \omega_p \;=\; \Omega\,. \tag{3.9b}$$

The parameters k and Ω represent the propagation constant and the angular frequency of the acoustic wave, respectively. Nevertheless, the mode coupling coefficient depend on the symmetry of each mode and also on the symmetry of the refractive index perturbation [4]. The symmetry of the refractive index perturbation changes as function of the acoustic mode groups, *i.e.*, longitudinal, torsional, and flexural acoustic modes [7, 8].

In order to analyse the refractive index perturbation induced by each acoustic mode group, the propagation of the acoustic wave in the optical fiber is analysed. Following [8], the radial, $u_r(\mathbf{r},t)$, azimuthal, $u_\phi(\mathbf{r},t)$, and longitudinal, $u_z(\mathbf{r},t)$, displacement components induced in the fiber by the acoustic wave can be written as the real parts of

$$u_r(\mathbf{r},t) = U(r)\Phi_r(\phi)e^{-i(kz-\Omega t)}\,, \tag{3.10a}$$

$$u_\phi(\mathbf{r},t) = V(r)\Phi_\phi(\phi)e^{-i(kz-\Omega t)}\,, \tag{3.10b}$$

$$u_z(\mathbf{r},t) = W(r)\Phi_z(\phi)e^{-i(kz-\Omega t)}\,, \tag{3.10c}$$

respectively. The $\mathbf{\Phi}(\phi) = [\Phi_r, \Phi_\phi, \Phi_z]$ represent the circumferential displacement distribution, where Φ_r, Φ_ϕ and Φ_z are the radial, azimuthal and longitudinal components, respectively. The circumferential displacement distribution for longitudinal acoustic modes is defined by $\mathbf{\Phi}(\phi) = [1,0,1]$, see [8]. The circumferential distribution for flexural acoustic modes can assume two solutions: $[\sin(m\phi),\cos(m\phi),\sin(m\phi)]$ and $[\cos(m\phi),-\sin(m\phi),\cos(m\phi)]$, where the m parameter represents an integer describing the circumferential field variation [8]. Acoustic modes with $m=1$ are called flexural modes because the acoustic waves bend the microwire. Modes with $m=2$, and higher, have been called flexural modes of higher circumferential order. The U(r), V(r) and W(r) parameters describe the axial variation of displacement distribution, and can be written as

$$U(r) = Ak_dJ'_m(k_dr) + BkJ'_m(k_tr) + C\frac{m}{r}J_m(k_tr)\,, \tag{3.11a}$$

$$V(r) = A\frac{m}{r}J_m(k_dr) + B\frac{km}{k_tr}J_m(k_tr) + Ck_tJ'_m(k_tr)\,, \tag{3.11b}$$

$$W(r) = -i[AkJ_m(k_dr) + Bk_tJ_m(k_tr)]\,, \tag{3.11c}$$

where J_m represents a Bessel function of the first kind and order m, J'_m represent the derivative of the Bessel function with respect to its argument, and

$$k_d = \frac{\Omega^2}{c_d^2} - k\,, \tag{3.12a}$$

$$k_t = \frac{\Omega^2}{c_t^2} - k\,, \tag{3.12b}$$

where $c_d^2 = \mu_M/\rho_M$ and $c_t^2 = (\lambda_M + 2\mu_M)/\rho_M$ represents the square of the bulk dilatational wave velocity and the transverse wave velocity, respectively. The $\lambda_M = 1.6\times10^{10}$ Nm^{-2}, $\mu_M = 3.1\times10^{10}$ Nm^{-2}, and $\rho_M = 2.2\times10^{3}$ kg/m^3 are the Lame's constants and the material density for silica, respectively [8]. The magnitudes of the constants A, B, and C can be calculated considering the maximum longitudinal displacement, u_z^{max}, induced by the acoustic wave in the microwire.

The frequency of the acoustic wave, Ω, can be calculated solving the dispersion equations, (3.13) and (3.14), that are obtained requiring that the three radial components of the stress

tensor $\mathbf{S}_{rr}$, $\mathbf{S}_{r\phi}$ and $\mathbf{S}_{rz}$ are null at the microwire radius $r = a$. The propagation constant for the longitudinal acoustic waves is obtained solving,

$$\begin{vmatrix} -\frac{1}{2}(q_t^2 - q_0^2)J_0(q_d) + q_d J_2(qd) & -q(q_t J_0(q_t) - J_1(q_t)) \\ 2q_d q J_1(qd) & -(q_t^2 - q^2)J_1(q_t) \end{vmatrix} = 0\,, \tag{3.13}$$

with $q_t = k_t a$, $q_d = k_d a$ and $q = ka$. For flexural acoustic waves, the propagation constant is obtained solving,

$$\begin{vmatrix} m^2 - 1 - q^2(x-1) & m^2 - 1 - q^2(2x-1 & 2(m^2-1)(\gamma_m(q_t) - m)) - q^2(2x-1) \\ \gamma_m(q_d) - m - 1 & \gamma_m(q_t) - m - 1 & 2m^2 - 2(\gamma_m(q_t) - m) - q^2(2x-1) \\ \gamma_m(q_d) - m & -(x-1)(\gamma_m(q_t) - m) & m^2 \end{vmatrix} = 0\,, \tag{3.14}$$

with $\gamma_m(k) = kJ_{m-1}(k)/J_m(k)$ and $x = \Omega^2/(kc_t)^2$ [7].

The propagation of the acoustic waves induces a periodic refractive index perturbation along the fiber due to the strain distribution. The longitudinal strain distribution leads to a geometrical deformation of the fiber and a change in the refractive index induced by the elasto-optic effect. Both contributions are taken into account in the change of the dielectric permittivity in the fiber [4],

$$\varepsilon(\mathbf{r}, t) = \Re\{\varepsilon_u[1 + 2(1-\chi)S_{zz}(\mathbf{r}, t)]\}\,, \tag{3.15}$$

where ε_u is the unperturbed dielectric permittivity (*i.e.* without acoustic perturbation), χ is the elasto-optic coefficient (for silica $\chi = 0.22$) and $S_{zz}(\mathbf{r}, t)$ is the strain distribution along the fiber,

$$S_{zz}(\mathbf{r}, t) = \frac{\partial}{\partial z} u_z(\mathbf{r}, t)\,. \tag{3.16}$$

3.3 Acousto-optic mode switching

3.3.1 Tapered fibers and optical microwires

Optical microwires, or microfibers, are cylindrical optical waveguides with diameters in the order of few micrometers. When the diameter of such waveguides is smaller, in the order of tens of nanometers, they are also called optical fiber nanowires, photonic nanowires and optical nanofibers. In the last 15 years, this unconventional kind of optical waveguides have considerably attracted the attention of the scientific community because of their optical and mechanical properties [10–12]. It should be emphasized that such properties depend strongly on the microwire diameter. In general, optical microwires and nanowires are manufactured using top-down techniques, such as fiber pulling [12, 13]. If manufactured from optical fibers, the microwires are connected by two conical transition regions (the so-called tapered fibers or tapered regions) to the original optical fiber, see Fig. 3.1. Furthermore, when properly designed, both tapered regions allow to launch/collect the optical signal in/from the microwire with negligible optical losses.

The reduction of the radius of the optical fiber changes the physical properties of the waveguide and, hence, the fundamental physical parameters of the optical field, such as the propagation constant and transverse electric field distribution. In Fig. 3.2, we show the effective refractive index as function of the microwire diameter. We assume that the microwire

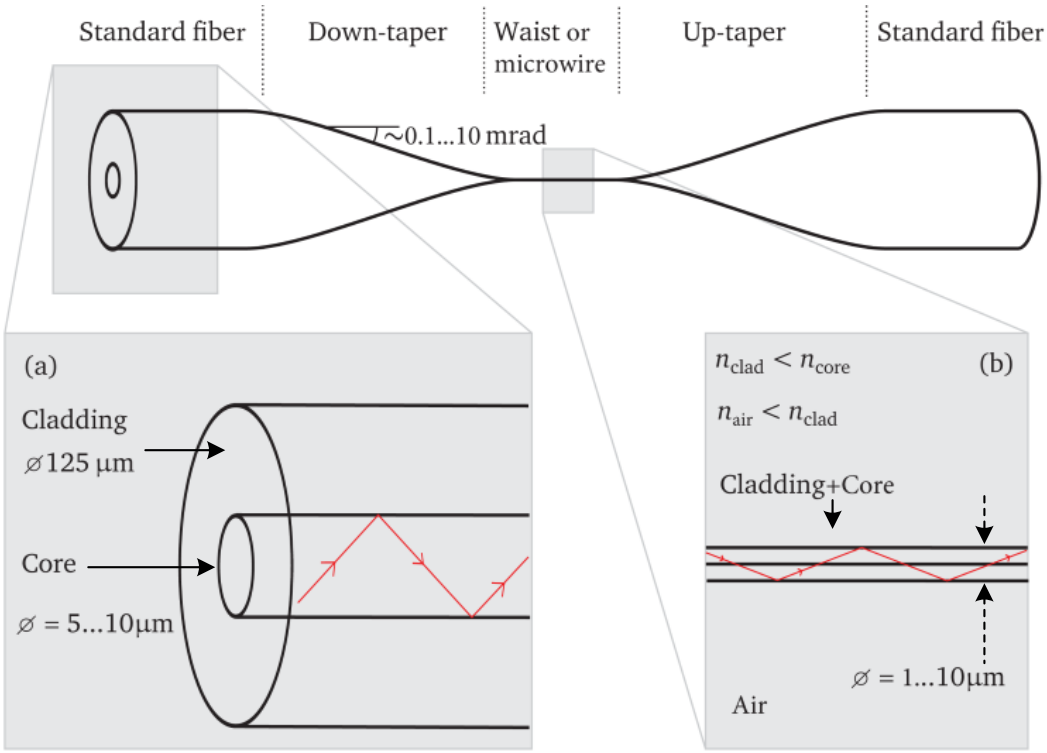

Figure 3.1: Schematic of a microwire manufactured by a top-down technique. (a) Schematic of a SSMF, the optical signal is guided in the core. (b) Schematic of the microfibre, the optical signal is guided in the cladding plus core [9].

is manufactured from a FMF able to guide the LP_{01}, LP_{11}, LP_{02}, LP_{12}, LP_{03} and LP_{13}, at the telecommunications wavelength ($\lambda = 1550$ nm). The optical parameters required to solve the analytical model presented in section 3.1, $\beta_l(\omega)$ and $\mathbf{F}_l(\mathbf{x},\omega)$, were obtained using the Comsol Multiphysics® software package. The numerical tool requires as input parameter the refractive index of the silica doped core and the silica cladding, n, that can be defined by a three term Sellmeier equation [14, 15],

$$n(\lambda)_i^2 - 1 = \sum_{j=1}^{3} \frac{[\mathrm{SA}_j + \mathrm{X}\,(\mathrm{GA}_j - \mathrm{SA}_j)]\,\lambda^2}{\lambda^2 - [\mathrm{SL}_j + \mathrm{X}\,(\mathrm{GL}_j - \mathrm{SL}_j)]^2} \tag{3.17}$$

where λ represents the signal wavelength and SA, Sl and GA, Gl are the Sellmeier coefficients for the SiO_2 and GeO_2 glasses, respectively [15]. The X parameter represents the mole fraction of GeO_2 [15]. Moreover, the FMF considered is characterized by a numerical aperture of NA = 0.22, a cladding and a core radius of 62.5 and 25 μm, respectively. In the numerical tool, we also consider an extra layer of air ten times larger than the silica cladding surrounding the fiber. As the fiber diameter decreases, the optical fields initially guided in the fiber core, are slowly spread by the fiber cladding. Hence, the effective refractive index for the guided modes tends to decrease. In a extreme case, the optical signal is no longer guided in the fiber core; it is guided in the cladding due to the index contrast between the silica and air, see for instance the modes LP_{02}, LP_{12}, LP_{03} and LP_{13} in Fig. 3.2. Further reducing the optical microwire diameter, the effective refractive index tends to decrease and all the core modes

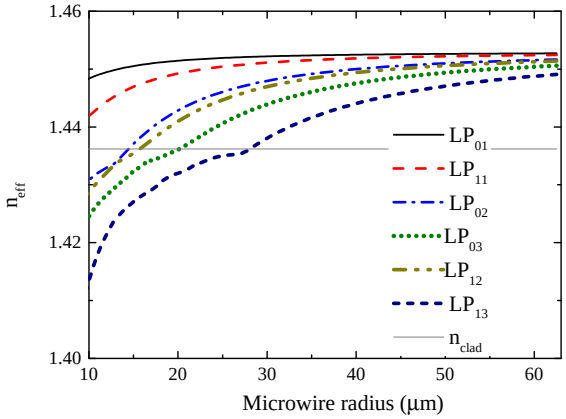

Figure 3.2: The effective refractive index as function of the microwire radius for the LP_{02}, LP_{12}, LP_{03} and LP_{13}. The n_{clad} denotes the refractive index of the fiber-optic cladding.

will be spread by the cladding.

In SSMF, the optical signal is guided in the core due to the weak index contrast between the core and cladding. Therefore, the optical signal is subject to the weak guiding regime. In contrast, in optical microwires the signal is usually guided in the cladding due to the strong index contrast between the silica microfiber and the air cladding. It should be noted that in the strong guiding regime the degeneracy of the LP modes is lifted.

According to the application target, the microwire diameter must be properly chosen. For instance, for sensor applications based on evanescent field and nonlinear signal processing applications, the microwire diameter should be in the order of the wavelength of the optical signal [10]. Optical microwires, with radius in the order of a few tens of micrometers, were also employed to develop A-O devices because they low radio frequency (RF) power consumption [4]. The tapered fiber has a concentrator effect on the acoustic waves, thereby increasing the index perturbation induced.

3.3.2 Operation principle

In Fig. 3.3, it is shown a schematic of the proposed A-O mode switch device, also called mode converter. In this device, a RF signal is applied to the piezoelectric transducer (PZT) disc leading to a vibration of the PZT, which in turn transmits this vibration to the silica horn. The horn is attached to the optical fiber where the optical microwire was produced[1]. The vibration frequencies of the PZT-horn-microwire system can be used to select the mode and frequency of the acoustic waves excited in the microwire. The perturbation induced by the acoustic wave produces a Bragg structure in the microwire, with a period defined by the acoustic mode and frequency. The Bragg structure leads to a resonant coupling between the optical modes. Therefore, the output optical mode can be selected by properly choosing the RF frequency. Moreover, the acoustic wave amplitude determines the refractive index difference induced by the acoustic wave and, consequently, the value of the coupling coefficient that defines the energy transference between optical modes. The mode conversion also depends of the refractive index symmetry induced by the acoustic wave in the microwire.

[1]It should be noted that A-O devices based on optical microwires require PZT with lower RF power consumption because the tapered region tends to concentrate the acoustic wave in the optical microwire.

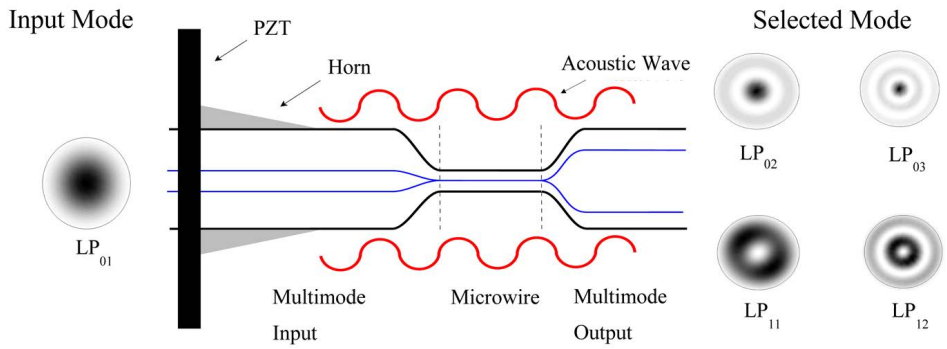

Figure 3.3: Schematic diagram of the proposed tunable inline mode converter. The appropriate selection of the frequency and amplitude of the acoustic wave can be used to control the coupling coefficients and, consequently, to adjust the output power in the output optical modes.

Longitudinal acoustic waves are axially symmetric and have no circumferential movement. On the other hand, flexural acoustic waves have all displacement components non-null and may be axially symmetric or antisymmetric (depending on the parity of the parameter m, which was defined in section 3.2) [7, 8].

In the proposed device, the few-mode microwire supports the same number of modes than the original FMF. Both tapered regions are properly designed in order to avoid the mode-coupling, therefore preserving the spatial selectivity. It should be emphasised that the insertion losses of the proposed mode switching device are mainly determined by the mode coupling in the tapered regions and by the waveguide losses in the microwire. Despite the tapered regions may induce mode coupling, the adiabatic theorem can be used to calculate the maximum angle of the tapered regions which allows to minimize the mode-coupling [10, 16]. The waveguide losses depends on the length of the microwire and varies as function of the radius of the microwire for each considered mode. In this way, a suitable choice of the microwire radius should be performed in order to minimize the waveguide losses.

3.3.3 Results

Phase-matching

The mode conversion between an input mode l and an output mode p can be obtained through a periodic perturbation induced by an acoustic wave. The acoustic propagation constant is defined by (3.9a). When the phase-matching condition between the p and l modes is achieved,

$$\beta_l(\omega_l) - \beta_p(\omega_p) \;=\; k\,, \tag{3.18}$$

the exponent in (3.7) becomes null and the mode conversion (induced by the resonant coupling) occurs efficiently. Thus, the acoustic propagation constant, k, is used in (3.13) as input parameter to calculate the acoustic frequency of longitudinal waves required to induce the mode conversion between symmetric, or antisymmetric optical modes. In a similar way, the acoustic frequency of flexural waves can be calculated from k by solving (3.14) for mode conversion between antisymmetric and symmetric, or symmetric and antisymmetric optical modes. The mode conversion also leads to a frequency shift in the optical signal, as defined in (3.9b). Thus, the acoustic frequency can be recalculated replacing the propagation constant of the output mode shift by Ω, in (3.9a), and estimating again the propagation constant

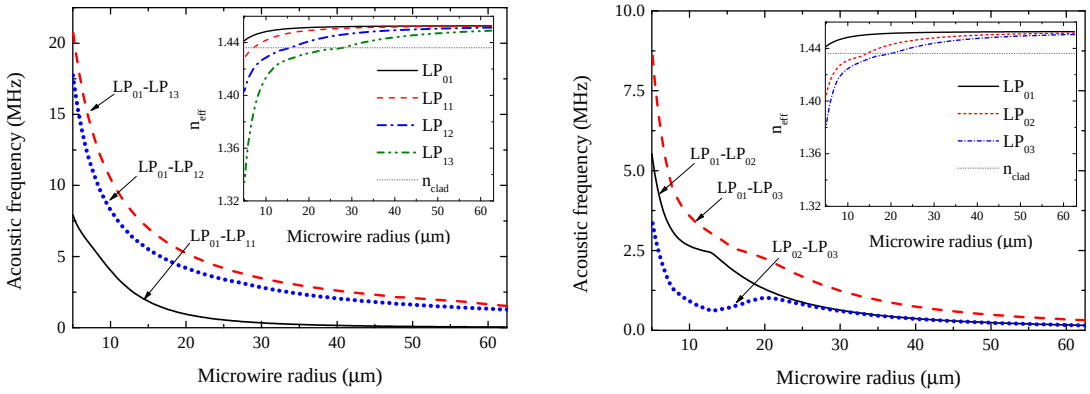

Figure 3.4: a) The acoustic frequency of a flexural acoustic wave required to promote the mode conversion between the fundamental mode and the first three antisymmetric modes (i.e., LP_{11}, LP_{12} and LP_{13}) as function of the microwire radius. In the inset is displayed the effective refractive index for the antisymmetric modes considered as function of the microwire radius, where the n_{clad} represent the refractive index of the cladding. b) Acoustic frequency of a longitudinal acoustic wave required to promote the mode coupling between the fundamental mode and the first two symmetric modes (i.e., LP_{02} and LP_{03}) and, between the LP_{02} and LP_{03}. In the inset is displayed the effective refractive index for the symmetric modes considered as function of the microwire radius.

for the output mode. The process is repeated iteratively in order to calculate the acoustic frequency. However, the frequency shift induced by the acoustic wave in the optical signal is extremely small (around $1{\times}10^{-5}$ nm) which leads to a fast convergence in the Ω calculations.

In Fig. 3.4(a) and 3.4(b) are shown the acoustic frequencies, Ω, required to induce the resonant coupling between different pairs of modes. Figure 3.4(a) displays the Ω of a flexural wave required to induce the mode conversion between the fundamental mode and the three first antisymmetric modes (LP_{11}, LP_{12} and LP_{13}). Both flexural and longitudinal waves show the same asymptotic behavior as function of the microwire radius. Figure 3.4(b) displays the Ω of a longitudinal wave able to promote the mode conversion from the fundamental mode to the LP_{02}, LP_{03} and from the LP_{02} to the LP_{03}. For radius larger than 25 μm the acoustic frequency required to promote the mode coupling between LP_{01}-LP_{02} and between LP_{02}-LP_{03} has similar values. However, for radius smaller than 25 μm, the LP_{03} becomes guided in the cladding and the acoustic frequency required to induce the mode conversion between the LP_{01}-LP_{02} is clearly distinct from the acoustic frequency required to promote the mode conversion between the LP_{02}-LP_{03}, which makes possible to select the desired output mode. Results also show that the acoustic frequency tends to decrease with the increment of the microwire radius.

The radius of the microwire can be used as an additional degree of freedom to adjust the range of acoustic frequencies required to induce the mode conversion. The separation between the aforementioned acoustic frequencies increases with the decreasing of the microwire radius. However, for small radius, the acoustic frequency may become excessively high to be achieved from an experimental point of view. Notice that the available PZTs are limited to frequencies lower than several tens of MHz. In this way, the microwire radius should be properly chosen in order to allow the excitation of the acoustic wave that leads to the resonant coupling between

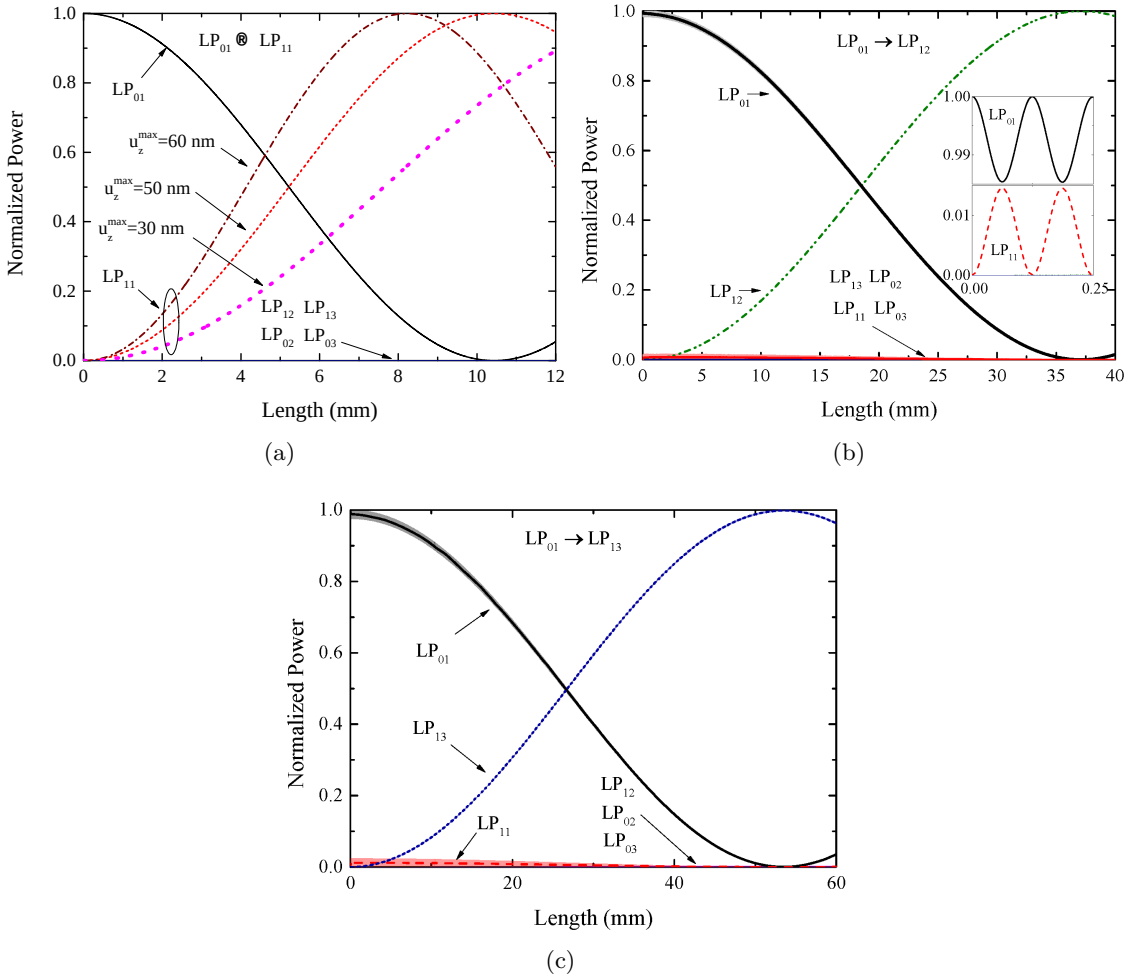

Figure 3.5: The power transfer as function of the length of an optical microwire with a radius of 23.7 μm considering a flexural wave. a) For $\Omega = 622$ kHz with three different maximum longitudinal displacements $u_z^{max} = 30$, 50 and 60 nm. The mode conversion between LP_{01}-LP_{11} is clearly achieved. b) For $\Omega = 3.33$ MHz and $u_z^{max} = 50$ nm is achieved the mode conversion between LP_{01}-LP_{12}. c) For $\Omega = 4.47$ MHz an $u_z^{max} = 50$ nm is obtained the mode conversion between LP_{01}-LP_{13}.

the desired modes.

Mode conversion

The propagation of the optical signal in silica microwire under the A-O effect is analysed for the previous referred modes. The energy transfer is described by (3.7) where the coupling coefficient is calculated replacing (3.10c) and (3.16) in (3.8),

$$\vartheta_{pl}^{ij} = \frac{\varepsilon_0 \omega n^2 k^2 (1-\chi)}{\beta_l^i(\omega) - \beta_p^j(\omega)} \int \frac{\mathbf{F}_p^j(\mathbf{x},\omega) \cdot \mathbf{F}_l^{i^*}(\mathbf{x},\omega)}{N_p(\omega) N_l(\omega)} W(r) \Phi_z(\phi) d\mathbf{x}\,, \tag{3.19}$$

where n and ε_0 are the refractive index and the vacuum permittivity, respectively. As previously explained, the superscript i and j denote the direction of the optical beam. The

coupling coefficient, (3.19), is defined by the symmetry of l and p optical modes, $\mathbf{F}_l(\mathbf{x},\omega)$ and $\mathbf{F}_p(\mathbf{x},\omega)$, and the symmetry of the acoustic wave, $\Phi_z(\phi)$. In this sense, an antisymmetric spatial displacement induced by a flexural wave can only be used for mode conversion between symmetric and antisymmetric or antisymmetric and symmetric optical modes. On the other hand, longitudinal waves show a symmetric spatial displacement allowing the mode conversion between optical modes with the same symmetry.

Henceforward, we consider a microwire with a radius of 23.7 μm. The input signal was assumed in the fundamental mode, whereas the other considered modes at the input were assumed to have no optical power. The coupling between the forward (transmitted) and backward (reflected) signal is analysed by solving (3.7). Despite the refractive index perturbation created by the A-O effect, no considerable reflections in any mode were observed. Therefore, (3.7) can be simplified considering only the forward equation, (3.7a), and neglecting also the reflections to the forward signal. It should be noted that A-O devices were already demonstrated with almost perfect phase matching, see for instance [3, 17] and [4]. Under this condition, the energy transfer between pairs of modes follows the response of the ideal A-O mode converter. Nevertheless, in a real device some penalty in the extinction ratio is expected to be observed due to index variations and diameter fluctuations. The following results were obtained considering the simplifications described above.

In Fig. 3.5 is shown the energy transfer between the six aforementioned LP modes considering a flexural wave. Figure 3.5(a) displays the modal evolution considering a flexural wave with a frequency of 622 kHz. The flexural wave allows to achieve the phase-matching between the LP_{01} and LP_{11} leading to the mode conversion between these modes. We do not observe any considerable energy transfer for the other modes considered (LP_{12}, LP_{13}, LP_{02} and LP_{03}). Moreover, the maximum longitudinal displacement that can be defined as function of the acoustic amplitude, was taken as $u_z^{max} = 30$, 50 and 60 nm in order to analyse the impact of u_z^{max} in the mode conversion. From (3.15), it is clear that the longitudinal displacement determines the value of the modal coupling, and consequently, the mode conversion efficiency, see Fig. 3.5(a). In this way, the longitudinal displacement, and consequently the achieved mode conversion, can be adjusted through the amplitude of the RF signal applied on the PZT. The following results were obtained considering the maximum longitudinal displacement of the acoustic wave as constant, $u_z^{max} = 50$ nm. In Fig. 3.5(b) is shown the energy transfer as function of the microwire length considering an acoustic wave with a frequency of 3.33 MHz. Despite the conversion between the LP_{01} and LP_{12} can be clearly achieved, the LP_{12} shows a small oscillatory behavior as result of the energy variation in the fundamental mode induced by the mode coupling between the fundamental mode and the LP_{11}, see insets in Fig. 3.5(b). The faint line shows the fast oscillatory energy exchange between the LP_{01} and LP_{13}, and the average value is represented as a line inside this region. The antisymmetric perturbation leads to the mode coupling between the fundamental mode and the two lowest antisymmetric modes. Nevertheless, the resonant coupling that leads to the mode conversion is only achieved between the fundamental mode and the LP_{12}. Figure 3.5(c) shows the energy transfer from the LP_{01} to LP_{13}, which is induced by a flexural wave with a frequency of 4.47 MHz. Analogously to the results above displayed in Fig. 3.5(b), the fundamental mode is also converted to the LP_{13} due to the antisymmetric perturbation inscribed by the acoustic wave. However, a small fraction of the fundamental mode is also coupled to the LP_{11}, which induces an oscillatory behavior in the LP_{01} and LP_{13}. Nevertheless, the energy transfer is dominated by the resonant coupling between the fundamental mode and the LP_{13}.

The mode conversion between symmetric modes (LP_{01},LP_{02} and LP_{03}) or between anti-

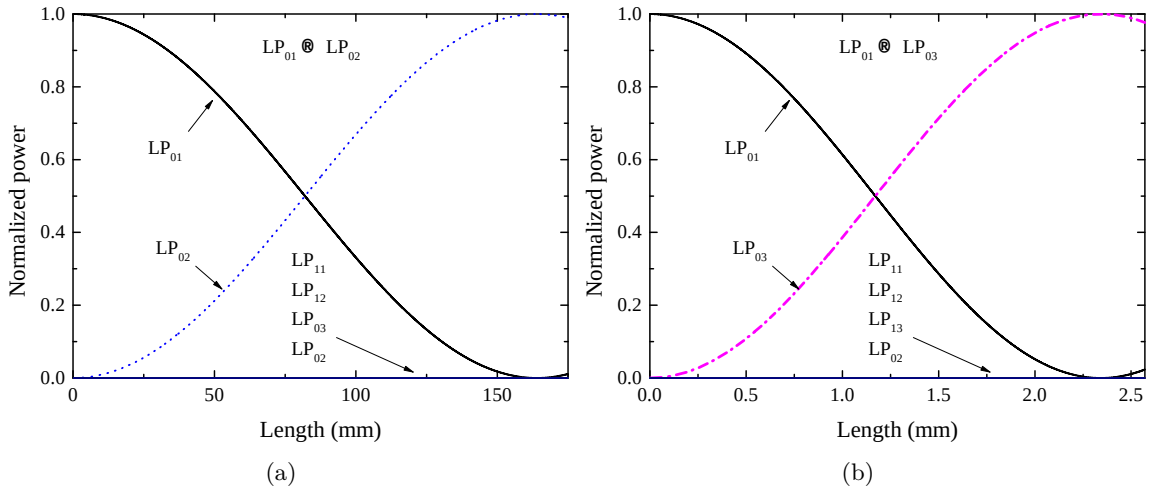

Figure 3.6: The power transfer as function of the length of an optical microwire with a diameter of 23.7 μm considering a longitudinal wave. a) For $\Omega = 897$ kHz and $u_z^{max} = 50$ nm is achieved the mode conversion between the LP_{01}-LP_{02}. b) For $\Omega = 1.97$ MHz and $u_z^{max} = 50$ nm is achieved the mode conversion between the LP_{01}-LP_{03}.

symmetric modes (LP_{11},LP_{12} and LP_{13}) can be achieved through the symmetric refractive index perturbations induced by longitudinal acoustic waves. In Fig. 3.6 is displayed the mode conversion between the fundamental mode and the LP_{02} induced by a longitudinal acoustic wave with a frequency of 897 kHz. Figure 3.6(b) displays power transfer as function of the length of an optical microwire considering a longitudinal wave with a frequency of 1.97 MHz. The energy transfer between the fundamental mode and the LP_{03} is achieved (clearly mode conversion) and we did not observe any considerable energy transfer for the other modes considered.

So far, the mode conversion between the fundamental mode and symmetric and antisymmetric high order modes was demonstrated. It should be also noted that the reverse process between high order and the fundamental mode can also be easily achieved and demonstrated. Moreover, the mode conversion between an arbitrary pair of optical modes can be achieved by properly choosing the acoustic wave. In this way, the device proposed allows the mode conversion between any pairs of modes by adjusting only the RF signal applied to the PZT.

Bandwidth

In order to characterize the bandwidth of the transmission window of the proposed mode switching, the fundamental mode is launched at the input of such device and the output signal is analysed for the several modes considered. This analysis is repeated varying the wavelength of the input signal between 1530 nm and 1570 nm. In Fig. 3.7 is shown the normalized transmission spectrum for the mode switch between the modes LP_{01}-LP_{12}, in which a flexural acoustic wave with a frequency of 3.33 MHz is considered. Results show that the efficient mode conversion between the fundamental mode and the LP_{12} occurs in a transmission window centered at 1550 nm. Furthermore, none appreciable energy transference for the others modes considered in the analysis is observed. The FWHM, or the transmission bandwidth, was calculated performing a Gaussian fit to the output power achieved at the

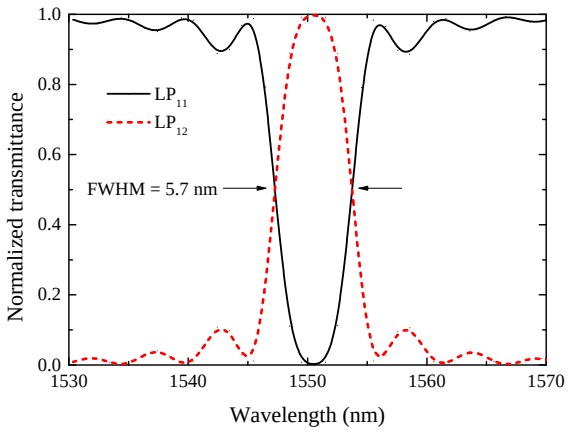

Figure 3.7: Transmittance spectrum of the proposed A-O mode converter considering a flexural acoustic wave with a frequency of 3.33 MHz and a $u_z^{max} = 50$ nm.

desired mode. For this particular case, the FWHM of the transmission window is ≈ 5.7 nm, see Fig. 3.7. This calculation was extended for the other scenarios previously analyzed. For the mode switch between the LP_{01}-LP_{02} and LP_{01}-LP_{03}, the transmission bandwidth found is ≈ 1.1 nm and 2.1 nm, respectively. For the remaining three cases, the bandwidth for the proposed device is ≈ 104.13 nm, 5.7 nm and 1.1 nm for the switching between the LP_{01}-LP_{11}, LP_{01}-LP_{12} and LP_{01}-LP_{13}, respectively. The range of found FWHMs can be explained by the different behaviors of the propagation constants and therefore it can be customized by properly choosing the microwire radius. The values of FWHM analyzed are larger than 0.8 nm for all considered switching process, making this device suitable to be used in add and drop spatial modes in dense WDM transmission systems.

3.4 Experimental validation of the mode switching

3.4.1 Microwire fabrication

The manufacturing of the optical microwires is carried out by using an experimental setup based on the so-called "flame brushing technique". In this setup, an optical fiber is heated locally above its softening point by an acetylene flame. Simultaneously, the optical fiber is displaced in an oscillatory movement and uniformly pulled apart with high precision stepper motors, moving according to a predefined velocity sequence [18], see Fig. 3.8(a). The hot region, which accounts for the final length of the microwire, is defined by the oscillatory movement (v' in Fig. 3.8(a)), whereas the stretching process determines the shape of both tapered regions. Notice that the stretching process results from the distinct velocities assumed for each stepper motor and the manufactured microwire results from several cycles, in which the local diameter of the fiber is reduced in a controllable way, see Fig. 3.8(b). The target profile of the optical microwire (i.e., taper profile, the length and diameter of the microwire) are previously established and designed in a Matlab environment. Using a mass-conservation algorithm [19] and taking as inputs the desired target profile and the width of the flame, a numerical application is employed to calculate the hot region, the flame brushing velocity, and the stretching velocity. We assume that the heat section has a constant temperature with a length of two millimeters. Notice that the flame width and the flame profile are critical factors

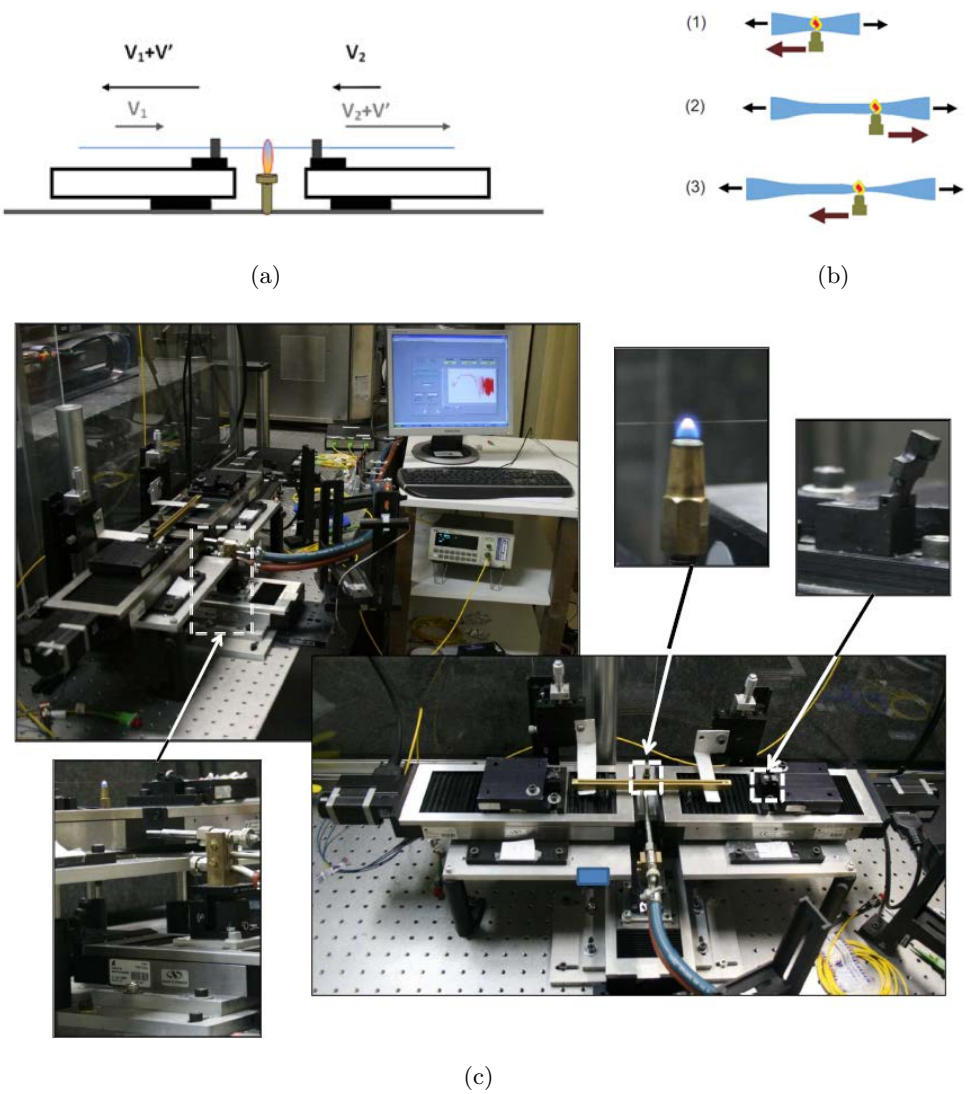

Figure 3.8: a) Schematic representation of the experimental setup for optical microwire production. The fiber is stretched by two linear stage engines with different velocities in order to distribute the temperature along the hot zone and to precisely control the profile of the tapered region and the length and radius of the microwire. b) Schematic representation of the microwire building process. The profile of tapered region and the length and diameter of the microwire is controlled through the relative movement between the fiber and the flame. c) Experimental setup employed for the optical microwire production.

to achieve the desired target profile. If the flame is not steady throughout the process, the resultant microwire and the tapered regions will differ from the target profile. In Fig. 3.8(c), it is shown the experimental setup employed for the microwire fabrication.

The tapered angle must be carefully chosen to avoid the mode coupling between the LP_{01} and the LP_{11}. The maximum angle for the tapered region can be estimated by using a length

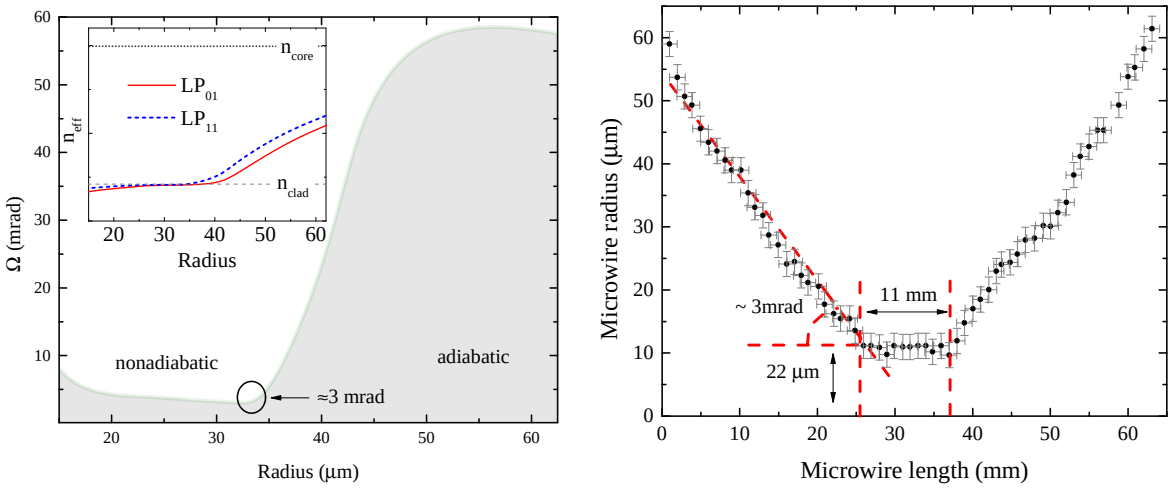

(a) (b)

Figure 3.9: (a) Adiabatic angle for LP_{01} and LP_{11} modes as a function of the microwire radius. (b) Profile measured for the taper region plus the optical microwire.

scale criterium or the adiabatic criterion [20],

$$\Omega_{Ad} = \frac{r_c(\beta_1 - \beta_2))}{2\pi}, \tag{3.20}$$

where β_i, with $i = 1$ and 2, is the propagation constant for the LP_{01} and the LP_{11} mode, r_c is the microwire radius and Ω_{Ad} is the adiabatic angle. If the tapered angle is lower than Ω_{Ad}, the mode coupling along the optical microwire is negligible. In Fig. 3.9(a), we show Ω_{Ad} as a function of the microwire radius[2]. To avoid mode coupling between LP_{01} and the LP_{11} modes, the tapered angle must be smaller than ≈ 3 mrad.

With the desired tapered profile defined, the initial positions and the velocities for both the linear stages can be calculated using the aforementioned mass conservation algorithm. Then, the data are loaded to the motion controller and the tapering process is started. In this experimental work, the optical fiber employed to produce the optical microwire is a SSMF (SMF-28), which is a multimode optical fiber at 630 nm. Both tapered regions have a tapering angle of 3.2 mrad, being the length and diameter of the microwire equal to 11 mm and 22 μm, respectively, see Fig. 3.9(b).

3.4.2 A-O setup for mode switching

Regarding the experiential validation of the A-O mode switch, a silica horn with a PZT disc fixed to its base was attached to a bare but unnarrowed portion of the fiber near the tapered region. Both ends of the microwire plus tapered regions are glued. Afterward, the microwire is carefully stretched until it is under tension. Then, the RF signal is applied to the PZT disc and turned on. Notice that the optical signal is injected/colletected in/from the optical microwire via the tapered fiber.

[2]The optical signal is assumed at 630 nm, which is properly explained in the following subsection.

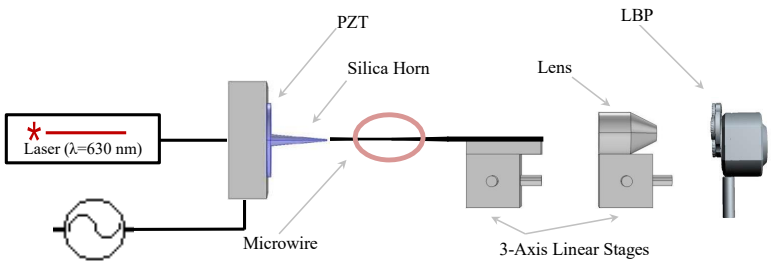

Figure 3.10: Schematic representation of the experimental setup, the tapered fiber is fixed to the silica horn. The fiber end is cleaved and aligned with a objective lens (×40) using 3-axis platform. The fiber end and the objective lens are afterwards aligned with a laser beam profiler (LBP). The RF signal is applied to the PZT and the spatial mode distribution is projected onto the laser beam profiler.

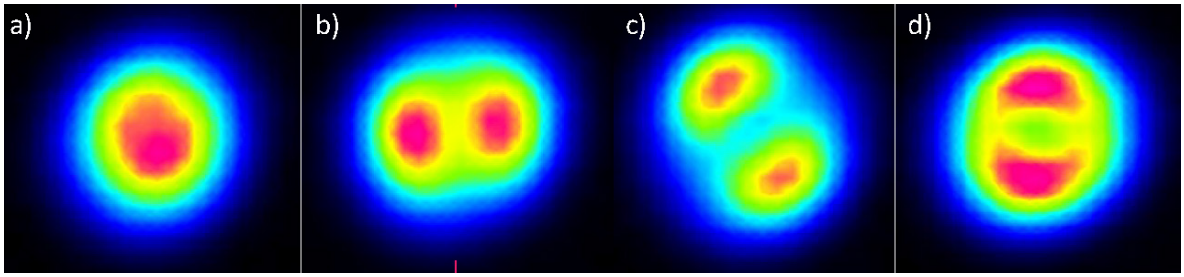

Figure 3.11: Experimental spatial mode distribution measured: a) fundamental mode, b) TE_{01}, c) HE_{21} and d) TM_{01}.

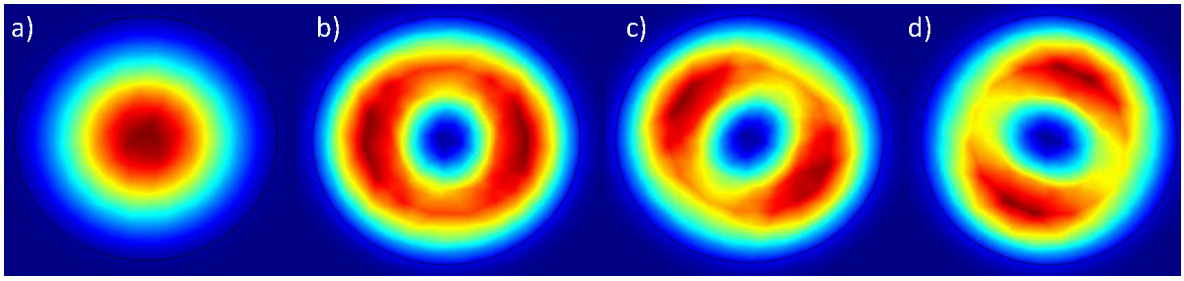

Figure 3.12: Numerical spatial mode distribution at the end of the multimode fiber for the wavelength of 630 nm: a) fundamental mode, b) TE_{01}, c) HE_{21} and d) TM_{01}.

3.4.3 Results

Far-field measurement

A laser beam with a central wavelength around the 630 nm is launched in the fundamental mode of the FMF employed to build the aforementioned device. The far-field, or spatial mode distribution, at the output of the cleaved fiber is launched in a objective lens (×40) and it is projected in a laser beam profiler, which allows to measure the far-field. The fiber end, the objective lens and the laser beam profiler are precisely aligned by means of two 3-axis platforms, see Fig. 3.10.

In Fig. 3.11(a), it is shown the far-field with the RF signal turned off, whereas, in

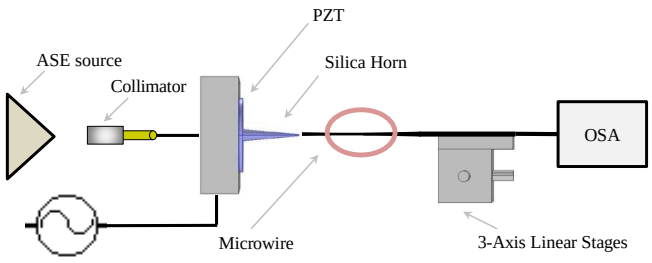

Figure 3.13: Schematic representation of the experimental setup. An optical broadband source is launched in the optical microwire. The RF signal is turned on and the transmission spectrum is analysed by an optical spectrum analyzer.

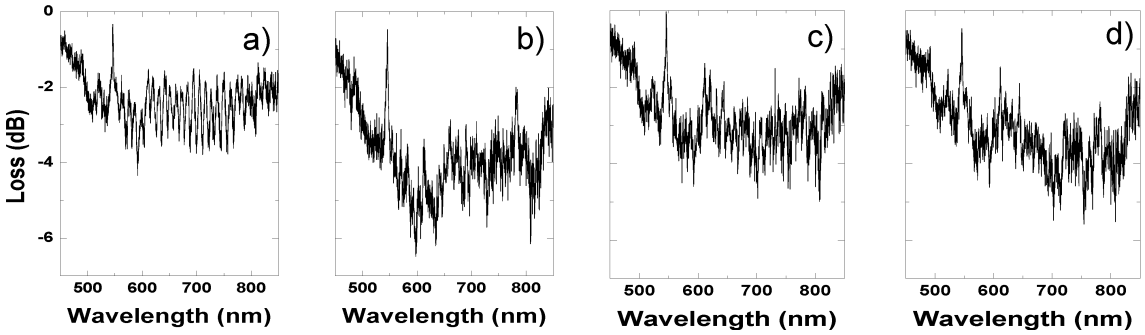

Figure 3.14: a) Spectrum with the RF signal turned off. b), c) and d) Spectra with the RF signal turned on assuming the following frequencies 387.8, and 462.1, and 465.7 kHz, respectively.

Fig. 3.11(b), 3.11(c) and 3.11(d), it is shown the far-field when applied a RF signal with 387.8, 462.1, and 465.7 kHz, respectively. In Fig. 3.11(b), 3.11(c) and 3.11(d) are shown the far-fields for the three degenerated LP_{11} modes, TE_{01}, HE_{21} and TM_{01}, respectively. Notice that the mode conversion is observed "*in situ*". For the three aforementioned modes, the far-fields are numerically calculated, see Fig. 3.12, and compared with the experimental ones. The numerical calculations are carried out by a finite element method in the Comsol Multiphysics® software package. The numerical and the experimental results are in good agreement, see Fig. 3.11 and 3.12.

In the absence of a RF signal, both adiabatic tapered regions plus the microwire induce a negligible mode coupling. When a light beam is launched in the fundamental mode, it remains in such mode. In other words, the proposed device preserves the spatial selectivity.

Insertion losses

In order to measure the insertion losses as a function of the wavelength, we replace the laser source by a broadband optical source. The optical signal is collected by an optical collimator and launched in the few-mode fiber. The output spectrum is measured by an optical spectrum analyzer, see Fig. 3.13. In contrast to the previous case, the following results are obtained considering a multimodal input signal. In that way, the losses measured results from all the coupling processes between the core and the cladding modes induced along the optical structure. The transmission spectrum of the tapered fiber plus the microwire shows

the characteristic beating due to the residual mode coupling, as displayed in Fig. 3.14(a). In Fig. 3.14(b), (c) and (d), we show the transmission spectrum with the RF signal turned on with frequencies of 387.8, 462.1, and 465.7 kHz, respectively. For the first case, assuming an RF signal with 387.8 kHz, the losses induced by the A-O effect was 2.42 dB at 630 nm. While, for the second and third case, with the RF signal at 462.1 and 465.7 kHz, the measured losses were 0.67 and 0.93 dB, respectively.

When considering an input signal only in the fundamental mode, the optical losses measured are lower than 0.5 dB for all the cases considered. Such results along with the ones presented in the previous subsection, show that mode conversion occurs efficiently.

3.5 Acousto-optic core switching

The resonant coupling induced by an acoustic wave can be also employed to induce the mode coupling between two arbitrary modes in MCFs. As previously mentioned, flexural acoustic waves are characterized by a bending motion. One side of the fiber is stretched and the opposite side compressed, such motion happens along the vibration plane of the flexural wave [8]. In MCFs, the magnitude and the symmetry of the refractive index perturbation induced in a particular core depends on the spatial orientation of the vibration plane. Therefore, the mode coupling between a given core mode and a cladding mode can be tuned by adjusting the vibration plane and the frequency of the acoustic wave. Such property can be employed for signal processing in MCF in several ways, as explained in the following subsections.

3.5.1 Operation principle

In order to adjust the vibration plane of the flexural wave, the experimental setup previously proposed for the generation of acoustic waves in optical fibers must be improved. By using two stacked PZTs with orthogonal vibration directions and applying in both PZTs equal in-phase RF signals, an arbitrary flexural acoustic wave can be generated [21], see right inset in Fig. 3.15(a). When both RF signals are properly synchronized, i.e., in-phase, the vibration plane of the acoustic wave can be adjusted by changing the amplitude ratio between both applied signals, see Fig. 3.15(b). In addition, the peak-to-peak voltage ($V_{p\text{-}p}$) of both RF signals allows to control the acoustic wave amplitude, see Fig. 3.15(b). Then, the acoustic wave is transmitted to the fiber through a horn [17]. Notice that, in this case, we are assuming a setup similar to the one used in [21] to generate acoustic vortex in optical fiber with a controllable amount of OAM.

In homogeneous MCF (HoMCF), the index perturbation induced by the flexural wave in the cores depends on the geometry of the HoMCF and in the spatial orientation of the flexural wave, i.e., the vibration plane. By adjusting the spatial orientation of this plane, the refractive index perturbation induced in a given core and, consequently the coupling coefficient between such core and the cladding mode can be adjusted. If the flexural wave enables the phase-matching condition, the sonic grating leads to the power transfer from the initial core mode to a cladding mode. Then, the coupling coefficients between the cladding mode and the remaining cores define the subsequent energy transfer from the cladding mode to the other cores of the MCF.

In HeMCF the resonant coupling induced by a single flexural wave occurs only between a given core and a cladding mode because each core has a different propagation constant. This flexural wave induces the energy transfer between a given core and a particular cladding

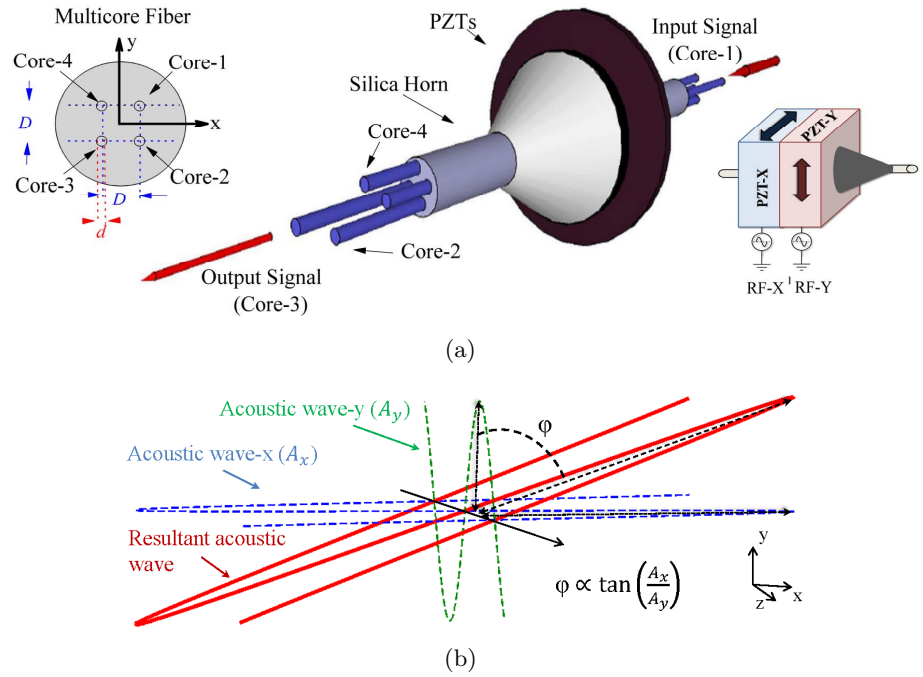

Figure 3.15: a) Schematic of the proposed tunable in-line core switch based on A-O effect. In the right-hand side, it is shown the configuration with two PZTs used to tune the spatial orientation of the flexural wave. In the left-hand side, it is shown the profile of the four cores MCF considered. b) The frequency and amplitudes of the RF signals applied to the PZTs can be tuned to adjust the spatial orientation, φ, of the resultant flexural wave.

mode. A second flexural wave, with the proper acoustic frequency, must be then applied to the HeMCF in order to induce the resonant coupling between the previous excited cladding mode and the desired output core. Both acoustic waves are propagated jointly in the optical fiber inducing two distinct Bragg structures and enabling the signal switching between any two cores by means of an "intermediary" cladding mode. It should be noted that the core switching in HeMCF using the double resonant coupling is independent of the fiber geometry.

3.5.2 Flexural acoustic waves in MCFs

In order to generalize the A-O theory for MCFs, we need to take into account the geometry of the fiber and the spatial orientation of the flexural wave. The spatial distribution of the cores in the MCF is considered in the dielectric permittivity, or in the index profile, of the MCFs, which depends on the axial and radial coordinates. The dielectric permittivity for the core/cladding is calculated considering $\varepsilon_i = n_i^2 \varepsilon_0$, where ε_0, n_i and ε_i are the vacuum permittivity, the refractive index and the dielectric permittivity for the region i, with i denoting the core and the cladding regions. After specified the refractive index profile of the MCF, we define a referential and the fiber is assumed to be fixed relatively to such referential, see Fig. 3.15(a). Then, the vibration plane of the flexural wave can be rotated relatively to the referential. Such rotation must be considered in the circumferential displacement as an additional phase induced in $\Phi_z(\theta)$. In that way, the circumferential displacement along the

MCF can be rewritten as: $\Phi_z(\phi,\varphi) = \sin(\phi+\varphi)$ or $\Phi_z(\phi,\varphi) = \cos(\phi+\varphi)$, where ϕ is the angular coordinate and the φ is the angle between the vibration plane of the flexural wave and the YZ plane.

Considering only the forward complex amplitude in (3.7) and an index perturbation induced by a set of acoustic flexural waves, the coupled equations that describe the energy transfer in an arbitrary MCF can be written as,

$$\frac{d}{dz}\mathcal{A}_p(z) = \sum_{j=0}^{m}\sum_{l=1}^{n}\mathcal{A}_l(z)\vartheta_{lp}^{j}e^{i[\beta_p(\omega)-\beta_l(\omega)-k_j]z}\,, \tag{3.21}$$

where ϑ_{lp}^{j} represents the coupling coefficient between the l and the p modes,

$$\vartheta_{pl}^{j} = \frac{\omega}{4}\iint\frac{\mathbf{F}_p(\mathbf{x},\omega)\cdot\mathbf{F}_l^{*}(\mathbf{x},\omega)}{N_p(\omega)N_l(\omega)}\frac{\partial\varepsilon_j}{\partial z}rdrd\phi\,, \tag{3.22}$$

being ε_j the perturbation induced by the j acoustic wave in the permittivity of the MCF. Notice that (3.21) comprises p coupled equations for the four cores and the $p-4$ cladding modes considered. Furthermore, (3.21) also allows to describe the energy transfer considering several index perturbations with distinct spatial distributions and periods.

The circumferential displacement induced by the flexural wave is given by

$$u_z(\mathbf{r},t) = W(r)\cos(\phi+\varphi)e^{-i(kz-\Omega t)}\,, \tag{3.23}$$

in which the relative orientation between the vibration plane of the flexural wave and the spatial distribution of the cores depends on φ. Assuming the index perturbation induced by the j flexural wave, the coupling coefficient between the p core mode and l cladding mode, ϑ_{pl}^{j}, can be calculated by replacing (3.23) in (3.16) and then using (3.22). By solving (3.14), the acoustic frequency, Ω, is calculated for the first order flexural mode, i.e., the fundamental mode[3]. It should be emphasized that the value of the mode coupling can be tuned by adjusting the amplitude of u_z^{max}, which is defined by the acoustic power applied to the MCF. As previously stated, from (3.23) clearly results that the index perturbation induced in a particular core of the MCF also depends on φ.

3.5.3 Core switching in homogeneous MCFs

In this subsection, we assume a HoMCF with a cladding diameter of 125 μm and four single-mode cores. The cores have a step-index profile with core diameter (d) of 7.2 μm and "square" arrangement with pitch (D) of 36.25 μm, see the left-hand inset in Fig. 3.15. The refractive index of the core/cladding is calculated considering in (3.17) the Sellmeier coefficients given in [15]. The mole fraction of GeO_2 considered for all the cores was X = 0.0516 [15]. The fiber considered in this analysis is similar to the commercial fiber, SM 4C1500(8.0/125) from the company Fibercore [22]. Using the previous parameters in the Comsol Multiphysics® software package, the parameters $\beta_l(\omega)$ and $\mathbf{F}_l(\mathbf{x},\omega)$ were calculated for the four core modes and the first 22 vectorial cladding modes with the highest effective refractive index. In the numerical tool, it was considered an extra layer of air surrounding the fiber two times larger than the silica cladding.

[3]Notice that acoustic modes of higher orders have higher acoustic frequencies and, therefore, are more difficult to achieve from the experimental point of view.

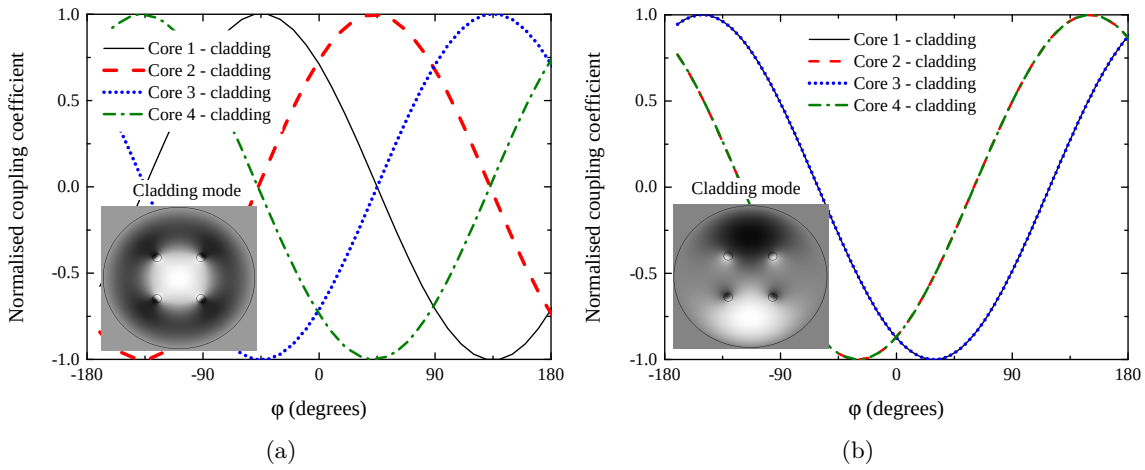

Figure 3.16: Normalised coupling coefficient between the cores and a symmetric cladding mode, (a), and an antisymmetric cladding mode, (b), at 1550 nm, as function of the angle between the vibration plane of the flexural wave and the YZ plane, φ. Inset figures show the real part of the x component of the electric field, black and white regions represent the positive and the negative values, respectively.

In single core fibers, a flexural wave enables the energy transfer between symmetric and antisymmetric modes or between antisymmetric and symmetric modes supported in the core or in the cladding [23]. In contrast, in MCFs the fiber cores are spatially separated and therefore the spatial overlap between the fundamental mode of two arbitrary cores tends to be negligible. In this case, the A-O effect can only induces the energy transfer between the fundamental mode guided in a given core and a cladding mode.

In MCFs, the magnitude and the transverse distribution of the refractive index perturbation induced in a particular core depends on the spatial orientation of the flexural wave. Hence, the magnitude of the coupling coefficient also depends on the spatial orientation of the flexural wave. When the vibration plane of the flexural wave is aligned with a given axis defined by two cores of the 4-core MCF which are diametrally opposed, in the other two cores is induced an antisymmetric index perturbation. For the remaining values of φ, the index perturbation does not show the antisymmetric index profile because the cores are shifted from the center of the optical fiber. Therefore, a flexural wave can induce the mode coupling between a core mode and a symmetric or a antisymmetric cladding mode. In Fig. 3.16 are shown the normalized coupling coefficients between the four core modes and a single symmetric, see Fig. 3.16(a), and antisymmetric, see Fig. 3.16(b), cladding mode as function of φ. For the symmetric cladding mode considered, the maximum/minimum value of the coupling coefficient is achieved when the vibration plane is aligned with one pair of cores, see Fig. 3.16(a). In this case, the relative shift between curves is 90° because the maximum overlap is achieved over the core region. For the considered antisymmetric cladding mode, see inset in Fig. 3.16(b), the opposite cores have the same coupling coefficient due to the antisymmetric refractive index perturbation induced by the flexural wave. In this case, the optical power of the cladding mode is mainly distributed between the cores and, thus the maximum overlap is achieved over the cladding region leading to a relative shift between curves of ≈ 60°, see Fig. 3.16(b).

In order to induce the resonant coupling between a core mode and a given cladding mode,

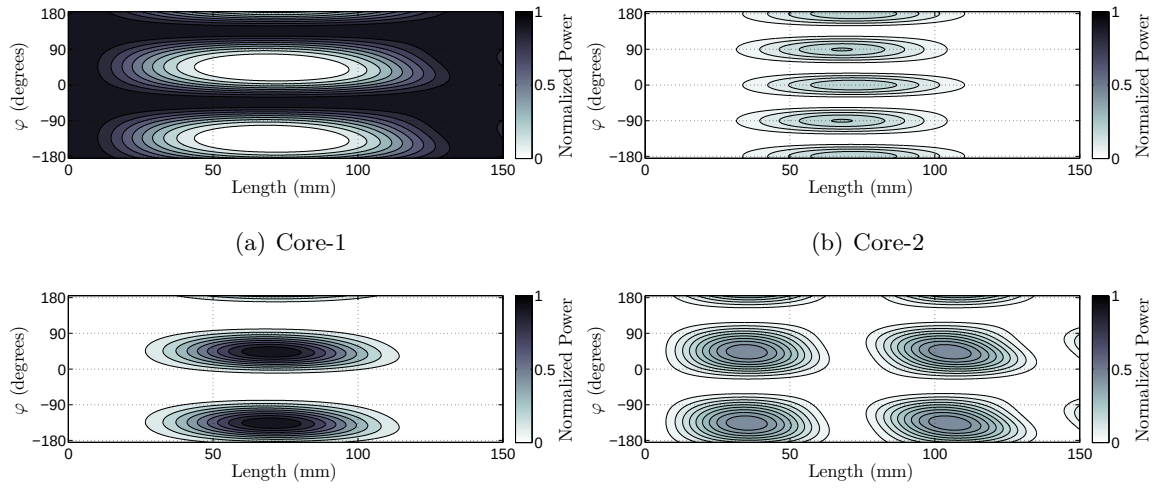

(a) Core-1

(b) Core-2

(c) Core-3

(d) Cladding Mode

Figure 3.17: Normalized power evolution as function of the fiber length and the angle of the acoustic wave, φ, assuming an optical signal launched in core-1 of the HoMCF at 1550 nm and considering a flexural wave with a frequency of 1282.95 kHz and peak deflection of 25 nm. In Figs. 3.17(a)-3.17(c), we show the normalized power evolution for core-1, core-2 and core-3, respectively. Note that the power evolution in core-4 and core-2 are similar and in that way only the power in the core-2 was shown. The sum of the power evolution in the two nearly degenerated cladding modes considered is shown in Fig. 3.17(d).

the acoustic propagation constant of the flexural wave is calculated considering in (3.9a) the propagation constant of the core and the cladding mode. When the phase-matching condition is achieved, the exponent in (3.21) becomes null and the resonant coupling occurs efficiently. Then, the acoustic frequency for the fundamental flexural mode is obtained using the acoustic propagation constant, k, in (3.14) and the index perturbation induced in the MCF was calculated using (3.15) in which the maximum longitudinal displacement was taken as $u_z^{max} = 25$ nm [23]. In (3.21), we consider a flexural wave with acoustic frequency of 1282.95 kHz and an optical signal in the core-1 of the HoMCF, whereas the other considered cores and the set of degenerated cladding modes were assumed to have no optical power. The power evolution for the cores and the cladding mode as function of the fiber length and φ are displayed in Fig. 3.17. Figure 3.17(a)-3.17(c) show the optical power in the core-1, core-2 and core-3, respectively. Note that the power evolution in core-2 and core-4 are similar and therefore only the power evolution in the core-2 is shown. In Fig. 3.17(d), it is shown the sum of the optical power for the two degenerated cladding modes with the second highest refractive index. In the calculations, we assume an almost perfect phase-matching condition between the core and a selected cladding mode at 1550 nm and therefore the resonant coupling only occurs between the cores and the set of degenerated cladding modes. Hence, the interaction with the remaining cladding modes can be neglected. Nevertheless, in real devices, such condition may not be completely achieved due to index variations and diameter fluctuations. Thereby, it is expected some penalty in the extinction ratio for real devices.

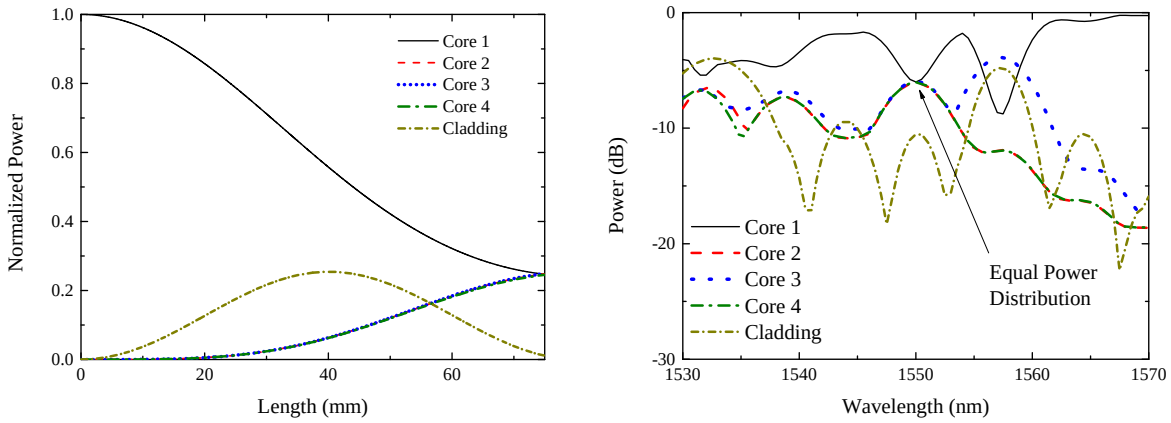

Figure 3.18: a) Power evolution in the four cores and the cladding mode of the HoMCF as function of the fiber length considering a flexural wave with peak deflection of 25 nm and acoustic frequency of 1282.95 kHz and $\varphi = 45°$. The optical signal is assumed at 1550 nm. b) Transmission spectrum considering all the cladding modes and the parameters used in a) considering a fiber length of 72 mm.

Switching between two opposite cores

Assuming an angle of $\varphi = 45°$ in Fig. 3.17, an efficient power conversion between the core-1 and the core-3 can be observed. As a result of the induced antisymmetric index perturbation, the same phenomena can also be achieved by rotating the vibration plane of the flexural wave by 180°, see Figs. 3.17(a) and 3.17(c). In addition, the power evolution as function of the fiber length assuming $\varphi = 45°$ is shown in Fig. 3.18(a). In this case, the power is transferred from core-1 to core-3 by means of the selected "intermediary" cladding mode without meaningful power transfer for the remaining cores.

In order to analyze the spectral response of the core switch, the transmission spectrum is calculated considering the aforementioned acoustic wave and all the cladding modes previously found. The transmission spectrum reflects the interaction between the core-1, core-3 and the cladding mode in the range from 1530 to 1570 nm, see Fig. 3.18(b). At 1550 nm, we note an attenuation band in core-1 and a transmission window in the core-3 with a FWHM (or bandwidth) of 5.2 nm. The bandwidth of the transmission window can be customized by engineering the dispersion profile of the HoMCF. In addition, the transmission bandwidth can be spectrally shifted by fine tuning the RF signal applied to the PZT.

Uniform signal distribution

Assuming an angle of $\varphi = 0°$ in Fig. 3.17, the uniform distribution of the signal over all the cores can be achieved. Notice that the uniform signal distribution can also be found for more three angles by rotating the vibration plane of the flexural wave of 90°, see Fig. 3.17. In Fig. 3.19(a), we show in detail the energy transfer as function of the fiber length for this particular case (i.e., $\varphi = 0°$). The signal guided in the core-1 is coupled to the cladding mode and then the signal is uniformly distributed by the remaining cores. In Fig. 3.19(b), it is shown the transmission spectrum, in which the uniform signal distribution is achieved at 1550 nm with a bandwidth of 5.2 nm. In this case, the spectra show several peaks at

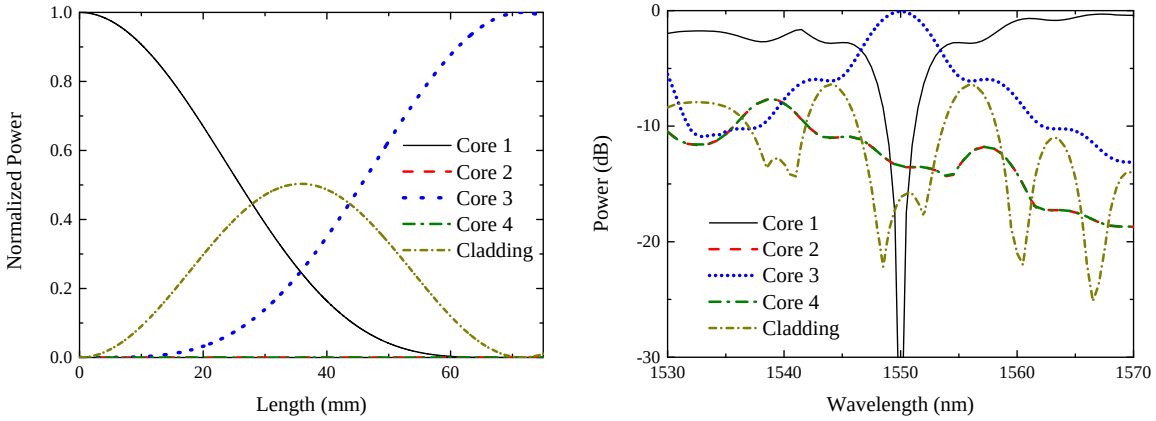

Figure 3.19: a) Power evolution in the four cores and the cladding mode of the HoMCF as function of the fiber length considering a flexural wave with peak deflection of 25 nm and acoustic frequency of 1282.95 kHz and $\varphi = 0°$ for an optical signal with a wavelength of 1550 nm. b) Transmission spectrum considering all the cladding modes and the parameters used in a).

both sides of 1550 nm. However, the optical bandwidth and the additional peaks in the transmission spectra are determined by the dispersion profile of the core and the cladding mode considered. In principle, the remaining peaks at both sides can be avoided by properly engineering the dispersion profile of the HoMCF [3]. In this configuration, the proposed device enables the signal distribution over all the cores of a HoMCF; therefore, it can be used to fuel optical amplifiers based on Erbium doped MCF transmission systems using a single pump source [24].

In order to achieve the mentioned uniform power distribution in HoMCF with ring geometry (i.e., all the cores have the same distance to the center of the fiber), the coupling coefficients between all the cores and the cladding mode should take the same value [24]. Depending on the number of cores and their relative position, this can be achieved with a single acoustic wave or eventually more acoustic waves can be required. For instance, in a two core MCF, the uniform power distribution can be achieved by properly adjusting the vibration plane of a single acoustic wave. However, in a eight cores MCF with ring geometry, two orthogonal flexural waves are required to uniformly distribute the optical power over all the cores.

The results above presented have been obtained for a particular cladding mode, with symmetric transverse distribution of the electric field, and assuming both degenerated modes. Nevertheless, similar results were achieved for other symmetric and even antisymmetric cladding modes with coupling coefficients described by Fig. 3.16(a). It should be noted that for different cladding modes are found distinct beat lengthes because the acoustic wavelength (or the length period) required to induce the resonant coupling also changes. Furthermore, the interaction between flexural waves and cladding modes with coupling coefficients described by Fig. 3.16(b) was also investigated. Such modes lead to a more complex power evolution in which the switching between two opposite cores is still possible. However, the uniform distribution of the optical signal through this kind of cladding modes is not found.

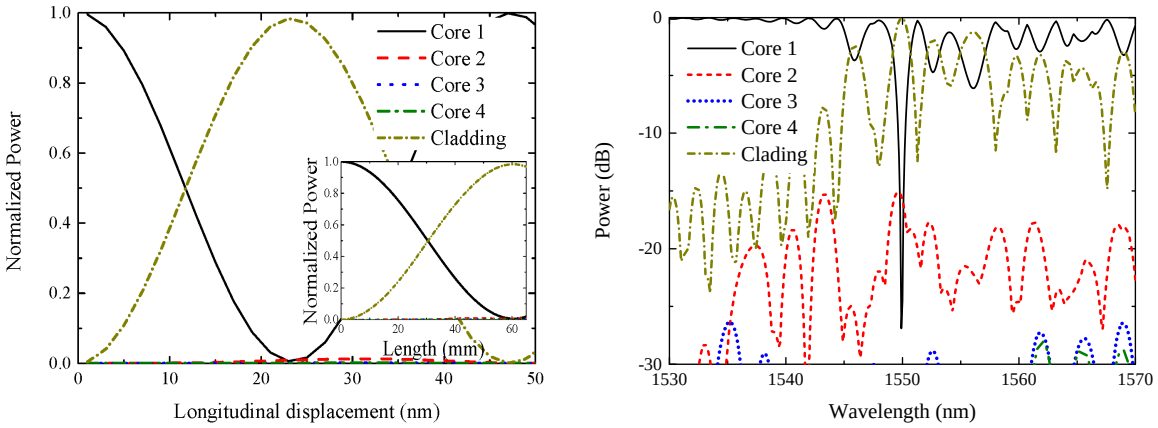

Figure 3.20: a) Output optical power as function of the peak deflection considering a fiber length of 60 mm. Inset figure shows the power evolution as function of the fiber length for the four cores and the selected cladding mode of the HeMCF. A flexural wave with a peak deflection of 25 nm, acoustic frequency of 1283.4 kHz and φ = 180°applied over the fiber. b) Transmission spectra considering a fiber length of 0.06 m and a peak deflection of 25 nm.

3.5.4 Core switching in heterogeneous MCFs

In this subsection the A-O effect is investigated in HeMCFs. We assume the same geometrical parameters as stated in section 3.5.3, only the mole fraction of GeO_2 for each core is changed. The refractive index of the cores-1, 2, 3 and 4, can be calculated by replacing the X parameter in (3.17) by X_1=0.0516, X_2=0.0525, X_3=0.0514 and X_4=0.0530, respectively. In that way, the degeneracy of the core modes can be lifted in terms of propagation constants.

Core selective attenuator

Using a single flexural wave in an HeMCF, we can induce a resonant coupling between any core and a cladding mode without energy transfer to the remaining cores. In Fig. 3.20(a), the inset shows the power transfer from the core-1 to a cladding mode as function of the fiber length without additional coupling to the remaining cores. As in SMFs [4], an inline selective core attenuator can be produced by coupling the optical power from a given core to a cladding mode. In addition, we can tune the induced attenuation in the selected core by adjusting u_z^{max}. In Fig. 3.20(a), we show the energy transfer between the core-1 and the two degenerated modes of the fourth cladding mode as function of u_z^{max} for a fiber length of 60 mm. In Fig. 3.20(b), we show the transmission spectrum of the proposed attenuator considering the maximum power transfer between the selected core and the cladding mode. In this example, the resonant coupling is achieved at 1550 nm with an attenuation bandwidth of 1.47 nm. Nevertheless, the central wavelength of the attenuation bandwidth can be spectrally shifted by fine tuning the RF signal applied in the PZT.

Selective core switching

The process behind the light switching between any pair of cores in HeMCF is based on a double resonant coupling induced by two flexural waves. The signal in the input core

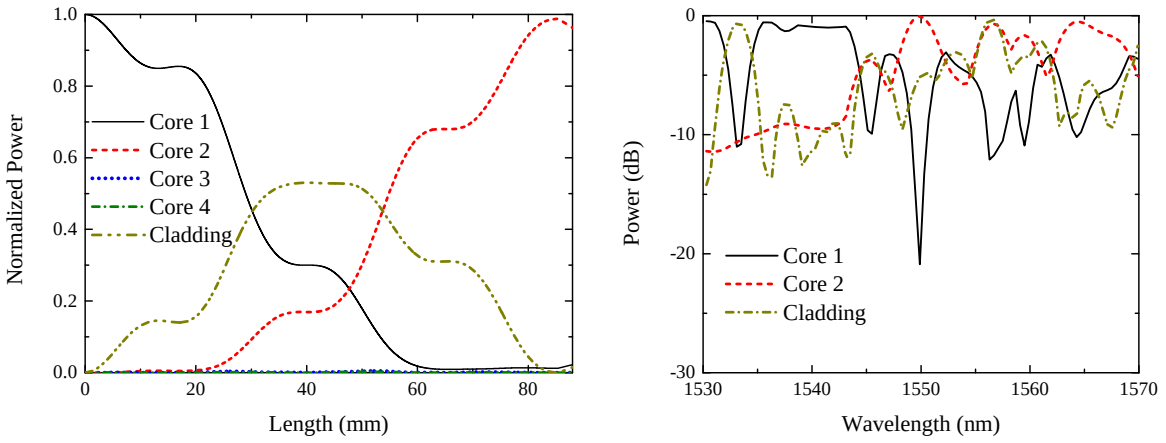

(a) (b)

Figure 3.21: a) Power evolution in a four core HeMCF considering two flexural waves with u_z^{max} = 25 nm, φ = 0° and Ω_1 = 1282.1 and Ω_2 = 1283.4 kHz. b) Transmission spectra considering a fiber length of 85 mm.

is transferred to a cladding mode by a flexural wave with frequency Ω_1. Applying another flexural wave with proper acoustic frequency Ω_2, the optical power in the excited cladding mode is switched to the desired output core. This resonant process can be described by a system of coupled equations considering m = 2 in (3.21). Such interaction is analogous to the lambda-type laser-driven atomic states with no dephasing terms for pure initial states. However, in this process, the effective index (n_{eff}) of each core mode corresponds to the energy level of the lambda-type configuration [25].

The acoustic frequencies of the flexural waves are calculated considering the propagation constant of the cores and the selected cladding mode in (3.9a). In Fig. 3.21(a), we show the power evolution as function of the length between the core-1, the cladding mode and the core-2. The power is progressively transferred from the core-1 to the cladding mode and then to the core-2 as function of the fiber length. The optical power guided in the core-1, core-2 and the cladding mode shows a small beating induced by an additional coupling between the cladding mode and the other two remaining cores, see Fig. 3.21(a). The switching between the core-1 and the core-3/core-4 can also be achieved by properly adjusting the Ω, u_z^{max}, and φ of both flexural waves. Note that, such parameters can be adjusted to achieve the same interaction length for the switching process between all the cores considered. From an analytical point of view, the complete power switch between two different cores is achieved when $\vartheta_{1-cl} \approx \vartheta_{cl-j}$, with $j = 2, 3$ and 4 [25].

The transmission spectrum for the core switch between the core-1 and core-2 is shown in Fig. 3.21(b), in which a transmission window at 1550 nm with a bandwidth of 3 nm was obtained. In this case, the energy transfer between the core-1 and the cladding mode also occurs at others wavelengths (*i.e.* at 1535 and 1561 nm). However, the transmission spectra are determined by the dispersion profile of the core and the cladding mode considered. Thus, the entire transmission spectra can be customized by engineering the dispersion profile of the HeMCF [3]. The transmission spectrum considering the core switching between the core-1 and core-3/core-4 was also obtained. The acoustic frequency required to induce the core switching between the core-1, core-2, core-3 and core-4 and cladding mode is 1283.40, 1282.16,

1280.02 and 1279.55 kHz, respectively. For the core switching between the core-1 and core-3, the transmission window shows a bandwidth of 2.22 nm, while for the core switching between the core-1 and core-4, a transmission window with a bandwidth of the 3.34 nm is measured at 1550 nm. Note that the different values obtained for the transmission bandwidth can be explained by the different dispersion profiles of each core.

3.6 Summary

Based on the MCT, we have developed an analytical model addressing the energy transfer induced by acoustic waves in FMFs and MCFs. Supported by this model, the energy transfer in few-mode microwires considering the A-O effect was numerically investigated. We show that the mode switching between two arbitrary modes can be achieved by properly choosing the kind (i.e., flexural or longitudinal) and the frequency of the acoustic wave. Furthermore, the acoustic wave amplitude allows to control the mode switching efficiency, whereas the acoustic frequency allows to select the center of the transmission window. Lastly, an experimental validation of the proposed mode switching device was also carried out. The optical microwire was produced using the flame brushing technique and an experimental setup to excite acoustic waves in the optical microwire was developed. The mode conversion between the fundamental mode and the TM_{01}, TE_{01} and HE_{21} was observed *in situ*.

Then, we have also investigated the energy transfer induced by flexural waves in HeMCFs and HoMCFs. In a 4-cores HoMCF with ring geometry, we have demonstrated the core switching between two diametrically opposed cores. In addition, we was also show the uniform signal distribution by all the cores. In both aforementioned process, the spatial orientation of the flexural wave plays a key role in the energy transfer between cores. By properly adjusting the vibration plane of the flexural wave, we can select between the uniform signal distribution and the core switching between opposite cores. In HeMCF, we have shown the selective core switching between any two cores using two flexural waves. It should be emphasized that the proposed switching device based on HeMCFs is independent of the core arrangement in the MCF. In addition, we have also proposed an in-line wavelength selective core attenuator using a single flexural wave.

Bibliography

[1] M. Delgado-Pinar, D. Zalvidea, a. Diez, P. Perez-Millan, and M. Andres, "Q-switching of an all-fiber laser by acousto-optic modulation of a fiber Bragg grating." *Optics Express*, vol. 14, no. 3, pp. 1106–12, Feb. 2006.

[2] T. Birks, P. Russell, and D. Culverhouse, "The acousto-optic effect in single-mode fiber tapers and couplers," *IEEE/OSA Journal of Lightwave Technology*, vol. 14, no. 11, pp. 2519–2529, Nov 1996.

[3] T. Matsui, K. Nakajima, K. Shiraki, and T. Kurashima, "Ultra-broadband mode conversion with acousto-optic coupling in hole-assisted fiber," *IEEE/OSA Journal of Lightwave Technology*, vol. 27, no. 13, pp. 2183–2188, July 2009.

[4] R. Feced, C. Alegria, M. Zervas, and R. Laming, "Acoustooptic attenuation filters based

on tapered optical fibers," *IEEE Journal of Selected Topics in Quantum Electronics*, vol. 5, no. 5, pp. 1278–1288, Sep 1999.

[5] D. Marcuse, *Theory of dielectric optical waveguides.* New York, Academic Press, 1974.

[6] E. Khoo, A. Liu, X. Zhang, E. Li, J. Li, D. Pinjala, and B. Luk'yanchuk, "Exact step-coupling theory for mode-coupling behavior in geometrical variation photonic crystal waveguides," *Physical Review B*, vol. 80, p. 035101, Jul 2009.

[7] R. Thurston, "Elastic waves in rods and clad rods," *Acoustical Society of America Journal*, vol. 64, pp. 1–37, Jul. 1978.

[8] H. Engan, B. Kim, J. Blake, and H. Shaw, "Propagation and optical interaction of guided acoustic waves in two-mode optical fibers," *IEEE/OSA Journal of Lightwave Technology*, vol. 6, no. 3, pp. 428–436, Mar. 1988.

[9] K. Karapetyan, "Single optical microfibre-based modal interferometer," Ph.D. dissertation, University of Bonn, 2012.

[10] G. Brambilla, "Optical fibre nanowires and microwires: a review," *Journal of Optics*, vol. 12, no. 4, p. 043001, 2010.

[11] L. Tong, R. R. Gattass, J. B. Ashcom, S. He, J. Lou, M. Shen, I. Maxwell, and E. Mazur, "Subwavelength-diameter silica wires for low-loss optical wave guiding," *Nature*, vol. 426, no. 6968, p. 816, 2003.

[12] G. Brambilla, "Optical fibre nanotaper sensors," *Optical Fiber Technology*, vol. 16, no. 6, pp. 331–342, 2010.

[13] G. Brambilla, V. Finazzi, and D. Richardson, "Ultra-low-loss optical fiber nanotapers," *Optics Express*, vol. 12, no. 10, pp. 2258–2263, May 2004.

[14] P. S. André and A. N. Pinto, "Chromatic dispersion fluctuations in optical fibers due to temperature and its effects in high-speed optical communication systems," *Optics Communications*, vol. 246, no. 4–6, pp. 303–311, 2005.

[15] J. Fleming, "Dispersion in GeO_2-SiO_2 glasses," *Applied Optics*, vol. 23, no. 24, pp. 4486–4493, Dec 1984.

[16] A. Fielding, K. Edinger, and C. Davis, "Experimental observation of mode evolution in single-mode tapered optical fibers," *IEEE/OSA Journal of Lightwave Technology*, vol. 17, no. 9, pp. 1649–1656, Sep 1999.

[17] G. M. Fernandes, M. Niehus, C. A. F. Marques, R. Nogueira, and A. N. Pinto, "Acousto-optic tunable mode coupler," in *Optical Fiber Conference (OFC).* Optical Society of America, 2012, p. JTh2A.2.

[18] M. Niehus, G. M. Fernandes, and A. N. Pinto, "Design of a tunable single photon interferometer based on modal engineered tapered optical fibers," in *Proceedings of SPIE*, vol. 7727. SPIE, 2010, pp. 194–212.

[19] T. Birks and Y. Li, "The shape of fiber tapers," *IEEE/OSA Journal of Lightwave Technology*, vol. 10, no. 4, pp. 432–438, 1992.

[20] J. D. Love, W. M. Henry, W. J. Stewart, R. J. Black, S. Lacroix, and F. Gonthier, "Tapered single-mode fibres and devices. I. Adiabaticity criteria," *IEE Proceedings J - Optoelectronics*, vol. 138, no. 5, pp. 343–354, Oct 1991.

[21] P. Dashti, F. Alhassen, and H. Lee, "Observation of orbital angular momentum transfer between acoustic and optical vortices in optical fiber," *Physical Review Letters*, vol. 96, p. 043604, Feb 2006.

[22] Datashet of SM 4C1500(8.0/125) from Fibercore [Online]. Avaliable: http://fibercore.com/product/multicore-fiber.

[23] G. M. Fernandes, N. J. Muga, and A. N. Pinto, "Tunable mode conversion using acoustic waves in optical microwires," *IEEE/OSA Journal of Lightwave Technology*, vol. 32, no. 19, pp. 3257–3265, Oct 2014.

[24] A. Rocha, T. Almeida, R. Nogueira, and M. Facão, "Analysis of power transfer on multicore fibers with long-period gratings," *Optics Letters*, vol. 40, no. 2, pp. 292–295, Jan 2015.

[25] H. Park and K. Song, "Acousto-optic resonant coupling of three spatial modes in an optical fiber," *Optics Express*, vol. 22, no. 2, pp. 1990–1996, Jan 2014.

Chapter 4

Multimodal four-wave mixing

The nonlinear effects will certainly be a limiting factor of the overall aggregated bit-rate in SDM-based transmission systems [1], as happens in the current SSMF-based transmission systems. Perhaps more important, however, nonlinear effects can also be employed to develop novel devices for optical signal processing in the multimodal regime. In the single-mode case, the optical signal processing based on the FWM process has been used for signal regeneration and wavelength conversion. In contrast, there is a lack of theoretical studies of the FWM process in the multimodal regime. Such theoretical studies will be required to lay the foundations of future parametric techniques for signal processing in transmission systems based on SDM.

In this chapter, we derive the multimodal NLSE for a nonideal optical fiber, i.e., with index inhomogeneities and geometric irregularities. From the extended multimodal NLSE, we found a set of coupled equations that allow to describe the multimodal FWM process in the presence of mode coupling. A silica-based FMF tends to have an effective area larger than a SSMF, making the nonlinear process in FMFs inefficient. In contrast, optical microwires are multimodal and highly nonlinear waveguides. In that way, optical microwires are chosen as a suitable waveguide in which the multimodal FWM process may occur efficiently. The phase-matching condition in optical microwires is analyzed for the intermodal and intramodal FWM processes. Lastly, the energy transfer induced by the multimodal FWM process in the presence of mode coupling is investigated.

4.1 Generalized multimode nonlinear Schrödinger equation

The generalized multimode NLSE is derived following the approach of Kolesik and Moloney [2], where we assume the optical field as described in (3.1). The Maxwell's equations for the homogeneous dielectric medium and the fiber geometry can be written as

$$\frac{\partial}{\partial t}\mathbf{P}_{\mathrm{NL}}(\mathbf{r},t) + \frac{\partial}{\partial t}\varepsilon\mathbf{E}(\mathbf{r},t) = \nabla\times\mathbf{H}(\mathbf{r},t)\,, \tag{4.1a}$$

$$-\mu_0\frac{\partial}{\partial t}\mathbf{H}(\mathbf{r},t) = \nabla\times\mathbf{E}(\mathbf{r},t)\,, \tag{4.1b}$$

where $\mathbf{P}_{\mathrm{NL}}(\mathbf{r},\mathrm{t})$ represents the nonlinear induced electric polarization, and ε represents the permittivity. The nonlinear polarization of the fused silica can be written as [3]

$$\mathbf{P}_{\mathrm{NL}}(\mathbf{r},t) = \varepsilon\chi^{(3)}(t-\tau)\mathbf{E}_j(\mathbf{r},t)\times\int R(t-\tau)\mathbf{E}_k^*(\mathbf{r},\tau)\cdot\mathbf{E}_s(\mathbf{r},\tau)d\tau\,, \tag{4.2}$$

where $\chi^{(3)}$ and $R(t)$ denote the 3rd order susceptibility and the fiber normalized nonlinear response function, respectively. The subindexes j, k and s denote the optical modes considered in the calculations of the nonlinear response of the multimodal fiber.

Scalar multiplying (4.1a) and (4.1b) by the complex conjugate of the transverse distribution of the electric and magnetic fields, including their time and z-dependent phase factors,

$$\mathcal{E}_p(\mathbf{r},t) = \mathbf{F}_p(x,y,\omega)e^{i(\beta^p(\omega)z-\omega t)}\,, \tag{4.3a}$$

and

$$\mathcal{H}_p(\mathbf{r},t) = \mathbf{G}_p(x,y,\omega)e^{i(\beta^p(\omega)z-\omega t)}\,, \tag{4.3b}$$

respectively, the following equations can be obtained [2]

$$\mathcal{E}_p^*(\mathbf{r},t)\cdot\left[\frac{\partial}{\partial t}\mathbf{P}_{\mathrm{NL}}(\mathbf{r},t)+\frac{\partial}{\partial t}\varepsilon\mathbf{E}(\mathbf{r},t)\right] = \tag{4.4a}$$
$$\nabla\cdot[\mathbf{H}(\mathbf{r},t)\times\mathcal{E}_p^*(\mathbf{r},t)]+\mathbf{H}(\mathbf{r},t)\cdot[\nabla\times\mathcal{E}_p^*(\mathbf{r},t)]\,,$$
$$-\mu_0\mathcal{H}_p^*(\mathbf{r},t)\cdot\frac{\partial}{\partial t}\mathbf{H}(\mathbf{r},t) = \tag{4.4b}$$
$$\nabla\cdot[\mathbf{E}(\mathbf{r},t)\times\mathcal{H}_p^*(\mathbf{r},t)]+\mathbf{E}(\mathbf{r},t)\cdot[\nabla\times\mathcal{H}_p^*(\mathbf{r},t)]\,.$$

The last terms of (4.4a) and (4.4b) are simplified using (4.1a) and (4.1b), for the complex conjugate modes, $\mathcal{E}_p(\mathbf{r},t)$ and $\mathcal{H}_p(\mathbf{r},t)$. Subtracting (4.4a) and (4.4b), we obtain [2]

$$\mathcal{E}_p^*(\mathbf{r},t)\cdot\frac{\partial\mathbf{P}_{NL}(\mathbf{r},t)}{\partial t} = \nabla\cdot[\mathbf{H}(\mathbf{r},t)\times\mathcal{E}_p^*(\mathbf{r},t)]-\nabla\cdot[\mathbf{E}(\mathbf{r},t)\times\mathcal{H}_p^*(\mathbf{r},t)]\,. \tag{4.5}$$

Integrating (4.5) over the x, y and t domains, and applying the orthogonality relation, leads to

$$\int\mathcal{E}_p^*(\mathbf{r},t)\cdot\frac{\partial\mathbf{P}_{NL}(\mathbf{r},t)}{\partial t}d\mathbf{x}dt = 4N_p(\omega)\frac{\partial\mathcal{A}_p}{\partial z}+\sum_{l\neq p}\frac{\mathcal{A}_l}{N_l(\omega)}(\mathcal{C}_{pl}-\mathcal{C}_{lp}^*)\,, \tag{4.6}$$

where,

$$\mathcal{C}_{lp} = \int\hat{z}\cdot\left[\frac{\partial\mathcal{H}_l(\mathbf{r},t)}{\partial z}\times\mathcal{E}_p^*(\mathbf{r},t)+\mathcal{H}_p^*(\mathbf{r},t)\times\frac{\partial\mathcal{E}_l(\mathbf{r},t)}{\partial z}\right]d\mathbf{x}dt\,, \tag{4.7a}$$

and

$$\mathcal{C}_{pl}^* = \int\hat{z}\cdot\left[\frac{\partial\mathcal{H}_p^*(\mathbf{r},t)}{\partial z}\times\mathcal{E}_l(\mathbf{r},t)+\mathcal{H}_l(\mathbf{r},t)\times\frac{\partial\mathcal{E}_p^*(\mathbf{r},t)}{\partial z}\right]d\mathbf{x}dt\,. \tag{4.7b}$$

Equation (6.19a) and (6.19b) can be written as [4, 5]

$$\mathcal{C}_{pl}-\mathcal{C}_{lp}^* = \int i[\beta^p(\omega)-\beta^{l*}(\omega)]\hat{z}\cdot\left[\frac{\partial\mathcal{E}_p(\mathbf{r},t)}{\partial z}\times\mathcal{H}_l^*(\mathbf{r},t)+\mathcal{E}_l^*(\mathbf{r},t)\times\frac{\partial\mathcal{H}_p(\mathbf{r},t)}{\partial z}\right]d\mathbf{x}dt\,. \tag{4.8}$$

The last term in (4.8) can be rewritten as

$$\int\nabla_T\cdot\left[\frac{\partial\mathcal{H}_p(\mathbf{r},t)}{\partial z}\times\mathcal{E}_l^*(\mathbf{r},t)+\mathcal{H}_p^*(\mathbf{r},t)\times\frac{\partial\mathcal{E}_l(\mathbf{r},t)}{\partial z}\right]d\mathbf{x}dt+\int i\frac{\partial\beta^p}{\partial z}\hat{z}\cdot\Big[\mathcal{H}_p(\mathbf{r},t)\times\mathcal{E}_l^*(\mathbf{r},t)+$$
$$\mathcal{H}_l^*(\mathbf{r},t)\times\mathcal{E}_p(\mathbf{r},t)\Big]d\mathbf{x}dt-\omega\varepsilon_0\int\frac{\mathcal{E}_p(\mathbf{r},t)\mathcal{E}_l^*(\mathbf{r},t)}{N_p(\omega)N_l(\omega)}\frac{\partial\varepsilon_r}{\partial z}d\mathbf{x}\,, \tag{4.9}$$

where, ∇_T represents the ∇ operator over the transverse coordinates, $\varepsilon_r = n^2$ represents the relative permittivity and n the refractive index. In (4.9), the first term can be converted from the surface integral to the line integral around the waveguide, i.e., Stokes theorem, and the line integral vanishes for all guided and radiation modes, with $p \neq l$. When the orthogonal relationship, (3.2), is applied, the second term is vanishes, and the modal coupling coefficient, $C_{pl} = \mathcal{C}_{pl} - \mathcal{C}^*_{lp}$, can be expressed as

$$C_{pl} = \frac{\omega\varepsilon_0}{2(\beta^{l*}(\omega) - \beta^p(\omega))} \int \frac{\mathcal{E}_p(\mathbf{r},t)\mathcal{E}^*_l(\mathbf{r},t)}{N_p(\omega)N_l(\omega)} \frac{\partial\varepsilon_r}{\partial z} d\mathbf{x}\,. \tag{4.10}$$

The $\partial\varepsilon_r/\partial z$ accounts for the dielectric discontinuity in the core-to-clading and clading-to-air interfaces in standard optical fibers or for the dielectric discontinuity in the microwire boundary. It should be noted that the index inhomogeneities and geometric irregularities along the entire multimode fiber should be considered in the variation of the electric permittivity. The propagation equation for the p mode envelope can be obtained from (4.6) using the field description given in (3.1a) and (3.1b),

$$\frac{\partial}{\partial z}\mathcal{A}_p(z,\omega) = -\frac{1}{4N_p(\omega)} \int \mathcal{E}^*_p(\mathbf{x},\omega) \cdot \frac{\partial}{\partial t}\mathbf{P}_{\mathrm{NL}}(\mathbf{r},t) d\mathbf{x} - \sum_{l\neq p} C_{pl}\mathcal{A}_l dt\,. \tag{4.11}$$

Then, we assume that the forward and backward propagating fields can be separated and any nonlinear interactions between them can be neglected. The multimodal NLSE can be obtained by replacing (4.2) in (4.11) and using,

$$\mathcal{A}_p(\mathbf{x},\omega) = A_p(\mathbf{x},\omega) e^{-i\left[\beta^p(\omega) - \beta^0(\omega)\right]z}\,, \tag{4.12}$$

where $\beta^0(\omega)$ represents the propagation constant for the fundamental mode. By expanding the propagation constant in a Taylor series to the jth order about ω_0, the multimodal NLSE can be obtained

$$\frac{\partial}{\partial z}A_p(z,t) = \sum_j \frac{i^{j+1}(\beta^p_j - \beta^0_j)}{j!}\frac{\partial^j}{\partial t^j}A_p(z,t) - \sum_l \left[\left(1 + i\zeta_{lp}\frac{\partial}{\partial t}\right)C_{pl}(\omega_0)\right]A_l(z,t) + i\frac{n_2\omega_0}{c}\sum_{l,m,n}\left(1 + i\tau_{plmn}\frac{\partial}{\partial t}\right)Q_{plmn}(\omega_0)\xi(z,t)\,, \tag{4.13}$$

where

$$\xi(z,t) = 2(1-f_R)A_l(z,t)A_m(z,t)A^*_n(z,t) + 3f_{\mathrm{R}}A_l(z)\int h(\tau)A_m(z,t-\tau)A^*_n(z,t-\tau)d\tau\,, \tag{4.14}$$

with c being the speed of light in vacuum, and n_2 the nonlinear refractive index. The parameters $\beta^0_j = \partial^j\beta^0(\omega)/\partial\omega^j$ and β^p_j are the jth order dispersion coefficient for the fundamental mode and the p mode, respectively. The f_{R} term is the fractional contribution of the Raman response to the total nonlinearity, and $h(\tau)$ is the delayed Raman response function [3]. The subindexes l, m and n in $\mathrm{A}(z,t)$ represent the envelope of the electric field for the modes considered. The $C_{pl}(\omega_0)$ and $Q_{plmn}(\omega_0)$ parameters represent the unidirectional linear coupling coefficient [5] and the unidirectional nonlinear mode coupling coefficient, respectively, at ω_0.

Both $C_{pl}(\omega_0)$ and $Q_{plmn}(\omega_0)$ are defined as overlap integrals over the transverse distribution of the electric field,

$$C_{pl}(\omega_0) = \vartheta_{pl}(\omega_0) = \frac{\omega_0 \varepsilon_0}{2(\beta^{l*}(\omega) - \beta^{p}(\omega))} \int \frac{\mathbf{F}_p(\mathbf{x},\omega_0)\mathbf{F}_l^*(\mathbf{x},\omega_0)}{N_p(\omega_0)N_l(\omega_0)} \frac{\partial n_0^2}{\partial z} d\mathbf{x}\,, \tag{4.15}$$

and

$$Q_{plmn}(\omega_0) = \frac{\varepsilon_0^2 n_0^2 c^2}{12} \int \frac{\left[\mathbf{F}_p^*(\mathbf{x},\omega_0)\cdot\mathbf{F}_l(\mathbf{x},\omega_0)\right]\left[\mathbf{F}_m(\mathbf{x},\omega_0)\cdot\mathbf{F}_n^*(\mathbf{x},\omega_0)\right]}{N_p(\omega_0)N_l(\omega_0)N_n(\omega_0)N_m(\omega_0)} d\mathbf{x}\,, \tag{4.16}$$

where n_0 represents the refractive index at ω_0. The parameter ζ_{pl} reflects the variation of C_{pl} with the frequency,

$$\zeta_{pl} = \frac{1}{\omega_0} + \frac{\partial}{\partial\omega} \ln[C_{pl}(\omega)]\Big|_{\omega_0}\,, \tag{4.17}$$

while the parameter τ_{plmn}, or the so-called shock time constant, reflects the variation of Q_{plmn} with the frequency,

$$\tau_{plmn} = \frac{1}{\omega_0} + \frac{\partial}{\partial\omega} \ln[Q_{plmn}(\omega)]\Big|_{\omega_0}\,. \tag{4.18}$$

In (4.13), the mode dependent propagation losses can be considered by allowing the complex values for the propagation constants. The second term in (4.13) accounts for the linear mode coupling between the considered mode and the remaining modes. The third term is responsible for the nonlinearities. The parameter Q_{plmn} is a measure of the confinement of the p, l, m and n modes inside of the microwire. In this way, the inverse of the Q_{plmn} can be interpreted as an effective area for the four aforementioned modes, and the $\gamma_{plmn} = (\omega_0 n_2/c)Q_{plmn}$ can be understood as the nonlinear coefficient in a multimode waveguide, which takes into account the interaction among the modes p, l, m and n [6].

4.1.1 Multimodal four-wave mixing

In order to describe the FWM process in the multimodal regime, we assume that the input signal consists of four waves: two pump beams (ω_{p_1} and ω_{p_2}), one signal (ω_s) and an idler (ω_i). On a fundamental level, in the FWM process, two photons from the pumps are annihilated and two photons at the signal and idler frequencies are created, respecting the energy conservation,

$$\omega_{p_1} + \omega_{p_2} = \omega_s + \omega_i\,. \tag{4.19}$$

We assume that the input waves are co-polarized, and due to the short microwire length they remain co-polarized along the propagation. We also assume that the microwire length is much shorter than the walk-off length. Therefore, the continuous wave approximations can be introduced, and the field can be written as [3, 7]

$$A(z,t) = A_{p_1}(z)e^{-i\Omega_{p_1}t} + A_{p_2}(z)e^{-i\Omega_{p_2}t} + A_s(z)e^{-i\Omega_s t} + A_i(z)e^{-i\Omega_i t}\,, \tag{4.20}$$

where $A_{p_1}(z)$ and $A_{p_2}(z)$ represent the pump amplitudes, $A_s(z)$ the signal amplitude, $A_i(z)$ the idler amplitude, and $\Omega_{p_1} = \omega_{p_1} - \omega_0$, $\Omega_{p_2} = \omega_{p_2} - \omega_0$, $\Omega_s = \omega_s - \omega_0$, and $\Omega_i = \omega_i - \omega_0$, where ω_0 represents the central frequency. Replacing (4.20) in (4.13), and neglecting the delayed nonlinear response of the fiber, we obtain a set of coupled equations for the amplitudes evolution,

$$\frac{\partial}{\partial z}A_{l,p_1}(z) = i\beta'_l(\omega_{p_1})A_{l,p_1}(z) + \frac{i}{2}\sum_j C_{lj}A_{j,p_1}(z) + i\frac{n_2\omega_0}{c}\Bigg\{Q_{llll}A_{l,p_1}(z)A_{l,p_1}(z)A^*_{l,p_1}(z)+ \sum_{k\neq p_1}\left[2\sum_p Q_{pllp}A_{p,p_1}(z)A_{l,k}(z)A^*_{m,k}(z)\right] + 2\sum_{p,m,n} Q_{lpmn}A_{p,s}(z)A_{m,i}(z)A^*_{n,p_2}(z)\Bigg\}, \quad (4.21a)$$

$$\frac{\partial}{\partial z}A_{l,p_2}(z) = i\beta'_l(\omega_{p_2})A_{l,p_2}(z) + \frac{i}{2}\sum_j C_{lj}A_{j,p_2}(z) + i\frac{n_2\omega_0}{c}\Bigg\{Q_{llll}A_{l,p_2}(z)A_{l,p_2}(z)A^*_{l,p_2}(z)+ \sum_{k\neq p_2}\left[2\sum_p Q_{pllp}A_{l,p_2}(z)A_{p,k}(z)A^*_{l,k}(z)\right] + 2\sum_{p,n,m} Q_{lpmn}A_{p,s}(z)A_{n,i}(z)A^*_{m,p_1}(z)\Bigg\}, \quad (4.21b)$$

$$\frac{\partial}{\partial z}A_{l,s}(z) = i\beta'_l(\omega_s)A_{p,s}(z) + \frac{i}{2}\sum_j C_{lj}A_{l,s}(z) + i\frac{n_2\omega_0}{c}\Bigg\{Q_{llll}A_{l,s}(z)A_{l,s}(z)A^*_{l,s}(z)+ \sum_{k\neq s}\left[2\sum_p Q_{pllp}A_{l,s}(z)A_{p,k}(z)A^*_{p,k}(z)\right] + 2\sum_{p,n,m} Q_{lpmn}A_{p,p_1}(z)A_{n,p_2}(z)A^*_{m,i}(z)\Bigg\}, \quad (4.21c)$$

$$\frac{\partial}{\partial z}A_{l,i}(z) = i\beta'_l(\omega_i)A_{l,i}(z) + \frac{i}{2}\sum_j C_{lj}A_{j,i}(z) + i\frac{n_2\omega_0}{c}\Bigg\{Q_{llll}A_{l,i}(z)A_{l,i}(z)A^*_{l,i}(z)+ \sum_{k\neq i}\left[2\sum_p Q_{pllp}A_{p,s}A_{l,k}(z)(z)A^*_{l,k}(z)\right] + 2\sum_{p,n,m} Q_{lpmn}A_{p,p_1}(z)A_{n,p_2}(z)A^*_{m,s}(z)\Bigg\}. \quad (4.21d)$$

These equations are quite general in the sense that they include the effects of the attenuation, the modal dispersion, the linear and the nonlinear modal coupling, the self-phase modulation (SPM), the cross-phase modulation (XPM), and the pump depletion on the FWM process. For convenience and to make the notation more clear, in equations (4.21) the dispersive term is written as,

$$\beta'_p = \sum_{j=0}^{\infty}\frac{\Omega_u^j(\beta_j^p - \beta_j^0)}{j!} + \frac{i}{2}\alpha_p\,, \quad (4.22)$$

where p represents the mode, $u = p_1, p_2, s$ or i[1], the α_p represent the optical losses for the p mode. The β_n^0 and β_n^p represent the jth order dispersion coefficient for the fundamental mode and the p mode, respectively. The third term in the right hand side of equations (4.21) accounts for the nonlinear effects. This has three contributions: the SPM, the multimodal XPM and the multimodal FWM, respectively. The symmetry rules show that two terms considered in the summations account equally for the process of multimodal XPM, $Q_{pllp} = Q_{plpl}$, and for the process of multimodal FWM process, $Q_{lpmn} = Q_{lmpn}$. Therefore, in (4.21) is considered a factor of 2 in both terms above mentioned.

4.2 Optical microwires

In optical microwires, the high index contrast between the silica core and the air cladding lifts the degeneracy of the LP modes of the weak guiding regime, and therefore the strong

[1]It should be note that the subindex i is related with physical properties of the idler signal, while the symbol i denotes the imaginary unity.

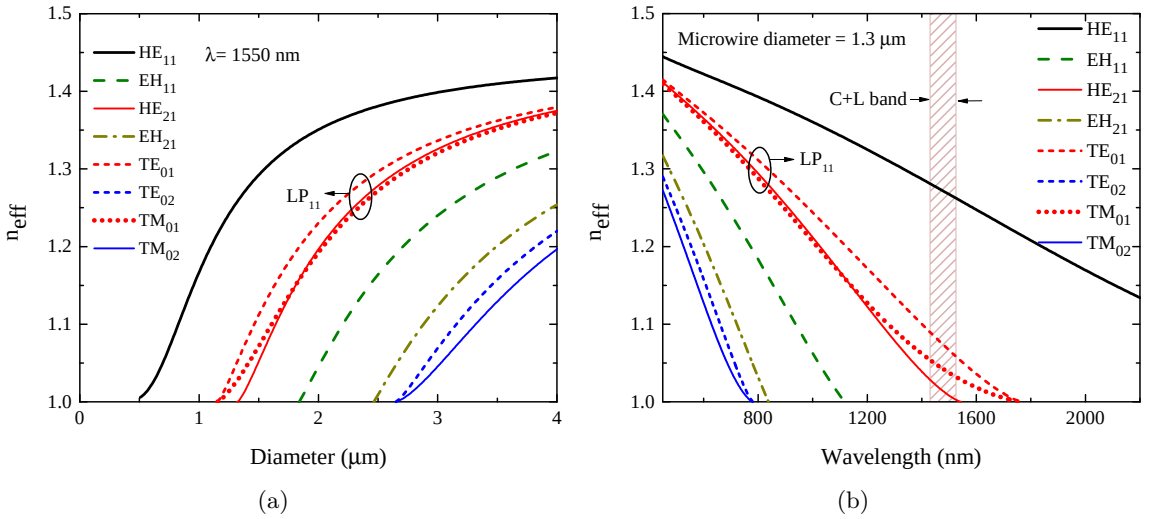

Figure 4.1: (a) Effective index, n_{eff}, as a function of the optical microwire diameter assuming an optical signal at 1550 nm. (b) Effective index as a function of the wavelength for an optical microwire with a diameter of 1.3 μm.

guiding regime must be considered [8, 9]. The effective index for the guided modes can be calculated by solving the Helmholtz equation for a step-index fiber with a silica core and an air cladding [10], in which the refractive index of the silica core is given by the Sellmeier equation as written in (3.17). Without loss of generality, the analyses of the multimodal FWM process is limited to the following vector modes: HE_{11}, EH_{11}, HE_{21}, EH_{21}, TE_{01}, TE_{02}, TM_{01} and TM_{02}.

The effective index as a function of the optical microwire diameter, assuming an optical signal with a wavelength of λ = 1550 nm, is shown in Fig. 4.1(a). While, in Fig. 4.1(b), it is shown the effective index as a function of the wavelength, assuming an optical microwire with a diameter of 1.3 μm. It should be noted that, as the microwire diameter decreases, the evanescent field in the air cladding increases and hence the effective index decreases until it reaches the cutoff-frequency, see Fig. 4.1(a). In the same way, as the wavelength increases, the evanescent field also increases and the effective index decreases until it reaches the cutoff-frequency, see Fig. 4.1(b).

4.2.1 Phase-matching in few-mode microwires

Besides the energy conservation, in the FWM process it is also required the momentum conservation, which is mathematically expressed as the phase-matching condition. Since all four beams propagate in the same direction, the phase-matching condition can be written as [11],

$$\Delta\beta_{plmn} = \Re\{\beta'_l(\omega_{p_1}) + \beta'_m(\omega_{p_2}) - \beta'_n(\omega_i) - \beta'_p(\omega_s)\}\,, \tag{4.23}$$

where $\beta'_i(\omega_j)$ denotes the propagation constant for the i mode at the frequency ω_j. When the phase-matching condition is achieved, i.e., $\Delta\beta_{plmn} = 0$, the FWM process occurs efficiently. As is well known from the single-mode case, in the FWM process the two annihilated photons may have the same frequency $\omega_{p_1} = \omega_{p_2}$, giving rise to the so-called degenerate FWM, or they can have distinct frequencies $\omega_{p_1} \neq \omega_{p_2}$, leading to the commonly called non-degenerate FWM.

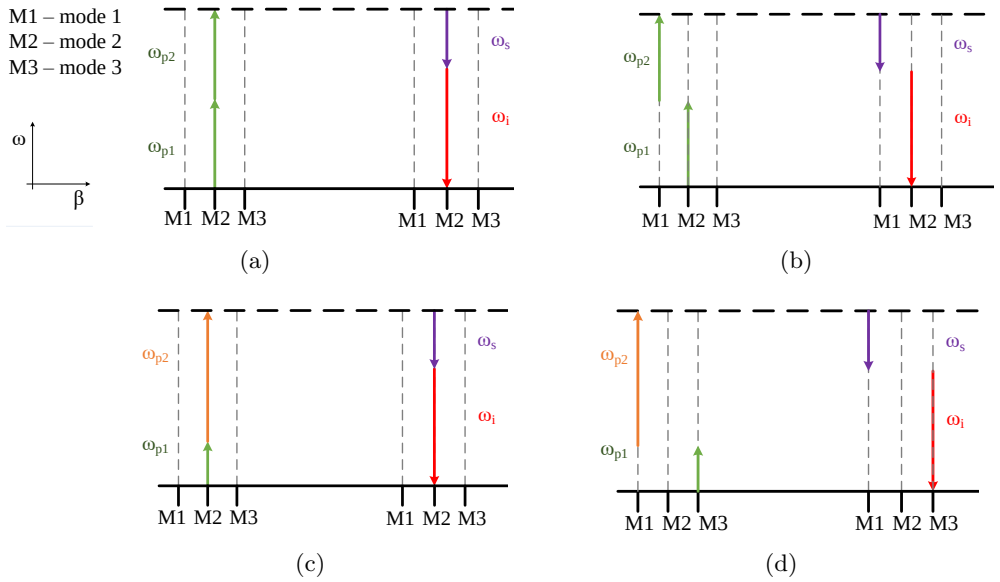

Figure 4.2: Schematic representation of: (a) degenerated intramode FWM, (b) degenerated intermode FWM, (c) nondegenerated intramode FWM and (d) nondegenerated intermode FWM.

In the multimodal regime, however, the phase-matching condition can be achieved among optical beams propagated in the same mode, i.e., the intramode FWM, or among optical beams in different modes, i.e., intermode FWM. These two distinct cases are schematically shown in Fig. 4.2. In Fig. 4.2(a) and 4.2(c), we show a schematic of the degenerate and the non-degenerate FWM process, respectively, in the intramode case, while the degenerate and the non-degenerate process in the intermode case are schematically shown in Fig. 4.2(b) and 4.2(d), respectively.

In the intramode degenerate FWM process, the propagation constants in (4.23) can be expanded in a Taylor series around the zero-dispersion wavelength. After some algebraic manipulations, the intramodal phase-matching condition can be written as,

$$\Delta\beta_m = \frac{2\pi c\lambda_0^m}{\lambda_p^3\lambda_s^2}(\lambda_p - \lambda_0^m)(\lambda_p - \lambda_s)^2 S(\lambda_0^m)\,, \tag{4.24}$$

where λ_0^m is the zero-dispersion wavelength for the m mode, λ_p is the pump wavelength, λ_s is the signal wavelength and $S(\lambda_0^m)$ is the dispersion slope for the m mode at the zero-dispersion wavelength. The phase-matching condition mainly depends on the separation between the zero-dispersion wavelength and the pump wavelength, and in the separation between the pump and the signal wavelengths. It should be noted that the dispersion and the dispersion slope can be tuned by properly choosing the microwire diameter [12] and fine tuned by means of a special cladding produced from material with adjustable refractive indexes, such as termo-optic materials [13]. In that way, the zero-dispersion wavelength and the dispersion slope of the microwire can be properly adjusted as a function of the pump wavelength. If the pump and the zero-dispersion wavelength match, the phase-matching can be easily achieved. In that way, the zero-dispersion wavelength plays a key role in the efficiency of the FWM in the intramode case. In Fig. 4.3, the contour graphics show the dispersion and the zero-dispersion wavelength as a function of the microwire diameter and the wavelength

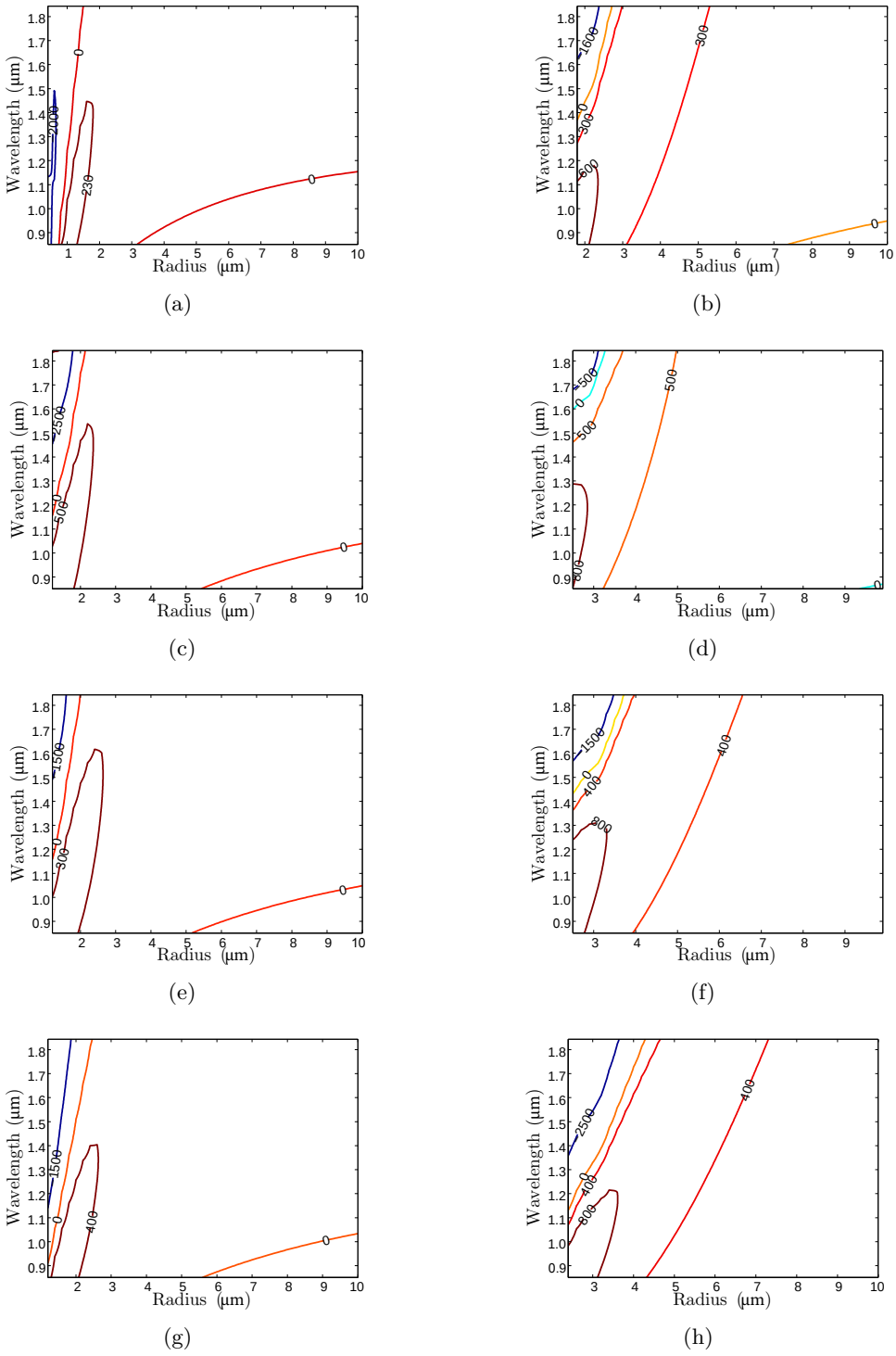

Figure 4.3: Dispersion maps for a silica microwire surrounded by an air cladding for the following modes a) HE_{11}, b) EH_{11}, c) HE_{21}, d) EH_{21}, e) TE_{01}, f) TE_{02}, g) TM_{01} and h) TM_{02}. The maps were calculated ranging the wavelengths from 800 to 1800 nm and the radius from the mode cutoff-frequency to 10 μm. The dispersion values pointed out are in ps/nm/km.

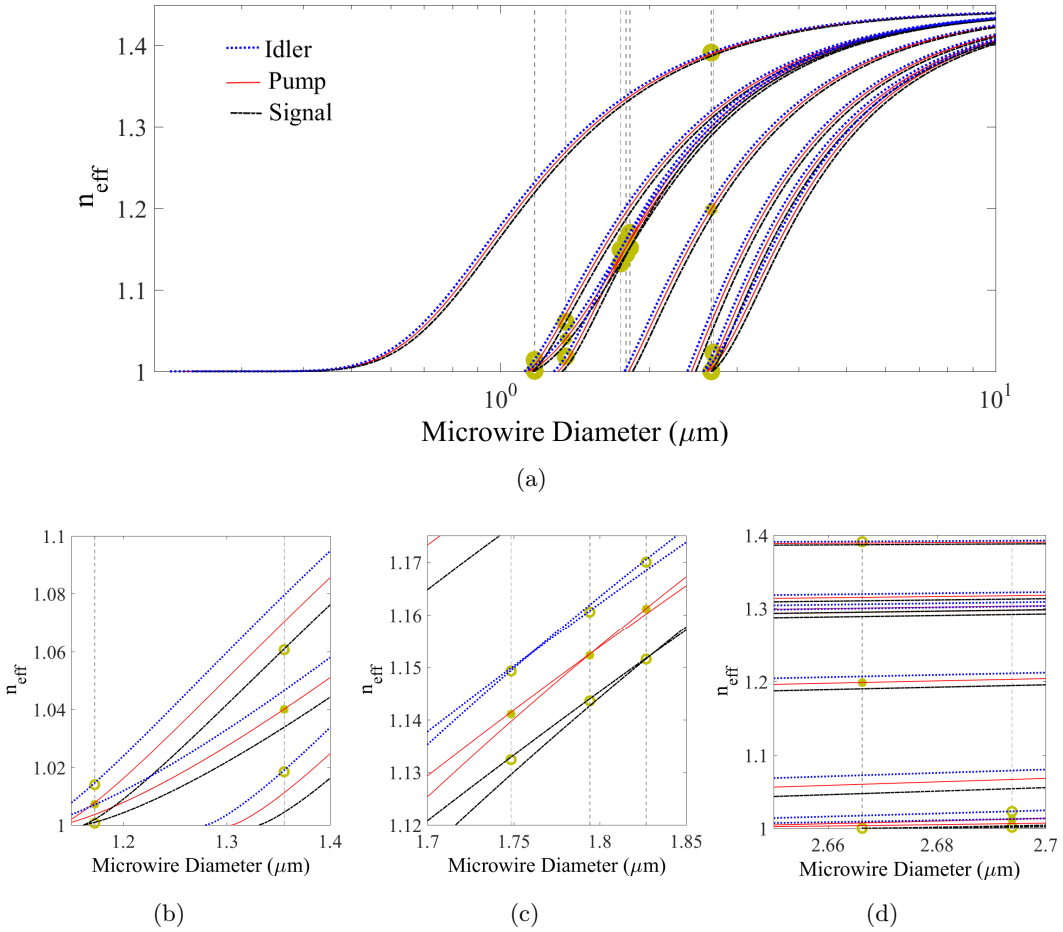

Figure 4.4: a) Effective index as a function of the microwire diameter for a pump beam at 1550 nm (solid line), signal at 1580 (dot line), and an idler beam at 1521 nm (dotted-dashed line). The intermodal phase-matching condition is achieved at the signalized microwire diameter by a vertical dashed line, in which the idler and signal modes are marked by a circle and the pump mode is marked by a star ("$*$"). b) c) and d) Zoom-in of the region in which the intermodal phase-matching condition is achieved.

separation between the pump and the signal for the modes considered in Fig. 4.1. The wavelengths are ranging from 800 to 1800 nm and the microwire diameter is changed from the cutoff-frequency up to 10 μm. In Fig. 4.3(a), it is shown the dispersion map for the fundamental mode, where two different regions with zero-dispersion can be found. However, when considering the telecommunications window, the zero-dispersion wavelength can only be achieved for a microwire diameter of 1.22 μm. The dispersion maps for the three degenerate modes from LP_{11} mode in weak guiding regime, i.e., HE_{21}, TE_{01} and TM_{01}, are shown in Fig. 4.3(c), 4.3(e) and 4.3(g), respectively. In this case, two zero-dispersion regions can be also identified. However, at the telecommunications window, the zero-dispersion wavelength is only achieved for microwire radius around 1.8 μm for the HE_{21} mode, 1.7 μm for the TE_{01} mode and 2.1 μm for the TE_{01} mode. In Fig. 4.3(b), we show the dispersion map for the EH_{11}. For this mode, the zero-dispersion wavelength at the telecommunication window is reached for a microwire diameter of 2 μm. Lastly, the dispersion map for the EH_{21}, TE_{02}

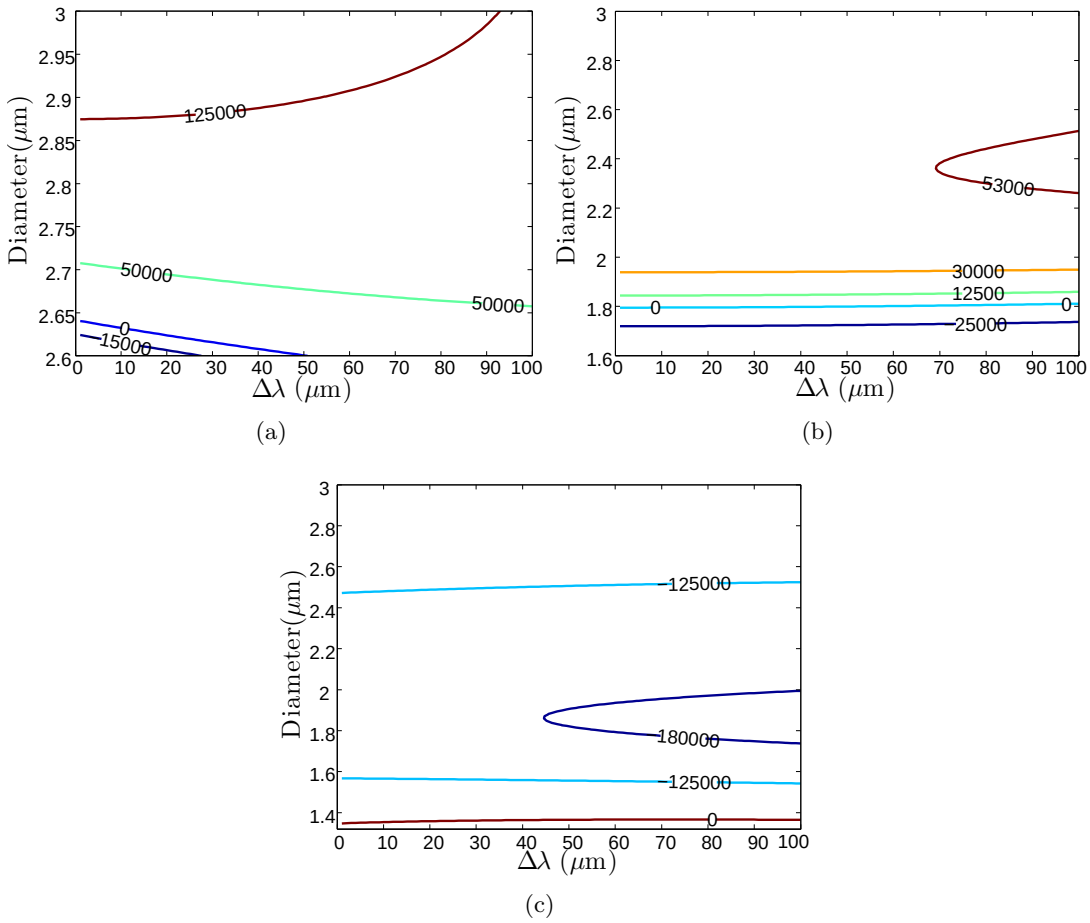

Figure 4.5: Phase-matching map as function of the microwire diameter and the separation between the pump wavelength and the signal wavelength, $\Delta\beta$, in which the diameter is ranging from the mode cutoff-frequency to 3 μm and the $\Delta\lambda$ is ranged from 0 to 100 nm, for the following configurations: a) The pump is considered at TM_{01} and the signal and idler at EH_{21}; b) The pump is considered at TM_{01}, the signal at TE_{01} and the idler at EH_{21}; c) the pump, signal and idler are launched in the fundamental mode, EH_{11} and TE_{02}, respectively. Note that the values pointed in the figures are in m^{-1}.

and TM_{02}, the three degenerated modes from the LP_{12} mode in the weak guiding regime, are displayed in Fig. 4.3(d), 4.3(f) and 4.3(h), respectively. The zero-dispersion wavelength is achieved at diameters of 2.5 μm, 3.1 μm and 3.7 μm for the EH_{21}, TE_{02} and TM_{02} modes, respectively. Notice that for these LP family modes only the EH_{21} mode shows two distinct zero-dispersion regions.

In the intermodal degenerate FWM process, the phase-matching is directly calculated by considering the respective propagation constants in (4.23). In Fig. 4.4(a), it is shown the refractive index as a function of the microwire diameter for a pump beam with a wavelength of 1550 nm (solid line), a signal beam at 1580 nm (dot line) and a idler beam at 1521 nm (dot-dash line). The intermodal phase-matching condition is achieved at several diameters pointed out by a vertical dashed line. The idler and signal modes are marked by a circle and the pump modes are signalized by a star ("$*$"). The eight modes considered in this analysis

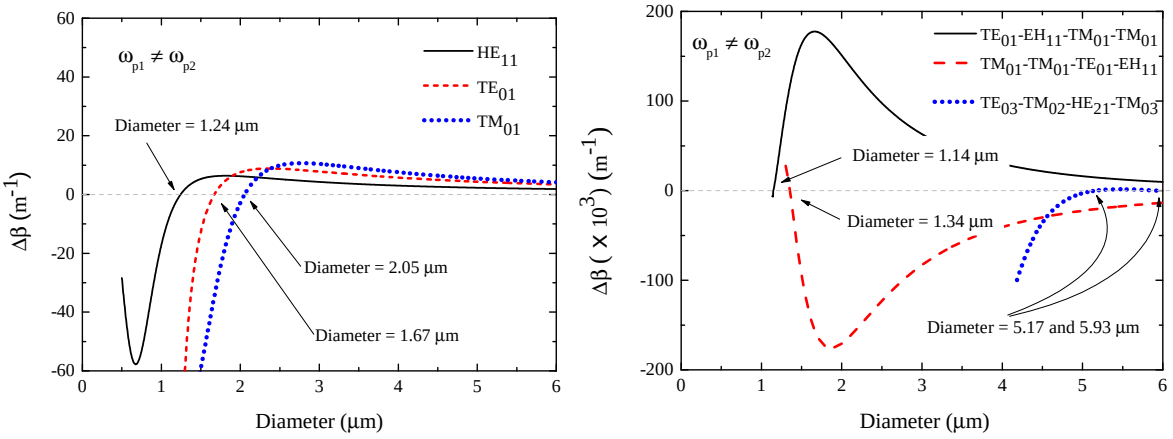

Figure 4.6: Phase-matching for the nondegenerated FWM as a function of the microwire diameter. In Fig. 4.6 a) the intramodal phase-matching for the fundamental mode is represented for λ_{p1}=1545 nm, λ_{p2}=1555 nm, λ_s=1540 nm and λ_i=1560 nm. In Fig. 4.6 b) the intermodal phase-matching is represented for the same wavelengths. The order of the modes in the legend corresponds to the two pumps (λ_{p1} and λ_{p2}), the signal (λ_s) and the idler (λ_s), respectively.

give rise to 512 different combinations. However, the phase-matching is achieved only for 18 different combinations, and only 8 of these respect the symmetry rules. In Fig. 4.4(b), 4.4(c) and 4.4(d), it is shown the zoom-in for the regions where the phase-matching occurs. Notice that the phase-matching is preferentially achieved between vector modes that form a LP family in the weak guiding regime, see for instance Fig. 4.4(b) and 4.4(c).

Here, we analyse the variation of phase-matching as a function of the separation between the pump and the signal wavelengths and the diameter of the microwire. The pump is assumed at 1550 nm and the difference between the signal and the pump wavelength, $\Delta\lambda$, is ranging from 0 to 100 nm. While, the microwire diameter is ranging from the largest cutoff-frequency of the considered modes up to 3 μm because the intermodal phase-matching condition is typically reached in the aforementioned range, see Fig. 4.4(a). In Fig. 4.5(a) and 4.5(b) are shown two different possible configurations for the set of modes HE_{21}, TE_{01} and TM_{01}, from the LP_{11} family in the weak guiding regime. Figure 4.5(a) shows the phase-matching map as a function of the microwire diameter and the $\Delta\lambda$ considering the pump in the TM_{01} mode and the signal and idler in the EH_{21} mode, in which the phase-matching condition is reached for a diameter around 2.6 μm. Here, the pump beam and the signal and idler beams are propagated in vector modes from the same LP families. Figure 4.5(b) shows the phase-matching map for the pump launched in the TM_{01}, the signal in the TE_{01} and the idler in the EH_{21}. In this case, the phase-matching condition is reached for a microwire diameter of 1.8 μm. Notice that the three optical signals are propagated in distinct vector modes from the same LP family. The phase-matching can also be achieved among three beams in different spatial modes that cannot be grouped in any set of LP family. In Fig. 4.5(c), the phase-matching is achieved for a microwire radius of 1.35 μm, with the signal beam at the fundamental mode, the pump beam at the EH_{11} and the idler beam at the TE_{02}. It should be emphasized that in Fig. 4.5(a) and 4.5(b) the considered modes are from the same LP family in the weak guiding regime and therefore the phase-matching changes slower than in Fig. 4.5(c).

The phase-matching condition for the non-degenerated FWM process in the intramode and intermode cases was also investigated. We assume two pump beams at 1545 nm and 1555 nm, the signal beam at 1540 nm and the idler beam at 1560 nm. In Fig. 4.6(a), the intramodal phase-matching is displayed for the fundamental mode, the TE_{01} and the TM_{01}. In Fig. 4.6(b), the intermodal phase-matching is displayed for several sets of modes as a function of the microwire diameter. For high order modes, the phase-matching condition can be reached more than one time for some set of modes. For instance, for the signal beam in the mode TE_{03}, the first and second pump beams in TM_{02} and in HE_{21}, and the idler beams in the TM_{03} the phase-matching is achieved at the radius of 5 and 6 μm. Around $\Delta\beta = 0$, the phase-matching tends to change faster in the intermodal FWM, see Fig. 4.6(b), than in the intramodal FWM, see Fig. 4.6(a). Consequently, the bandwidth of the intramodal FWM tends to be larger than in the intermodal FWM process.

4.2.2 Linear and nonlinear coupling coefficients in microwires

The linear, C_{pl}, and the nonlinear, Q_{plmn}, coupling coefficients are the two remaining parameters that must be considered in the multimodal NLSE to fully describe the FWM process. The linear mode coupling leads to the energy transfer between different modes with the same frequency. This energy transfer may change the energy available in each mode, and consequently the nonlinear process. In order to make a more realistic model of the signal propagation in few-mode microwires, the surface roughness of the microwire should be considered. We assume a small periodic perturbation in the microwire radius,

$$r_c(z) = \bar{r_c} + \delta r_c \sin(az), \tag{4.25}$$

where $\bar{r_c}$ represents the average microwire radius, δr_c represents the amplitude of the perturbation and a the frequency of the perturbation. The periodic perturbation in the microwire radius leads to a periodic perturbation of the effective refractive index, which can be written as [4]

$$n_{\text{eff}}(z) = \bar{n}_{\text{eff}} + \delta n_{\text{eff}} \sin(az), \tag{4.26}$$

where $\bar{n}_{\text{eff}}$ represents the effective index for $\bar{r_c}$ and δn_{eff} represents the amplitude of the index perturbation. A periodic perturbation of $\delta r_c = 10$ nm is reported in [14]. In this numerical analyses, we assume a $\delta r_c = 4$ nm inducing a particular index variation for each mode. For instance, the index variation in the first mode, HE_{11}, takes the value of $\delta n_{\text{HE}_{11}} = 1\times10^{-3}$, while for the TE_{01} and TM_{01} modes the index variation are around $\delta n_{\text{TE}_{01}} = 1.3\times10^{-3}$ and $\delta n_{\text{TM}_{01}} = 7.1\times10^{-4}$, respectively. For small perturbations, the coupling coefficient given by (4.15) can be rewritten as

$$C_{pl}(\omega_0) = \frac{\omega_0\varepsilon_0}{2(\beta^{l*}(\omega_0) - \beta^{p}(\omega_0))}\frac{\partial n_0^2}{\partial z}\int \frac{\mathbf{F}_p(\mathbf{x},\omega_0)\mathbf{F}_l^*(\mathbf{x},\omega_0)}{N_p(\omega_0)N_l(\omega_0)}d\mathbf{x}, \tag{4.27}$$

where we assume that the transverse distribution of the electric field remains invariable despite the index perturbation. Therefore, the factor $\partial n_0^2/\partial z$ can be removed from the integration over x and y domain. In Fig. 4.7(a), it is shown the mode coupling coefficient normalized by the index perturbation,

$$\Gamma_{lm} = C_{pl}\left(\frac{\partial n_0^2(z)}{\partial z}\right)^{-1}, \tag{4.28}$$

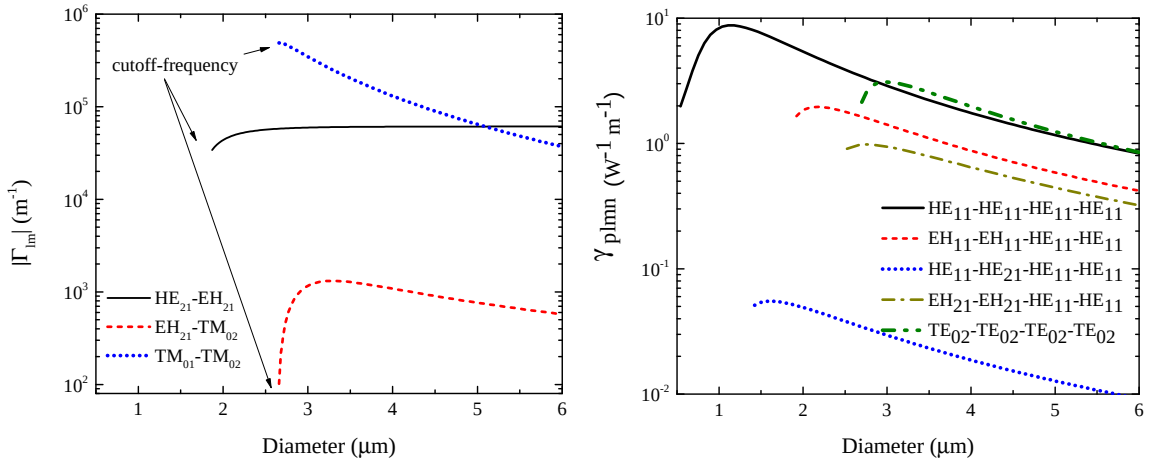

Figure 4.7: a) Linear modal coupling coefficient between several modes as a function of the microwire diameter at the wavelength $\lambda = 1550$ nm. b) Nonlinear multimodal parameter, γ_{plmn}, for several modes at λ=1550 nm.

as a function of the microwire diameter for a signal with a wavelength of 1550 nm. The value of the normalized mode coupling coefficient tends to decrease near the cutoff-frequency, due to the increase of the evanescent field.

The nonlinear coupling coefficient depends on the symmetry of the modes considered in the nonlinear interaction; the overlap integral defined in (4.16) only assumes non-null values for the combination of modes that respect the following rule, $m_p - m_l - m_m + m_n = 0$ [6]. The γ_{plmn} parameter reflects the efficiency of the intermodal nonlinear energy transfer, and it changes several orders of magnitude as function of the considered modes. In Fig. 4.7(b), we display the γ_{plmn} parameter for several modes assuming an optical signal with a wavelength of $\lambda = 1550$ nm. When the diameter decreases, the parameter γ_{plmn} tends to increase because the optical modes tend to be more and more confined inside the microwire. Before achieving the cutoff-frequency, however, the γ_{plmn} decreases slightly because the evanescent field increases tremendously. It should be emphasised that in the calculations of τ_{plmn}, or in (4.16), the evanescent field outside of the microwire is neglected because the nonlinear refractive index of the air is much lower than in the silica.

4.2.3 Energy transfer induced by multimodal FWM

In order to investigate the multimodal FWM process in the presence of the mode coupling, (4.21) are numerically solved for a silica microwire with a length of 50 mm, a nonlinear refractive index of $n_2 = 2.7 \times 10^{-20}$ [3], and a diameter of 1.2 μm with a small periodic perturbation, as described in (4.26), where $\delta r = 4$ nm and $a = 3000$ m^{-1}. The analysis is performed around the central wavelength of 1550 nm. In the phase-matching condition, the third-order dispersion coefficients are considered for the four optical beams. At the microfiber input, we assume the two pump beams at $\lambda_{p_1} = 1546$ nm and $\lambda_{p_2} = 1554$ nm, the signal beam at $\lambda_s = 1540$ nm and the idler beam at $\lambda_i = 1560$ nm. In terms of spatial channels, we consider the first three low order modes HE_{11}, TE_{01} and TM_{01}. Note that the mode HE_{21} is a non-guided

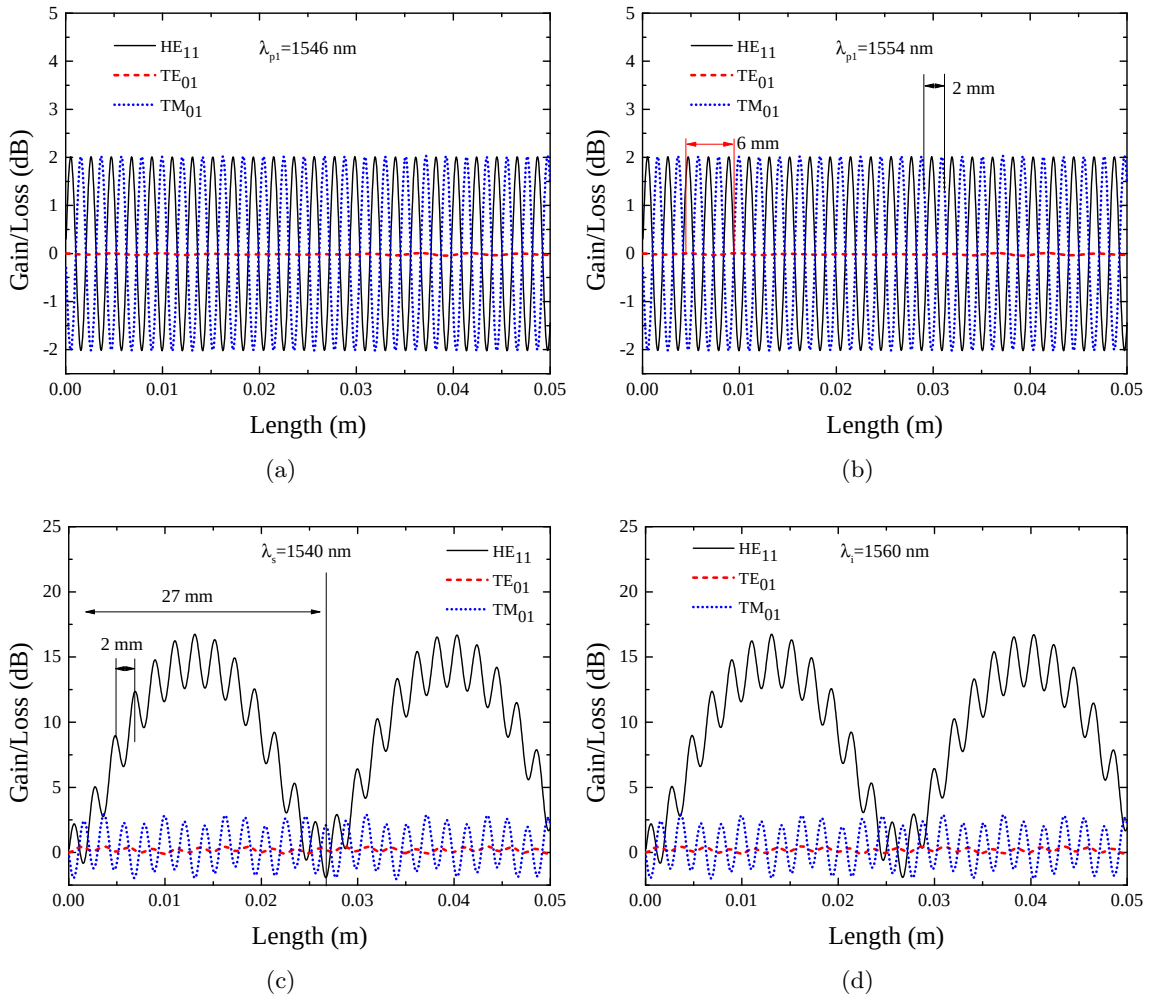

Figure 4.8: Gain/Losses as a function of the microwire length for the three modes considered, HE_{11}, TE_{01}, TM_{01}, for the signal beam. The gain/losses for the two pump beams, at λ_{p_1} = 1546 nm and λ_{p_2} = 1554 nm, are shown in a) and b), respectively, while, the signal, λ_s = 1540 nm, and the idler, λ_i = 1560 nm, beam are shown in c) and d), respectively.

mode for the microwire diameter considered; therefore, such mode is not taken into account in the numerical analysis. In order to solve (4.21), we assumed that the two pumps are launched into the microwire with incident power of 5 W in the fundamental mode ($P_{HE_{11}} = 5$ W) and 1 mW for the other modes considered ($P_{TE_{01}} = P_{TM_{01}} = 1$ mW). The powers of the signal and the idler are 1 mW in all modes considered ($P_{HE_{11}} = P_{TE_{01}} = P_{TM_{01}} = 1$ mW).

Assuming the above described microwire, the phase-matching condition is only achieved among the four beams propagated in the fundamental mode, see Fig. 4.6(a). Hence, the FWM process leads to a periodic energy transference from the fundamental mode of the two pump beams to the fundamental mode of the signal and the idler beams. In Fig. 4.8(a), it is shown the gains/losses for the two pumps, the signal and the idler beams as a function of the microwire length. In the fundamental mode, the energy transfer from the pumps to the signal and idler beams via FWM gives rise to a beating with length of ≈ 27 mm. In Figs. 4.8(a)

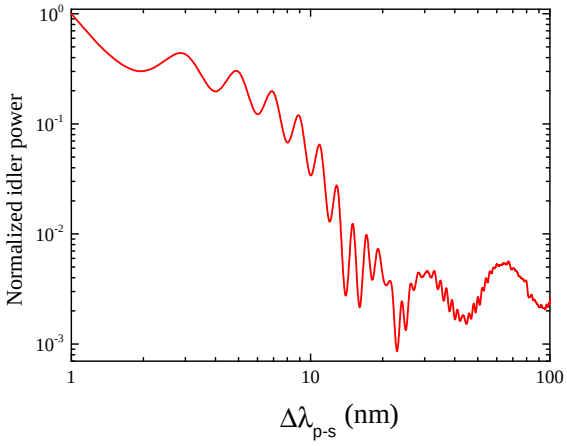

Figure 4.9: The efficiency curve for the FWM process as function of the wavelength separation between pump and idler.

and 4.8(b) the two pumps show an energy transfer via linear mode coupling for the two other modes, with beat lengths of ≈ 2 mm and ≈ 6 mm for the coupling between HE_{11} - TM_{01} and HE_{11} - TE_{01}, respectively. At the signal and idler beams, the gain for the TM_{01} and the TE_{01} modes is much smaller than the one observed for HE_{11}. The linear mode coupling induces the energy transfer between the TM_{01} and HE_{11}, and the TE_{01} and HE_{11} modes gives rise to the oscillatory power exchange between modes. At the end of the microwire, the optical power for the signal beam in the mode HE_{11} is analysed as a function of the wavelength separation between the pump and the signal beams, i.e. the efficiency of the FWM process as a function of the pump-signal spacing, see Fig. 4.9. The optical power transferred from the pump to the idler/signal beam tends to decrease with the separation between the pump and the signal, following the well known sinc-squared function. However, the mode coupling coefficient changes with the wavelength, in that way the optical power available in the HE_{11} mode also changes as a function of the wavelength. Therefore, the mode coupling leads to a energy oscillation at the signal and idler wavelengths giving rise to an additional beating in the FWM efficiency transfer function, which modifies the ideal sinc-squared function.

4.3 Summary

The multimodal generalized NLSE was extended to take into account the linear mode coupling. Based on the theoretical formalism developed, the role of the linear and nonlinear mode coupling in the signal propagation was discussed. We focused on the analysis of the multimode FWM process; the coupled equations that describe such phenomena were derived. After, we analyse the FWM process in optical microwire, a multimodal and highly nonlinear waveguide. In optical microwires, the propagation constant strongly depends on the microwire diameter due to the high-index contrast between the core and cladding. Therefore, the microwire diameter can be used as an adjustable degree of freedom to ensure that phase-matching condition is reached. The intramode and the intermode phase-matching conditions were analyzed. We note that the intramodal FWM tends to have a larger bandwidth than the intermodal FWM process.

During propagation, the gain and the loss of the signal and the idler present two different

beats, the first characteristic of the modal coupling, and the second beat comes from the oscillatory power exchange due to FWM process. The modal coupling allows the energy transfer between different modes at the same frequency. On the other hand, the FWM process allows the energy transference between different wavelengths for different modes, i.e., the intermodal FWM, or the same mode propagation, i.e., the intramodal FWM.

Bibliography

[1] F. Ferreira, S. Jansen, P. Monteiro, and H. Silva, "Nonlinear semi-analytical model for simulation of few-mode fiber transmission," *IEEE Photonics Technology Letters*, vol. 24, no. 4, pp. 240–242, Feb 2012.

[2] M. Kolesik and J. Moloney, "Nonlinear optical pulse propagation simulation: From Maxwell's to unidirectional equations," *Physical Review E*, vol. 70, no. 11, p. 036604, Sep 2004.

[3] G. P. Agrawal, *Nonlinear Fiber Optics*. Academic Press, 2001.

[4] D. Marcuse, *Theory of dielectric optical waveguides*. New York, Academic Press, 1974.

[5] E. Khoo, A. Liu, X. Zhang, E. Li, J. Li, D. Pinjala, and B. Luk'yanchuk, "Exact step-coupling theory for mode-coupling behavior in geometrical variation photonic crystal waveguides," *Physical Review B*, vol. 80, p. 035101, Jul 2009.

[6] F. Poletti and P. Horak, "Description of ultrashort pulse propagation in multimode optical fibers," *Journal of the Optical Society of America B*, vol. 25, no. 10, pp. 1645–1654, Oct 2008.

[7] N. A. Silva, N. J. Muga, and A. N. Pinto, "Effective nonlinear parameter measurement using FWM in optical fibers in a low power regime," *IEEE Journal of Quantum Electronics*, vol. 46, no. 3, pp. 285 –291, 2010.

[8] R. Zhang, X. Zhang, D. Meiser, and H. Giessen, "Mode and group velocity dispersion evolution in the tapered region of a single-mode tapered fiber," *Optics Express*, vol. 12, no. 24, pp. 5840–5849, 2004.

[9] U. Wiedemann, K. Karapetyan, C. Dan, D. Pritzkau, W. Alt, S. Irsen, and D. Meschede, "Measurement of submicrometre diameters of tapered optical fibres using harmonic generation," *Optics Express*, vol. 18, no. 8, pp. 7693–7704, 2010.

[10] A. Snyder and J. Love, *Optical Waveguide Theory*. Chapman and Hall, 1991.

[11] R. Stolen, J. Bjorkholm, and A. Ashkin, "Phase-matched three-wave mixing in silica fiber optical waveguides," *Applied Physics Letters*, vol. 24, no. 7, pp. 308–310, 1974.

[12] I. Rand, L. Timothy, D. Ming, B. Mohammed, and B. Gilberto, "Optical microfiber passive components," *Laser & Photonics Reviews*, vol. 7, no. 3, pp. 350–384.

[13] M. Niehus, G. M. Fernandes, and A. N. Pinto, "Dispersion engineered high index contrast silica microfibers," in *IEEE - International Conference on Computer as a Tool (EUROCON)*, April 2011, pp. 1–4.

[14] G. Brambilla, V. Finazzi, and D. Richardson, "Ultra-low-loss optical fiber nanotapers," *Optics Express*, vol. 12, no. 10, pp. 2258–2263, May 2004.

Chapter 5

HoPs-based space-demultiplexing

Crosstalk arises as the main performance limiting factor in SDM transmission systems without spatial selectivity and therefore it must be compensated by digital or optical techniques at the receiver side. As happens in current commercial transmission systems, in SDM systems the space-demultiplexing in the digital domain has been preferred due to their flexibility and fast adaptation. However, the large number of tributaries that needed to be post-processed tends to substantially increase the computational complexity of the DSP at the optical coherent receiver. In that way, space-demultiplexing algorithms for future flexible SDM-based networks should have tolerable computational complexity and, additionally, they should also be free of training sequences and modulation format agonistic, giving an unprecedent flexibility to the optical network. Nevertheless, the development of such kind of algorithms is still in a very early stage.

In this chapter, we introduce the signal representation in HoPss. Then, we discuss the intrinsic connection between the HoPss and the GSS. Based on the signal representation in HoPss, we develop space-demultiplexing algorithms. It should be emphasized that these algorithms are modulation format agnostic, free of training sequences and tend to be robust against phase fluctuations and frequency offsets. Firstly, we demonstrate the operation principle behind the space-demultiplexing based on HoPss. Secondly, we propose a reduced-complexity space-demultiplexing algorithm with faster convergence speed.

5.1 Digital space-demultiplexing

SDM allows to transmit several parallel data streams through a single fiber using orthogonal modes of a FMF/CC-MCF or multiple cores in a MCF [1]. For both approaches, the optical signals may suffer from crosstalk like the two quasi-degenerated modes in standard SMF [2, 3]. Therefore, and analogously to the single-mode case, this pernicious effect must be equalized at the optical coherent receiver using advanced digital space-demultiplexing techniques [1, 2].

In a broad sense, the concept of spatial diversity is a generalization of the widely used concept of polarization diversity [1]. In SSMF-based transmission systems with PDM, both orthogonal polarization states are employed to transmit two independent tributary signals at the same wavelength [3]. However, the propagation through the fiber rotates the polarization states, which is usually compensated in the digital domain by polarization-demultiplexing algorithms based on MIMO algorithms [3]. The constant modulus algorithm (CMA) is one

of the most popular polarization de-multiplexing (PolDemux) algorithms due to its simplicity and robustness [3]. However, this algorithm is modulation format dependent, which may represent a major problem in some flexible networks where the baud rate and the modulation format of the signals are dynamically defined by software. Moreover, it also has a moderate convergence speed and a singularity problem [4]. An alternative PolDemux algorithm based on Stokes space was proposed to overcome the singularity problem improving at the same time the convergence speed [5]. This algorithm is also robust against the residual frequency offset [5, 6]. In the Stokes space based PolDemux algorithm the demultiplexing matrix is defined using the spatial orientation of the best fit plane to the received samples in the Stokes space [4, 5, 7–9].

5.2 Signal representation on higher-order Poincaré spheres

The GSS was proposed as a D-dimensional representation, with $D = 4n^2 - 1$ where n denotes the number of spatial channels, of the multimodal signal with similar properties to their counterpart in the single-mode case, i.e., the Stokes space. However, this D-dimensional space is not suitable to geometrically represent the multimodal signal, emerging in that sense another alternative signal representations, the so-called HoPss. The HoPss are defined as a full set of geometric representations of a given vector space where a pair of orthogonal states is represented in a single HoPs, likewise the Bloch or the Poincaré spheres [10]. Initially, it was introduced to represent light carrying OAM by incorporating in the basis, both polarization and OAM states [11, 12]. In [11], the Jones circular polarization basis is rewritten by replacing the set of two orthogonal polarization states by two orthogonal vector modes. In [12], a signal with two distinct spatial modes and two polarizations is described in terms of a hybrid spatio-polarization representation, in which the polarization and space are simultaneously considered in the two spheres. Lastly, a method to determine the principal modes of a FMF was proposed by expanding the mode dispersion operator from the GSS to the HoPss [13].

5.2.1 Generalized Stokes space

Henceforward, the Dirac notation is employed to represent the signal in the Jones space, $|\psi\rangle$ [14]. Since all the tributary signals are coupled, $|\psi\rangle$ allows to describe a signal transmitted through a SDM-based transmission system without spacial diversity. In the following sections, and without loss of generality, it is assumed a SDM system supporting n spatial channels in which a single channel comprises two orthogonal polarization states. In the Jones space, the electrical field vector of a given multimodal signal can be represented as a $2n$ dimensional complex ket vector [1]

$$|\psi\rangle = \left(\upsilon_x^1, \upsilon_y^1, ...\upsilon_x^n, \upsilon_y^n\right)^T , \tag{5.1}$$

where υ_l^j, with $j = 1, 2...n$ and $l = x, y$, represents the electrical field of a tributary signal multiplexed in the j mode and in the l polarization state, and T means transpose. This signal can be rewritten as

$$|\psi\rangle = \left(\upsilon_1, \upsilon_2, ...\upsilon_h, ...\upsilon_{2n}\right)^T , \tag{5.2}$$

being υ_i the electric field of the i tributary signal, with $i = 1...2n$, and

$$\upsilon(z,t)_i = A_i(z,t)e^{[-i(\omega t + \phi_i(z,t))]} , \tag{5.3}$$

where t is the temporal coordinate, z is the longitudinal coordinate, ω is the angular frequency of the carrier, $A(z,t)$ is the envelope amplitude and $\phi(z,t)$ is the phase. In (5.3), the transverse distributions of the electric field, which account to the intensity of linear and nonlinear crosstalk, is not considered because in the propagation model is only assumed linear propagation effects in which the linear crosstalk strongly mixes all the tributaries. Notice that the phase noise and the carrier frequency offsets can be considered in ϕ as a perturbation. We would like to stress that it is more convenient to write the electrical field vector in the form 5.2. This choice will become clear in the course of this analysis.

The optical signal can be represented in the GSS by using a particular set of generalized Pauli matrices, $\boldsymbol{\Lambda}_i$, where $i = 1, 2 \ldots D$, chosen to facilitate the interpretation of the signal in this space [15]. These D matrices can be grouped in three different subsets, and are generated as follows:

(a) the first subset contains $3n$ matrices which can be sequentially written as the three Pauli matrices in the main diagonal, from the leftmost to the rightmost, and normalized by $\sqrt{n}$, while the other elements are set to zero;

(b) the second subset, with $4n^2 - 4n$ matrices, is written by considering the elements outside of the 2×2 blocks in the main diagonal and sequentially set to either 1 or $i = \sqrt{-1}$ and the symmetric element to 1 or $-i$, respectively. The remaining elements are set to zero and the normalization coefficient $\sqrt{n}$ is again required;

(c) the third subset contains $n-1$ matrices that are generated by writing as a 2×2 blocks in the main diagonal. The first n_l diagonal elements, with $n_l = 1, 2 \ldots n-1$, are set to a 2×2 unitary matrix, $\boldsymbol{\sigma_0}$, and the $(n_l + 1)$ 2×2 diagonal elements are set to $-n_l \boldsymbol{\sigma_0}$. The remaining elements are set to zero and, in this case, the normalization coefficient is $\sqrt{n/(n_l^2 + n_l)}$.

In the GSS, the signal $|\psi\rangle$ is written as a D-length real vector [15]

$$\boldsymbol{\Psi} = (\Psi_1, \Psi_2, ..., \Psi_D)^T \ , \tag{5.4}$$

where the Stokes parameters, Ψ_i, can be calculated as

$$\Psi_i = \langle \psi | \, \boldsymbol{\Lambda}_i \, | \psi \rangle \ . \tag{5.5}$$

The above subsets of matrices described in points (a), (b) and (c) show how the generalized Pauli matrices, i.e., the generators of the GSS, can be obtained. In the next subsections, these subsets are called to properly explain the decomposition of the GSS in several 3-dimensional subspaces, i.e., HoPs. The HoPs-based signal representation allows to represent all the possible combinations of pairs of signals; including pairs of signals from the same mode, i.e., the intramode case, and the pairs of signals from distinct modes, i.e., intermode case.

5.2.2 Definition of HoPs

The generalized Pauli matrices, $\boldsymbol{\Lambda}_i$, can be also used to define the structure of a Lie algebra of a special unitary group of dimensionality $2n$, SU($2n$) [13]. Therefore, the mode dispersion and the crosstalk operator can be expanded by the generators of a Lie algebra of SU($2n$). Special unitary groups with dimensionality larger than 2 are semi-simple and,

hence, can be decomposed in $g_s = \binom{2n}{2} = n(2n-1)$ subgroups of SU(2) [13]. The structure of the Lie algebra of each subgroup SU(2) has an isomorphism in SO(3), i.e., a given pair of tributary signals in the Jones space, SU(2), can be represented in a HoPs, SO(3). Using a semi-simple representation of the GSS, it can be decomposed in g_s subspaces. These g_s subspaces or HoPss provide a hybrid spatio-polarization description which allows to represent simultaneously the polarization and the space. In each subspace, the relative state between two arbitrary tributaries can be represented by the respective Stokes vectors,

$$\mathbf{\Psi}^{(f,g)} = \left(\Psi_1^{(f,g)}, \Psi_2^{(f,g)}, \Psi_3^{(f,g)}\right)^T , \tag{5.6}$$

where $\Psi_1^{(f,g)}$, $\Psi_2^{(f,g)}$ and $\Psi_3^{(f,g)}$ are the Stokes parameters.

In (5.6), the superscript indices, g and f, indicate two arbitrary tributary signals, υ_f and υ_g, selected from the signal $|\psi\rangle$ considered in (5.2). Each Stokes parameter represented in (5.6) can be obtained from $|\psi\rangle$ as follows [11],

$$\Psi_1^{(f,g)} = |\langle e_f|\psi\rangle|^2 - |\langle e_g|\psi\rangle|^2 , \tag{5.7a}$$

$$\Psi_2^{(f,g)} = 2\mathrm{Re}(\langle e_f|\psi\rangle^* \langle e_g|\psi\rangle) , \tag{5.7b}$$

$$\Psi_3^{(f,g)} = 2\mathrm{Im}(\langle e_f|\psi\rangle^* \langle e_g|\psi\rangle) , \tag{5.7c}$$

being $\langle e_h|$, with $h = f, g$, the complex conjugated of $|e_h\rangle$. The vector $|e_h\rangle$ defines the basis of the HoPs and, therefore such spheres can be used to describe signals transmitted over MCF or FMF considering LP, OAM or vector modes [16, 17]. For more details, the reader can see in section 5.2.4 the calculation of the Stokes parameters for the particular case of two spatial channels.

In order to realize the physical meaning of the Stokes parameters pointed out in Eq. (5.7), one considers that a given signal is made to pass through a mode filter system (to select only the signals υ_f and υ_g) followed by a polarizer. The parameter $\Psi_1^{(f,g)}$ describes the difference between the emerging powers obtained when the υ_f and υ_g signals are made to pass through a linear polarizer aligned at 0^o and a linear polarizer aligned at 90°, respectively. It gives the preponderance of linear horizontal light over linear vertical light. The parameter $\Psi_2^{(f,g)}$ describes the difference between the emerging powers obtained when the signals υ_g and υ_f are made to pass through a linear polarizer aligned at an angle of 45° and a linear polarizer aligned at an angle of -45°, respectively, i.e., it gives the preponderance of 45° linear polarized light over -45° linear polarized light. The parameter $\Psi_3^{(f,g)}$ describes the difference between the emerging powers obtained when the signals υ_f and υ_g are made to pass through a right-circular polarizer and a left-circular polarizer, i.e., it gives the preponderance of right-circular polarizer light over left-circular polarizer light.

Intramode case

As previously mentioned, the first subset of $3n$ matrices pointed out in (a) is obtained from the Pauli matrices and, therefore, we can write

$$\mathbf{\Lambda}^{(f,g)} = (\boldsymbol{\Lambda}_1^{(f,g)}, \boldsymbol{\Lambda}_2^{(f,g)}, \boldsymbol{\Lambda}_3^{(f,g)})^T , \tag{5.8}$$

with

$$\boldsymbol{\Lambda}_1^{(f,g)}(k,l) = \begin{cases} \sqrt{n} & \text{if } k = g, l = g \\ -\sqrt{n} & \text{if } k = f, l = f \\ 0 & \text{otherwise} \end{cases}, \tag{5.9a}$$

$$\boldsymbol{\Lambda}_2^{(f,g)}(k,l) = \begin{cases} \sqrt{n} & \text{if } k = f, l = g \\ \sqrt{n} & \text{if } k = g, l = j \\ 0 & \text{otherwise} \end{cases}, \tag{5.9b}$$

$$\boldsymbol{\Lambda}_3^{(f,g)}(k,l) = \begin{cases} -i\sqrt{n} & \text{if } k = f, l = g \\ i\sqrt{n} & \text{if } k = g, l = f \\ 0 & \text{otherwise} \end{cases}, \tag{5.9c}$$

where the subscript index $g = f + 1$, with f taking all the odd values in the range $[1 : 2n - 1]$, i.e., in (5.9), the superscript indexes f and g denote the x and y polarization of a given mode. As the conventional Pauli spin vector in the single-mode case, the vector $\boldsymbol{\Lambda}^{(f,g)}$ (henceforth called of Pauli spin vector) can be used to calculate the Stokes parameters of the multimodal signal in a given HoPs.

Using (5.9) in (5.1), the relative state between the signals υ_f and υ_g (and its evolution) can be represented in a single HoPs with radius $\sqrt{n}(a_g^2 + a_f^2)$, and Stokes parameters

$$\Psi_1^{(f,g)} = \langle\psi|\, \boldsymbol{\Lambda}_1^{(f,g)}\, |\psi\rangle = \sqrt{n}(a_f^2 - a_g^2)\,, \tag{5.10a}$$

$$\Psi_2^{(f,g)} = \langle\psi|\, \boldsymbol{\Lambda}_2^{(f,g)}\, |\psi\rangle = 2\sqrt{n} a_f a_g \cos\delta_{fg}\,, \tag{5.10b}$$

$$\Psi_3^{(f,g)} = \langle\psi|\, \boldsymbol{\Lambda}_3^{(f,g)}\, |\psi\rangle = 2\sqrt{n} a_f a_g \sin\delta_{fg}\,, \tag{5.10c}$$

where $\delta_{fg} = \phi_f - \phi_g$ represents the phase difference between the signals υ_f and υ_g in the Jones space.

Intermode case

The remaining matrices $\boldsymbol{\Lambda}_i$ employed to written the multimodal signal in the GSS must be handled to produce $g_s - n$ vectors $\boldsymbol{\Lambda}^{(f,g)}$ in order to fully describe the multimodal signal in HoPss. In these spheres, one considers the remaining pairs of signals accounting for the space and polarization states from distinct modes. In this case, we identify two distinct sets; firstly, the subscript index f can take all the available values between 1 and $2n - 2$ ($f = 1, 2, 3, ...2n-2$); meanwhile, for each f value, the subscript index g changes between $f+2$ and $2n$ ($g = f + 2, ...2n$). Secondly, the subscript index $g = f + 1$, with f taking all the even values in the range $[1 : 2n - 2]$.

The matrices $\boldsymbol{\Lambda}_2^{(f,g)}$ and $\boldsymbol{\Lambda}_3^{(f,g)}$ are included in the set of generalized Pauli matrices introduced in section 5.2, i.e., the second subset of $4n^2 - 4n$ matrices previously pointed out in (b). However, the matrix $\boldsymbol{\Lambda}_1^{(f,g)}$ is not explicitly written in this set of generalized Pauli matrices. In that way, the third subset of $n - 1$ matrices pointed out in (c) must be properly decomposed in order to produce a set of linearly independent matrices in which each matrix acts only on two tributary signals, i.e., the matrices only have two non-null elements in the main diagonal. Since all these matrices are linearly independent, it is possible to extend

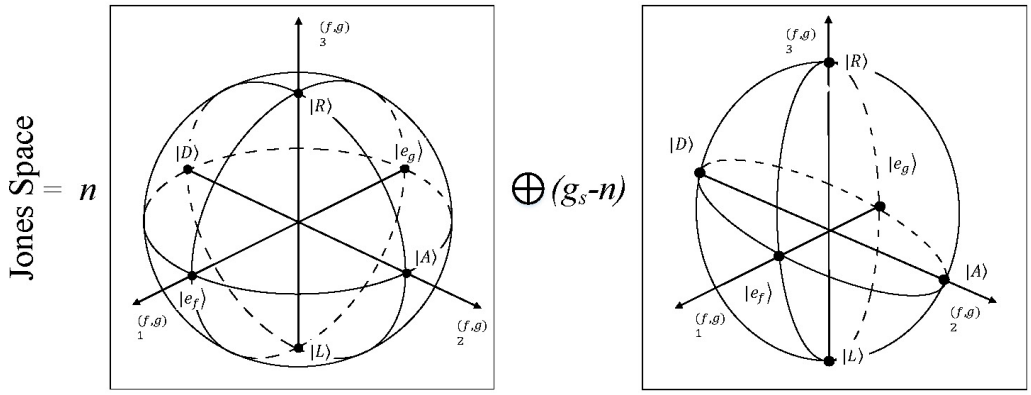

Figure 5.1: Schematic representation of the decomposition of the Jones space in HoPs. The tributary signals from the same spatial channel are represented in a sphere (i.e., intramode case), whereas the tributary signals from distinct spatial channels are represented in a ellipsoid.

this kind of decomposition to any dimension of the GSS. Having properly decomposed these matrices, they can be written as

$$\boldsymbol{\Lambda}_1^{(f,g)}(k,l) = \begin{cases} \sqrt{\frac{n}{n_l^2+n_l}}\kappa & \text{if } k=g, l=g \\ -\sqrt{\frac{n}{n_l^2+n_l}}\kappa & \text{if } k=f, l=f \\ 0 & \text{otherwise} \end{cases}, \tag{5.11a}$$

$$\boldsymbol{\Lambda}_2^{(f,g)}(k,l) = \begin{cases} \sqrt{n} & \text{if } k=f, l=g \\ \sqrt{n} & \text{if } k=g, l=f \\ 0 & \text{otherwise} \end{cases}, \tag{5.11b}$$

$$\boldsymbol{\Lambda}_3^{(f,g)}(k,l) = \begin{cases} -i\sqrt{n} & \text{if } k=f, l=g \\ i\sqrt{n} & \text{if } k=g, l=f \\ 0 & \text{otherwise} \end{cases}, \tag{5.11c}$$

being the parameter κ a normalization constant introduced by the projection of the generalized Pauli matrix in the set of linearly independent matrices. Note that, we explain in detail this decomposition for the particular case of two modes in subsection 5.2.4.

Using (5.11) in (5.1), the Stokes parameters for signals v_g and v_f can be written as

$$\Psi_1^{(f,g)} = \langle\psi|\,\boldsymbol{\Lambda}_1^{(f,g)}\,|\psi\rangle = \sqrt{\frac{n}{n_l^2+n_l}}\kappa\left(a_f^2 - a_g^2\right), \tag{5.12a}$$

$$\Psi_2^{(f,g)} = \langle\psi|\,\boldsymbol{\Lambda}_2^{(f,g)}\,|\psi\rangle = 2\sqrt{n}a_f a_g\cos\delta_{fg}, \tag{5.12b}$$

$$\Psi_3^{(f,g)} = \langle\psi|\,\boldsymbol{\Lambda}_3^{(f,g)}\,|\psi\rangle = 2\sqrt{n}a_f a_g\sin\delta_{fg}. \tag{5.12c}$$

In this case, the Poincaré sphere is replaced by an ellipsoid because the maximum value of the Stokes parameter $\Psi_1^{(f,g)}$ is smaller than the other Stokes parameters $\Psi_2^{(f,g)}$ and $\Psi_3^{(f,g)}$.

In Fig. 5.1, it is shown a schematic representation of the HoPss here proposed. Using a semi-simple representation, the Jones space is represented in n spheres and $g_s - n$ ellipsoids. In the n spheres are represented the intramode cases; whereas, in the $g_s - n$ ellipsoids are

represented the intermode cases. In each sphere/ellipsoid, it is possible to represent any relative state between the two signals e_f and e_g. Note that both signals considered are orthogonal, even in the case of CC-MCF or for ultra long MCFs in which the overlap integral between distinct cores is ideally null. In order to illustrate the signal representation in HoPss, in Fig. 5.1 are represented the diagonal basis written as,

$$|D\rangle = \frac{1}{\sqrt{2}}\left(|e_f\rangle + |e_g\rangle\right), \tag{5.13a}$$

$$|A\rangle = \frac{1}{\sqrt{2}}\left(|e_f\rangle - |e_g\rangle\right), \tag{5.13b}$$

and the circular basis written as

$$|R\rangle = \frac{1}{\sqrt{2}}\left(|e_f\rangle + i\,|e_g\rangle\right), \tag{5.14a}$$

$$|L\rangle = \frac{1}{\sqrt{2}}\left(|e_f\rangle - i\,|e_g\rangle\right), \tag{5.14b}$$

in both cases, inter and intramode. In the intermode case, the signal representation in a ellipsoid allows to connect the HoPss to the GSS representation by properly summing the parameters $\Psi_1^{(f,g)}$. The norm of the Stokes vector in such ellipsoids is not constant or unitary, although the norm of the generalized Stokes vector remains constant.

5.2.3 Complex-modulated signals in HoPs

In order to represent an arbitrary complex-modulated signal in HoPss, we assume a hypothetical modulation format that is confined to an unit circle in the complex plane. Although the signal needs be normalized, such condition does not restrict the modulation format in any way because all realizable signals are always bounded [5]. In that way, we assume an amplitude signal,

$$|\Upsilon\rangle = \frac{1}{\sqrt{2n}}\left(1, ..., 1, re^{-i\varphi}\right)^T, \tag{5.15}$$

where the parameters r, with $0 < r \leq 1$ and φ, with $0 \leq \varphi < 2\pi$, represent the amplitude and phase of the signal, respectively. In (5.15), the hypothetical complex modulated signal is considered in the last entry, while the remaining signals are assumed to have constant phase and amplitude. By replacing (5.15) in (5.12), the set of parametric equations can be obtained

$$\Psi_1^{(f,g)} = \frac{\kappa}{2}\sqrt{\frac{1}{n(n_l^2 + n_l)}}(1 - r^2), \tag{5.16a}$$

$$\Psi_2^{(f,g)} = \frac{r}{\sqrt{n}}\cos\varphi, \tag{5.16b}$$

$$\Psi_3^{(f,g)} = \frac{r}{\sqrt{n}}\sin\varphi. \tag{5.16c}$$

In Fig. 5.2, it is shown the paraboloidal surface described by (5.16) in a given HoPs for the region $\Psi_1 > 0$. Note that, a given point in the HoPs represents the relative state between two signals. When a signal is assumed with constant amplitude and phase, it allows to calculate

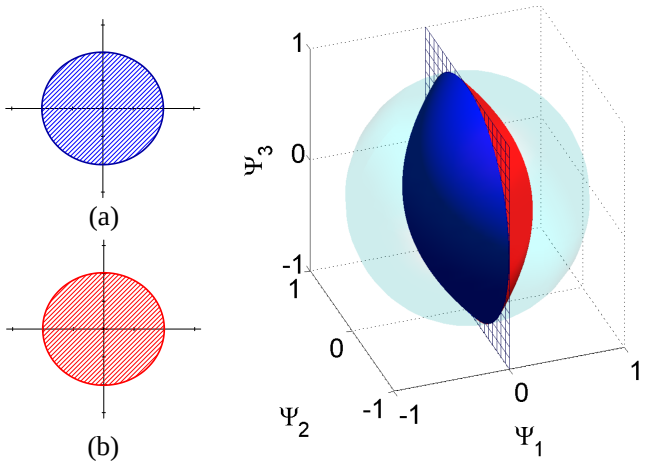

Figure 5.2: Boundaries of the arbitrary modulated signals in a HoPs. Insets (a) and (b) show the unit circle which contains the arbitrary modulation format.

the boundary of such object in the HoPs, without loss of generality, we use this assumption to visualize the lens-like objects. For $\mathbf{\Lambda}^{(g,2n)}$, with $g \neq 2n-1$, the other paraboloidal surface in the region $\Psi_1 < 0$ can be obtained in a similar way replacing

$$|\Upsilon\rangle = \frac{1}{\sqrt{2n}}\left(1, ..., re^{-i\varphi}, ..., 1\right)^T \tag{5.17}$$

in (5.12). This leads to the equation of the second surface and hence to the symmetrical lens-like object inscribed in HoPss. Both surfaces are quite similar with the exception that Ψ_1 and Ψ_3 have opposite signs. The flips in Ψ_1 invert the paraboloidal surface resulting in the complete lens-like object and therefore clearly defining a symmetry plane. Likewise, using (5.15) in (6.4) a similar lens-like objects for the remaining sets $\mathbf{\Lambda}^{(f,g)}$ can be written as,

$$\Psi_1^{(f,g)} = \frac{1}{2\sqrt{n}}(1-r^2)\,, \tag{5.18a}$$

$$\Psi_2^{(f,g)} = \frac{r}{\sqrt{n}}\cos\varphi\,, \tag{5.18b}$$

$$\Psi_3^{(f,g)} = \frac{r}{\sqrt{n}}\sin\varphi\,. \tag{5.18c}$$

Note that such lens-like objects are independent of the considered tributary signals and respective modulation formats. The residual frequency offset and the phase noise only affect the Stokes parameters $\Psi_2^{(f,g)}$ and $\Psi_3^{(f,g)}$. The parameter $\Psi_1^{(f,g)}$ remains unaffected because it only depends on the amplitude of both signals considered in a given HoPs, like in the single-mode case [5, 6, 18]. Space-demultiplexing algorithms based on the signal representation in HoPss are therefore robust against the frequency offsets and phase noise.

5.2.4 Two spatial channels in HoPs

In order to illustrate the signal representation in HoPss, and without loss of generality, we consider two distinct spatial channels, each one supporting two orthogonal polarizations.

For this particular case, the eigenvectors can be written as

$$|e_1\rangle = (1,0,0,0)^T, \tag{5.19a}$$

$$|e_2\rangle = (0,1,0,0)^T, \tag{5.19b}$$

$$|e_3\rangle = (0,0,1,0)^T, \tag{5.19c}$$

$$|e_4\rangle = (0,0,0,1)^T, \tag{5.19d}$$

where $|e_1\rangle$ and $|e_2\rangle$ represent the x and y polarizations of the first mode, respectively. In the same manner, $|e_3\rangle$ and $|e_4\rangle$ represent the x and y polarizations of the second mode, respectively. For this particular case, the set of the generalized Pauli matrices is comprised by 15 matrices. The two Pauli spin vectors, $\mathbf{\Lambda}^{(1,2)}$ and $\mathbf{\Lambda}^{(3,4)}$, can be arranged by the examination of the set of generalized Pauli matrices, which are described in (a). For the remaining Pauli spin vectors, only the matrices $\boldsymbol{\Lambda}_2^{(f,g)}$ and $\boldsymbol{\Lambda}_3^{(f,g)}$ are presented in generalized Pauli matrices, see the second subset of matrices pointed out in (b). However, the $\boldsymbol{\Lambda}_1^{(f,g)}$ matrices are not explicitly written in the basis of generalized Pauli matrices. In that sense, the last subset of matrices pointed out in (c) must be decomposed in four matrices,

$$\begin{pmatrix} 1 & 0 & 0 & 0 \\ 0 & 1 & 0 & 0 \\ 0 & 0 & -1 & 0 \\ 0 & 0 & 0 & -1 \end{pmatrix} = \frac{1}{2}\begin{pmatrix} 1 & 0 & 0 & 0 \\ 0 & 0 & 0 & 0 \\ 0 & 0 & -1 & 0 \\ 0 & 0 & 0 & 0 \end{pmatrix} + \frac{1}{2}\begin{pmatrix} 1 & 0 & 0 & 0 \\ 0 & 0 & 0 & 0 \\ 0 & 0 & 0 & 0 \\ 0 & 0 & 0 & -1 \end{pmatrix} + \frac{1}{2}\begin{pmatrix} 0 & 0 & 0 & 0 \\ 0 & 1 & 0 & 0 \\ 0 & 0 & -1 & 0 \\ 0 & 0 & 0 & 0 \end{pmatrix} + \frac{1}{2}\begin{pmatrix} 0 & 0 & 0 & 0 \\ 0 & 1 & 0 & 0 \\ 0 & 0 & 0 & 0 \\ 0 & 0 & 0 & -1 \end{pmatrix}, \tag{5.20}$$

where the factor 1/2 results from the projection of the matrix represented on the left-hand side of (5.20) into the considered set of linearly independent matrices. The matrices on the right-hand side only take into account the interaction between two given signals and therefore can be used as $\boldsymbol{\Lambda}_1^{(f,g)}$. For instance, the subset of matrices $\mathbf{\Lambda}^{(1,3)}$ can be obtained by the examination of the remaining elements of the generalized Pauli matrices and taking into account (5.20),

$$\boldsymbol{\Lambda}_1^{(1,3)} = \frac{1}{2}\begin{pmatrix} 1 & 0 & 0 & 0 \\ 0 & 0 & 0 & 0 \\ 0 & 0 & -1 & 0 \\ 0 & 0 & 0 & 0 \end{pmatrix}, \tag{5.21a}$$

$$\boldsymbol{\Lambda}_2^{(1,3)} = \sqrt{2}\begin{pmatrix} 0 & 0 & 1 & 0 \\ 0 & 0 & 0 & 0 \\ 1 & 0 & 0 & 0 \\ 0 & 0 & 0 & 0 \end{pmatrix}, \tag{5.21b}$$

$$\boldsymbol{\Lambda}_3^{(1,3)} = \sqrt{2}\begin{pmatrix} 0 & 0 & -i & 0 \\ 0 & 0 & 0 & 0 \\ i & 0 & 0 & 0 \\ 0 & 0 & 0 & 0 \end{pmatrix}. \tag{5.21c}$$

The remaining three subsets $\boldsymbol{\Lambda}^{(f,g)}$ can be arranged in the same way considering the following pairs of signals: $(1,4)$, $(2,3)$ and $(2,4)$.

5.3 Channel modeling

In order to emulate the signal propagation in a SDM link without spacial diversity, we use the multi-section model [19], in which both approaches, FMF and CC-MCF, can be properly described by considering a section with a length slightly longer than the correlation length and the dispersive properties for each spatial channel. For a SDM transmission system with n orthogonal channels, the propagation operator can be represented by,

$$|\psi_{out}\rangle = \boldsymbol{M}_{\text{tot}}(\omega)\,|\psi_{in}\rangle\ , \tag{5.22}$$

where $|\psi_{out}\rangle$ and $|\psi_{in}\rangle$ represent the output and the input signals, respectively, and the channel impulse response is given by

$$\boldsymbol{M}_{\text{tot}}(\omega) = \boldsymbol{M}_{\text{MD}}(\omega)e^{\frac{i}{2}\omega^2\bar{\beta}_2 L}\,, \tag{5.23}$$

being L the total length of the link, $\bar{\beta}_2$ the mode-averaged chromatic dispersion per unit length, and $\boldsymbol{M}_{\text{MD}}(\omega)$ represents the mode-dependent effects, such as MDL, MD, and crosstalk [19]. This link is divided in n_s spans,

$$\boldsymbol{M}_{\text{MD}}(\omega) = \prod_{k=1}^{n_s} \boldsymbol{M}^k_{\text{MD}}(\omega)\,, \tag{5.24}$$

where $\boldsymbol{M}^k_{\text{MD}}(\omega)$ represents the mode-dependent effects in the k^{th} span. Assuming that each span can be subdivided into n_{step} sections and that MDL can be compensated by inline amplifiers, (5.24) can be rewritten as

$$\boldsymbol{M}^k_{\text{MD}}(\omega) = \text{diag}\left(e^{\frac{g^k_1}{2}}...e^{\frac{g^k_{2n}}{2}}\right)\prod_{l=1}^{n_{\text{step}}} \boldsymbol{V}_{kl}\,\boldsymbol{\Theta}(\omega)\,\boldsymbol{U}^H_{kl}\,, \tag{5.25}$$

with the superscript H denoting the Hermitian conjugate operator. The $\boldsymbol{V}_{kl}$ and $\boldsymbol{U}_{kl}$ matrices denote the frequency-independent random unitary matrices (which represent the crosstalk caused by random mode coupling) and g^k_i, with $i = 1, 2 ... 2n$, represents the gain/loss for each tributary signal. Matrix $\boldsymbol{\Theta}(\Omega)$ accounts for the modal dispersion in a single section,

$$\boldsymbol{\Theta}(\omega) = \text{diag}\left(e^{i\omega\tau_1}, ..., e^{i\omega\tau_i}, ..., e^{i\omega\tau_{2n}}\right)\,, \tag{5.26}$$

where τ_i is the uncoupled group delay for the i^{th} tributary signal.

5.4 Space-demultiplexing algorithm

First of all, a "real" complex-modulated signal with two PM signals space-multiplexed is represented in HoPss. In each tributary, we assumed a pseudorandom binary sequence (PRBS) of 2^{18} bits mapped into the I and Q components of a QPSK signals with a signal-to-noise ratio (SNR) of 17 dB. Using (5.10) and (5.12), the Stokes parameters are calculated and represented in the respective HoPs, see Fig. 5.3. In each sphere, it is clear that the symbols are symmetrically distributed around the best fit plane which coincides with $\Psi_1^{(f,g)} = 0$.

The idea behind the SpDemux based on HoPss proposed in this thesis lies in the sequential signal equalization between pairs of tributary signals. As previously pointed out in section 5.2.2, the crosstalk operator can be expanded in g_s operators $\boldsymbol{\mathcal{M}}^{(f,g)}$. Notice that

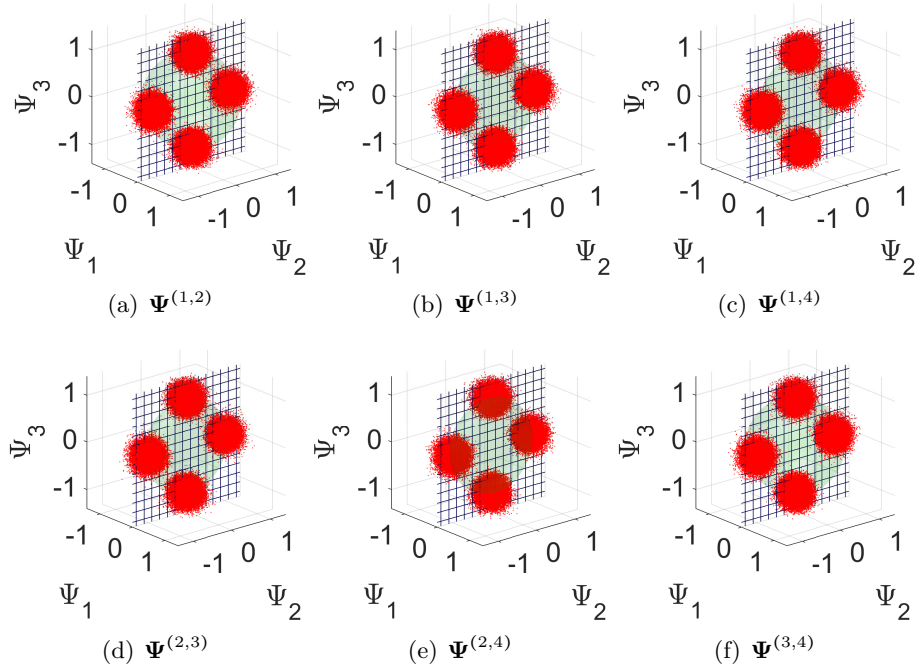

(a) $\mathbf{\Psi}^{(1,2)}$ (b) $\mathbf{\Psi}^{(1,3)}$ (c) $\mathbf{\Psi}^{(1,4)}$

(d) $\mathbf{\Psi}^{(2,3)}$ (e) $\mathbf{\Psi}^{(2,4)}$ (f) $\mathbf{\Psi}^{(3,4)}$

Figure 5.3: Four tributary QPSK signals, i.e., two modes with two polarization-multiplexed tributaries, are represented in the HoPss with the symmetric plane, i.e., the best fit plane, to the samples. The sub-captions indicate the pair of tributaries (f, g) represented in each subspace.

each operator $\boldsymbol{\mathcal{M}}^{(f,g)}$ only takes into account the crosstalk between a given pair of tributary signals. In that sense, the channel matrix can be written as

$$\boldsymbol{M}_{\text{tot}} = \prod_{g=1}^{2n-1} \prod_{f=g+1}^{2n} \boldsymbol{\mathcal{M}}^{(f,g)} . \tag{5.27}$$

Therefore, we need to properly apply g_s sequential space-demultiplexing steps to equalize the crosstalk among the g_s pairs of tributary signals. To assess the efficiency of the algorithm proposed, it is only considered the crosstalk induced by the SDM link. In this way, we are assuming a previous compensation of the remaining linear impairments, e.g., chromatic dispersion, MDL, and MD. As happens in the single-mode case with Stokes-based PolDemux, the symmetry plane in the HoPs is not affected by the frequency offset and phase noise. Hence, such transmission impairments are not considered. The dispersive effects (e.g., chromatic dispersion and MD) are not considered because it is assumed that they can be compensated before space-demultiplexing. We also assume that the tributary signals are synchronized before the space-demultiplexing. In CC-MCF based transmission systems, the deviation from the ideal sampling instant is quite similar to the ones observed in standard communications systems based on SSMF. Therefore, in such transmission systems the clock recovery and downsampling can be performed after the space-demultiplexing based on HoPss. Conversely, in MDM transmission systems the MD can desynchronize the tributary signals. Nevertheless, these signals can be again synchronized by using a subsystem which allows to compensate the MD; like in [20] the polarization-mode dispersion (PMD) is compensated before the polarization-demultiplexing.

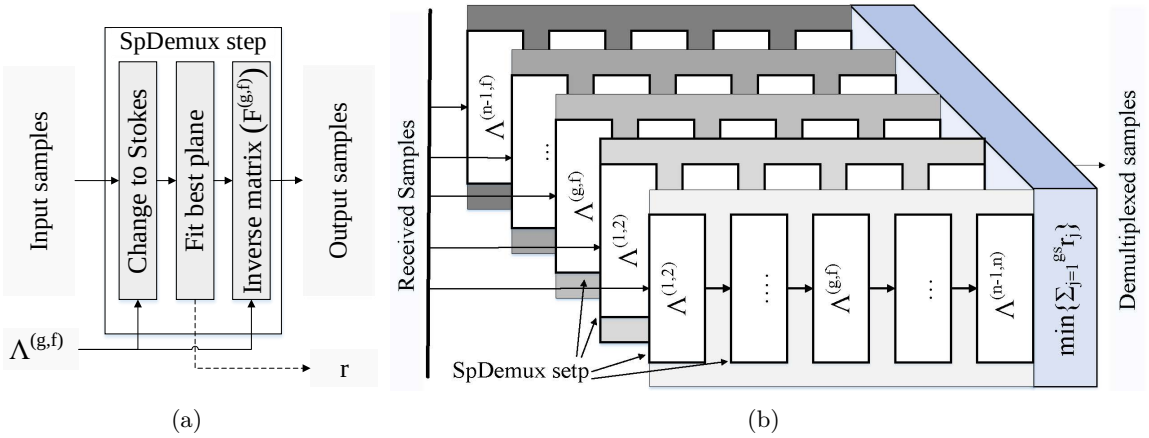

Figure 5.4: a) Schematic of the proposed space-demultiplexing step algorithm. The samples are represented in a HoPs in order to estimate the normal to the best fit plane. Then, the matrix $\boldsymbol{F}^{(f,g)}$ is calculated and applied to the signal. b) Schematic of the proposed space-demultiplexing algorithm. The received samples are sequentially launched in g_s space-demultiplexing steps. Then, the suitable sequence of these steps is chosen by minimizing the sum of the absolute values of the residuals, i.e., the parameter ζ.

5.4.1 Operation principle and algorithm description

The Stokes parameters, $\boldsymbol{\Psi}^{(f,g)}$, are calculated for the sampled signal. These samples are represented in the HoPss and the best fit plane (and its normal) is computed through a linear least square regression by minimizing the sum of squared residuals, i.e., the squared of the offsets among the points and the plane. The plane equation is written as

$$a\Psi_1^{(f,g)} + b\Psi_2^{(f,g)} + c\Psi_3^{(f,g)} = 0\,, \tag{5.28}$$

where $\mathbf{n}_p = (a,b,c)^T$ represents its normal. Like in the single-mode case, this normal can be rotated in the 3-dimensional subspace to match $(1,0,0)^T$, reversing the crosstalk between the pair of signals considered. Such rotation is applied to the samples in the Jones space,

$$|\varphi_{out}\rangle = \boldsymbol{F}^{(f,g)}\,|\varphi_{in}\rangle\ , \tag{5.29}$$

where $|\varphi_{out}\rangle$ and $|\varphi_{in}\rangle$ represent the signal after and before the demultiplexing stage, respectively. The unit matrix $\boldsymbol{F}^{(f,g)}$

$$\boldsymbol{F}^{(f,g)}(k,l) \;=\; \begin{cases} \cos(p)e^{i\frac{q}{2}} & \text{if } k=g, l=g \\ \sin(p)e^{-i\frac{q}{2}} & \text{if } k=g, l=f \\ -\sin(p)e^{i\frac{q}{2}} & \text{if } k=f, l=g \\ \cos(p)e^{-i\frac{q}{2}} & \text{if } k=f, l=f \\ 1 & \text{if } k=l \text{ and } k,l\neq f,g \\ 0 & \text{otherwise} \end{cases}\ , \tag{5.30}$$

allows to reverse the crosstalk between the tributary signal v_g and v_f, with k and l denoting the indices of each element of matrix $\boldsymbol{F}$. The parameters $p = \arctan(a, \sqrt{b^2+c^2})$

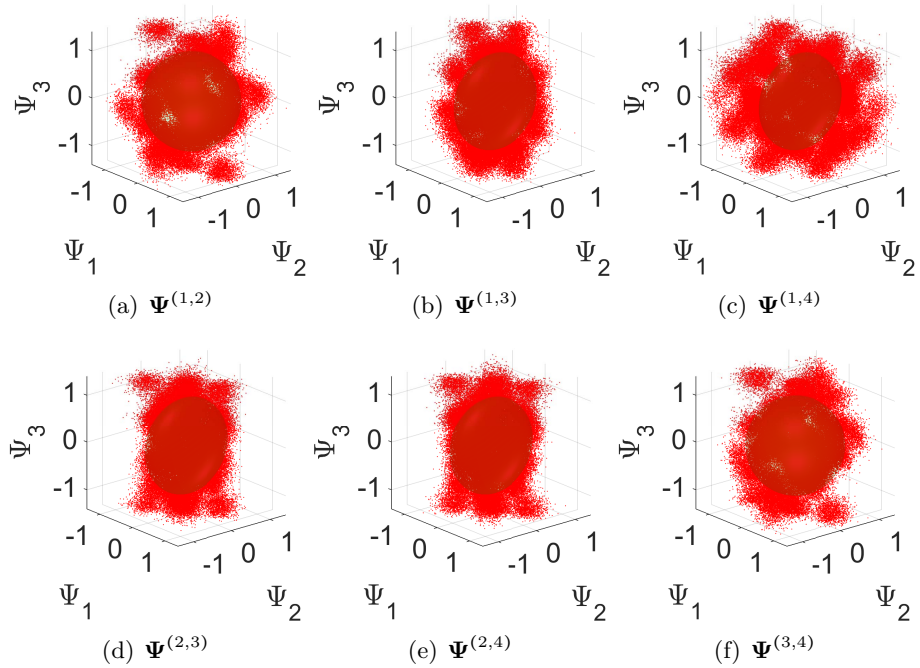

(a) $\mathbf{\Psi}^{(1,2)}$ (b) $\mathbf{\Psi}^{(1,3)}$ (c) $\mathbf{\Psi}^{(1,4)}$

(d) $\mathbf{\Psi}^{(2,3)}$ (e) $\mathbf{\Psi}^{(2,4)}$ (f) $\mathbf{\Psi}^{(3,4)}$

Figure 5.5: Representation in the HoPss of the QPSK signal, shown in Fig. 5.3, after transmission through the SDM link. In each figure, the deeper red color disks represent the HoPs.

and $q = \arctan(b/c)$ are the polar and azimuthal angles between the normal to the best fit plane and $(1,0,0)^T$. In Fig. 5.4(a), it is schematically represented this procedure, henceforth, called of "SpDemux step". Afterwards, the output samples are launched in the next SpDemux step and the process is repeated g_s times. At each step, we take into account the two possible spatial orientation of the normal, i.e., $\mathbf{n}_p$ and $-\mathbf{n}_p$. Note that, both normals allow the space-demultiplexing. However, an unsuitable direction of the normal leads to a signal commutation between the signals υ_g and υ_f. Such signal commutation can hinder the fully space-demultiplexing because two given tributary signals are demultiplexed two times, while the interaction with other tributary signal is not taken into account. Furthermore, the operators $\boldsymbol{F}^{(f,g)}$ do not commute because they are rotation matrices of dimension $2n$, with $n > 1$ [21]. In that way, the performance of the SpDemux algorithm strongly depends on the sequence of the SpDemux steps.

The smaller residual the larger symmetry, using this heuristic a suitable sequence to apply the g_s SpDemux steps can be found by minimizing the sum of the absolute value of the residuals. Figure 5.4(b) shows a schematic representation of all the steps comprising the algorithm. Initially, all possible sequences of SpDemux steps are computed and their residuals are evaluated. For each sequence of SpDemux steps, the parameter ζ is calculated considering the sum of the absolute values of the residuals. This parameter can be used to "quantify" the symmetry of the samples relatively to the best fit plane for a given sequence of SpDemux steps. For a particular sequence of g_s steps, lower values of ζ means larger symmetries of the samples. Therefore, the sequence of SpDemux steps with lower value of ζ is the chosen one. Note that, to use the residuals minimization as a reliable criterion all the residuals must be equivalent and therefore the residuals provided by (5.11a) must be multiplied by $\sqrt{n_l^2 + n_l}/\kappa$.

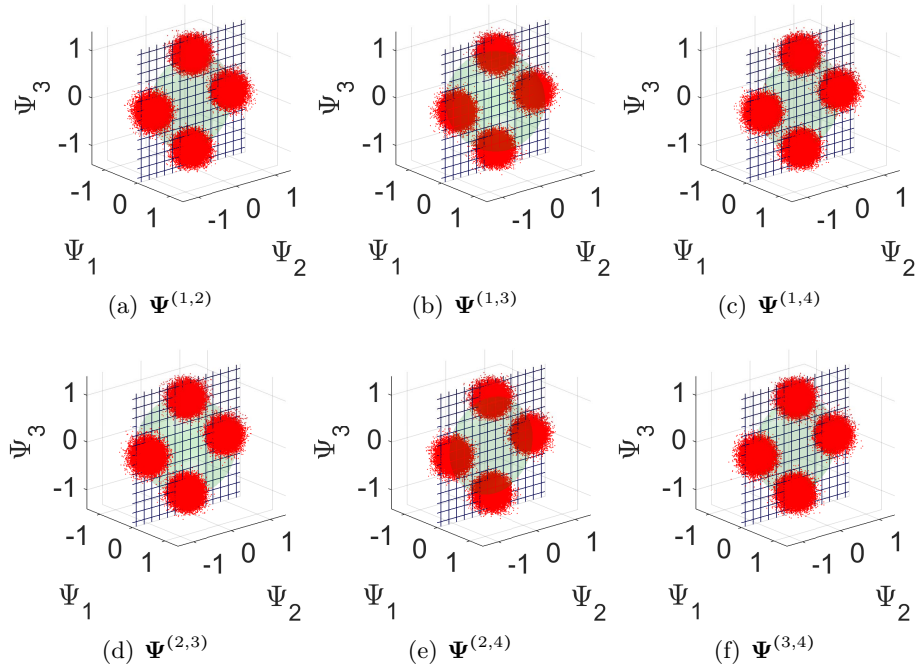

(a) $\mathbf{\Psi}^{(1,2)}$ (b) $\mathbf{\Psi}^{(1,3)}$ (c) $\mathbf{\Psi}^{(1,4)}$

(d) $\mathbf{\Psi}^{(2,3)}$ (e) $\mathbf{\Psi}^{(2,4)}$ (f) $\mathbf{\Psi}^{(3,4)}$

Figure 5.6: Representation in the HoPss of the four QPSK tributaries after space-demultiplexing. These signals are obtained from the signal represented in Fig. 5.5. The constellations after post-processing compared well with input constellations present in Fig. 5.3.

5.4.2 Results

In this subsection, we investigate the performance of the proposed space-demultiplexing algorithm by numerically calculating the imposed penalties on demultiplexing of different complex-modulation formats, e.g., PM-QPSK, PM-16QAM, and PM-64QAM. We assume a PRBS of 2^{18} (2^{19}) bits mapped into the I and Q components of a QPSK (16QAM and 64QAM) with an averaged SNR of 17 dB (23 and 30 dB, respectively) and a standard deviation of 0.1 dB. We assume a transmission system based on CC-MCF with a spatial diversity of 2^1, e.g., a 2-core CC-MCF. For the SDM transmission system, and without loss of generality, we are going to consider that all linear and nonlinear transmission impairments can be fully compensated. In that way, we assume that the signals is only affected by optical noise and by the linear crosstalk.

The following method description considers the QPSK signal for a question of simplicity, but it can be also extended to the other higher-order modulation formats. Figure 5.5 shows the representation of the received QPSK signal in HoPss, i.e., the signal represented in Fig. 5.3 after propagated trough the SDM link discussed above. In order to demultiplex the four QPSK tributaries the proposed algorithm requires six SpDemux steps. In each step, we must provide the signal and the Pauli spin vector $\mathbf{\Lambda}^{(f,g)}$, with $(f,g) = (1,2), (1,3), (1,4), (2,3), (2,4)$ and $(3,4)$. Then, the Stokes parameters are calculated and the signal samples are represented in

[1]The proposed algorithm can be also used in FMF-based transmission systems, if MD is negligible or was previously compensated.

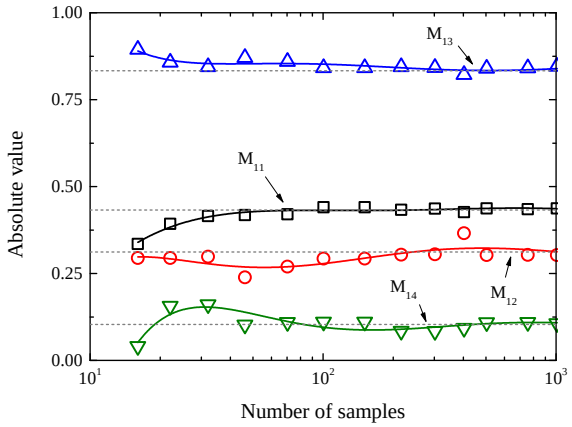

Figure 5.7: Convergence of the elements of the first line demultiplexing matrix as function of the number of samples for a QPSK signal. The dashed line represents the elements of the channel matrix, $\boldsymbol{M}_{\text{tot}}$.

the respective HoPs. By means of a linear regression, the best fit plane to those samples is computed and the residual provided by the linear regression is saved. The normal to the best fit plane is used to calculate the matrix $\boldsymbol{F}^{(f,g)}$, according to (6.15), which is then applied to the signal in the Jones space to space-demultiplex both tributary signals v_g and v_f, as shown in Fig. 5.4(a). After that, the four tributary signals are launched in the next SpDemux step where the above process is repeated. When all the sequences of SpDemux steps are applied to the signal, we choose the sequence of SpDemux steps with lower ζ, as shown in Fig. 5.4(b). The sequence of SpDemux steps is applied to the received signal, yielding the post-processed signal. The post-processed signal shown in Fig. 5.6 compares very well with the input signal shown in Fig. 5.3, which confirms the successful demultiplexing of the signal.

Convergence speed

In Fig. 5.7, it is shown the values of the components for the first line of matrix $\boldsymbol{M}$ as function of the number of sample considered in the calculations of the inverse channel matrix. Results show that the algorithm converges to the expected results, dashed line, after only 100 samples. In terms of remaining penalty in the SNR of the post-processed signal, the performance of the space-demultiplexing algorithm can be assessed according to,

$$\Delta = \text{SNR}_{in} - \text{SNR}_{out}\,, \tag{5.31}$$

with Δ denoting the remaining penalty induced by the algorithm, and SNR_{out} and SNR_{in} being the SNR for the post-processed signal and for the back-to-back signal, respectively. The SNR_{out} is calculated considering the error vector magnitude (EVM) of the tributary signal with higher EVM. In the calculations of the SNR, it is assumed a perfect phase and frequency recovery [22],

$$SNR = \frac{1}{EVM^2}\,. \tag{5.32}$$

In Fig. 5.8(a), it is shown the SNR penalty as function of the number of samples considered in the calculations of the inverse channel matrix for the QPSK, 16QAM and 64QAM signals.

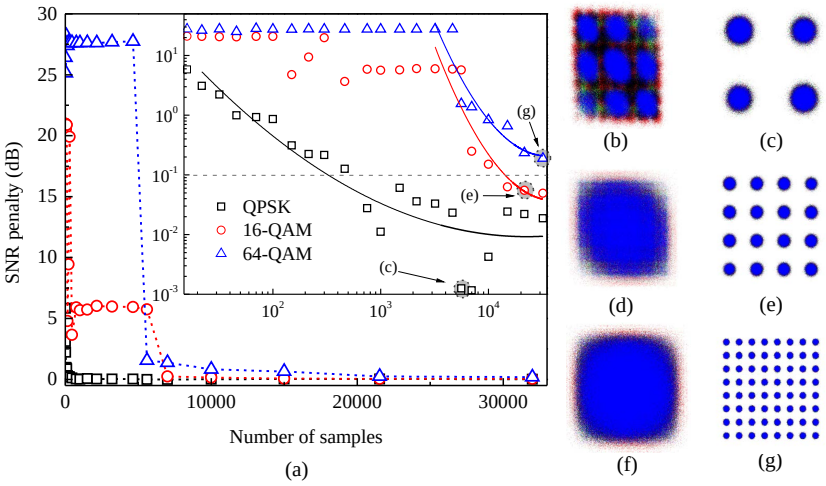

Figure 5.8: (a) SNR penalty induced by the space-demultiplexing algorithm as function of the number of samples considered in the calculations of the inverse channel matrix. Inset show in log scale the SNR penalty as function of the number of samples. The QPSK signals are assumed with an optical SNR of 17 dB. The 16QAM and the 64QAM signals are assumed with an optical SNR of 23 and 30 dB, respectively. Figure 5.8(b), (d) and (f) show the constellation diagram before demultiplexing for the QPSK, the 16QAM and the 64QAM, respectively. Figure 5.8(c), (e) and (g) show the constellation diagram after demultiplexing for the QPSK, the 16QAM and the 64QAM, respectively. Note that, the number of samples used to calculate the inverse channel matrix are pointed out in Fig. 5.8(a).

For the QPSK signal, the algorithm needs ≈ 500 samples to achieve a penalty as low as $\Delta = 0.1$ dB. In Figs. 5.8(b) and 5.8(c) are shown the constellation diagrams for the four tributary QPSK signals before and after demultiplexing, respectively. For the 16QAM signal, the algorithm needs ≈ 12000 samples to achieve a penalty as low as $\Delta = 0.1$ dB. The constellation diagram for the four tributary 16QAM signal before and after demultiplexing are shown in the Fig. 5.8(d) and 5.8(e), respectively. Regarding the 64QAM signal, the algorithm needs ≈ 20000 samples to achieve a penalty of $\Delta = 0.2$ dB. Figure 5.8(d) and 5.8(e) show the constellation diagram for the four tributary 64QAM signal before and after demultiplexing, respectively. These results show that higher-order modulation formats require more samples to accurately calculate the best fit plane and, therefore, the space-demultiplexing algorithm also requires a larger number of samples to find a suitable sequence of space-demultiplexing steps. These results are in good agreement with discussion reported in [4, 7], where the convergence analysis of Stokes space based PolDemux in single-mode fibers has shown a slower convergence ratio for the higher order constellations.

SNR tolerance

This algorithm is quite robust to additive Gaussian noise because the noise increases the dispersion of the points without breaking the symmetry proprieties of complex-modulated signals in HoPss. Nevertheless, the performance of the space-demultiplexing algorithm can be constrained by the optical SNR, namely in terms of convergence speed. A lower optical SNR in the received signal may require a large number of samples in the demultiplexing algorithm to calculate a suitable sequence of space-demultiplexing stages. In Fig. 5.9, it is shown the value of the remaining penalty, Δ, as function of the number of samples considered in the

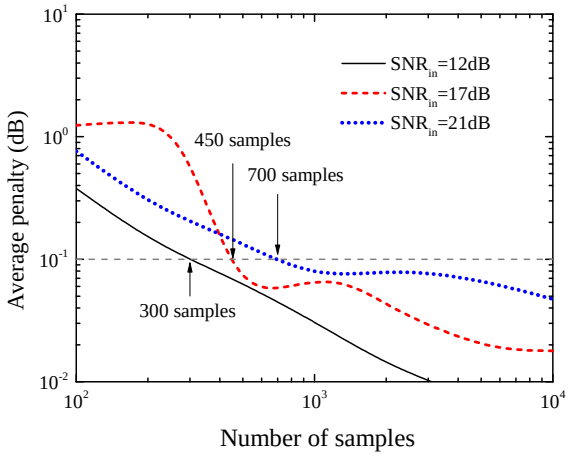

Figure 5.9: Remaining penalty as function of the number of samples for the QPSK with SNR of 12,17 and 21 dB.

calculations of the inverse channels matrix for the SDM transmission system above described assuming a PM-QPSK signal with the following values of $\mathrm{SNR}_{\mathrm{in}}$ = 12, 17 and 21 dB. The algorithm can achieve a Δ smaller than 0.1 dB for the cases considered. Results show that the algorithm tends to be robust to lower SNR. Notice that the SNR calculations are averaged over 10 trials.

5.5 A reduced-complexity space-demultiplexing algorithm

In order to reduce the computational complexity of the HoPs-based SpDemux algorithm above presented, we propose an alternative approach in which the inverse channel matrix is calculated in a iterative way. The SpDemux algorithm remains modulation format agnostic, free of training sequences and robust to the local oscillator phase fluctuations and frequency offsets.

First of all, the computation of the Pauli spin vector can be also considerably simplified for this particular application. The factor $\sqrt{n}$ can be neglected because we are mainly interested in the spatial orientation of the best fit plane and this factor only changes the norm of the "Stokes" vector for each sample, without changing the spatial orientation of the best fit plane. This multiplicative factor also changes the value of the residual obtained from the calculations of the best fit plane; however, all the g_s residuals are affected in the same way. Notice that the factor κ was previously introduced to describe the mathematical relationship between the GSS and the HoPss. Such factor depends on the number of spatial channels considered in the Jones space and, it can be calculated from the generalized Pauli matrices and the Pauli spin vector matrices for the respective HoPs. In the SpDemux algorithm previously proposed, the factor κ is not considered in the calculations of the Stokes vectors enabling the use of the residual as a reliable criterion to choose a suitable sequence of HoPss, i.e., the sequence with better least squares regression. In the following sections, the factor κ will be neglected in order to make the residual a metric of the "quality" of the least square calculations and, additionally, to simplify the computation of the Pauli spin vector and following calculations.

5.5.1 Operation principle and algorithm description

In the HoPs-based SpDemux algorithm proposed in the previous section, the received signal is space-demultiplexed by iteratively reversing the crosstalk between all the pairs of tributaries. This means that, for an arbitrary pair of tributaries, the samples are represented in the respective HoPs and the crosstalk is compensated by means of a SpDemux step. The SpDemux step adopted in the reduced-complexity approach is quite similar to the one described in subsection 5.4.1, but with the difference that the two possible spatial orientations of the normal, i.e. $\mathbf{n}_p$ and $-\mathbf{n}_p$, are considered in the demultiplexing process; see the schematic representation in Fig. 5.10(a).

As in the previous space-demultiplexing algorithm, in the reduced-complexity approach the sequence of SpDemux steps is also extremely important to achieve a perfect space-demultiplexing. In order to find the first pair of tributaries for space-demultiplexing, the g_s SpDemux steps are applied to the received signal. After that, the pair of tributaries with the best fit is chosen for space-demultiplexing. In this sense, the "quality" of the fit can be assessed by the residual provided by the least square calculations. Then, a similar process is used to choose the second pair of tributaries for space-demultiplexing, and so on; until all the g_s SpDemux steps are properly applied to the received signal. Notice that the pair of tributaries previously considered is not taken into account in the following calculations.

For an arbitrary HoPs, however, the best fit plane can be described by two distinct spatial orientations of the normal. Although both spatial orientations can be successfully used to calculate the demultiplexing matrix, an unsuitable orientation induces a signal permutation between both tributaries considered; as above mentioned in subsection 5.4.1. It should be highlighted, once again, that after applied a given SpDemux step this one is no longer considered in the following calculations. Therefore, the change in the sequence of tributaries may lead to a double space-demultiplexing of a given pair of tributaries, while another pair of tributaries is not space-demultiplexed; this can jeopardize the accurate space-demultiplexing of the received signal. In order to avoid this effect, one considers all possible combinations of two consecutive pairs of tributaries, instead of a single pair, and their normals. The sequence with minimum residual at the second SpDemux step is chosen. Then, the signal is space-demultiplexed considering the first SpDemux step and their normal. Using this heuristic, the two possible spatial orientations of the normal can be considered in the residual minimization, or in other words, in the search for a suitable sequence of SpDemux steps. The above process is consecutively repeated until all the tributaries are space-demultiplexed. The set of operations described above are called SpDemux filter, see the schematic representation in Fig. 5.10(b).

The aforementioned simplification tremendously reduces the complexity of the SpDemux algorithm at the expense of a certain SNR penalty. Such impairments in the space-demultiplexing are due to a residual misalignment between the best fit plane and the $\Psi_1 = 0$ plane in one or more HoPss. This misalignment can be compensated by again applying the SpDemux filter to the post-processed signal. With this idea in mind, we introduce the parameter,

$$\zeta = \sum_{j=1}^{g_s} |r_j| \,, \tag{5.33}$$

where $|r_j|$ denotes the residual for the least squared regression at the j^{th} SpDemux step considered in the SpDemux filter. As the iterative process goes forward, the crosstalk is progressively compensated and the parameter ζ tends asymptotically to a given value; which

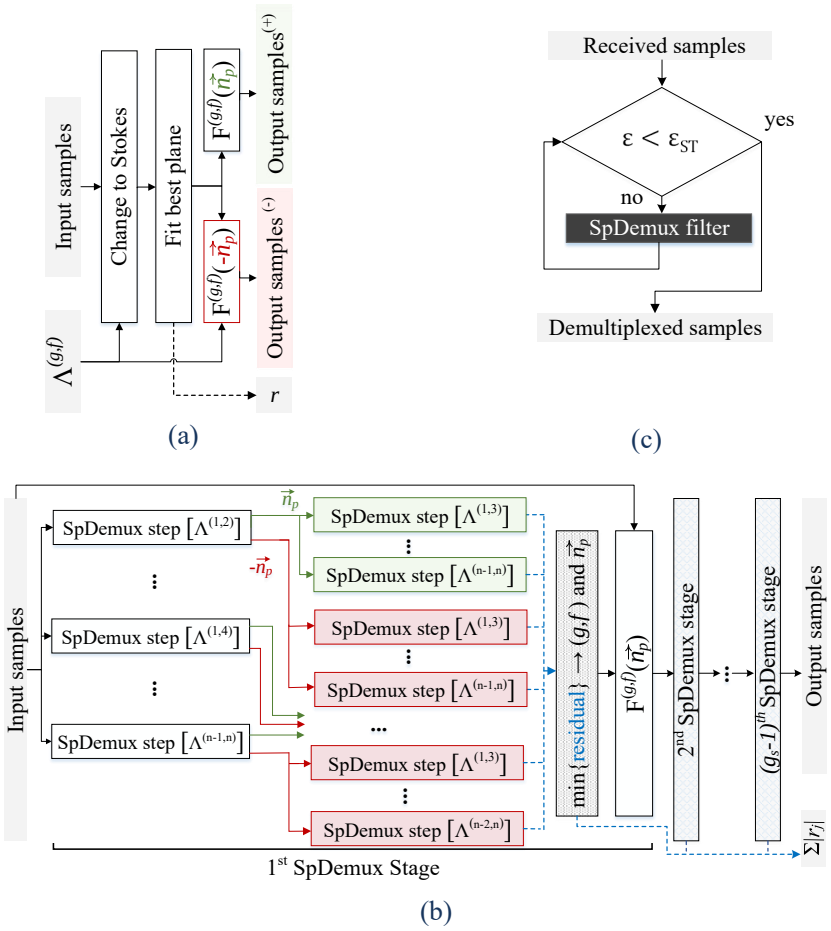

Figure 5.10: Schematic representation of the reduced-complexity SpDemux algorithm: (a) SpDemux step, (b) SpDemux filter and (c) iterative process or reduced-complexity algorithm. Note that, dashed lines depict the path for the residuals while solid lines represent the path of the samples.

depends on the number of tributaries supported by the transmission system and in the SNR of the received signal. Of course, the difference between consecutive values of ζ tends to decrease with the number of SpDemux filters because the next filter only takes into account the remaining misalignments between the best fit plane and the respective $\Psi_1 = 0$ plane. In that way, the relative difference between two consecutive parameters ζ can be used to assess the performance of the space-demultiplexing. Using the residuals as a metric of the space-demultiplexing performance, we define the parameter

$$\varepsilon_{\mathrm{R}} = \frac{\zeta^{(n+1)} - \zeta^{(n)}}{\zeta^{(n+1)}} \times 100\%\,, \tag{5.34}$$

with ζ^n defined as in (5.33) and the superscript denoting the n^{th} SpDemux filter. When this relative variation, ε_{R}, is below a given threshold, $\varepsilon_{\mathrm{ST}}$, it is assumed that the algorithm achieved the steady state. Hence, the iterative process is stopped. The iterative process of the reduced-complexity SpDemux algorithm is schematically represented in Fig. 5.10(c).

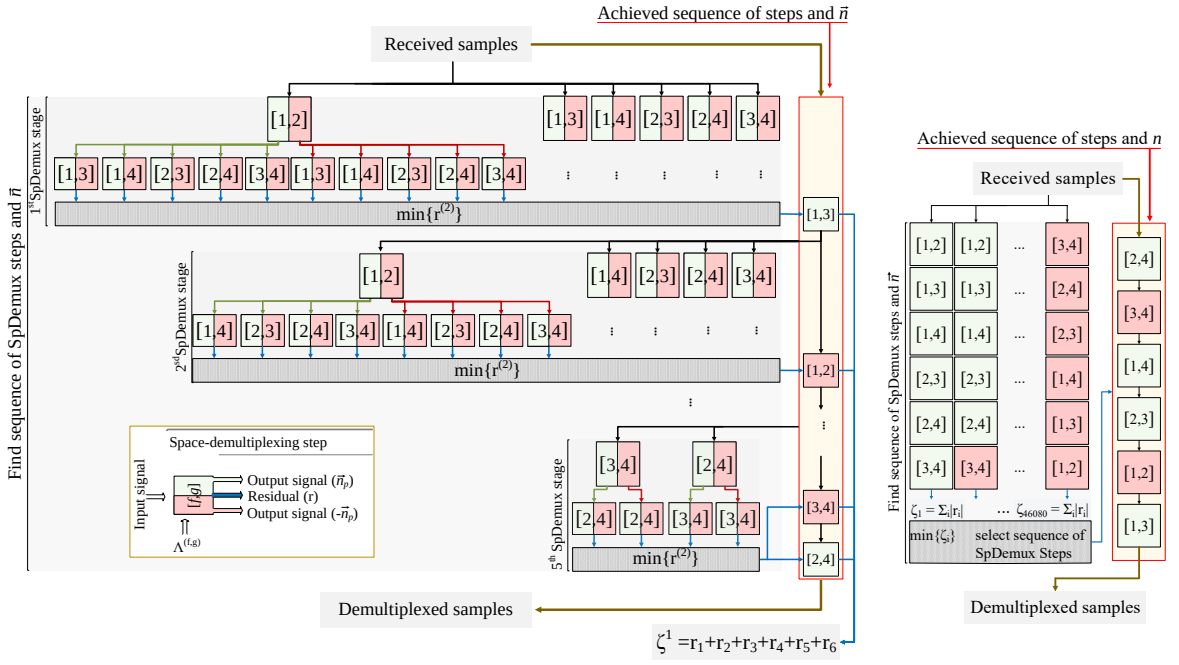

Figure 5.11: (a) Schematic representation of a SpDemux filter using the reduced-complexity space-demultiplexing algorithm. (b) Schematic representation of the space-demultiplexing algorithm previusly proposed. The SpDemux step, which is common to both algorithms, is represented by a block with two sides (gray and white) corresponding to the two output signals obtained with $\mathbf{n}_p$ and $-\mathbf{n}_p$, respectively.

Algorithm assessment

In this subsection, the proposed algorithm is assessed in terms of operation principle. In that way, the cornerstone of the reduced-complexity SpDemux algorithm, i.e., the SpDemux filter, is schematically represented in Fig. 5.11(a), assuming a transmission system with four tributaries. Furthermore, it is also schematically represented in Fig. 5.11(b) the algorithm previously proposed and described in section 5.4.1. In that way, the operation principle of both aforementioned algorithms can be easily compared. In the case of the SpDemux filter, the six pairs of tributaries are space-demultiplexed giving rise to twelve output signals; afterwards, each one of these signals is again space-demultiplexed. In the second set of SpDemux steps, the SpDemux step previously applied to the signal is not taken into account, see Fig. 5.11(a). For instance, the tributaries 1 and 2 are initially space-demultiplexed; subsequently the resultant signal is again space-demultiplexed taking into account only the remaining combinations of tributaries. By choosing the sequence with the lower value of residual for the second set of SpDemux steps, the suitable SpDemux step and the spatial orientation of the normal are found. In Fig. 5.11(a), this operation is denoted by $\min\{r^{(2)}\}$, with the superscript index pointed out the SpDemux step considered at the SpDemux stage. Such sequence comprises two concatenated SpDemux steps and the respective signs for the normals, the first SpDemux step and its normal are chosen. In addition, the SpDemux step also provides the first residual, r_1, considered in the calculation of ζ. In the second SpDemux stage, a similar operation is

performed in which the SpDemux step with the Pauli spin vector $\mathbf{\Lambda}^{(1,3)}$ is not considered in the SpDemux stage because it was already chosen as the first suitable SpDemux step.

In the SpDemux algorithm initially proposed, all the possible sequences of SpDemux steps and normals are evaluated in order to calculate the inverse channel matrix. Therefore, it is considered the permutations of the six pairs of tributaries taking into account for each SpDemux step both possible spatial orientations of the normal, $\mathbf{n}_p$ and $-\mathbf{n}_p$. Due to the two possible spatial orientations of the normal, each sequence of SpDemux steps has 64 additional combinations giving rise to a total of 46080 possible solutions. For each sequence, the parameter ζ is defined as: $\zeta = \sum_{i=1}^{6} |r_i|$, with r_i being the residual for the i^{th} SpDemux step. Lastly, the sequence with the lower value of ζ is chosen, see Fig. 5.11(b).

5.5.2 Results

The performance of the reduced-complexity space-demultiplexing algorithm was analyzed for several scenarios, including distinct degree of spatial diversity, modulation formats and SNR. The tributary signals considered in this subsection are similar to the ones considered in the previous section. It should be noted that the results presented in this section are obtained by averaging over 100 trials, with the exception of subsection 5.5.3 in which are averaged by 10 trials.

We assume a CC-MCF based transmission system in which all linear and nonlinear transmission impairments are fully compensated. It is assumed that the optical losses are compensated by in-line amplifiers, and that the chromatic and modal dispersions can be fully compensated by suitable digital signal processing subsystems before the space-demultiplexing. After space-demultiplexing, a Viterbi-Viterbi algorithm for carrier phase estimation was employed [3].

Convergence speed

We start by analyzing the convergence speed for a SDM transmission system based on a 3-core CC-MCF, in which it is launched in each core a PM-QPSK signal. In Fig. 5.12(a), we show the average value for Δ after the i^{th} SpDemux filter, with $i = 1, 2$ and 3, and the reduced-complexity algorithm with $\varepsilon_{\mathrm{ST}} = 10\%$ and 1% as function of the number of samples. After a single SpDemux filter, the average value of Δ takes values between 7 and 10 dB. Therefore, the demultiplexed signal still presents a considerable amount of crosstalk. When a second SpDemux filter is applied to the post-processed signal, the remaining penalty decreases, i.e., $\Delta \approx 3$ dB. For a third SpDemux filter, the penalty decreases again for values lower than 1 dB. However, the remaining penalty still exceeds the value of 0.1 dB. Such value is assumed as the minimum acceptable value to consider that space-demultiplexing was successfully achieved. For the reduced-complexity algorithm with $\varepsilon_{\mathrm{ST}} = 10\%$, the Δ target is achieved for ≈ 850 samples. The average value of Δ substantially decreases for the first ≈ 200 samples; whereas, for a larger number of samples > 200, Δ decreases slowly. As the SpDemux filter only takes into account two consecutive SpDemux steps in the demultiplexing process, the crosstalk cannot be fully compensated by a single filter. However, the remaining crosstalk, or the misalignments between the best fit plane and the $\Psi_1 = 0$ plane, can be successfully compensated by the progressive application of several SpDemux filters. In that way, the algorithm produces an enhanced space-demultiplexing matrix by each SpDemux filter considered. For instance, in the case of $\varepsilon_{\mathrm{ST}} = 1\%$, the average number of SpDemux

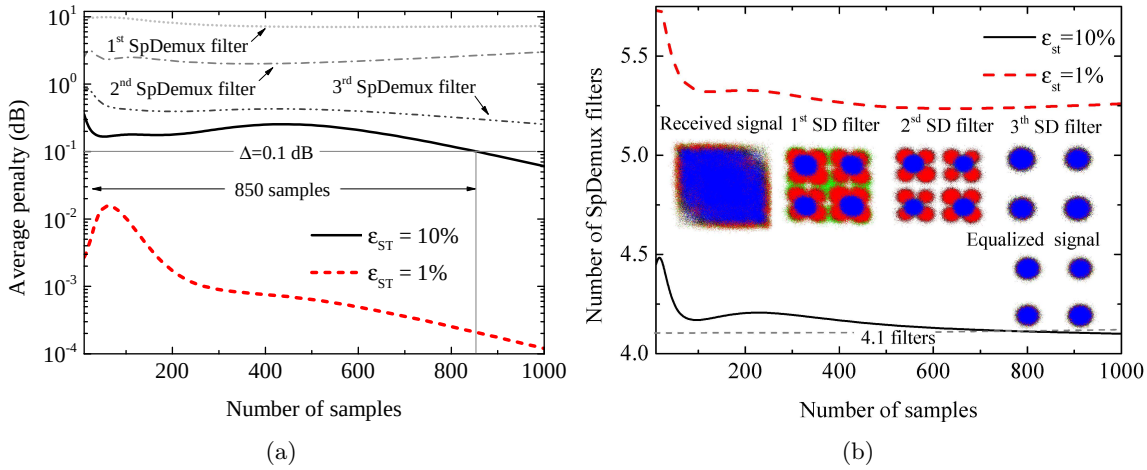

Figure 5.12: (a) Average SNR penalty after applying 1, 2 and 3 SpDemux filters along with the reduced-complexity SpDemux algorithm, considering $\varepsilon_{\mathrm{ST}}$ = 10% and 1% for a PM-QPSK signal with a SNR of 17 dB. (b) Average number of SpDemux filters required by the algorithm for $\varepsilon_{\mathrm{ST}}$ = 10% and 1%. Insets show the received PM-QPSK signals after space-demultiplexing assuming $\varepsilon_{\mathrm{ST}}$ < 10%.

filter increase to ≈ 5 and the average value of Δ decreases from a maximum of ≈ 0.02 dB, see Fig. 5.12. These results show that the SNR penalty of the post-processed signal can be substantially enhanced by considering lower ε_{ST}, which tends to increases the numbers of SpDemux filters employed by the reduced-complexity SpDemux algorithm. In that way, the SNR improvements are due to the progressive use of SpDemux filters and, therefore, the performance of the algorithm is not mainly limited by the number of samples employed in the calculation of the inverse channel matrix. Such behavior can be observed in Fig. 5.12(a), where the improvements in the SNR penalty produced by the progressive application of the SpDemux filters are evident. In Fig. 5.12(b), it is shown the average number of SpDemux filters, N_f, required by the reduced-complexity algorithm as a function of the number of samples for both cases aforementioned. Inset shows the constellations for the received signal and the space-demultiplexed signal at the end of the first, second, third SpDemux filters and the reduced-complexity algorithm with $\varepsilon_{\mathrm{ST}}$ = 10%; assuming 1000 samples in the calculations of the inverse channel matrix. Like the average SNR penalty, the average number of SpDemux filters required by the algorithm tends to substantially decrease from the first ≈ 200 samples; whereas, after ≈ 200 samples, the average number of SpDemux tends to stabilize for both cases considered, see Fig. 5.12(b). For $\varepsilon_{\mathrm{ST}}$ = 10%, the average number of SpDemux filters tends to 4.1. For $\varepsilon_{\mathrm{ST}}$ = 1%, the algorithm requires on average 5.25 SpDemux filters. Notice that although the number of SpDemux filters considered in the iterative process is an integer, the aforementioned non-integer values result of the averaging over 100 trials.

In Fig. 5.13, it is shown the average value for Δ and the N_f required by the reduced-complexity SpDemux algorithm as a function of $\varepsilon_{\mathrm{ST}}$, assuming several number of samples in the calculations of the inverse channel matrix. Figure 5.13(a) shows the results in terms of convergence speed for the case of a PM-QPSK signal. For all the cases considered, the reduced-complexity SpDemux algorithm allows for a successful space-demultiplexing of the received signal. The average number of SpDemux filters is approximately the same for all the

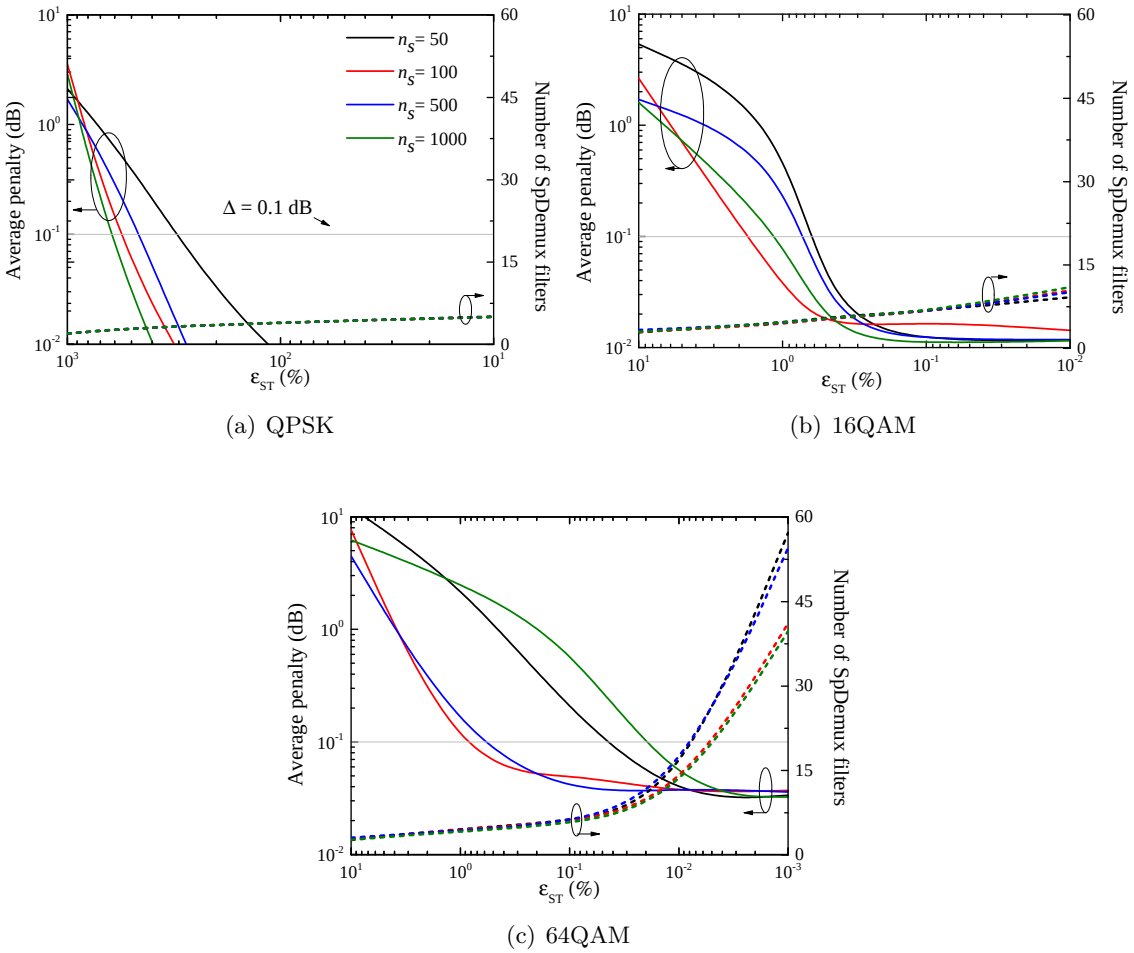

(a) QPSK (b) 16QAM

(c) 64QAM

Figure 5.13: Average SNR penalty (solid lines) and number of SpDemux filters (dashed lines) as function of ε_{ST} for several numbers of samples considered in the calculations of the inverse channel matrix for: (a) PM-QPSK signal; (b) PM-16QAM signal; and (c) PM-64QAM.

cases considered and its value tends to increase for smaller values of ε_{ST}. Figure 5.13(b) shows the results for the case of PM-16QAM signals. When compared with the QPSK, the space-demultiplexing of the 16QAM requires a smaller ε_{ST}. Regarding the number of SpDemux filters, results show that its value tends to increases as ε_{ST} decreases. In Fig. 5.13(c), it is shown the average value of Δ as a function of the ε_{ST} for a PM-64QAM signal. As in the previous cases, the received signal is successfully space-demultiplexed. However, the values of ε_{ST} required to keep Δ below than 0.1 dB is even smaller. The remaining penalty apparently tends for $\Delta \approx 0.03$ dB, with the number of SpDemux filters required by the algorithm varying between $\approx$ 40 and $\approx$ 60. This set of results show that the convergence speed tends to be faster for larger sets of samples and the number of SpDemux filters required by the algorithm tends to increase with the density of the modulation format. The increment in the number of SpDemux filters makes the algorithm more complex in terms of computational effort and, additionally, increases it's latency because the filters are consecutively applied to the received signal. However, the algorithm has a degree of freedom in ε_{ST}, which can be used to adjust

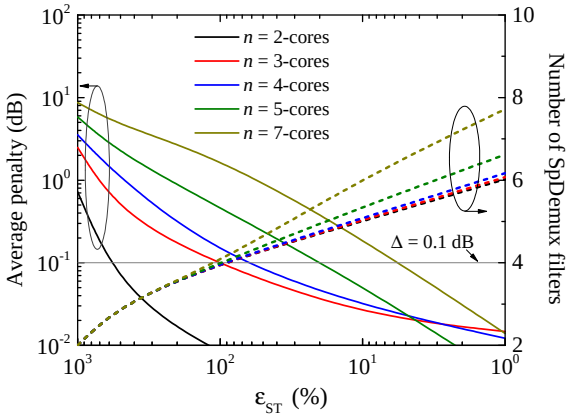

Figure 5.14: Average value of SNR penalty (solid lines) and number of SpDemux filters (dashed lines) as function of $\varepsilon_{\mathrm{ST}}$ for a SDM system based on 2-, 3-, 4-,5- and 7-cores CC-MCF, with each core carrying a PM-QPSK signal. In the calculation of the inverse channel matrix are assumed 100 samples.

the remaining penalty and, therefore, to control the number of SpDemux filters applied by the algorithm.

In order to analyse the scalability of the reduced-complexity SpDemux algorithm, we have performed simulations considering a SDM system supporting a large number of tributaries. In Fig. 5.14, it is shown the average value of Δ and N_f as function of $\varepsilon_{\mathrm{ST}}$ for a SDM system based on $n = 2, 3, 4, 5$ and 7-cores CC-MCF, where each core carries a PM-QPSK signal. Such results are obtained considering 100 samples in the calculations of the inverse channel matrix. For all the cases considered, the algorithm is able to successfully space-demultiplex the received signal. It should be noted that the successful space-demultiplexing is first achieved for SDM transmission systems with a lower degree of spatial diversity. As the number of tributaries increases, the algorithm tends to require more SpDemux filters because it needs to take into account more HoPss, hence increasing the computational complexity of the reduced-complexity SpDemux algorithm. Such increment in the number of HoPss tends to increase the number of iterations needed to successfully realign the best fit plane with the $\Psi_1 = 0$ plane in all the HoPss considered.

SNR tolerance

The role of the SNR in the convergence speed of the reduced-complexity algorithm is also analysed. For this purpose, we assume a PM-QPSK signal with SNR_{in} equal to 10, 20 and 30 dB. The average value of Δ as function of $\varepsilon_{\mathrm{ST}}$ is shown in Fig. 5.15, for the three aforementioned SNR and assuming 100 samples in the calculations of the inverse channel matrix. The algorithm is able to successfully space-demultiplex the received signals in the three cases analyzed. In addition, we note that the algorithm shows a faster convergence speed for signals with lower SNR_{in}. Although not shown in Fig. 5.15, the number of SpDemux filters tends to increase as the parameters $\varepsilon_{\mathrm{ST}}$ decrease, like in Fig. 5.13. For the three cases considered, the algorithm require approximately the same number of SpDemux filters to achieve the steady state. Nevertheless, the number of SpDemux filters marginally increases

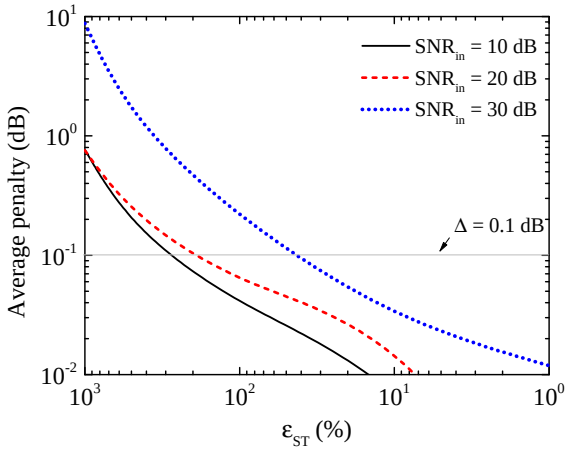

Figure 5.15: Average value of SNR penalty as function of $\varepsilon_{\mathrm{ST}}$ for a SDM system with a 3-core CC-MCF, each core carrying a PM-QPSK signal, considering values of SNR equal to 10, 20 and 30 dB.

for signals with higher SNR_{in}.

5.5.3 Performance assessment

Here, we compare the convergence speed and complexity of the two HoPs-based space-demultiplexing algorithms and a 4×4 time-domain equalizer based on data-aided normalised least mean squares (NLMS) algorithm with 1 tap [23]. Furthermore, both HoPs-based SpDemux algorithms are compared in terms of SNR tolerance. Without loss of generality, we assume a SDM transmission system based on a 2-core CC-MCF in which a single core carries a PM-QPSK signal with a SNR of 17 dB.

Convergence speed

The average value of the SNR penalty as function of the number of samples for both HoPs SpDemux and the NLMS algorithms is shown in Fig. 5.16. For a small amount of samples, both HoPs-based SpDemux algorithms achieve a better performance than the NLMS. In terms of SNR penalty, the NLMS requires ≈64 and ≈201 samples, for a step size of μ = 0.1 and 0.01, respectively, to achieve a penalty as low as Δ = 0.1 dB , see Fig. 5.16(b). While, the HoPs-based SpDemux algorithm requires 375 samples to achieve the same penalty. If we assume $\varepsilon_{\mathrm{ST}}$ = 90% in the reduced-complexity SpDemux algorithm, the space-demultiplexing can be carried out with an average SNR penalty of ≈0.7 dB. For a $\varepsilon_{\mathrm{ST}}$ = 50%, the algorithm needs 1250 samples to achieve a SNR penalty of 0.1 dB, despite the SNR penalty does not exceed the value of 0.2 dB for all the sets of samples considered. For $\varepsilon_{\mathrm{ST}}$ = 5%, the value of the SNR penalty is lower than 0.1 dB for all the sets of samples considered in the calculations of the inverse channel matrix. Despite Δ may present small fluctuations when assumed a lower number of samples, these results show that the performance of the reduced-complexity algorithm mainly depends on the choice of the parameter $\varepsilon_{\mathrm{ST}}$. While, in the static algorithm, the performance mainly depends on the number of samples considered in the calculation of the inverse channel matrix. Notice that we require 10 points in the HoPss as the minimum amount of samples to accurately estimate the best fit plane, see Fig. 5.16(b). Assuming

$\varepsilon_{\mathrm{ST}}$ = 5% and 10 samples in the calculations of the inverse channel matrix, the reduced-complexity SpDemux algorithm shows an improvement of the convergence speed of 84.38% over the NLMS with faster convergence speed. It should also be noted that the NLMS algorithm is working on data-aided mode to estimate the inverse channel matrix, while both HoPs-based space-demultiplexers are free of training symbols. When comparing both HoPs-based space-demultiplexing algorithms, the results show an improvement in the convergence speed of 97.33% for the reduced-complexity SpDemux algorithm.

Computational complexity

Since both HoPs-based space-demultiplexing algorithms trace the best fit plane by means of a linear least square regression, the computational complexity depends on the number of best fit planes evaluated and on the number of samples considered in the calculations of the best fit plane. The number of HoPss required by the static algorithm is given by

$$N_{\mathrm{HoPs,\ ref}} = 2^{g_s} g_s! \,, \tag{5.35}$$

and, therefore, the complexity evolves as $\sim O(n_t^2!)$, with n_t denoting the number of tributary signals. For the reduced-complexity SpDemux algorithm, the number of HoPss required by a single SpDemux filter can be expressed as

$$N_{\mathrm{HoPs}} = \sum_{g=2}^{g_s} g[2(g-1)] = \frac{2g_s}{3}(g_s^2 - 1) \,, \tag{5.36}$$

resulting in a $\sim O(n_t^6)$ complexity. In each HoPs, the number of real multiplications, N_{m}, and additions, N_{s}, required by the least-mean square algorithm to calculate the best fit plane is given by [24]

$$N_{\mathrm{m}} = 12n_s^2 + 5n_s + 198 \,, \tag{5.37a}$$

and

$$N_{\mathrm{s}} = 12n_s^2 + 5n_s + 196 \,, \tag{5.37b}$$

respectively, with n_s denoting the number of samples. Therefore, the complexity reduction gain, G_{CR}, of the reduced-complexity approach over the first one can be written as

$$G_{CR}(\mathrm{dB}) = -10 \log\left(\frac{N_f N_{\mathrm{HoPs}} N_{\mathrm{m}}}{N_{\mathrm{HoPs,\ ref}} N_{\mathrm{m}}}\right) . \tag{5.38}$$

The complexity reduction gain is calculated for a SNR penalty of 0.1 dB and the number of samples is chosen taking into account this threshold. Note that, such values were stated in the previous subsection. Moreover, the reduced-complexity SpDemux algorithm needs on average N_f = 4 for successful space-demultiplexing the received signal, thus leading to a complexity reduction gain of G_{CR} = 50.36 dB or 99.99%.

The NLMS based SpDemux algorithm needs n_t^2 FIR filters with 1 tap, each filter requiring $N_{\mathrm{m}} = 20n_s$ and $N_{\mathrm{s}} = 4n_s$. When the reduced-complexity SpDemux algorithm is compared with the NLMS in terms of computational complexity, one obtains a complexity reduction gain of G_{CR} = −19.41 dB, which means that the reduced complexity approach is 98.86% more complex than the NLMS. Note that, such values were obtained assuming n_s = 64.

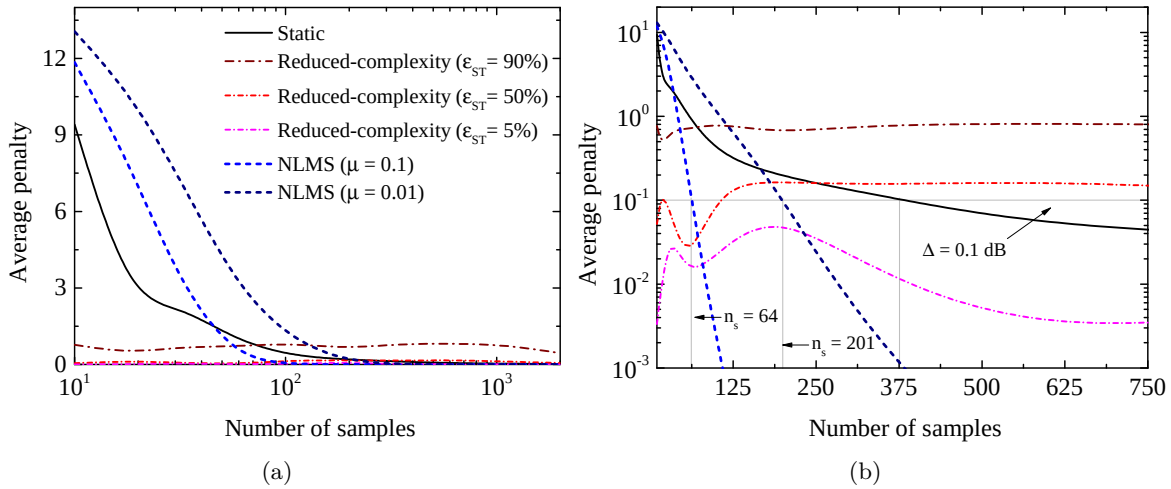

Figure 5.16: (a) Average value of SNR penalty in dB as function of the number of samples computed after space-demultiplexing through the static, the reduced-complexity algorithm, assuming $\varepsilon_{\mathrm{ST}} = 90, 50$ and 5%, and with the NLMS, assuming $\mu = 0.1$ and 0.01. (b) Zoom in of Fig. 5.16(a), with the SNR penalty in log scale and the threshold of $\Delta = 0.1$ dB pointed out by a solid line. It is used a SDM system based on a 2-core CC-MCF transmitting PM-QPSK signals with a SNR of 17 dB.

SNR tolerance

Both HoPs-based SpDemux algorithms are compared in terms of SNR tolerance. Thus, the SNR penalty after the space-demultiplexing considering signals with distinct SNR are compared. In Fig. 5.17, it is shown the SNR penalty after space-demultiplexing considering the first developed approach for SpDemux based on HoPss, with $n_s = 2000$, and the reduced-complexity SpDemux algorithm with $\varepsilon_{\mathrm{ST}} = 5\%$ and $n_s = 700$. For the first approach, Δ tends to slightly increase with the SNR. However, such penalty can be reduced by increasing the number of samples considered in the calculations of the inverse channels matrix. The SNR penalty provided by the reduced-complexity SpDemux algorithm is substantially lower than the first developed approach, in the entire range of SNRs considered in the analyses. Furthermore, the SNR penalty also tends to slightly increase with the SNR.

5.5.4 Impact of fiber-optic impairments

In this section, we briefly discuss the remaining effects of fiber propagation in the signal representation in HoPss, including MD and chromatic dispersion. A detailed analysis of optical link impairments is beyond the scope of this subsection. It should be noted that the effects of MDL are extensively analysed in Chapter 6.

HoPs-based SpDemux algorithms still have some constraints, namely the high sensitivity to the MD. In the single-mode case, the PMD can break the symmetry plane of the received samples when represented in the Stokes space, hindering the digital PolDemux. In SDM transmission systems, the MD, the counterpart of PMD in the single-mode case, can also break the symmetry plane of the received samples in the HoPss. In fact, this is a major limitation of HoPs-based space-demultiplexing algorithms.

The mitigation of MD must be addressed by improving and developing a new kind of optical fibers or by developing more efficient MIMO post-processing techniques. In fact, any

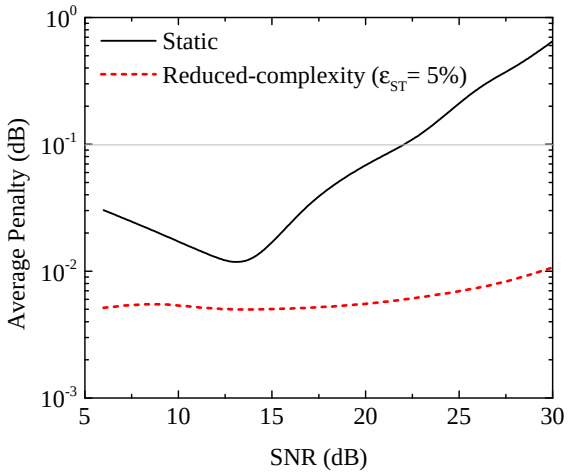

Figure 5.17: Average value of SNR penalty for the reduced-complexity and the static algorithm as function of the SNR of the transmitted signal for a SDM system with a 2-core CC-MCF, each core carrying a PM-QPSK signal.

commercial solution must involve both approaches. In the optical domain, the MD can be mitigated by using new fibers with optimized index profiles [25], by link engineering [2, 26, 27] and even by pre-compensation [28]. The development of novel fibers with low, or even negligible, values of MD is a key step, that actually was already started with the fabrication of CC-MCF and dispersion compensated links based on FMFs. On the other hand, residual amounts of MD should be compensated by digital subsystems at the coherent receiver. In the single-mode case, it was proposed a sequential algorithm in which the PMD is compensated neglecting the state of polarization and, afterward, a PolDemux algorithm is employed to demultiplexing both polarizations [20]. Moreover, a joint equalization scheme for PMD compensation and PolDemux was also proposed by employing extended Kalman filter [29]. In principle, these digital stages can be extended to SDM-based transmission systems in order to substantially decrease the MD before the HoPs-based space-demultiplexing.

The chromatic dispersion tends to affect both polarization states in the same way. Therefore, these distortions increases the dispersion of the samples in the HoPss without breaking the symmetry plane. In that way, HoPs-based space-demultiplexing algorithms tend to be robust against the chromatic dispersion.

5.6 Summary

In this Chapter, we have analysed the signal representation in HoPss. The Pauli spin vector for each HoPs was obtained by properly handling the generators of the GSS. Then, we show that an arbitrary pair of complex-modulated signals can be described by a lens-like object in the respective HoPs and that crosstalk induces a rotation of such object in the HoPs. In order to compensate the crosstalk, the lens-like object or in a practical case the best fit plane to the received samples must be realigned. The inverse channel matrix is calculated through a progressive space-demultiplexing of all pairs of signals, in which the sequence with lower sum of the absolute value of the residuals is chosen. However, in this algorithm, all the possible sequences of SpDemux steps must be evaluated. In order to decrease the computational effort

of the HoPs-based space-demultiplexing algorithm, it was proposed a reduced-complexity algorithm in which the inverse channels matrix is iteratively constructed. For the particular case of four tributaries, the complexity-reduced algorithm presents improvements of 97% in terms of convergence speed and 99% in terms of computational complexity over the previously proposed algorithm. Both algorithms proposed are also compared with the NLMS, showing the reduced complexity approach an improvement of 84% over the NLMS in the convergence speed. It should be noted that HoPs-based space-demultiplexing do not require training symbols, in contrast to the NLMS algorithm, and is modulation format agnostic and robust to phase fluctuations and frequency offsets.

Bibliography

[1] D. J. Richardson, J. M. Fini, and L. E. Nelson, "Space-division multiplexing in optical fibres," *Nature Photonics*, vol. 7, pp. 354–362, May 2013.

[2] G. Li, N. Bai, N. Zhao, and C. Xia, "Space-division multiplexing: the next frontier in optical communication," *Advances in Optics and Photonics*, vol. 6, no. 4, pp. 413–487, Dec 2014.

[3] S. Savory, "Digital coherent optical receivers: algorithms and subsystems," *IEEE Journal of Selected Topics in Quantum Electronics*, vol. 16, no. 5, pp. 1164–1179, 2010.

[4] S. Ziaie, N. J. Muga, F. P. Guiomar, G. M. Fernandes, R. M. Ferreira, A. Shahpari, A. L. Teixeira, and A. N. Pinto, "Experimental assessment of the adaptive Stokes space-based polarization demultiplexing for optical metro and access networks," *IEEE/OSA Journal of Lightwave Technology*, vol. 33, no. 23, pp. 4968–4974, Dec 2015.

[5] B. Szafraniec, B. Nebendahl, and T. Marshall, "Polarization demultiplexing in Stokes space," *Optics Express*, vol. 18, no. 17, pp. 17 928–17 939, 2010.

[6] M. Visintin, G. Bosco, P. Poggiolini, and F. Forghieri, "Adaptive digital equalization in optical coherent receivers with Stokes-space update algorithm," *IEEE/OSA Journal of Lightwave Technology*, vol. 32, no. 24, pp. 4759–4767, Dec 2014.

[7] N. J. Muga and A. N. Pinto, "Adaptive 3-D Stokes space-based polarization demultiplexing algorithm," *IEEE/OSA Journal of Lightwave Technology*, vol. 32, no. 19, pp. 3290–3298, 2014.

[8] N. J. Muga and A. N. Pinto, "Digital PDL compensation in 3D Stokes space," *IEEE/OSA Journal of Lightwave Technology*, vol. 31, no. 13, pp. 2122–2130, 2013.

[9] N. J. Muga and A. N. Pinto, "Extended Kalman filter vs. geometrical approach for Stokes space-based polarization demultiplexing," *IEEE/OSA Journal of Lightwave Technology*, vol. 33, no. 23, pp. 4826–4833, Dec 2015.

[10] D. Naidoo, F. S. Roux, A. Dudley, I. Litvin, B. Piccirillo, L. Marrucci, and A. Forbes, "Controlled generation of higher-order Poincaré sphere beams from a laser," *Nature Photonics*, vol. 10, no. 5, pp. 327–332, 2016.

[11] G. Milione, H. Sztul, D. Nolan, and R. Alfano, "Higher-order Poincaré sphere, Stokes parameters, and the angular momentum of light," *Physical review letters*, vol. 107, no. 5, p. 053601, 2011.

[12] A. Holleczek, A. Aiello, C. Gabriel, C. Marquardt, and G. Leuchs, "Classical and quantum properties of cylindrically polarized states of light," *Optics Express*, vol. 19, no. 10, pp. 9714–9736, May 2011.

[13] G. Milione, D. A. Nolan, and R. R. Alfano, "Determining principal modes in a multimode optical fiber using the mode dependent signal delay method," *Journal of the Optical Society of America B*, vol. 32, no. 1, pp. 143–149, Jan 2015.

[14] J. P. Gordon and H. Kogelnik, "PMD fundamentals: Polarization mode dispersion in optical fibers," *Proceedings of the National Academy of Sciences*, vol. 97, no. 9, pp. 4541–4550, 2000.

[15] C. Antonelli, A. Mecozzi, M. Shtaif, and P. Winzer, "Stokes-space analysis of modal dispersion in fibers with multiple mode transmission," *Optics Express*, vol. 20, no. 11, pp. 11 718–11 733, May 2012.

[16] G. Milione, M. Lavery, H. Huang, Y. Ren, G. Xie, T. Nguyen, E. Karimi, L. Marrucci, D. Nolan, R. Alfano *et al.*, "4× 20 Gbit/s mode division multiplexing over free space using vector modes and a q-plate mode (de) multiplexer," *Optics Letters*, vol. 40, no. 9, pp. 1980–1983, 2015.

[17] H. Huang, G. Milione, M. Lavery, G. Xie, Y. Ren, Y. Cao, N. Ahmed, T. Nguyen, D. Nolan, M.-J. Li *et al.*, "Mode division multiplexing using an orbital angular momentum mode sorter and MIMO-DSP over a graded-index few-mode optical fibre," *Scientific Reports*, vol. 5, p. 14931, 2015.

[18] G. Bosco, M. Visintin, P. Poggiolini, and F. Forghieri, "A novel update algorithm in stokes space for adaptive equalization in coherent receivers," in *In proceedings of the Optical Fiber Conference (OFC)*, March 2014, p. Th3E.6.

[19] S. Arik, D. Askarov, and J. Kahn, "Adaptive frequency-domain equalization in mode-division multiplexing systems," *IEEE/OSA Journal of Lightwave Technology*, vol. 32, no. 10, pp. 1841–1852, May 2014.

[20] F. Buchali, H. Buelow, K. Schuh and W. Idler, "4D-CMA: Enabling separation of channel compensation and polarization demultiplex," in *In proceedings of the Optical Fiber Conference (OFC)*. Optical Society of America, 2015, p. Th2A.15.

[21] S. K. Stein, *Calculus and analytic geometry*. McGraw-Hill Companies, 1982.

[22] R. Shafik, M. S. Rahman, and A. Islam, "On the extended relationships among EVM, BER and SNR as performance metrics," in *International Conference on Electrical and Computer Engineering*. IEEE, 2006, pp. 408–411.

[23] I. Kaminow, T. Li, and A. Willner, *Optical fiber telecommunications VB: systems and networks*. Elsevier, 2010, ch. 11.

[24] G. Golub and C. Van Loan, *Matrix computations*. Johns Hopkins University Press, 2012, vol. 3.

[25] F. Ferreira, D. Fonseca, and H. da Silva, "Design of few-mode fibers with M-modes and low differential mode delay," *IEEE/OSA Journal of Lightwave Technology*, vol. 32, no. 3, pp. 353–360, 2014.

[26] S. Arik, K.-P. Ho, and J. Kahn, "Group delay management and multiinput multioutput signal processing in mode-division multiplexing systems," *IEEE/OSA Journal of Lightwave Technology*, vol. 34, no. 11, pp. 2867–2880, June 2016.

[27] S. Arık, K.-P. Ho, and J. Kahn, "Delay spread reduction in mode-division multiplexing: Mode coupling versus delay compensation," *IEEE/OSA Journal of Lightwave Technology*, vol. 33, no. 21, pp. 4504–4512, 2015.

[28] M. B. Shemirani, J. P. Wilde, and J. M. Kahn, "Adaptive compensation of multimode fiber dispersion by control of launched amplitude, phase, and polarization," *IEEE/OSA Journal of Lightwave Technology*, vol. 28, no. 18, pp. 2627–2639, Sept 2010.

[29] H. Xu, X. Zhang, X. Tang, C. Bai, L. Xi, W. Zhang, and H. Zheng, "Joint scheme of dynamic polarization demultiplexing and PMD compensation up to second order for flexible receivers," *IEEE Photonics Journal*, vol. 9, no. 6, pp. 1–15, Dec 2017.

Chapter 6

HoPs-based Compensation of MDL

Conversely to MD, which can be fully compensated by digital techniques at the optical coherent receiver, mode dependent gains or losses (collectively referred to as MDL), are a fundamental and stochastic performance-limiting factor of SDM-based transmission systems [1–3]. In a extreme case, the signal degradation induced by MDL is equivalent to a reduction in the number of propagating channels, leading to a proportional decrease in the aggregated bit-rate of the SDM transmission system. Compensation and monitoring of such pernicious effect is therefore of paramount importance in future flexible optical networks based on SDM.

In this Chapter, we analyse the effect of MDL in the signal representation of complex-modulated signals in HoPss. Based on such analyses, we show that the MDL vector can be accurately estimated in HoPss and therefore the signal distortions arising from MDL can be also successfully compensated. After demonstrated the operation principle of HoPs-based MDL compensation, we propose a simplified approach with lower computational complexity. Lastly, the proposed technique is analyzed in terms of SNR enhancements of the post-processed signal.

6.1 MDL compensation

The MDL in the multi-modal regime is the counterpart of the polarization-dependent loss (PDL) in the single-mode regime. The latter is usually monitored and compensated at the coherent receiver by means of advanced DSP algorithms, improving in that way the SNR of the post-processed signal [4–6]. If the transmission channel is free of PDL, the best fit plane to the received samples represented in the Stokes space contains the center of the Poincaré sphere and it can be employed to calculate a demultiplexing matrix [7, 8]. Conversely, in the presence of PDL, the constellation of points representing the state of polarization of the signal samples suffers a small translation and consequently the best fit plane is shifted from the center of the Poincaré sphere [5, 9]. For lower or moderated values of MDL, the demultiplexing matrix can still be estimated from the best fit plane. However, the PolDemux stage may induce an additional penalty in the post-processed signal. By assessing the aforementioned shift, the PDL can be estimated and the signal distortions arising from PDL can be compensated, improving the PolDemux stage and avoiding any additional (or substantially mitigating the remaining) penalty in the post-processed signal [5, 9].

As described in Chapter 5, the HoPs-based DSP for SDM transmission systems was

also recently proposed [10–12]. Using the signal representation in HoPs, the task of space-demultiplexing was accomplished without training sequences. Furthermore, these algorithms are modulation format agnostic and tends to be robust against phase fluctuations and frequency offsets [10, 11]. However, their performance will certainly benefit from the availability of new impairment compensation techniques. In particular, techniques whose principle of operation is also based on the HoPs representation.

6.2 MDL monitoring and compensation techniques

Throughout this Chapter, we follow the definition of HoPs introduced in section 5.2.1. Thus, the Stokes parameters for the GSS can be directly written as a linear combination of the Stokes parameters for the g_s HoPs [10]. Such property can be very useful to assess the channel capacity [1]. However, for the purpose of DSP, or more precisely MDL monitoring and compensation, the Pauli spin vector can be computed neglecting the parameters $\sqrt{n}$ and κ introduced in section 5.2.1, which can substantially simplify the computation of the Pauli spin vector and further calculations. This simplification will be explained along the subsection 6.2.

Scenario 1: channel only with MDL

Firstly, we assume the simplest case: the SDM link is only affect by MDL, i.e., crosstalk and dispersion are not taken into account. Assuming a transmission system with a spatial diversity of 2 (four tributaries), the channel transfer matrix can be written as

$$\boldsymbol{M}_{\text{tot}} = \text{diag}\{\rho_1, \rho_2, \rho_3, \rho_4\}\,, \tag{6.1}$$

where ρ_j^2, with $j = 1, ...4$, is the gain/loss for the j tributary and diag$\{\cdot\}$ denotes the diagonal matrix. For this particular case, the MDL vector is defined as $\boldsymbol{\Gamma} = (\rho_1, \rho_2, \rho_3, \rho_4)^2$, and the average value of MDL is given by [2],

$$\text{MDL}_{\text{AVG}} = 10\log\left\{\max\left\{\boldsymbol{\Gamma}\right\}/\min\left\{\boldsymbol{\Gamma}\right\}\right\}. \tag{6.2}$$

In the general case, the MDL vector is comprised by the eigenvalues of the channel transfer matrix. By applying (6.1) in (5.2), the received signal in the Jones space can be written as,

$$|\phi\rangle = \text{MDL}_{\text{AVG}}\,|\psi\rangle = \left(\rho_1 \upsilon_1, \rho_2 \upsilon_2, \rho_3 \upsilon_3, \rho_4 \upsilon_4\right)^T\,, \tag{6.3}$$

and the Stokes parameters, for a given HoPs, are calculated by using (6.3) in (5.4) as follows,

$$\Psi_1^{(g,f)} = \langle\phi|\,\boldsymbol{\Lambda}_1^{(g,f)}\,|\phi\rangle = \rho_g^2 a_g^2 - \rho_f^2 a_f^2\,, \tag{6.4a}$$

$$\Psi_2^{(g,f)} = \langle\phi|\,\boldsymbol{\Lambda}_2^{(g,f)}\,|\phi\rangle = 2\rho_g^2 \rho_f^2 a_g a_f \cos\left(\delta_{gf}\right), \tag{6.4b}$$

$$\Psi_3^{(g,f)} = \langle\phi|\,\boldsymbol{\Lambda}_3^{(g,f)}\,|\phi\rangle = 2\rho_g^2 \rho_f^2 a_g a_f \sin\left(\delta_{gf}\right), \tag{6.4c}$$

with $\delta_{f,g} = \varphi_f - \varphi_g$.

Without loss of generality, the operation principle of the proposed technique is demonstrated for the first and second tributaries represented in the respective HoPs. Following similar steps, the same results can be achieved for the remaining pairs of tributaries. For

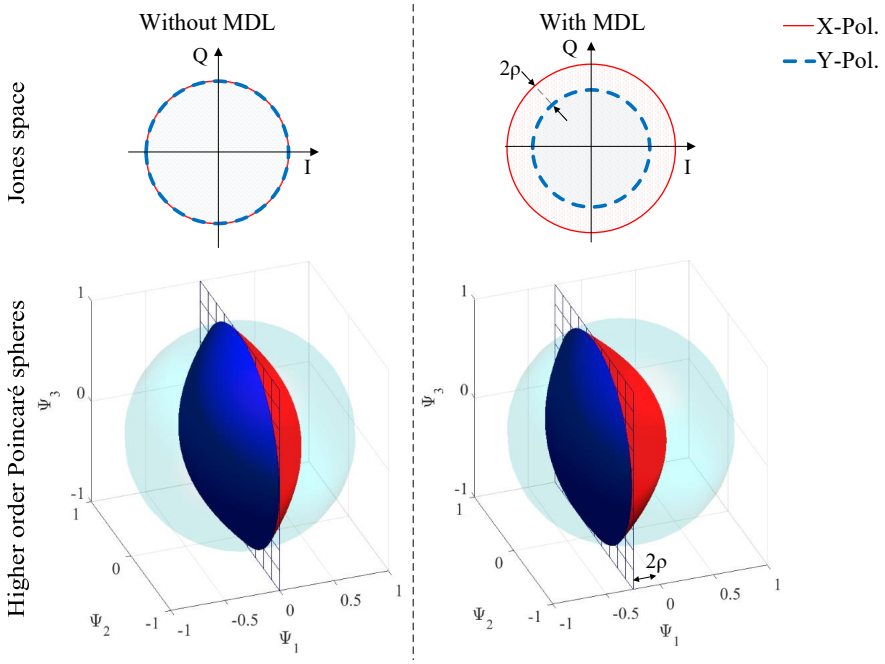

Figure 6.1: Upper row: schematic representation of an arbitrary modulation format in the Jones space without and with MDL. Lower row: schematic representation of the first and second tributaries containing arbitrary modulation formats in the HoPs after propagation through a SDM link with and without MDL.

this purpose, we assume that only a single tributary signal is modulated, while the remaining tributaries have constant phase and amplitude. Note that such assumption does not impose any limitation to the transmission system. For the tributary signal that carries the complex-modulated signal, we assume a hypothetical complex-modulation format that is confined to an unit circle in the Jones space,

$$|\psi\rangle = \left(1, re^{\theta}, 1, 1\right)^{T}, \tag{6.5}$$

with $0 < \theta \leq 2\pi$ and $0 < r \leq 1$, see Fig. 6.1. By using (6.5) in (6.4), a set of parametric equations can be written as

$$\Psi_1^{(1,2)} = \left(1 - r^2\right) - \rho^{(1,2)}\left(1 + r^2\right), \tag{6.6a}$$

$$\Psi_2^{(1,2)} = 2r\sqrt{1 + \rho^{(1,2)}}\sqrt{1 - \rho^{(1,2)}}\cos\left(\delta_{1,2}\right), \tag{6.6b}$$

$$\Psi_3^{(1,2)} = 2r\sqrt{1 + \rho^{(1,2)}}\sqrt{1 - \rho^{(1,2)}}\sin\left(\delta_{1,2}\right), \tag{6.6c}$$

describing a paraboloidal surface in the respective HoPs. In Fig. 6.1, the surface described by (6.6) is drawn in red. While in blue, it is drawn the paraboloidal surface representing an arbitrary complex-modulated signal carried in the first tributary assuming the remaining tributaries with constant phase and amplitude. If the parameters $\sqrt{n}$ and κ were considered in the written of the Pauli spin vector, the parameter $\Psi_1^{(1,2)}$ and the left side of (6.6) would be also affect by the aforementioned parameters, canceling each other. For a normalized signal, i.e., $r = 1$, the lens-like object is shifted along the axis $\Psi_1^{(1,2)}$ by a maximum value of

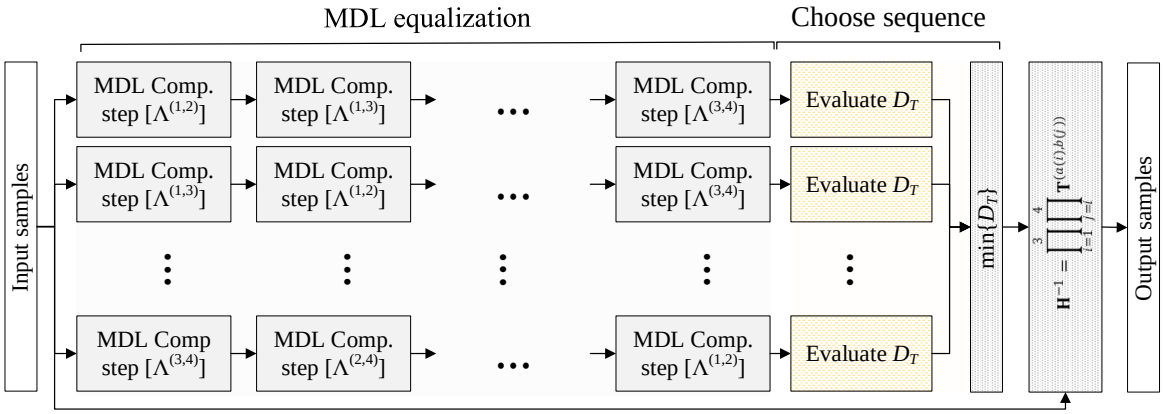

Figure 6.2: Schematic of MDL monitoring and compensation technique.

$2\rho^{(1,2)}$, which can be calculated from (6.6a). On the other hand, the parameter $\rho^{(1,2)}$ can be estimated from the plane containing the boundary between both paraboloidal surfaces,

$$\rho^{(1,2)} = -\frac{d^{(1,2)}}{2}\,, \tag{6.7}$$

where $d^{(1,2)}$ is given by the average value of $\langle \Psi_1^{(1,2)} \rangle$. Thus, in a given HoPs, the gain/loss power imbalances can be successfully compensated by re-center the constellations at the origin of the HoPs; as in the single-mode case. Each one of the g_s matrices $\boldsymbol{T}^{(f,g)}$, henceforward called of translation matrices, can be written as

$$\boldsymbol{T}^{(f,g)}(k,l) = \begin{cases} \sqrt{1+\rho^{(f,g)}} & \text{if } k = g, l = g \\ \sqrt{1-\rho^{(f,g)}} & \text{if } k = f, l = f \\ 1 & \text{if } k = l \text{ and } k, l \neq g, f \\ 0 & \text{otherwise} \end{cases}. \tag{6.8}$$

However, the entire MDL vector can only be assessed by analysing the gain/loss power imbalances in all HoPss. In that way, the inverse of the channel transfer matrix (6.1) is rewritten as

$$\boldsymbol{M}_{\text{tot}}^{-1} = \prod_{f=1}^{n-1} \prod_{g=f+1}^{n} \boldsymbol{T}^{(f,g)}\,, \tag{6.9}$$

where the matrix $\boldsymbol{T}^{(f,g)}$ only accounts for the power imbalances between the f and g tributaries. The g_s translation matrices are calculated one after other. In other words, the power imbalances for the pair of tributaries considered in the first HoPs are compensated before the calculation of the second matrix $\boldsymbol{T}^{(f,g)}$, and so on.

Although the g_s matrices $\boldsymbol{T}^{(f,g)}$ commute, the procedure that leads to the calculations of the matrices does not commute. In that way, the calculations of the inverse channel matrices, $\boldsymbol{M}_{\text{tot}}^{-1}$, depends on the sequence of HoPs considered. Therefore, in the calculations of the MDL vector, all possible combinations of HoPs are considered. After performed the MDL compensation following a particular sequence, the parameter d_t is evaluated according to

$$d_t = \sum_{f=1}^{n-1} \sum_{g=h}^{n} |d^{(f,g)}|\,. \tag{6.10}$$

For all possible sequences of HoPs, the parameter d_t is evaluated and the sequence with lower value of d_t is chosen, see the schematics shown in Fig. 6.2. In Fig. 6.2, the "MDL compensation step" denotes the set of operations required to calculate the translation matrix. It should be emphasized that a space-multiplexed signal without MDL (or fully compensated) has $d_t \approx 0$. In that sense, the minimum value of parameter d_t allows to find a suitable sequence of translation matrices. A detailed explanation is pointed out in the following subsection.

Scenario 2: channel with crosstalk and MDL

Among other effects, the propagation through a real SDM link induces crosstalk and MDL. The conjugation of both phenomena adds complexity to the MDL monitoring and compensation technique. In this subsection, we are going to show that the methodology presented in the previous subsection can be properly enhanced in order to estimate the MDL vector in the presence of crosstalk. In this scenario, the lens-like object appears rotated (due to crosstalk) and shifted from the origin of the sphere (due to MDL). Therefore, the best fit plane is no longer parallel to the $\Psi_1^{(f,g)} = 0$ plane, and the mean point of the constellation does not belong to the $\Psi_1^{(f,g)}$ axis. The value of gain/loss power imbalance is given by the distance between the central point of the distorted lens-like object, or in practical terms the central point of the constellation, and the origin of the sphere according to

$$\rho^{(f,g)} = -\frac{D^{(f,g)}}{2}, \tag{6.11}$$

with the central point of the constellation, $D^{(f,g)}$, calculated as

$$D^{(f,g)} = \sqrt{{d_1^{(f,g)}}^2 + {d_2^{(f,g)}}^2 + {d_3^{(f,g)}}^2}, \tag{6.12}$$

where $d_j^{(f,g)} = \langle \Psi_j^{(f,g)} \rangle = \frac{1}{N} \sum_{l=1}^{N} \Psi_j^{(f,g)}(l)$, with $j = 1, 2$ and 3. Notice that a statistically significant number of samples must be considered in the calculations of $D^{(f,g)}$ to assure that the center of the constellation was accurately estimated.

In order to compensate for the MDL in the presence of crosstalk, the center of the constellation must be shifted to the origin of the HoPs. For such purpose, a set of rotations and translations matrices are applied to the received samples [5],

$$\begin{aligned} |\psi\rangle_{out} = &\left\{ \boldsymbol{U}_2^{(f,g)}\left(-\frac{\pi}{2}\right) \boldsymbol{T}^{(f,g)}(d_3)\, \boldsymbol{U}_2^{(f,g)}\left(\frac{\pi}{2}\right) \right\} \times \\ &\left\{ \boldsymbol{U}_3^{(f,g)}\left(-\frac{\pi}{2}\right) \boldsymbol{T}^{(f,g)}(d_2)\, \boldsymbol{U}_3^{(f,g)}\left(\frac{\pi}{2}\right) \right\} \boldsymbol{T}^{(f,g)}(d_1)\, |\psi\rangle_{in}, \end{aligned} \tag{6.13}$$

with $|\psi\rangle_{in}$ and $|\psi\rangle_{out}$ denoting the signal before and after MDL compensation, respectively. In the Jones space, the rotation matrices $\boldsymbol{U}_3(\theta)$ and $\boldsymbol{U}_2(\theta)$ can be written as,

$$\boldsymbol{U}_3(\theta)^{(g,f)}(k,l) = \begin{cases} \cos(\theta/2) & \text{if } k = g, l = g \\ -\sin(\theta/2) & \text{if } k = g, l = f \\ \sin(\theta/2) & \text{if } k = f, l = g \\ \cos(\theta/2) & \text{if } k = f, l = f \\ 1 & \text{if } k = l \text{ and } k, l \neq g, f \\ 0 & \text{otherwise} \end{cases}, \tag{6.14}$$

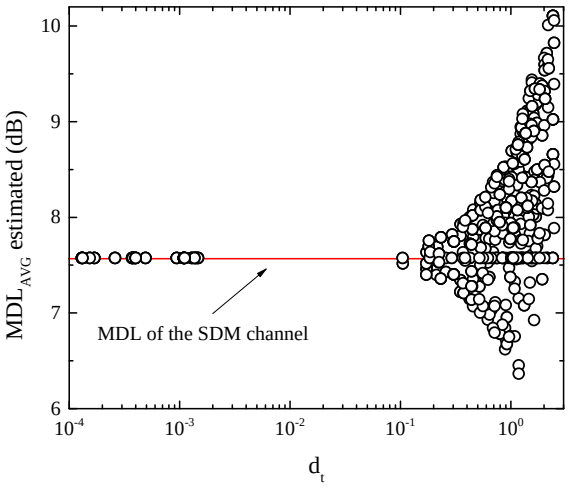

Figure 6.3: $\mathrm{MDL_{AVG}}$ as function of the parameter d_t for all the possible sequences of HoPS. The MDL vector can be found by choosing the lower value of d_t. The real value of $\mathrm{MDL_{AVG}}$ is pointed out by the solid line.

and

$$\boldsymbol{U}_2(\theta)^{(g,f)}(k,l) = \begin{cases} \cos(\theta/2) & \text{if } k=g, l=g \\ i\sin(\theta/2) & \text{if } k=g, l=f \\ i\sin(\theta/2) & \text{if } k=f, l=g \\ \cos(\theta/2) & \text{if } k=f, l=f \\ 1 & \text{if } k=l \text{ and } k,l \neq g,f \\ 0 & \text{otherwise} \end{cases}, \tag{6.15}$$

respectively. The set of operations performed in (6.13) can be summarized as follows: the constellation is shifted by d_1 along the axis $\Psi_1^{(f,g)}$ using $\boldsymbol{T}^{(f,g)}(d_1)$. Then, the lens-like object is shifted along the axis $\Psi_2^{(f,g)}$. Before shifted, the samples must be rotated around the axis $\Psi_3^{(f,g)}$ employing $\boldsymbol{U}_3^{(f,g)}$ and afterwards displaced of d_2 along the axis $\Psi_2^{(f,g)}$. In order to get back the original spatial orientation of the constellation, this is again rotated in the inverse way by applying again $\boldsymbol{U}_3^{(f,g)}$. Lastly, a similar procedure is employed at the third stage, which accounts for shift the samples along the axis $\Psi_3^{(f,g)}$. In this case, the rotations are made around the axis $\Psi_2^{(f,g)}$.

6.2.1 Performance assessment

In order to demonstrate the operation principle of the MDL compensation technique, we consider a PM-QPSK signal transmitted through a SDM transmission system with 7.6 dB of MDL. Firstly, the MDL is compensated assuming a given sequence of translation matrices or HoPss. Secondly, the parameter d_t is calculated for this particular sequence. Following this procedure, the parameter d_t is computed for the remaining sequences. In Fig. 6.3, it is shown the value of the $\mathrm{MDL_{AVG}}$ estimated as function of d_t for all possible sequences of HoPs. Results show that the sequence with lower value of d_t provides an optimal estimation of $\mathrm{MDL_{AVG}}$. Hence, this sequence is chosen to perform the MDL compensation.

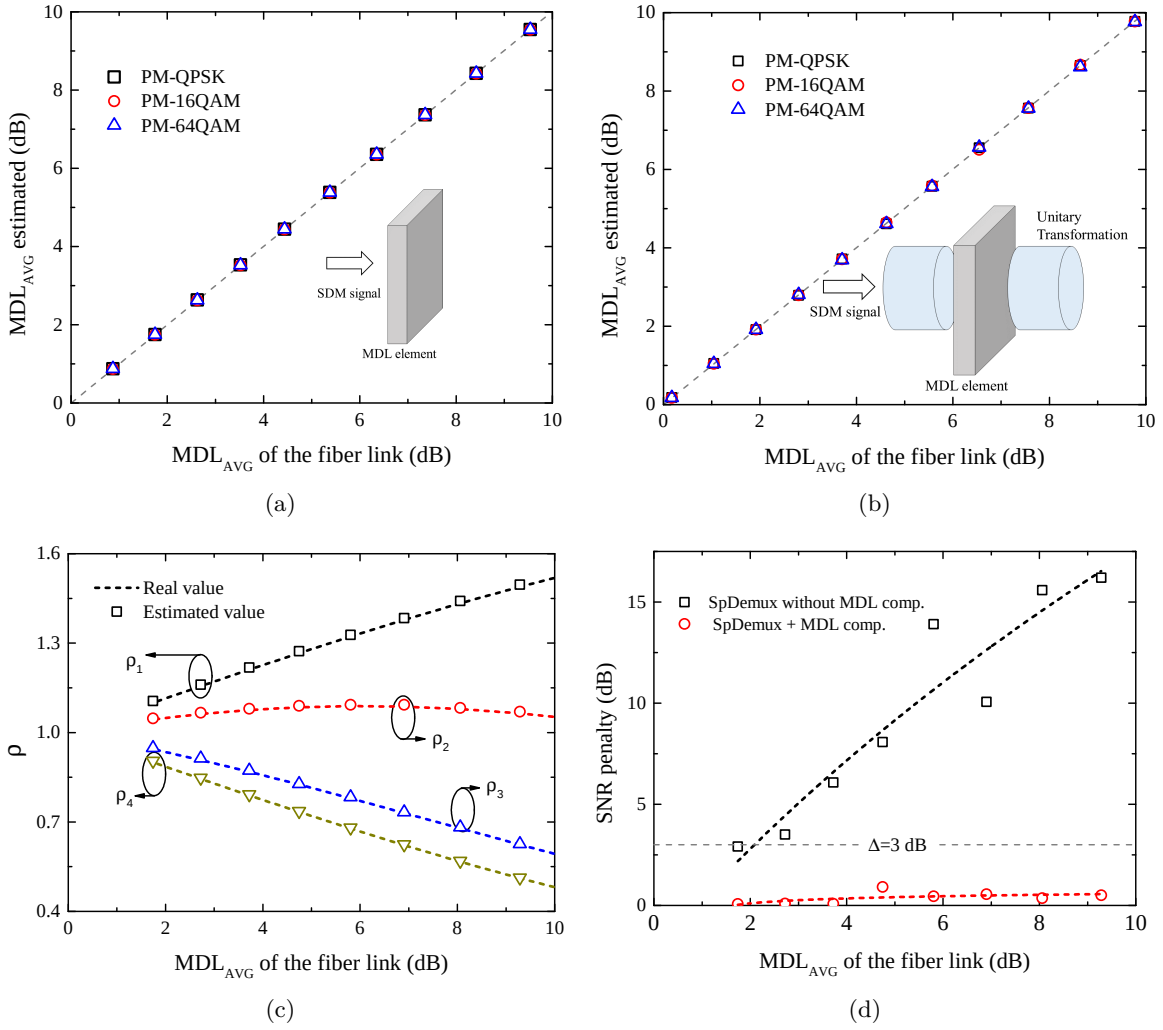

Figure 6.4: (a) Estimated MDL_{AVG} as function of the real value of MDL, assuming a PM-QPSK, PM-16QAM and PM-64QAM signals. In the link is only considered MDL. (b) Estimated value of MDL as a function of the real value of MDL, considering PM-QPSK, PM-16QAM and 64-QAM signals. In the link is considered crosstalk and MDL. (c) MDL vector as function of the MDL of the link. In the link is considered crosstalk and MDL. (d) SNR penalty as function of the MDL_{AVG} for a PM-QPSK signal after space-demultiplexing with and without MDL compensation.

The performance of the proposed MDL monitoring and compensation technique is analysed in terms of the value of MDL_{AVG} estimated and the SNR penalty of the post-processed signal, respectively. In each spatial channel, we assume a PRBS of 2^{18} bits coded in different complex-modulation formats, including PM-QPSK, PM-16QAM and PM-64QAM, with optical SNRs of 17, 23 and 30 dB, respectively. The SDM link is described by the multisection propagation model, described in section 5.3. We assume a SDM transmission link based on CC-MCF with a spatial diversity of 2 (i.e., a 2-core CC-MCF). Without loss of generality, we are also assuming that all linear and nonlinear transmission impairments can be fully compensated before the SpDemux plus the MDL compensation stage, with the exception of optical noise, crosstalk and MDL.

Channel only with MDL

In order to analyze the performance of the proposed MDL monitoring technique, the real and the estimated values of MDL_{AVG} are compared assuming a transmission system only with MDL. The HoPs-based monitoring technique provides an accurate estimation of the MDL_{AVG} for values as high as 10 dB for the three complex-modulation formats aforementioned, see Fig. 6.4(a). It should be noted that the proposed technique also allows the MDL compensation, although such results are not presented in this subsection.

Channel with MDL and crosstalk

Then, we consider a scenario in which the signal suffers of crosstalk induced after and before crossing the gain/loss dependent element. Therefore, in the multisection model are considered two spans of fiber, where each span has ten sections, and no in-line amplification is considered at the end of the second span of fiber.

In Fig. 6.4(b), it is shown the estimated MDL_{AVG} as function of the real value of MDL. The results obtained are quite similar to the ones previously presented for the link with MDL only. Moreover, the estimated and real values of the entire MDL vector as a function of the real value of MDL is also shown in Fig. 6.4(c). Results show that the proposed monitoring technique allows the successfully MDL estimation in the range 0 to 10 dB. For the MDL monitoring technique, the space-demultiplexing of the received signal is not required because the MDL estimation only comprises the calculation of the center of the constellations in the respective HoPs.

Due to crosstalk, the received signal appears mixed at the receiver side and therefore a space-demultiplexing stage must be considered in order to allow for the performance analysis of the MDL compensation technique. In that way, we consider a space-demultiplexing subtask, which is carried out by the complexity-reduced space-demultiplexing algorithm previously reported [11]. It should be emphasised that the performance of the space-demultiplexing can be affected by the MDL and, therefore, the MDL compensation must be performed before the space-demultiplexing. After the space-demultiplexing plus the MDL compensation, a Viterbi-Viterbi algorithm was employed for phase estimation; lastly, the phase offset is compensated. The SNR penalty is calculated according to 5.31, in which the average value of the EVM is considered in the calculations of the SNR. In Fig. 6.4(d), it is shown the SNR penalty of the post-processed signal with and without MDL compensation stage as a function of the MDL_{AVG}. For the case of space-demultiplexing without MDL equalization, the MDL induces a severe SNR degradation in the post-processed signal. For ≈ 5 dB of MDL_{AVG}, it is achieved a SNR penalty higher than 5 dB. In contrast, the space-demultiplexing aided by the proposed MDL compensation technique provides a SNR penalty almost negligible.

6.3 Simplified MDL monitoring and compensation technique

In order to decrease the computational complexity of the previously proposed MDL compensation technique, we have developed another approach in which the g_s translation matrices are independently calculated from the received signal, see 6.5. In this case, each translation matrix is calculated only once. Such simplification, however, implies a redefinition of the

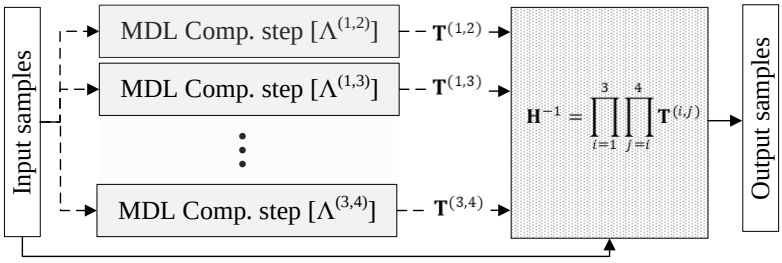

Figure 6.5: Schematic of simplified MDL monitoring and compensation technique.

parameter $\rho^{(f,g)}$ according to

$$\rho^{(f,g)} = -\frac{\max\left(\rho_f, \rho_g\right)^2 - \min\left(\rho_f, \rho_g\right)^2}{2n_k}, \tag{6.16}$$

with n_k denoting a normalization parameter. Since the matrices $\boldsymbol{T}^{(f,g)}$ are independently calculated from the received signal, the estimated inverse channel matrix receives several repeated contributions for the same MDL coefficient, hence over-estimating the MDL vector. In that way, we introduce the parameter n_k to compensate for such repeated contributions. Note that, n_k only depends on the number of spatial channels considered in the SDM transmission system. For the particular case of 2 and 3 spatial channels, n_k takes the value of 2 and 3, respectively. For the general case, equation (6.9) must be solved in order to calculate n_k. Then, the g_s translation matrices are calculated and employed to construct the inverse channel matrix. In each translation matrix, it is considered the parameter $\rho^{(f,g)}$ in order to cancel the power imbalances and re-center the constellation at the origin of the HoPs. It should be also emphasised that the translation matrices commute and, therefore, the sequence how such matrices are calculated and applied to the received signal can be neglected. The schematic of the simplified HoPs-based MDL monitoring and compensation technique is shown in Fig. 6.5.

6.3.1 Performance assessment

The performance of the simplified MDL compensation technique is analysed in terms $\mathrm{MDL_{AVG}}$ estimated and SNR penalty of the post-processed signal. We assume that the SDM transmission system induces crosstalk and MDL in the received signal and, therefore, the MDL compensation must be performed before the space-demultiplexing subtask.

Single MDL element and crosstalk

In this subsection, we assume that the signal suffers of crosstalk after and before crossing the gain/loss dependent element, as described in subsection 6.2.1. In Fig. 6.6(a), it is shown the estimated value of $\mathrm{MDL_{AVG}}$ as function of the real ones. For values higher than $\approx$ 6 dB, the error on the MDL estimation is higher than 0.5 dB, which can jeopardize the MDL monitoring and compensation. The estimated and real values of the entire MDL vector are also shown in Fig. 6.6(b), in which the values of ρ_i, with $i = 1, 2, 3$ and 4, were estimated from the PM-QPSK signals. Although not represented here, the results show that the performance of the MDL monitoring technique is quite similar for the three considered modulation formats. Nevertheless, the error on the MDL estimation tends to increase with

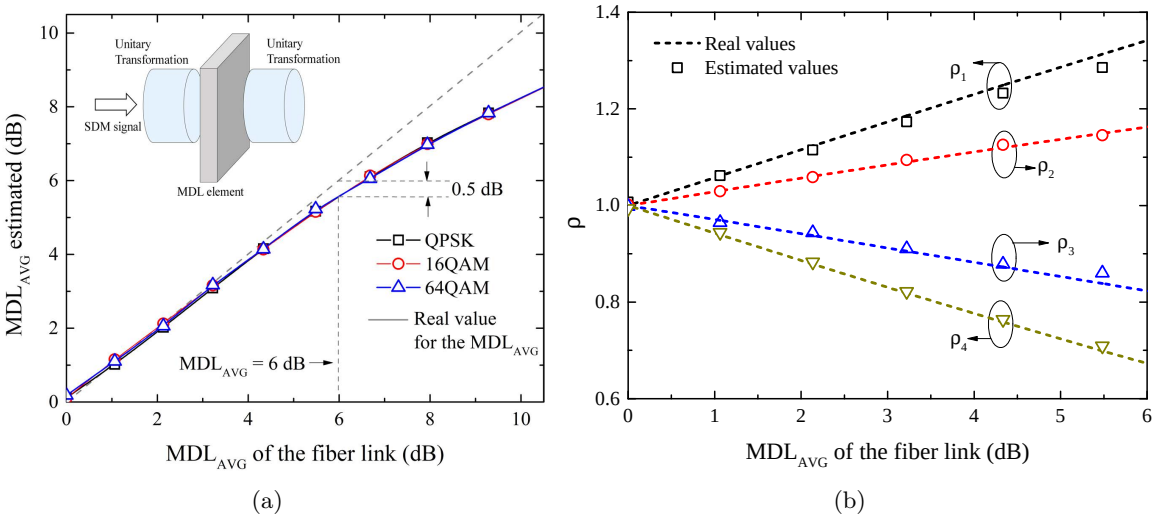

Figure 6.6: (a) Estimated value of MDL as function of the real value of MDL for a transmission system with two spatial channels, considering PM-QPSK, PM-16QAM and PM-64QAM signal. (b) Components of the MDL vector as function of the real ones. The four values of ρ are estimated from a PM-QPSK signal.

the real value of MDL. Such inaccuracies in the calculations of the MDL vector are due to the antisymmetric deformations induced by MDL, see Fig. 6.1. For a $\mathrm{MDL_{AVG}}$ = 0, the channel is free of MDL and therefore the transfer channels matrix can be described by a unity matrix with the eigenvalues equal to one. Henceforth, the value of 6 dB of $\mathrm{MDL_{AVG}}$ is assumed as the maximum value of MDL considered in the following performance analyses. However, it should be emphasised that such value is not the maximum amount of MDL that can be monitored and compensated by the proposed technique because, even in the presence of high values of MDL, the accurate MDL monitoring and compensation can be successfully carried out by considering several consecutive MDL compensation stages. In principle, the aforementioned symmetry distortions can be also considered in (6.7). In this sense, the error on MDL estimation can be substantially reduced by increasing the application range of the MDL monitoring and compensation technique.

In Fig. 6.7, it is shown the SNR penalty after the space-demultiplexing with and without MDL compensation stage as a function of the $\mathrm{MDL_{AVG}}$. Results show that MDL can induce severe SNR degradations in the received signal. However, when the space-demultuplexing is aided by the simplified MDL compensation technique the signal distortions arising from MDL can be fully compensated in the range of 0 to $\approx$ 5 dB. For large values of MDL and higher order modulation formats, the post-processed signal still present a nonnegligible SNR penalty. It should be emphasized that signals with higher orders of QAM constellations tend to show larger SNR penalties. Thus, the modulation format can apparently constrain the performance of the MDL compensation technique in the way that higher orders of QAM signals require larger numbers of samples to accurately estimate the center of the constellation. Such limitations can be overcome by using another MDL compensation stage placed after the space-demultiplexing plus the MDL compensation stage. In Fig. 6.7(c), we employ an additional MDL compensation stage to enhance the calculation of the inverse channel matrix, therefore improving the SNR of the post-processed signal. The two MDL compensation stages

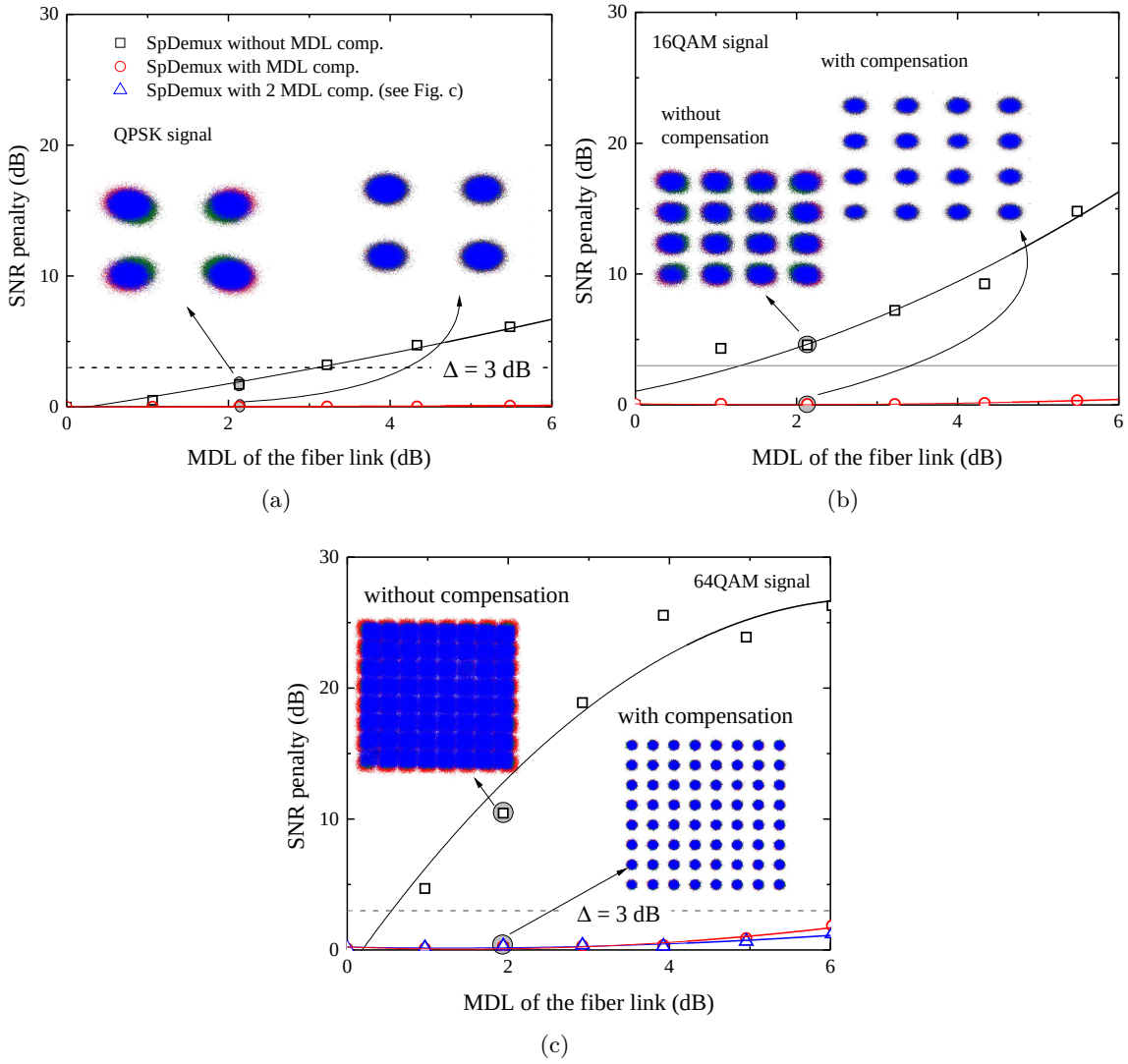

Figure 6.7: SNR penalty as function of the MDL_{AVG} for a (a) PM-QPSK, (b) PM-16QAM and (c) PM-64QAM signals after space-demultiplexing with and without MDL compensation. Insets show both constellations with and without MDL compensation. It is assumed that MDL is induced by a single element.

are considered after and before of the space-demultiplexing subtask.

As previously mentioned, the sample distributions in the HoPs are changed by crosstalk an MDL. Such distributions can be employed to deeply analyse the effect of the MDL compensation technique in the post-processed signal. With this aim in view, the Stokes parameters for the received signal and the post-processed signal with and without MDL compensation are compared with the B2B signal, see Fig. 6.8. The sample distributions analyzed in Fig. 6.8 are obtained from a PM-QPSK signal after propagated through a SDM link with 3 dB of MDL. The histograms with the Stokes parameters for a given HoPs are grouped by columns. While, the histograms with the Stokes parameters, $\Psi_1^{(f,g)}$, $\Psi_2^{(f,g)}$ and $\Psi_3^{(f,g)}$, are shown in the up, middle and down row, respectively. In dashed (black) line, it is drawn the histograms

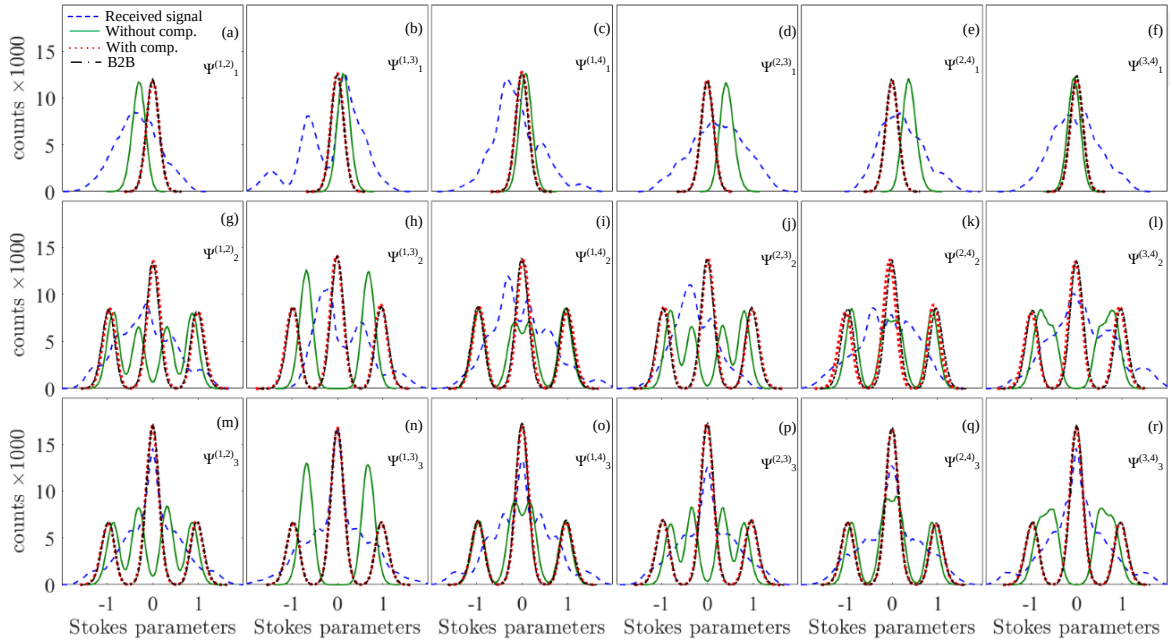

Figure 6.8: Stokes parameters histograms for a PM-QPSK signal transmitted transmitted through a SDM link with 3 dB of MDL. In blue the received signal before space-demultiplaxing and MDL compensation. In green/red the post-processed signal after MDL compensation using the parallel/series approach. In black the B2B signal. Lines are used (instead of 500 bars) to smooth the representation of all data in the same plot.

for the B2B signal, whose are characterized by a symmetry around the origin of the HoPs. The histograms for the received signal are drawn in short dash (blue) line. In this case, the aforementioned symmetry property is broken due to the crosstalk and MDL induced by the propagation along the SDM link. In solid (green) line, it is shown the histograms for the post-processed signal without MDL compensation. The shape of both distributions compare very well, i.e., the post-processed and the B2B signal. However, the entire distributions for the post-processed signal is shifted from the origin. By applying the MDL compensation stage, the achieved distributions match perfectly with the ones from the B2B signal showing therefore that MDL was fully compensated, see dotted (red) line in Fig 6.8.

6.3.2 Channel with distributed MDL and crosstalk

In this subsection, we assume a link with 10 spans of fiber, in which each span has 10 sections, and no in-line amplification is considered at the end of the last span of fiber. The performance of the MDL compensation technique is analysed for a SDM transmission system with a spatial diversity of 2, including the three aforementioned modulation formats. The SNR penalty after the space-demultiplexing with and without the MDL compensation is assessed as a function of the $\mathrm{MDL_{AVG}}$, see Fig. 6.9. In the three cases considered, the SNR penalty is substantially reduced when the second MDL compensation stage is considered. Therefore, the two MDL compensation stages allow to substantially improve the calculation of the inverse channels matrix, resulting in an almost negligible SNR penalty, see Fig. 6.9. When the transmission system has several elements with MDL, the space-demultiplexing

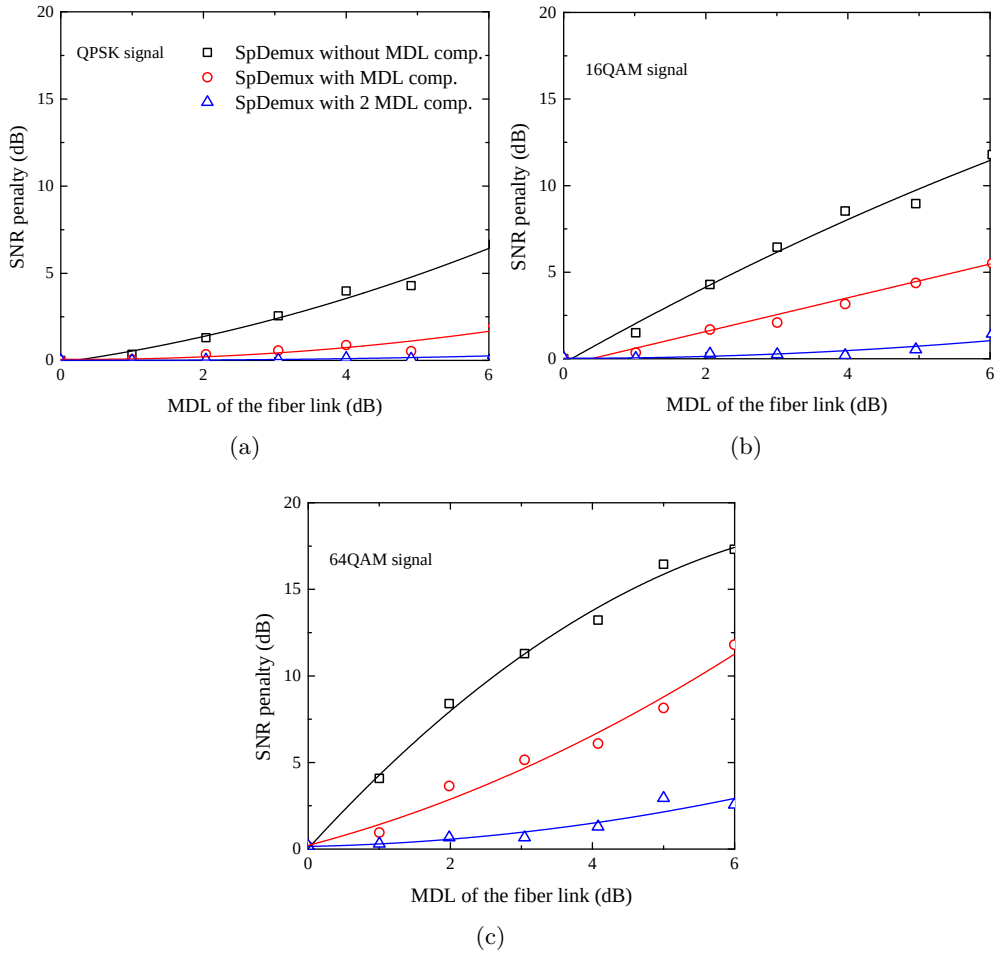

Figure 6.9: SNR penalty as function of the MDL_{AVG} for a (a) PM-QPSK, (b) PM-16QAM and (c) PM-64QAM signals after space-demultiplexing without MDL compensation, with a MDL compensation stage and with two MDL compensation stages. It is assumed that MDL is distributed along of the transmission system.

aided the simplified MDL compensation technique tends to require more than a single MDL compensation stage to successfully calculate the inverse channel matrix. Notice that the several rotations and translations suffered by the signal can difficult the accurate calculation of the central point of the constellation.

We also analyse the performance of the simplified technique for several transmission systems with distinct degrees of spatial diversity. In Fig. 6.10, it is shown the SNR penalty as a function of the MDL for the aforementioned transmission system with a spatial diversity of 3, 4, 6 and 7, i.e., assuming a 3-, 4-, 6- and 7-core CC-MCF. When considered the two MDL compensation stages, the SNR penalty can be almost fully compensated independently of the number of spatial channels considered in the transmission system. Results show that the MDL compensation technique is independent of the number of channels supported by the SDM transmission system.

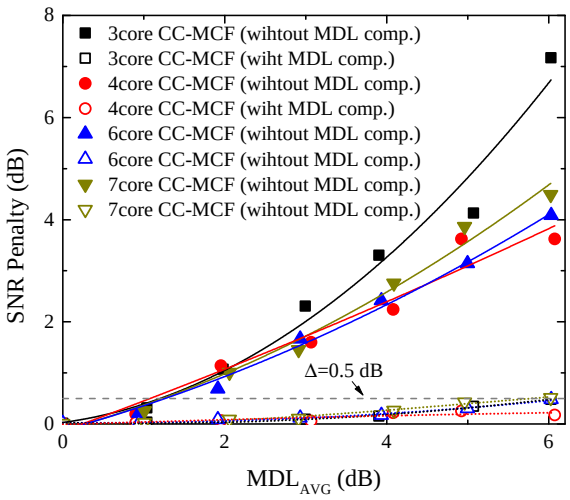

Figure 6.10: SNR penalty as function of the $\mathrm{MDL_{AVG}}$ for a SDM transmission system based on 3-core CC-MCF, 4-core CC-MCF, 6-core CC-MCF and 7-core CC-MCF. In the calculations of the inverse channels matrix is assumed two simplified MDL compensation stages placed after and before the space-demultiplexing subsystem. In each spacial channel, it is assumed a PM-QPSK signal.

Computational complexity

Since both HoPs-based MDL monitoring and compensation techniques require the calculation of the central point of the constellation, the computational complexity depends on the number of HoPs considered. The number of HoPss required by the first approach is given by

$$N_{\mathrm{HoPs,\ ref}} = 2g_s! \,. \tag{6.17}$$

While, for the simplified approach, the number of HoPss required by this one can be expressed as

$$N_{\mathrm{HoPs}} = g_s \,, \tag{6.18}$$

In each HoPs, the number of real multiplications, N_{m}, and additions, N_{s}, required to calculate the central point of the constellation is given by

$$N_{\mathrm{m}} = 9n_s + 1 \,, \tag{6.19a}$$

and

$$N_{\mathrm{s}} = 12n_s \,, \tag{6.19b}$$

respectively, with n_s denoting the number of samples. Thereby, the complexity reduction gain, G_{CR}, of the reduced-complexity approach over the first one can be written as

$$G_{CR}(\mathrm{dB}) = -10\log\left(\frac{N_{\mathrm{HoPs}}N_{\mathrm{m}}}{N_{\mathrm{HoPs,\ ref}}N_{\mathrm{m}}}\right). \tag{6.20}$$

The complexity reduction gain is calculated for a scenario with a single MDL element. It is assumed the results presented above for the PM-QPSK signal for an $\mathrm{MDL_{AVG}}$=3 dB, which results in a negligible SNR penalty for both cases. The number of samples considered in both cases is n_s = 10000 samples. Resulting in a complexity reduction gain of G_{CR} = 23.80 dB.

6.4 Summary

We show that MDL can induce a severe signal degradation in SDM transmission systems supported by digital space-demultiplexing based on HoPs. In this regard, we proposed a HoPs-based MDL monitoring and compensation technique which is modulation format agnostic, free of training sequences and robust to phase fluctuations and frequency offsets. The MDL vector is simply estimated by assessing the central point of the constellation in all HoPs, and the signal distortions induced by this phenomenon can be successfully compensated by re-centering the constellations at the center of the HoPs. After demonstrating the operation principle behind the HoPs-based MDL compensation, we propose a simplified approach with lower computational complexity, which allows to deal with MDL values as high as 6 dB. Furthermore, the technique is successfully tested in scenarios with MDL induced by a single element or distributed along the SDM link. In terms of SNR improvements, the MDL compensation stage provides a SNR gain of $\approx$ 3, 7 and 18 dB for a PM-QPSK, PM-16QAM and a PM-64QAM signals, respectively, assuming a single MDL element in a SDM transmission system with a spatial diversity of 2 and MDL of 3 dB.

Bibliography

[1] A. Andrusier, M. Shtaif, C. Antonelli, and A. Mecozzi, "Characterization of mode-dependent loss in SDM systems," in *Optical Fiber Communications Conference (OFC)*, March 2014, pp. 1–3.

[2] R. Ryf and N. K. Fontaine, "Space-division multiplexing and MIMO processing," *Enabling Technologies for High Spectral-Efficiency Coherent Optical Communication Networks*, pp. 547–608, 2016.

[3] G. Li, N. Bai, N. Zhao, and C. Xia, "Space-division multiplexing: the next frontier in optical communication," *Advances in Optics and Photonics*, vol. 6, no. 4, pp. 413–487, Dec 2014.

[4] S. Savory, "Digital coherent optical receivers: algorithms and subsystems," *IEEE Journal of Selected Topics in Quantum Electronics*, vol. 16, no. 5, pp. 1164–1179, 2010.

[5] N. Muga and A. Pinto, "Digital PDL compensation in 3D Stokes space," *IEEE/OSA Journal of Lightwave Technology*, vol. 31, no. 13, pp. 2122–2130, July 2013.

[6] H. Li, G. Huang, Z. Tao, H. Chen, S. Oda, Y. Akiyama, T. Yamauchi, and T. Hoshida, "An accurate and robust PDL monitor by digital signal processing in coherent receiver," in *Optical Fiber Conference (OFC)*. Optical Society of America, 2018, pp. M2F–6.

[7] B. Szafraniec, B. Nebendahl, and T. Marshall, "Polarization demultiplexing in Stokes space," *Optics Express*, vol. 18, no. 17, pp. 17 928–17 939, 2010.

[8] Z. Yu, X. Yi, Q. Yang, M. Luo, J. Zhang, L. Chen, and K. Qiu, "Polarization demultiplexing in Stokes space for coherent optical PDM-OFDM," *Optics Express*, vol. 21, no. 3, pp. 3885–3890, Feb 2013.

[9] J. N. Damask, *Polarization optics in telecommunications*. Springer Science & Business Media, 2004, vol. 101.

[10] G. M. Fernandes, N. J. Muga, and A. N. Pinto, "Space-demultiplexing based on higher-order Poincaré spheres," *Optics Express*, vol. 25, no. 4, pp. 3899–3915, Feb 2017.

[11] G. M. Fernandes, N. J. Muga, and A. N. Pinto, "Reduced-complexity algorithm for space-demultiplexing based on higher-order Poincaré spheres," *Optics Express*, vol. 26, no. 10, pp. 13 506–13 506, May 2018.

[12] F. J. Vaquero Caballero, A. Zanaty, F. Pittala, G. Goeger, Y. Ye, I. Tafur Monroy, and W. Rosenkranz, "Efficient SDM-MIMO Stokes-space equalization," in *European Conference on Optical Communication*, 2016.

Chapter 7

Conclusions and Future Work

In this dissertation, we have proposed novel techniques for signal processing in SDM transmission systems. The techniques developed in the framework of this thesis comprise both the optical and the digital domain. In the optical domain, we have developed novel mode/core switching techniques. In addition, we also have proposed analytical models for signal propagation in the multimodal regime. In the digital domain, we have developed a novel SpDemux algorithm and a MDL monitoring and compensation technique based on the signal representation in HoPss. In this Chapter, we overview the developed work, summarize the main conclusions, and present suggestions for future work.

7.1 Conclusions

The first major contribution of this thesis is presented in Chapter 3, where the signal switching between distinguishable spatial channels were numerically analyzed and experimentally demonstrated. The switching techniques are based on the A-O effect, in which an acoustic wave inscribes a sonic grating, or a periodic refractive index perturbation, in the core (or cores) of an optical fiber. In FMF, we have demonstrated the mode switching between two arbitrary optical modes, in which the mode switching depends in the period and in the symmetry of the index perturbation. By properly selecting the kind of acoustic waves, i.e., longitudinal or flexural, the transverse profile of the index perturbation can be properly chosen as symmetric or antisymmetric, respectively, while the period of the refractive index perturbation can be tuned by properly adjusting the RF signal applied on the PZT. Furthermore, we carried out an experimental validation of the proposed mode switching technique. In contrast, MCF possess physically unbundled cores requiring an additional mode to mediate the process of core switching. In this case, the optical signal is firstly coupled from a given core mode to a cladding mode, and afterwards, from this cladding mode to the desired core mode. In a 4-core MCF, it was demonstrated the core switching between two cores diametrally opposed and the uniform signal distribution by all the cores. Nevertheless, the core switching between two arbitrary cores can only be achieved using two flexural acoustic waves in HeMCF. Using a single acoustic wave, we have also shown that the proposed core switch can work as a tunable core attenuator.

Still regarding the mode switching, we have also investigated the possibility of all-optical mode switching by means of the nonlinear process of FWM in Chapter 4. Firstly, the multimodal generalized NLSE was extended to take into account the linear mode coupling in

order to accurately model the nonlinear signal propagation in the multimodal regime. From such equation, it was deduced a set of coupled equations that fully describe the multimodal FWM process. In optical few-mode microwires, which are multimodal and highly nonlinear waveguides, we have analyzed the phase matching condition between optical signals propagating in the same mode, intramodal phase matching condition, and between optical signals propagating in distinguishable modes, intermodal phase matching condition. Afterwards, we analysed the energy transfer induced by the multimodal FWM in optical microwires. Lastly, we have demonstrated that the multimodal FWM process can induce the signal switching in the multimodal regime, making the all-optical mode switching via nonlinear process feasible.

The digital space-demultiplexing for SDM-based transmission systems without spatial selectivity was addressed in Chapter 5. Firstly, we have analyzed the relation between the GSS and the HoPss. Secondly, the signal representation of complex-modulated signals in HoPss was introduced. Supported by this analyzes, we have developed digital HoPs-based space-demultiplexing techniques. In the respective HoPs, we have shown that an arbitrary pair of complex-modulated signals can be described by a lens-like object, and that object is rotated in the presence of crosstalk. Therefore, the lens-like object, or in a practical case the best fit plane to the received samples in the respective HoPs, must be realigned in order to compensate for the crosstalk between both tributaries. We have shown that the inverse channel matrix can be calculated through a progressive space-demultiplexing of all pairs of signals, in which the suitable sequence of HoPss presents the best least-square calculations. In order to decrease the computational effort of the space-demultiplexing algorithm, a reduced-complexity approach was proposed in which the inverse channel matrix is interactively constructed. The signal is space-demultiplexed in the g_s HoPss. After that, the pair of tributaries with the best least-square calculation is chosen for space-demultiplexing. Then, a similar process is employed to choose the second pair of tributaries, and so on; until all the g_s pairs of tributaries are space-demultiplexed. The process described above is repeated until all the best fit planes are successfully realigned. For the particular case of four tributaries, the complexity-reduced algorithm presents improvements of 97% in terms of convergence speed and 99% in terms of computational complexity over the previously proposed HoPs-based SpDemux algorithm. The proposed algorithm is also compared with the NLMS, showing an improvement of 84% in the convergence speed. It should also be emphasized that both HoPs-based space-demultiplexing algorithms do not require training symbols, are modulation format agnostic and robust to phase fluctuations and frequency offsets.

The subject of MDL monitoring and compensation is addressed in Chapter 6. Firstly, we have shown that MDL can induce a severe signal degradation in SDM transmission systems supported by digital space-demultiplexing based on HoPss. Then, the effect of MDL in a complex-modulated signal represented in HoPss was analyzed. We have shown that the MDL vector can be simply estimated by assessing the central point of the constellation in all HoPss, and the signal distortions induced by this phenomenon can be successfully compensated by re-centering the constellations at the center of the HoPss. Exploiting such principle, we have developed a HoPs-based MDL monitoring and compensation technique which is modulation format agnostic, free of training sequences and robust to phase fluctuations and frequency offsets. The proposed technique allows to deal with MDL values as higher as 6 dB. Furthermore, the technique is successfully tested in scenarios with MDL induced by a single element or distributed elements along the SDM link.

7.2 Future work

We consider that the results presented in this thesis are valuable and useful, and we believe that some subjects can be explored more thoroughly. Thus, from this work, several research directions remain open, from which we highlight the following:

- The switching techniques proposed in Chapter 3 are extensively analyzed using numerical methods. In addition, the mode switching is also experimentally validated at 630 nm. However, the experimental validation of both switching techniques at the standard telecommunications wavelengths remains as an open issue. We believe that the experimental validation and characterization of both proposed switching techniques will be certainly a step forward in the development and production of in-line switching devices based on the A-O effect. Such experimental validation may comprise the spectral characterization of the transmission window, the characterization of the transient time and the power consumption of the proposed devices.

- In Chapter 4, the signal switching through the multimodal FWM process is numerically investigated. Nevertheless, the experimental validation of these results is not addressed. Notice that this analysis is carried out for optical microwires, in which the value of the phase matching changes strongly due to the strong guiding regime. Therefore, we believe that highly nonlinear FMF with engineered dispersion profiles can pave the way for optical signal processing for SDM transmission systems based on multimodal FWM.

- The performance of the DSP algorithms developed in this thesis in Chapters 5 and 6, the space-demultiplexing algorithms and the MDL monitoring and compensation technique, respectively, was assessed from simulation results. Therefore, the performance assessment over experimental data remains as an open issue. The offline processing from experimental data is also needful to reinforce the validity of the proposed digital techniques, simultaneously assessing their performance from real data. After accurate assessment from experimental data, the proposed algorithms developed in the MATLAB environment can also be migrated to a hardware description language, such as VHDL, in order to allow for a hardware implementation. We also believe that real-time implementation can be carried out at low enough baud-rates using a field programmable gate array (FPGA) or several FPGAs connected in a parallel architecture.

- The digital techniques proposed in Chapters 5 and 6 are very sensitive to the cumulative effect of MD. In the single-mode case, the Stokes space-based PolDemux is also sensitive to the effect of PMD and therefore several digital subsystems for previous PMD compensation were proposed. Such stages tremendously increase the PMD tolerance of the PolDemux subsystem. In principle, the operation principle of such digital techniques can be also extended to SDM transmission systems and similar compensation stages for the MD can be employed before the HoPs-based SpDemux algorithm at the optical coherent receiver. We believe that such compensation techniques will be certainly a key tool in HoPs-based coherent receivers.

- We also believe that the HoPs-based digital techniques developed in Chapters 5 and 6 can be integrated into a single stage, thus allowing the run of the MDL compensation and the space-demultiplexing at a lower computational effort. Besides these two fundamental tasks, we also believe that the signal representation in HoPss can be also employed to

carry out other fundamental tasks in flexible optical networks with SDM, including phase tracking and modulation format recognition. It should be noted that algorithms for phase tracking and modulation format recognition based in the Stokes space were already reported for SSMF-based transmission systems.